RHEO-NMR AS A TECHNIQUE TO STUDY SHEAR-INDUCED TRANSITIONS IN NANOCOLLOIDAL SUSPENSIONS

by

Maribelle Anastasia Stanley

A dissertation submitted in partial fulfillment
of the requirements for the degree

of

Doctor of Philosophy

in

Chemical Engineering

MONTANA STATE UNIVERSITY
Bozeman, Montana

May 2025

©COPYRIGHT

by

Maribelle Anastasia Stanley

2025

All Rights Reserved

DEDICATION

"We pass through this world but once. Few tragedies can be more extensive than the stunting of life, few injustices deeper than the denial of an opportunity to strive or even to hope, by a limit imposed from without, but falsely identified as lying within."
-Stephen Jay Gould

I dedicate this to all students who have experienced domestic violence, abuse, assault, poverty, discrimination, or isolation.

When life says you can't, trust that you can.

ACKNOWLEDGEMENTS

I would like to acknowledge...

...Dr. Joseph Seymour and Dr. Sarah Codd for their kindness, support, and guidance. Their humility, professionalism, rigorous understanding of research, and enthusiasm both for science and people is an inspiration. I am incredibly grateful for their mentorship.

...Dr. Jim Wilking and Dr. Jen Brown. They have both been supportive role models for me throughout my PhD, and I am grateful for their willingness to serve on my committee.

...Kathryn Zimlich, who has been an incredible friend - especially when I most needed one.

...Dr. Scott Busse and Dr. Brian Tripet, who have kept the MR Lab equipment running smoothly, sometimes against the odds.

...Dr. Matthew Young, and his family, for their endless kindness and support. Matt and our dog, Keem, consistently shower me with unconditional love and corgi glitter, and I wouldn't have it any other way.

...my mother, Mary Stanley, and my sister, Dr. Meghaan Ferreira (née Smith). Without their examples as strong women in STEM, and the importance they both placed on education, I would not have endeavored on a PhD. I love you both.

...the MSU Norm Asbjornson College of Engineering and the Chemical and Biological Engineering Department for their gracious funding and support.

TABLE OF CONTENTS

1. INTRODUCTION 1

Outline 5

2. BASICS OF NUCLEAR MAGNETIC RESONANCE 7

Nuclear Magnetic Resonance Theory 7
Spin Theory and Larmor Precession 7
Net Magnetization 9
Excitation and Relaxation (T_1, T_2) 10
The Spin Echo and Carr-Purcell-Meiboom-Gill Echo-Train Pulse Sequences 13
The Bloch-Torrey Equations 15
Spectral Density Functions 15
The Fourier Transform and Inverse Laplace Transform 18
Gradients 19
Phase Encoding: The PGSE and Gradient Echo Sequences 21
Inverse Spaces: k-space and q-space 23
Selective and Non-selective Excitation 24
The Basic Components of an NMR Spectrometer 25
The B_0 Magnetic Field 27
The RF Coil 27
Gradient and Shim Coils 29
The Transmitter and the Receiver 30
Rheo-NMR: Drive-shafts 31
Sample cell 32
Motor 32
Microcontroller 33
Computer 33
Torque-sensing drive-shaft 33
NMR and Complex Motion 34
The Complex Motion Motivation 34
The Effective Gradient 36
Case 1: No spin motion 38
Case 2: Common motional behavior 40
Case 3: Brownian motion 42
Signal Attenuation 44
The Stejskal-Tanner Experiment 45
Expressing Echo Signal in Terms of Velocity 46
The Effect of Gradient Rise and Fall Times 47

TABLE OF CONTENTS – CONTINUED

The Pulsed Gradient Stimulated Echo Sequence 48
The Bloch-Torrey Analysis of Diffusion and Flow 50
Examining General Motion with the PGSE Using Propagator Formalism 51
The Narrow Gradient Pulse Approximation 51
Restricted Diffusion 55
Hydrodynamic Dispersion 56
Velocity Fluctuations 58
Double PGSE 58
Velocimetry 61
Physical constraints - Capillary flow 63
The basic velocimetry pulse sequence, signal, Fourier analysis, and propagator 63
The Two q-step Method 66
Fourier Analysis of the Two q-step Method 67
The Reference Phase Processing Method 68
Rapid Velocimetry Techniques 68
Velocimetry Applications 69
Rheo-NMR 69

3. RHEOLOGY AND COMPLEX FLUIDS 71

Rheology 71
Introduction 71
Rheological Models 74
Rheometer Basics 76
Complex Fluids 81
Introduction 81
Colloid Theory 82
Basics 82
Stability of Colloids 83
Van der Waals Interactions 84
The Hamaker Constant 85
Rigid (Stern) and Diffuse Layers 86
Debye Screening Length and Zeta Potential 87
DLVO Theory 88
Stable and Unstable Colloidal Suspensions 89
Spatially Resolved Rheometry 90
Nanocrystalline Cellulose (NCC) 91
Doi-Edwards and Leslie-Ericksen Theories for Modeling NCC's 92
Use of NMR to Understand NCC Mesostructure 93

TABLE OF CONTENTS – CONTINUED

Laponite® 94

4. RHEO-NMR VELOCIMETRY OF NANOCRYSTALLINE CELLULOSE SUSPENSIONS 96

Contribution of Authors and Co-Authors 96
Manuscript Information 97
Abstract 97
Introduction 97
Methods and Materials 99
Sample Preparation 99
Rheometry 99
Rheo-NMR Velocimetry 99
Results and Discussion 101
Rheometry 101
Rheo-NMR Velocimetry 101
Large-velocity Fluctuations 105
Funding Information 107
Author Contributions 107
Conflict of Interest 107
Ethical Approval 107
Data Availability Statement 107
References 107

5. RHEO-NMR VELOCIMETRY OF NANOCRYSTALLINE CELLULOSE SUSPENSIONS IN SODIUM CHLORIDE 109

Contribution of Authors and Co-Authors 109
Manuscript Information 110
Abstract 111
Introduction 111
Theory 113
Materials and Methods 114
Sample Preparation 114
Rheometry 115
Rheo-NMR Velocimetry 115
Results 119
Rheometry 119
Rheo-NMR Velocimetry 120
Discussion 123

TABLE OF CONTENTS – CONTINUED

Steady State Velocity Profiles....123
Velocity Fluctuations....125
Conclusion and Future Directions....126
Acknowledgments....127

6. RHEO-NMR VELOCIMETRY OF LAPONITE® NANOPARTICLE SUSPENSIONS....128

Contribution of Authors and Co-Authors....128
Manuscript Information....129
Abstract....130
Introduction....130
Rheometry with Laponite® RD suspensions....132
Materials and Methods....133
Sample Preparation....133
Rheo-NMR Velocimetry....133
Results and Discussion....135
Results....135
Discussion....152
Acknowledgments....152

7. NMR RELAXOMETRY OF NANOCRYSTALLINE CELLULOSE POROUS MEDIA
....154

Contribution of Authors and Co-Authors....154
Manuscript Information....155
Abstract....156
Introduction....156
Materials and Methods....158
Sample Preparation....158
Methods....159
Relaxation Measurements....159
Data Processing for Relaxation Measurements....160
Results and Discussion....160
1D-T_2 Distributions from ILT Analysis....160
Mono-Exponential Fits to 1D-T_2 Experiments....165
Discussion....167
Conclusion....169
Acknowledgments....169

TABLE OF CONTENTS – CONTINUED

8. CONCLUSION 170

Future Directions 171

REFERENCES CITED 175

APPENDIX: SUPPORTING INFORMATION FOR RHEO-NMR VELOCIMETRY OF NANOCRYSTALLINE CELLULOSE SUSPENSIONS IN SODIUM CHLORIDE 192

LIST OF TABLES

Table Page

1. Table 1 Rotor slip percentage and localized shear rates at rotor and stator....103

2. Table 2 Mean and standard deviation of velocity at three gap positions for transient data. 103

3. Table 3 Gap positions (mm) where $\dot{\gamma}_H$ and $\dot{\gamma}_L$. 106

4. Table 6.1 Rotor slip percentages for all $\dot{\gamma}$, days, and Laponite® concentrations 136

5. Table 6.2 Mean and % RMS of velocity at three gap positions for transient data, Day 1....136

6. Table 6.3 Mean and % RMS of velocity at three gap positions for transient data, Day 2....137

7. Table 6.4 Mean and % RMS of velocity at three gap positions for transient data, Day 3....137

8. Table 6.5 Mean and % RMS of velocity at three gap positions for transient data, Day 4....138

9. Table 6.6 Mean and % RMS of velocity at three gap positions for transient data, Day 5....138

10. Table 7.1 T_2 values from 1D-T_2 distributions at 0, 10, and 100 hours for 30% w/v NCC 162

11. Table 7.2 T_2 values from 1D-T_2 distributions at 0, 10, and 100 hours for 50% w/v NCC 162

12. Table 7.3 T_2 values from 1D-T_2 distributions at 0, 10, and 100 hours for 70% w/v NCC 162

LIST OF FIGURES

Figure Page

1. Figure 2.1 Spins in a magnetic field and Larmor precession.....8
2. Figure 2.2 The Zeeman Effect - Energy diagram 9
3. Figure 2.3 T_1 relaxation - vector diagram.....11
4. Figure 2.4 Hahn Echo - T_2 relaxation 12
5. Figure 2.5 Spin Echo and CPMG pulse sequences 13
6. Figure 2.6 T_1-T_2 correlation plot 17
7. Figure 2.7 The gradient magnetic field 20
8. Figure 2.8 PGSE and Gradient Echo Pulse Sequences 22
9. Figure 2.9 Slice-selective and non-selective excitation 25
10. Figure 2.10 Hardware components of an NMR spectrometer. 26
11. Figure 2.11 RF coil circuit.....28
12. Figure 2.12 RF coil configurations. 28
13. Figure 2.13 Rheo-NMR Drive-Shafts 31
14. Figure 2.14 Rheo-NMR sample cell 32
15. Figure 2.15 Examples of complex motion, (I).....35
16. Figure 2.16 Examples of complex motion, (II). 35
17. Figure 2.17 Effective gradients.....37
18. Figure 2.18 Spin translating under a gradient 38
19. Figure 2.19 Gradient pulse sequences and the plots of their successive gradient moments. 41
20. Figure 2.20 CPMG diffusion hops 42
21. Figure 2.21 The Stejskal-Tanner Experiment 46
22. Figure 2.23 Pulsed Gradient Stimulated Echo.....49
23. Figure 2.24 Propagator formalism for PGSE.....53

LIST OF FIGURES – CONTINUED

Figure Page

24. Figure 2.25 Restricted diffusion as a function of gradient flow encoding time 56

25. Figure 2.26 Taylor dispersion in a pipe..... 57

26. Figure 2.27 Examples of fluid dispersion..... 57

27. Figure 2.28 Double PGSE (Compensated)..... 59

28. Figure 2.29 The basic velocimetry pulse sequence 64

29. Figure 2.30 The two q-step velocimetry pulse sequence..... 66

30. Figure 3.1 The Two-Plate Model..... 72

31. Figure 3.2 Rheometer modes of deformation. 72

32. Figure 3.3 Schematic of the shear-banding phenomenon in complex fluids. 73

33. Figure 3.4 Stress σ vs. shear rate $\dot{\gamma}$ for common rheological models. 77

34. Figure 3.5 Stress response of a fluid to strain described by the phase angle δ..... 78

35. Figure 3.6 Ideal elastic and ideal viscous stress-strain relationships..... 79

36. Figure 3.7 Real and ideal bouncy ball analogy..... 79

37. Figure 3.8 Comparison of rheometer geometries. 80

38. Figure 3.9 DLVO Theory..... 89

39. Figure 3.10 Schematics of Laponite® structures 95

40. Figure 1 Viscosity vs. applied shear rate and shear stress vs. applied shear rate from bulk rheometry experiments on NCC suspensions. 100

41. Figure 2 Rheo-NMR Couette cell schematic. 100

42. Figure 3 PGSE pulse sequence with double slice selection used to acquire 1D velocity profiles.....101

43. Figure 4 1D NMR velocimetry experiments for NCC2, 3% w/v suspension. 102

LIST OF FIGURES – CONTINUED

Figure Page

44. Figure 5 1D NMR velocimetry experiments for NCC3, 5% w/v suspension. 104

45. Figure 6 1D NMR velocimetry experiments for NCC1, 7% w/v suspension. 105

46. Figure 7 1D NMR velocimetry experiments for NCC4, 12% w/v suspension. 106

47. Figure 5.1 Rheo-NMR sample Couette cell schematic. 116

48. Figure 5.2 PGSE with double slice selection. 117

49. Figure 5.3 Shear stress vs. applied shear rate and viscosity vs. applied shear rate for NCC-salt suspensions. 119

50. Figure 5.4 1D NMR velocimetry experiments for NCC-salt suspensions. 121

51. Figure 5.5 1D NMR transient velocimetry experiments for NCC-salt suspensions. 122

52. Figure 6.1 Rheo-NMR sample Couette cell schematic. 134

53. Figure 6.2 Steady-state velocimetry experiments for Laponite® concentrations over multiple days. 139

54. Figure 6.3 Steady-state up and down ramp velocimetry experiments for 2.0% w/v Laponite®. 140

55. Figure 6.4 Steady-state up and down ramp velocimetry experiments for 3.2% w/v Laponite®. 141

56. Figure 6.5 Steady-state up and down ramp velocimetry experiments for 4.0% w/v Laponite®. 142

57. Figure 6.6 Steady-state up and down ramp velocimetry experiments for 5.0% w/v Laponite®. 143

58. Figure 6.7 Transient velocimetry experiments for 2% w/v Laponite®. 144

59. Figure 6.8 Transient velocimetry experiments for 3.2% w/v Laponite®. 145

60. Figure 6.9 Transient velocimetry experiments for 4% w/v Laponite®. 146

61. Figure 6.10 Transient velocimetry experiments for 5% w/v Laponite®. 147

LIST OF FIGURES – CONTINUED

Figure Page

62. Figure 7.1 The Carr-Purcell-Meiboom-Gill (CPMG) pulse sequence and depiction of the resulting RF echo signal. 159

63. Figure 7.2 1D T_2 Probability distributions for 30%, 50%, and 70% w/v NCC with 0, 0.05, and 0.1 M NaCl. 161

64. Figure 7.3 Average T_2 values for 30%, 50%, and 70% w/v NCC with 0, 0.05, and 0.1 M NaCl. 165

65. Figure A.1 1D NMR velocimetry experiments for a 3% w/v NCC suspension. 193

66. Figure A.2 1D NMR velocimetry experiments for a 5% w/v NCC suspension. 194

67. Figure A.3 1D NMR velocimetry experiments for a 7% w/v NCC suspension. 195

68. Figure A.4 1D NMR velocimetry experiments for a 12% w/v NCC suspension. 196

69. Figure A.5 1D NMR velocimetry experiments for a 3% w/v NCC suspension in 0.1 M NaCl. 197

70. Figure A.6 1D NMR velocimetry experiments for a 5% w/v NCC suspension in 0.05 M NaCl. 198

71. Figure A.7 1D NMR velocimetry experiments for a 5% w/v NCC suspension in 0.1 M NaCl. 199

72. Figure A.8 1D NMR velocimetry experiments for a 7% w/v NCC suspension in 0.1 M NaCl. 200

73. Figure A.9 1D NMR velocimetry experiments for a 12% w/v NCC suspension in 0.1 M NaCl. 201

74. Figure A.10 Velocity autocorrelation functions for 10k cSt silicone oil Newtonian control. 202

75. Figure A.11 Velocity autocorrelation functions for 3% w/v NCC with 0 and 0.1 M NaCl. 202

76. Figure A.12 Velocity autocorrelation functions for 5% w/v NCC with 0, 0.05, and 0.1 M NaCl. 203

LIST OF FIGURES – CONTINUED

Figure Page

77. Figure A.13 Velocity autocorrelation functions for 7% w/v NCC with 0 and 0.1 M NaCl. 204

78. Figure A.14 Velocity autocorrelation functions for 12% w/v NCC with 0 and 0.1 M NaCl. 204

79. Figure A.15 Fourier transforms of velocity autocorrelation functions for 3% w/v NCC with 0 and 0.1 M NaCl. 205

80. Figure A.16 Fourier transforms of velocity autocorrelation functions for 5% w/v NCC with 0, 0.05, and 0.1 M NaCl. 206

81. Figure A.17 Fourier transforms of velocity autocorrelation functions for 7% w/v NCC with 0 and 0.1 M NaCl. 207

82. Figure A.18 Fourier transforms of velocity autocorrelation functions for 12% w/v NCC with 0 and 0.1 M NaCl. 208

ABSTRACT

Complex fluids like ketchup, toothpaste, and yogurt exhibit shear-rate dependent material properties such as viscosity and can be challenging to measure and study. Nanocrystalline cellulose (NCC) and Laponite® are two complex fluids composed of nanoscale rods and discs, respectively. Due to their nanoscale constituents which can form mesoscale structures, both fluids exhibit complicated flow behavior. This behavior depends on variables like concentration, shear rate, time, ionic species concentration, and others. NCC and Laponite® find use in applications ranging from tissue engineering to electric sensors, and it is necessary to understand their flow behavior to properly design industrial products and processes.

Standard rheometry techniques complemented with Rheo-NMR velocimetry and relaxometry have been leveraged to measure the flow of NCC and Laponite® aqueous suspensions. While standard rheometry provides bulk flow information which is readily comparable to known fluid flow models, Rheo-NMR velocimetry and relaxometry offer insight into the mesoscale flow behavior. In this work, Rheo-NMR has been used to generate velocity profiles with spatial resolution on the order of tens of microns and temporal resolution on the order of seconds. With this data we have observed short time-scale velocity fluctuations in a 5% w/v liquid crystal NCC suspension which have previously only been modeled for rod-like liquid crystal polymers. In addition, we have observed concentration, shear, and time-dependent complex fluid flow behavior, e.g. yield stress, stick-slip and shear banding, for both NCC and Laponite®. Additional experiments on NCC with added NaCl have revealed a dependence of flow behavior on ionic concentration which correlates to solid to liquid phase transitions, including viscoelastic liquid, gel and glass-type behavior. NMR relaxometry experiments of highly concentrated NCC suspensions ($\geq$ 30% w/v) undergoing hydration show magnetization signal changes that indicate a dependence of water distribution on ionic concentration, as well as a dependence on hydration time.

This data provides information about mesoscale flow behavior not attainable with traditional rheometry and offers insight into the structural changes of NCC and Laponite® during shear. Such information can be used to inform fluid models, product design, and manufacturing processes that enable a broader application of these fluids for consumer use.

1

INTRODUCTION

"Everything flows and nothing abides; everything gives way, and nothing stays fixed."
-Heraclitus (circa 500 BC)

The human experience involves constant change, and Heraclitus captured this well many centuries ago with the expression, "everything flows" [132]. The sentiment must have seemed purely philosophic for a great many years, but within it hid physical wisdom which we now understand. The rivers and oceans flow with ease, yet the seat you sit in stubbornly (and graciously) will not give way, and the mountains sit solidly in place. Liquids flow, while solids do not. But is that really so?

Therein lies the problem. How exactly does one define a liquid, or a solid, for that matter? Most learn early in their education that we define a solid as a crystalline network of atoms with a definite size, and a liquid as a loosely associated collection of atoms which flow to fill the space of their container. But if you have ever squeezed a tube of toothpaste, or kneaded a ball of bread dough, you may have already realized that there are solid-like liquids, and liquid-like solids, and all manner of matter in between.

Throughout early history, observers noticed these curious, but useful fluids, like clay and soap, and sought to understand their flow better. In 1687, when Sir Isaac Newton described the phenomenon of a fluid's resistance to flow, which we now call viscosity, humanity took a revolutionary step forward in understanding fluids [114]. Newton recognized that the internal friction of molecules within a fluid gives rise to this resistance. This explains why, for instance, water flows more readily than honey. Despite how revolutionary Newton's discovery was, Newtonian fluids – fluids that flow at a rate proportional to the force applied to them, and thus have a constant viscosity – would come to describe only a small fraction of the

fluids that exist. The remaining curious fluids, which flow at a rate that is not proportional to the force applied to them, are called complex fluids [96]. Throughout the 17th, 18th, and 19th centuries, works from Pascal, Bernoulli, Navier, Stokes, Maxwell, Boltzmann, Einstein, and numerous others would provide the foundations to describe fluid flow in many different contexts [15, 23, 24, 66, 102, 113, 121, 153]. Yet there lacked a concentrated field of study dedicated to understanding complex fluids.

Throughout the second industrial revolution in the latter part of the 19th century, it had become increasingly apparent that complex fluids were both a blessing and a curse. The advent of the paper, chemical, and petroleum manufacturing industries enabled incredible advancements in technology and quality of life [111]. Yet, they required an understanding of unpredictable and temperamental fluids that thwarted progress at every turn. In 1929, Eugene C. Bingham proposed the term rheology to describe this burgeoning field that desperately needed organization and focused effort. The word was derived from the Greek words for "everything flows", *panta rhei*, on the suggestion of Bingham's colleague Markus Reiner [18]. This field, which remains alive and well today, concerns itself with the study of the flow and deformation of fluids [11, 110].

So, rheology was born, to understand the many curious fluids that humanity has not only observed from antiquity but has now learned to develop for its own ends. What we find is what Heraclitus once observed: everything does, indeed, flow. And it is the character of that flow which offers us a glimpse into the structure of a fluid. Fluids may be as simple as honey, or as complex as the oil found deep beneath the Earth's surface, but by careful measurement of the flow, we can uncover the connections between a fluid's molecular structure and its mesoscale structure [96]. A great deal of progress has been made in the field with the advent of standard techniques introduced in the late 19th and 20th century [60]. However, modern advancements in rheology necessitate the use of alternative techniques, both experimental and mathematical, which complement standard measurements.

The basic concept of rheometry – the measurements used in rheology - is that by sliding a fluid along a surface in a controlled way, or by extending or compressing that fluid against a surface, we can measure how the fluid flows in response [109, 110]. This response tells us useful information about how we might expect this fluid to flow in different situations. We can not only gain new information about known fluids but also use that to inform the development of new fluids.

The most common instrument used for this purpose is called a rheometer (a more detailed description of the rheometer can be found in Chapter 3). Rheometers operate with what is known as the viscometric flow assumption, which assumes that the fluid flows with a laminar flow profile [110]. Complex fluids, however, have complicated internal structures on the nanometer or micrometer scale that disturb flow and defy the rheometer's critical assumption. This means experiments with rheometers on complex fluids often struggle to fully describe the behavior of these important materials [96].

In the past several decades, numerous alternative and complementary strategies to measure complex fluid flow have arisen. Many rely on optical methods. These often suffer from challenges with sample transparency constraints, require certain sample geometries, or are invasive from addition of tracer particles. In addition, they may have high precision, but they also have limitations in the time and length scales which are measurable [35].

A method which mitigates many of these limitations, called Rheo-NMR, is employed in the works described here. Nuclear Magnetic Resonance (NMR) is commonly associated with trips to the medical clinic, where it is called magnetic resonance imaging (MRI). In that context, NMR differentiates between fat and water molecules, and the tissue the molecules are in, to image health problems. However, NMR can also differentiate between molecules moving at different speeds and track their motion at a variety of length and time scales [37]. This means that NMR can show the microscale disordered motion that rheometers cannot. NMR fulfills this function because it can measure the intrinsic physical property of

atoms known as spin. Spin is a complicated quantum mechanical property with no classical analogue, but it is influenced by magnetic fields in predictable ways that are exploited by NMR technology [37]. It is this ability to manipulate and detect changes in spins that allows for the powerful molecular tracking of NMR on various scales. In addition, NMR does not require transparent samples, is not invasive, and does not generally have prohibitive constraints on sample geometry and size, which can make it better suited for many fluids than optical methods [35].

In addition to experimental analysis, there is a long history of mathematical theory and modeling to understand complex fluids [60, 177]. Theory and models exist symbiotically with experiments. Experimental data inform models and aid in the generation of new theory, while theory and models complement and extend experimental knowledge. In many cases, mathematical modeling provides a surrogate for experiments which, at the current level of technology, cannot be performed. Models such as these often focus on complex fluids, which, as mentioned, defy common experimental techniques and can exhibit dynamics across multiple scales – simple to probe computationally, but less so experimentally.

The fluids studied in the works described here include colloids, which are a subclass of complex fluids [96]. Colloids, also called colloidal suspensions, exhibit properties between a true solution and a true suspension. True solutions contain a solute and a solvent that are of similar sizes and are chemically miscible, while true suspensions contain solute particles that are often much larger than the solvent and have a greater density, such that they settle due to gravity. Typical colloidal suspensions contain solute sizes on the order of nanometers to micrometers, which generally do not settle both because of their size relative to the solvent (inducing Brownian motion) and their electrostatic charges relative to each other and the solvent molecules [138]. Colloidal suspensions also range widely in their constituents and their different applications. They commonly occur in food, like milk and mayonnaise (emulsions), as well as personal care products, like shaving creams (foams) and lotions

(gels and creams) but can also include solid suspensions such as plastics with dispersed pigments [96]. Many next-generation materials are also colloids. These include the nanoscale suspensions described in this work, nanocrystalline cellulose (NCC) and Laponite® RD (described in detail in Chapter 3).

At present, both NCC and Laponite® RD are being explored for biomedical applications such as drug composites, tissue engineering, medical implants, and numerous others [39, 74, 117, 159]. NCC has also found important applications in electronics, such as in sensors and batteries, flexible printed circuitry, and windows with voltage-controlled opacity, among others [144, 146, 159]. Additionally, both materials are used in cosmetics and personal care products, and even for geotechnical purposes, such as soil replacements [159]. As the popularity of these materials increases, so does the interest in their physical behaviors and the discovery of new and exciting utilities for them [39, 128, 146, 159].

The works which encompass this manuscript describe successful attempts to characterize the mesoscale structure and behavior of NCC and Laponite® RD in various experimental contexts, including Rheo-NMR velocimetry, diffusion, and relaxation experiments. The authors hope that these works will contribute to other experimental and modeling efforts that build upon the knowledge base of these materials and others like them.

Many centuries have past, but Heraclitus's words have never rung truer than they do today. As more materials are discovered and developed that continually defy the established understanding of fluid physics, we still find that everything flows – and certainly, nothing stays fixed.

Outline

Chapter 2 describes the basics of NMR, including the fundamental physics, instrument hardware, and experimental techniques which underlie the research works herein. A summary of rheology and complex fluids, including the two fluids explored in these works –

nanocrystalline cellulose and Laponite® RD – can be found in Chapter 3. NMR velocimetry of aqueous suspensions of nanocrystalline cellulose at various concentrations (3%, 5%, 7%, and 12% w/v) and shear rates ($\dot{\gamma} = 0.9$, 2.8, and 4.6 s^{-1}) are explored in Chapter 4 [149]. The data demonstrates notable velocity fluctuations at the 5% w/v liquid crystal concentration, which are investigated through velocimetry with a different NCC material source, which alters the behavior, in Chapter 5. Chapter 5 also provides velocimetry for 3%, 7%, and 12% w/v concentrations with the different source NCC, and addresses the impact of ionic species on flow behavior with the addition of 0.05 M and 0.1 M NaCl. Velocimetry experiments on Laponite® RD at varying concentrations (2%, 3.2%, 4%, and 5% w/v) and shear rates ($\dot{\gamma} =$ 0.9, 2.8, and 4.6 s^{-1}) as a function of aging over the course of several days constitute Chapter 6 and show significant stick-slip behavior. In Chapter 7, a study of hydration dynamics with NMR relaxometry for NCC at varying concentrations (30%, 50%, and 70% w/v) with added NaCl (0, 0.05 M and 0.1 M) over the course of approximately 5 days provides insight into the structural rearrangements with hydration and the effect of electrostatic screening.

BASICS OF NUCLEAR MAGNETIC RESONANCE

Nuclear Magnetic Resonance Theory

Spin Theory and Larmor Precession

Atomic nuclei with odd numbers of nucleons possess a quantum mechanical property known as spin, also referred to as nuclear angular momentum, which dictates their behavior in a magnetic field [36]. Nuclei which possess spin will precess around a magnetic field similar to how a spinning top precesses around an axis in the gravitational field (Figure 2.1). This process is known as Larmor precession, and the frequency of this precession, called the Larmor frequency, depends on a quantity called the magnetogyric ratio (γ). The magnetogyric ratio, a constant property of a given nuclei ($\gamma = 2.675\,221\,874\,4 \times 10^8 \frac{\text{rad}}{\text{T s}}$ for a hydrogen nucleus), represents the ratio of a nuclei's magnetic moment to its angular momentum ($\gamma = \frac{\mu}{L}$) [36]. The Larmor frequency depends not only on the magnetogyric ratio of the spin species of interest, but also on the strength of the static magnetic field, B_0, shown in Equation 2.1:

$$\omega_0 = \gamma B_0 \tag{2.1}$$

A spin in a magnetic field can exist in two discrete energy levels based on its nuclear angular momentum quantum number, I [36]. For a hydrogen nucleus denoted ^{1}H, $I = \pm\frac{1}{2}$, and demonstrates a "spin $\frac{1}{2}$ nucleus". The two available values for I indicate "spin up" and "spin down" states, which correspond to energy levels within the magnetic field based on the Zeeman interaction. The spin Hamiltonian, demonstrated below, expresses this energy in terms of the Zeeman interaction [36]:

$$\mathcal{H} = -\gamma\hbar B_0 I_z \tag{2.2}$$

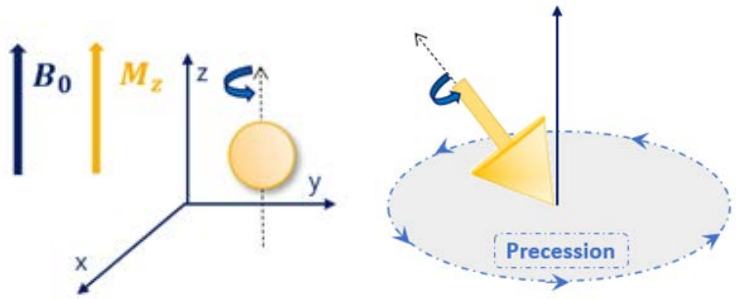


Figure 2.1: Left: An individual spin in a static magnetic field, B_0 depicted in the typical x-y-z coordinates, with net magnetization M_z depicted in the $+z$ direction. Right: A classical spinning top which precesses about a gravitational axis. This analogy can serve as an intuitive, semi-classical description of Larmor precession, a quantum phenomenon in spin-active nuclear species [37].

This expression indicates the kinetic energy ($\mathcal{H}$) as a function of the magnetic field strength and the spin angular momentum quantum number (where constants are γ, already defined as the magnetogyric ratio, and $\hbar$, which represents the reduced Planck's constant). The interaction of spins with a magnetic field thus exhibits a relationship with the strength of the magnetic field where the energy gap between the energy levels increases as B_0 increases. Regardless of the value of I_z, $\mathcal{H} = -\gamma\hbar B_0$ always represents the gap between the energy levels [36].

The spin up state ($I = +\frac{1}{2}$) represents a lower energy state, where the spin aligns (parallel) with the direction of the magnetic field (e.g., how a bar magnet would align with an external magnetic field). Conversely, the spin down state ($I = -\frac{1}{2}$) represents the higher energy state, where the spin aligns antiparallel with the magnetic field. [36] In a population of spins, a Zeeman equilibrium state between the two energy levels exists where the spins are in thermal equilibrium with their surroundings. The Boltzmann distribution represents this equilibrium state, shown below [36]:

$$\frac{N_{+\frac{1}{2}}}{N_{-\frac{1}{2}}} = \exp\left(-\frac{\Delta E}{k_B T}\right) \tag{2.3}$$

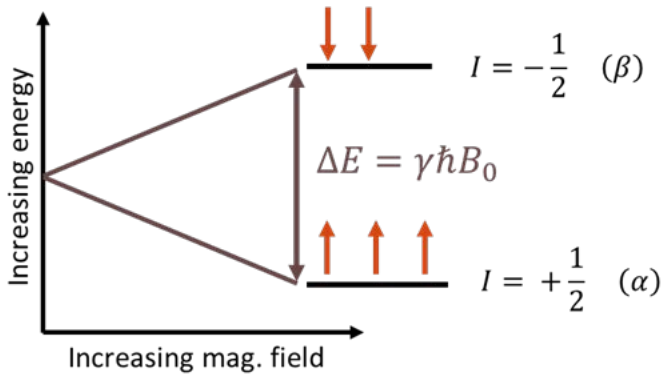


Figure 2.2: A depiction of the Zeeman effect, which describes the equilibrium splitting of energy levels for a population of spins in a magnetic field.

Manipulation of the magnetic field can disturb the equilibrium population between these two states. Nuclear magnetic resonance (NMR) techniques measure the disturbance and the restoration of this equilibrium. This process underlies the excitation and relaxation processes critical to nuclear magnetic resonance studies [36].

Net Magnetization

In a sample of water used in NMR, approximately 10^{23} hydrogen atoms exist as a spin system [37]. A population of spins in a static magnetic field, each with their own small individual magnetization, will collectively exhibit a macroscopic **net magnetization**. NMR spectrometers measure subtle changes of this value [37].

In magnetic resonance, this net magnetization aligns with the static B_0 field. Custom dictates that the B_0 field should point in the $+z$ direction and refer to the net magnetization as M_{net}, depicted as M_z in Figure 2.1 [37]. This depiction exists in the *rotating frame*, which contrasts with the lab frame [22]. The lab frame describes the point of view of a researcher in the lab, where hydrogen nuclei precess at their Larmor frequency within the static magnetic field. NMR experiments necessitate, as described in the next section, that we perturb a sample with an additional magnetic field, applied in the form of a pulse which oscillates at

the Larmor frequency. This pulse and the mathematics which describe the resulting effects can be greatly simplified by assuming a rotating coordinate frame, where the frame rotates at the Larmor frequency. To imagine the effect of a rotating coordinate frame, you can imagine two vantage points (an analogy adapted from [22]). In one, you stand in the middle of a traffic round-a-bout; in the other, you sit as a passenger in a car that drives around the round-a-bout. If you stand in the middle, it appears that you are at rest while all the cars are moving; however, if you sit as a passenger, it may seem that the person in the middle of the round-a-bout rotates while you feel motionless in the car. In the remainder of the discussion presented, all descriptions and expressions of magnetization take place in the rotating frame, unless otherwise noted.

Excitation and Relaxation (T_1, T_2)

The application of a magnetic pulse that oscillates at the Larmor frequency excites spins in the spectrometer [37]. This pulse is called an "applied pulse", "resonant pulse", or simply "RF pulse", and it oscillates "on resonance" with the Larmor precession frequency of the spins, causing spins to raise their energy levels in a process known as "excitation". A pulse applied precisely on resonance can change the initial net magnetization position, aligned with the magnetic field, based on the duration of the pulse. This shifts the net spin phase by $\gamma B_1 t_p$, where B_1 is the strength of the applied B_1 magnetic field pulse, and t_p is the duration of the field pulse. Commonly, one designs pulses to render the net magnetization perpendicular (90°, or $\frac{\pi}{2}$) or antiparallel (180°, or π) to its initial position based on the duration of the pulse [37]. Pulses not precisely on resonance have applications in selective excitation NMR, described in a later section.

With spin excitation naturally comes spin relaxation. As mentioned, excitation increases the energy levels of the spins, and alters the direction of the net magnetization vector, yet on a quantum level more subtle effects occur [37]. A 180° pulse, which causes

spins to orient antiparallel to the static magnetic field, will change the Boltzmann distribution such that nearly all spins are in the higher energy, spin down state. Such a high energy state, once the perturbation ceases, must necessarily return to its equilibrium state, or "relax". The process by which this occurs is known as longitudinal, or T_1, relaxation [37].

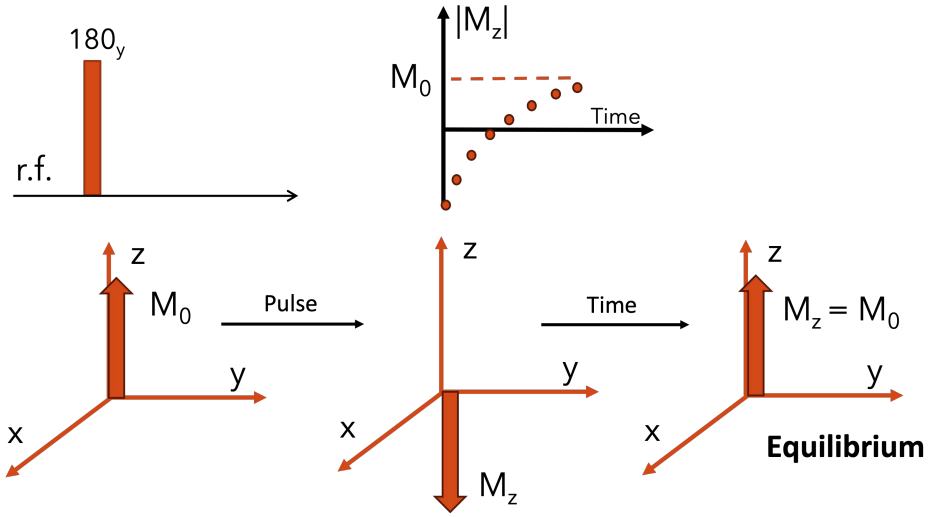


Figure 2.3: The process of T_1 relaxation in vector format. A 180° pulse causes the inversion of the $+z$-direction net magnetization, which eventually returns to the equilibrium magnetic signal with the time constant T_1.

Longitudinal relaxation involves interactions of spins with their molecular thermal and magnetic environment [76]. The excitation of a spin "flips" it to its higher energy spin state, and it will subsequently dissipate energy by its interactions with the fluctuating electric/magnetic domains of other molecules as they undergo various modes of thermal motion (e.g., vibration, rotation, and translation). One should note that the term "spin-lattice" relaxation still commonly replaces "longitudinal relaxation" as the term for this process in the literature [76]. "Spin-lattice" acknowledges the early days of solid-state NMR experiments where the "lattice" indicated an interaction between the excited spins and the solid molecular crystal that held them in place. The term "lattice" in modern NMR usage of "spin-lattice" is understood as a reference to the surrounding thermal reservoir of various

material states (solid, semi-solid, and liquid). Longitudinal relaxation causes an exponential decay of magnetization signal over time and is thus also called T_1 relaxation, since T_1 is the time constant of this decay. Figure 2.3 depicts the effect of T_1 relaxation on net magnetization after a 180° pulse.

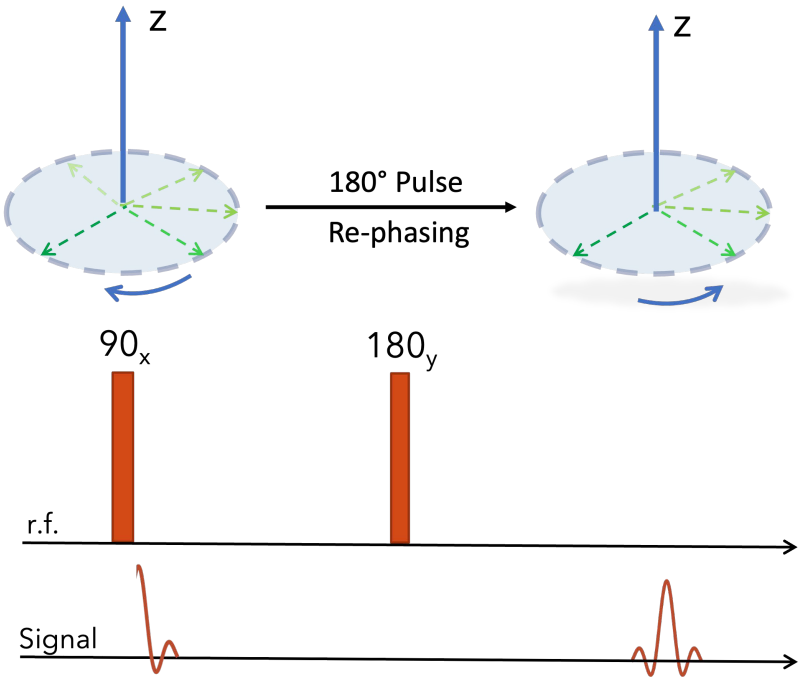


Figure 2.4: A depiction of spin vector dephasing (after a 90° pulse) and recoherence (after a 180° pulse) in the transverse plane, characteristic of T_2 relaxation. The expected decay and echo signals correspond to dephasing and recoherence, respectively.

Another type of relaxation called transverse relaxation also occurs after spin excitation. In this case, spins mainly relax by interacting with other spins as opposed to interacting with the fluctuating thermal and magnetic environment [76]. After applying a 90° pulse, the Zeeman equilibrium state of the spins remains, but the spins which contributed to the net magnetization, M_z, now orient in the transverse plane. This causes a change in the spin phase. Initially, all spins that re-orient precess with the same new phase (these spins precess in coherence). However, the spins eventually no longer have the same phase, instead having

phases that are "spread out". Figure 2.4 depicts this process, called, decoherence, along with recoherence, which will be described in the next section. This process mainly occurs as spins sample other spins' magnetic domains and exchange longitudinal angular momentum. A spin "flip-flop" colloquially describes the purely T_2 relaxation interaction, where both spins in a pair alter their spin state (e.g., one spin will change state from up to down, and the other will change state from down to up) [36, 98]. If this process occurs to an even pairing of spins (e.g., every spin with a partner that simultaneously switches spin state with it), no net change in the energy distribution of the spin state occurs (the proportion of spins in up and down states remains the same). However, if an unequal pairing of spins undergo this exchange, a net change to the energy population distribution does occur, which thus impacts the longitudinal relaxation. As a result, the process of spin phase decoherence known as T_2 relaxation can also induce longitudinal relaxation [37].

The Spin Echo and Carr-Purcell-Meiboom-Gill Echo-Train Pulse Sequences

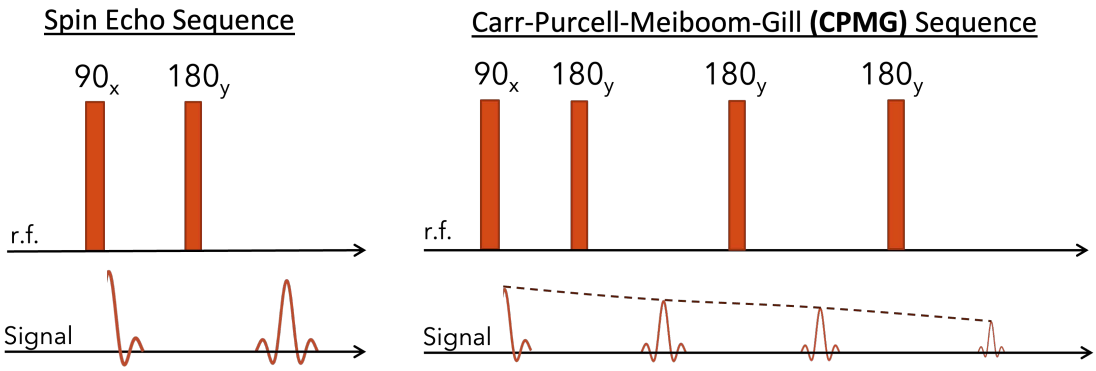


Figure 2.5: Left: The spin-echo pulse sequence, consisting of a 90° pulse and a 180° pulse, which gives rise to the Hahn echo. Right: The Carr-Purcell-Meiboom-Gill (CPMG) pulse sequence, which provides a sequence of echo signals. The fitting of the amplitudes of each echo provides a decay curve which will have a time constant representative of the "true T_2".

The spin-echo pulse sequence (Figure 2.5, left), discovered by Erwin Hahn in 1950 [78], consists of a 90° RF pulse, followed by a 180° RF pulse after a designated time τ. The

90° pulse serves to tip the spins into the transverse plane. There, the spins sample the magnetic field in their localities as well as the magnetic fields of the spins which surround them, allowing for both reversible and irreversible changes in phase [37]. The 180° pulse then brings the spins back into coherent phase. This causes a build-up, and eventual decay, of signal, as the spins come into coherence and again decoherence when they sample the magnetic environment once again [37].

This pulse sequence measures T_2 relaxation through the decay of the echo signal, as described in the section above; however, an important distinction must be made between the T_2 relaxation value obtained from this sequence and the one obtained from a Carr-Purcell-Meiboom-Gill ("Echo Train", CPMG) sequence. The CPMG sequence, described in detail in the next section, measures the true T_2 value. In contrast, the T_2 value obtained from a spin-echo pulse sequence is known as the T_2^* ("tee-two-star") value [37].

The CPMG pulse sequence (Figure 2.5, right), developed by Carr and Purcell in 1954 [40] and subsequently modified by Meiboom and Gill [105], measures the "true" T_2 value. Multiple 180° RF pulses after the initial 90° pulse enable a repeated refocusing of the decoherent spin signal, and the time delay between pulses allows the measurement of a full echo signal from each refocusing pulse. This results in a series of echoes, the amplitudes of which form a signal "envelope" that exhibits exponential decay. The time-constant of this decay, perhaps unsurprisingly, is T_2. A particular benefit of the CPMG sequence as opposed to the spin-echo lies in its ability to average the signal, thus obtaining an advantage in signal to noise [37].

The distinction between T_2^* and T_2 comes mainly from the inhomogeneities of the magnetic field [37]. The irreversible change of phase which develops when a spin samples their magnetic surroundings results directly from the Brownian, stochastic motion of that spin. The paths that a spin takes in the field, which naturally alters the spin's phase, cannot be re-traced due to this randomness which renders it irreversible. *Reversible* changes of spin

phase occur because of magnetic field inhomogeneities (a property of both the spectrometer field and the field inhomogeneities in the sample, but *not* related to the Brownian motion of spins). The CPMG pulse sequence refocuses this inhomogeneity, causing the spins to repeatedly "retrace" their paths and lose the associated phase changes. As a result, the true T_2 value, ideally, expresses a quantity independent of the field which measured it. Since the measurement of T_2^* does not refocus magnetic field inhomogeneities, the value of T_2^* includes both the loss of phase from magnetic field inhomogeneities – a function of the field itself – as well as the random phase decoherence that occurs from Brownian motion of spins, a natural and unavoidable experimental reality [37].

The Bloch-Torrey Equations

The Bloch-Torrey equations (Equations 2.4-2.6), derived in 1956 [21], [158], describe the process of spin-equilibrium in a semi-classical fashion. They derive from a phenomenological basis and offer a fundamental connection between spin magnetization changes, the B_0 and B_1 fields, and T_1 and T_2. Their use in describing magnetization "transport" will prove fruitful in later discussions of diffusion and flow (see the subsection *The Bloch-Torrey Analysis of Diffusion and Flow* in the *NMR and Complex Motion* section).

$$\frac{dM_x}{dt} = \gamma M_y(B_0 - \frac{\omega}{\gamma}) - \frac{M_x}{T_2} \tag{2.4}$$

$$\frac{dM_y}{dt} = \gamma B_1 - \gamma M_x(B_0 - \frac{\omega}{\gamma}) - \frac{M_y}{T_2} \tag{2.5}$$

$$\frac{dM_z}{dt} = \gamma M_y B_1 - \frac{M_z - M_0}{T_1} \tag{2.6}$$

Spectral Density Functions

Other expressions for transverse and longitudinal relaxation exist. Through a simple statistical mechanic treatment of the discrete energy transitions underlying longitudinal relaxation (for which the reader may consult [37] for the relevant derivation), and the use of

representative correlation functions, one can obtain a lab-frame expression for T_1 (Equation 2.7) in terms of spectral density functions, shown as $J^{(n)}(n \cdot \omega_0)$.

$$1/T_1 = (\mu_0/4\pi)^2\gamma^4\hbar^2\frac{3}{2}I(I+1)[J^{(1)}(\omega_0) + J^{(2)}(2\omega_0)] \tag{2.7}$$

These functions occur from the Fourier transform of the correlation functions and represent the *frequencies of molecular motion present in the signal* which contribute to the relaxation time [90]. A similar expression exists for T_2 (Equation 2.8); in this case, given that transverse relaxation is best described in the rotating frame, the derivation requires a different approach. For the purposes of this manuscript it suffices to note that Equation 2.8 results from the use of density operator formalism in the rotating frame applied to the dipolar Hamiltonian, the solution of which provides a linear differential equation (LDE) that depicts exponential relaxation [37]. The oscillatory phase factors in the resulting LDE exhibit dipolar correlation functions as in the case of longitudinal relaxation. Naturally, when Fourier transformed, they also express spectral density functions.

$$1/T_2 = (\mu_0/4\pi)^2\gamma^4\hbar^2\frac{3}{2}I(I+1)\Big[\frac{1}{4}J^{(0)}(0) + \frac{5}{2}J^{(1)}(\omega_0) + \frac{1}{4}J^{(2)}(2\omega_0)\Big] \tag{2.8}$$

Different spectral density functions can model different types of molecular motion. When substituted into Equations 2.7 and 2.8, these will provide expressions for expected T_1 and T_2 behavior given that type of molecular motion. In the case of a simple, isotropic rotational diffusion model (which nicely describes the fluctuations that occur in many simple

liquids), the following functions apply [37]:

$$J^{(0)}(\omega) = \frac{24}{15r_{ij}^6}\frac{\tau_c}{1+\omega^2\tau_c^2} \tag{2.9}$$

$$J^{(1)}(\omega) = \frac{4}{15r_{ij}^6}\frac{\tau_c}{1+\omega^2\tau_c^2} \tag{2.10}$$

$$J^{(2)}(\omega) = \frac{16}{15r_{ij}^6}\frac{\tau_c}{1+\omega^2\tau_c^2} \tag{2.11}$$

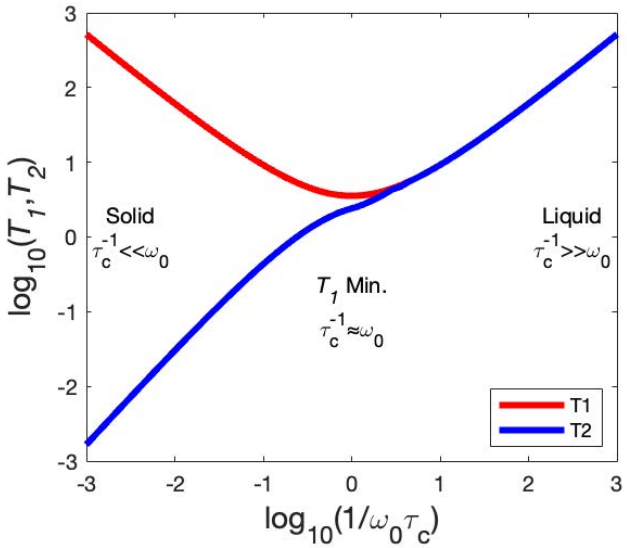


Figure 2.6: The relationship between T_1, T_2, and τ_c. This plot demonstrates three distinct regions of motion that correspond to different levels of molecular motion, which represent different states of matter; T_1 and T_2 values can thus indicate what types of motion exist in a sample. Figure reproduced with permission from Matthew C. Young, 2023.

On substitution of these functions into the expressions for T_1 and T_2, an important relationship between the two relaxation times emerges, depicted in Figure 2.6. This plot describes the changes in T_1 and T_2 as functions of changing correlation time, τ_c, and for a fixed Larmor frequency, ω_0. Three important features result: firstly, a region of divergence on the left side of the plot, where $T_1 \gg T_2$ and $1/\tau_c \ll \omega_0$, called the *motionally broadened regime*; a minimum in T_1, where $\omega_0\tau_c = 1$; and a region where $T_1 \approx T_2$ and $1/\tau_c \gg \omega_0$, called the *motionally narrowed regime*. The motionally broadened regime describes slow molecular

motion which results from highly viscous liquids and polymer solutions, while the motionally narrowed regime describes fast molecular motion from simple, small molecule liquids [37].

Importantly, these relationships hold regardless of how many dipolar interactions occur, only requiring a simple scaling. In addition, alterations of the spectral density functions can represent other interactions, such as those due to translational motion or quadrupole interactions [90], and still result in the same general relationship between T_1 and T_2 [36]. As a result, this figure offers a powerful conceptual resource for relaxation studies.

The Fourier Transform and Inverse Laplace Transform

The data generated by NMR experiments initially exist as electronic signals in time; as described in the *The Basic Components of an NMR Spectrometer* section, the spectrometer will sample and digitize this data according to its settings. The result, a discrete, time-domain signal, contains a variety of information at multiple length and time scales. The experimenter then must determine what analysis method will isolate the data of interest to their system.

Two main mathematical transforms, required for a variety of science and engineering enterprises, also underpin the analysis methods central to NMR: the Fourier transform (FT), and the inverse Laplace transform (ILT). The Fourier transform takes the time-domain signal as an input and outputs a spectrum of the sinusoidal frequencies which occur in it – a fine-grain process powerful for applications ranging from spectroscopy to imaging [36, 37]. The inverse Laplace transform, on the other hand, takes the time-domain (complex) signal and provides a real probability distribution of a quantity (e.g., diffusion coefficients, or relaxation rates) represented by the decay characteristics of the signal. It also provides powerful information about the structure of a sample through a more coarse-grained approach [37].

Equations 2.12 - 2.13 below shows the mathematical pair of a time-domain signal and

its Fourier transform; similarly, Equations 2.14 - 2.15 shows the pair of a time-domain signal and its inverse Laplace transform [37]. One should note that the experimenter cannot apply the analytical solution of the ILT to the time-domain signal. Though a discretized expression exists for the solution, it tends to approach an infinite asymptote as noise enters the signal (since the expression multiplies the time-domain signal by an exponential function in time). As a result, the discretized ILT expression must come from a process of non-negative least squares, the application of prior knowledge, and the use of Tikhonov regularization, which serves to estimate a solution to a Fredholm integral of the first kind [69]; for a detailed explanation, the reader may consult Callaghan (2011), Sections 9.1-9.3 [37].

Fourier transform pair:

$$f(\omega) = \mathcal{F}\{S(t)\} = (2\pi)^{-1/2} \int_{-\infty}^{\infty} e^{i\omega t} S(t)\, dt \tag{2.12}$$

$$S(t) = \mathcal{F}\{f(\omega)\} = (2\pi)^{-1/2} \int_{-\infty}^{\infty} e^{i\omega t} f(\omega)\, d\omega \tag{2.13}$$

Inverse Laplace transform pair:

$$f(R) = \mathcal{L}^{-1}\{S(t)\} \tag{2.14}$$

$$S(t) = \mathcal{L}\{f(R)\} = \int_{0}^{\infty} f(R) e^{-Rt}\, dR \tag{2.15}$$

Gradients

The basic NMR pulse sequences described thus far exhibit great utility in measuring relaxation rates. These sequences and their measurements, however, represent only one part of NMR capabilities. Those which remain rely mostly on the use of magnetic field *gradients*.

Since, as we recall from the previous sections, the frequency of a spin in a magnetic field depends on the strength of the field, it follows that if the strength differs spatially, the spin frequency will also differ spatially (exhibited mathematically in Equations 2.16-

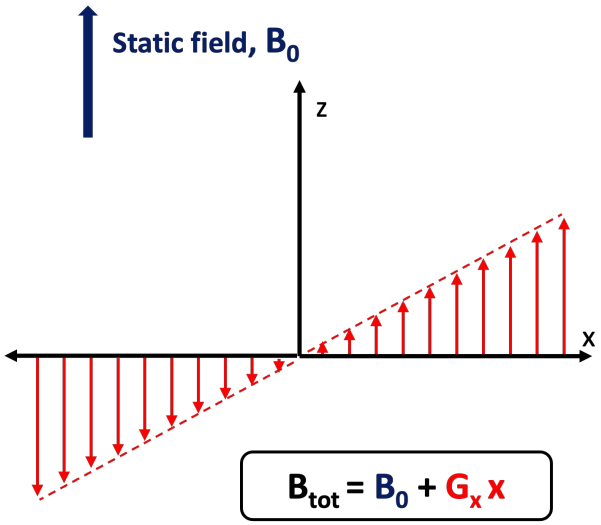


Figure 2.7: The depiction of a gradient which provides a linearly calibrated magnetic field, in addition to the static field and resonant applied field. A gradient field allows for the measurement of spin position and motion.

2.18, where we consider a single gradient in the z direction which varies spatially in x, y, and/or z). Such a concept explains the purpose of magnetic field gradients and underpins an entire experimental technique (magnetic resonance imaging, or MRI), perhaps one of the most important imaging discoveries in the past century (especially in medical research and diagnostics) [36]. Magnetic field gradients allow for a spatial calibration of the B_0 field. The B_0 field, after the addition of a gradient, will exhibit a linear dependence on position, as exhibited by Figure 2.7.

$$\omega_0 = \gamma \left| \mathbf{B}_{tot} \right| \tag{2.16}$$

$$\mathbf{G} = \nabla B_z \tag{2.17}$$

$$\omega_0(\mathbf{r}) = \gamma B_0 + \mathbf{r} \cdot \mathbf{G} \tag{2.18}$$

This, of course, makes not only imaging possible, since we can know the location of a spin in the field, but also flow measurements. We can measure a spin's change in location *and*

measure the time which passes during the change, providing velocity. We can also measure higher moments of motion that give more intricate information about the dynamics of our system (discussed in the *NMR and Complex Motion* section) [37]. The implications make for a plethora of experiments with powerful spatial and motional information.

Gradients operate with an RF pulse sequence. The act of putting a gradient "on" involves sending RF current to the gradient coils (explained in the *The Basic Components of an NMR Spectrometer* section) for a specific time duration, called a *gradient pulse*. RF pulse sequence diagrams often demonstrate these pulses as rectangular boxes that indicate the "sign" of the gradient, the duration, and the time between successive pulses [37, 90].

Phase Encoding: The PGSE and Gradient Echo Sequences

The application of a gradient to a B_0 magnetic field, as mentioned, applies a linearly varying spatial magnetic field, and spins in the field have a frequency associated with their position. If all spins are stationary, their phases (dependent on their frequencies) will exhibit a dependence on the linear field in a helical fashion, described by Figure 2.8 [139]. A single gradient pulse, paired with a 90° RF pulse, can *phase encode* the spins with their locations. The resulting echo signal decay contains these phases, and the corresponding locations revealed after a simple Fourier transform. This forms the most basic imaging sequence [37].

However, upon a subsequent application of a 180° RF pulse after the initial gradient pulse, this phase-encoded helix becomes inverted (phases flip their direction); another gradient pulse then "unwinds", or recalls, the spin phases [37]. This - a 90° RF pulse, followed by a gradient pulse, a 180° RF pulse, and another gradient pulse - forms the *pulsed gradient spin echo* (PGSE) pulse sequence [103], [152], depicted in Figure 2.8.

This sequence may not immediately appear useful, but consider the highlighted phases connected by the red arrow shown in Figure 2.8. If a spin moves from position z_1 to z_2

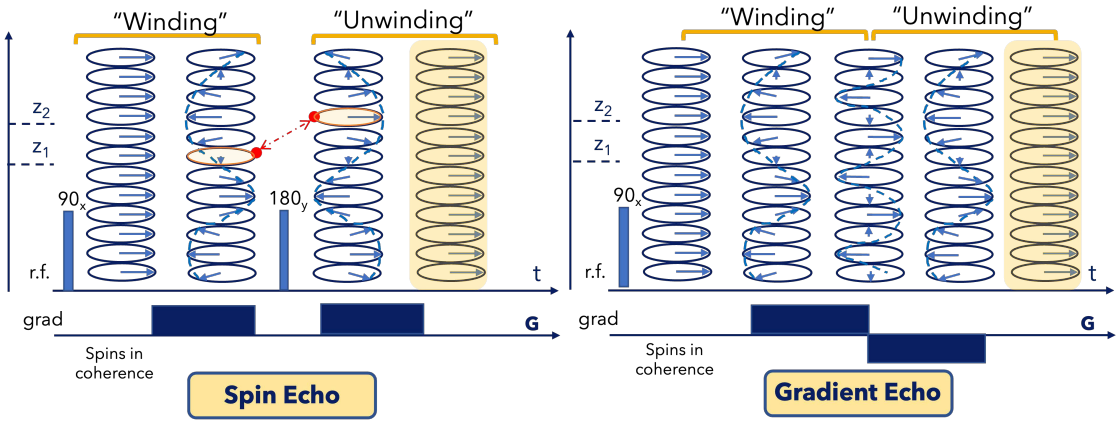


Figure 2.8: A depiction of the pulsed gradient spin echo (left) and the gradient echo (right) pulse sequences, and the spin "helices" which help to explain the "winding" and "unwinding" effect. This effect gives rise to phase encoding, and the cumulative phase change (Equation 2.19) allows for a determination of spin motion. Adapted from Paul Callaghan, 2011 [37]

in the field, its phase will change in accordance with the gradient helix, thus encoding its location in the field through its phase. The second gradient pulse recalls this change in phase by "unwinding" the helix. The spin returns to phase coherence with the other spins in the sample at the end of the sequence, but the individual spin's location change now exists in the echo signal as a cumulative phase change, shown in Equation 2.19 (naturally, a large number of spins must change location to generate a sizable change in signal, but we consider this individual spin's situation as a thought experiment) [37]. When one knows the displacement of a species, as well as the time over which displacement occurred, one also knows the species' velocity. This pulse sequence forms the basis for analyzing motion with NMR, upon which much more complicated sequences exist.

$$\Delta\phi = \gamma\delta g(z_1 - z_2) \tag{2.19}$$

Another simple pulse sequence for motion analysis also exists: the *gradient echo*. In this pulse sequence, a 90° RF pulse excites the spins, a positive gradient encodes the spins, and

a negative gradient both reverses the phase and unwinds the gradient [37]. Though a nearly identical procedure to the PGSE, it does not require a 180° RF pulse.

Inverse Spaces: k-space and q-space

A characteristic wavelength describes the phase-encoding helix of spin phases under a gradient [36]. This wavelength, λ, expresses a relationship with an inverse space based on the strength of the gradient and the magnetogyric ratio. In the case of NMR, two inverse spaces, k-space and q-space, facilitate the description of imaging and motion respectively [36, 37]. In these spaces, $\mathbf{k}$ and $\mathbf{q}$ represent vectors expressed in either angular or cyclic frequency. The Equations below, 2.20 and 2.21 - 2.22, explain the relationship between the helix wavelength, the $\mathbf{k}$ and $\mathbf{q}$ vectors (synonymous, but defined based on the context of imaging or motion), and the aforementioned variables; they also express these vectors in terms of the gradient pulse length, δ.

$$\lambda = \frac{2\pi}{\gamma \mathbf{g} t} \tag{2.20}$$

$$\mathbf{k} = \gamma \delta \mathbf{g} = \frac{2\pi}{\lambda}, [\mathrm{m}^{-1}], \text{ for imaging} \tag{2.21}$$

$$\mathbf{q} = \gamma \delta \mathbf{g} = \frac{2\pi}{\lambda}, [\mathrm{m}^{-1}], \text{ for motion} \tag{2.22}$$

From these definitions, we can represent our signal and its inverse (Fourier conjugate) with the following equations [37]:

$$S_N(\mathbf{k}) = \int \rho_{(\mathbf{r})} e^{(i\mathbf{k}\cdot\mathbf{r})} d\mathbf{r} \tag{2.23}$$

$$\rho(\mathbf{r}) = \int (2\pi)^{-1} S_N(\mathbf{k}) e^{(-i\mathbf{k}\cdot\mathbf{r})} d\mathbf{k} \tag{2.24}$$

Where $\mathbf{r}$ describes a generic vector in space $(x, y, \text{or} z)$, $S_N(\mathbf{k})$ describes our signal in k-space, and $\rho(\mathbf{r})$ represents our *spin density*.

Imaging requires that we sample at discrete points, and since we chose to describe our signal in k-space, we must collect our data at discrete points in this inverse space. This presents little challenge, but does dictate that we consider our sampling range in k-space and its conjugate relation, field-of-view (FOV), in real space (Equations 2.25 and 2.26 below), [37]:

$$\Delta l = \frac{1}{2\check{k}_{max}} \tag{2.25}$$

$$\text{FOV} = \frac{1}{\Delta\check{k}} = \frac{N}{2\check{k}_{max}} \tag{2.26}$$

Where $\check{k}$ represents the cyclic frequency form of the k vector, $\check{k}_{max}$ describes the largest magnitude of the k vector, $\Delta\check{k} = \dfrac{2\check{k}_{max}}{N}$ expresses the stepping interval in k-space, and Δl expresses the stepping interval in real space; N, naturally, represents the number of steps or discrete points. Synonymous relationships exist for q-space. For a more in-depth description of these spaces and their purpose in NMR, the reader should refer to [36].

Selective and Non-selective Excitation

Gradients also facilitate *selective excitation*. A gradient can phase encode the spins in a sample, and a simultaneous *selective* RF pulse can excite spins in a specific slice of the sample by matching the frequency of those spins with the frequency of the pulse [37]. A sinc-shaped pulse in time performs this function, which, given the Fourier relationship, represents a hat function in the frequency domain (and conveniently, the spatial domain, as our gradient proportionally relates frequency to location). This presents the characteristic rectangular "slice" of an MRI image, often associated with cross-sections of the human body. Figure 2.9 (left) shows examples of slice-selective excitation.

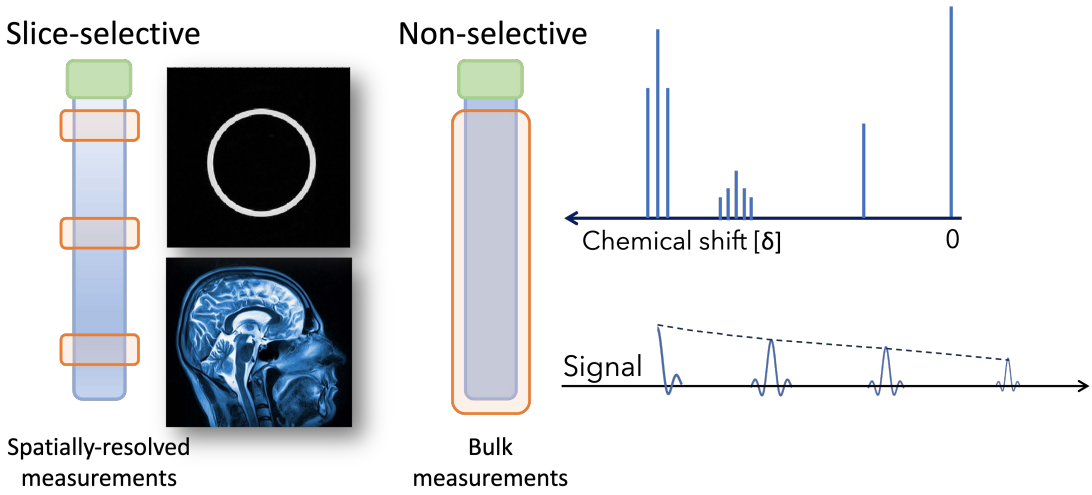


Figure 2.9: A depiction of slice-selective excitation (left) and non-selective excitation (right) and corresponding applications. Slice-selective application finds applications in areas which require cross-sectional imaging or fluid motion (top, an MRI image of a fluid gap of a Rheo-NMR Couette sample cell; bottom, an MRI image of a human brain (© Adobe Stock Images)). Non-selective excitation finds use in bulk measurements of samples, like chemical frequency spectra (top) or bulk relaxation CPMG decays (bottom).

Non-selective excitation occurs in the absence of gradients, with RF pulses that excite all frequencies present within the sample. Directly converse to the case of a slice-selective pulse, non-selective pulses use hat shapes in time, which represent sinc-shaped pulses in the frequency domain. A well-configured hat-shaped RF pulse will appropriately excite most frequencies within its first lobe [37]. RF pulse sequences, like those shown in this manuscript, depict rectangular-shaped pulses to indicate non-selective, or total, excitation. Figure 2.9 (right) shows examples of bulk measurements which require non-selective excitation.

The Basic Components of an NMR Spectrometer

Nuclear magnetic resonance spectrometers vary in their geometries, strengths, and purposes but generally require the same basic components. These are depicted in Figure 2.10, and include [83]:

- A stable, strong, and homogeneous magnetic field.
- A probe design that allows radiofrequency coils used to excite and detect the signal.
- A high-power radiofrequency transmitter which delivers short pulses.
- A sensitive receiver which can amplify NMR signals from the excited spin sample.
- A converter/digitizer which converts NMR signals to digital form for computer storage.
- A pulse programming system to produce precise pulses and delays.
- A central computer system to control these functions and process data.

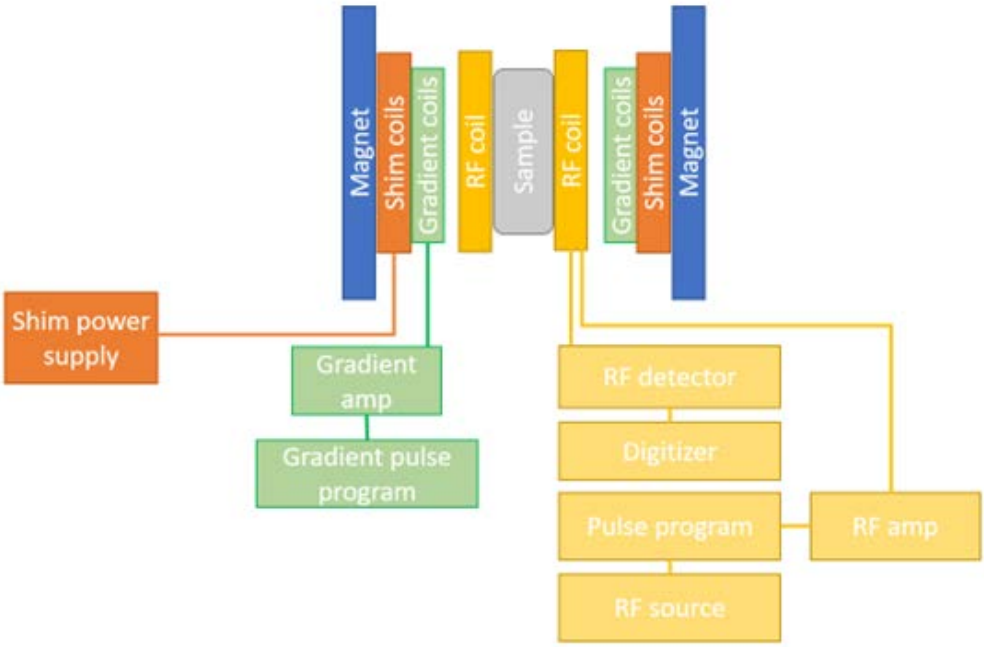


Figure 2.10: An open-shell depiction of the components of a NMR spectrometer, which consist of RF coils, gradient coils, shim coils, and the magnet itself, with power and electronic components to allow for RF pulse application and RF signal detection. Adapted from J.P. Hornak [83].

The B_0 Magnetic Field

A superconducting coil of wire with current passed through generates the B_0 magnetic field. This coil can support current indefinitely without a loss of power so long as it is operated below 6 K [90]. This temperature is maintained in many modern spectrometers through an inner jacket of liquid helium and an outer, insulating jacket of liquid nitrogen. This maintains an efficient magnetic field with the only substantial costs related to periodic replenishment of liquid helium and liquid nitrogen. One can refer to a spectrometer in terms of its B_0 field strength (e.g. 7 Tesla) or the frequency of a spin in the field (e.g., 300 MHz for a ^{1}H atom); both describe the same phenomenon, as they exhibit the relationship between a magnetic field and the frequency of a spin with a given magnetogyric ratio within it ($B_0 = \frac{\omega_0}{\gamma}$).

The RF Coil

The radiofrequency (RF) coil exists as part of the sample probe and forms a circuit with the transmitter and receiver (Figure 2.11). This circuit enables the coil to either transmit RF energy to the sample (excitation) or receive RF energy from the sample (detection). It is the current flowed through this coil which induces the applied B_1 field by Faraday induction [90].

In addition, the circuit which includes the RF coil also utilizes *tuning* and *matching* through the manipulation of two or more capacitors [90]. A *tune* capacitor tunes the circuit to the resonant frequency of the sample. A *match* capacitor matches the overall impedance with that of the load (e.g., the transmitter/receiver cable). In this way, the tune and match process maximizes signal and power transfer [90].

A simple solenoid coil may function as an RF coil (Figure 2.12, right), but other configurations offer an alternative to produce a B_1 field perpendicular to the static B_0 field.

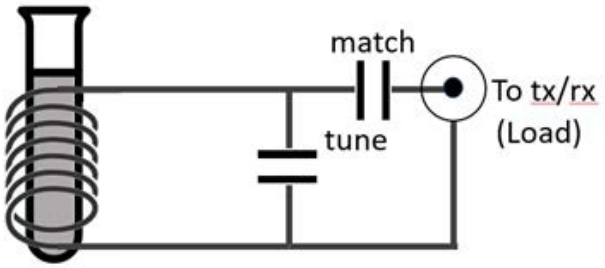


Figure 2.11: A diagram which demonstrates the RF coil circuit configuration. Tune and match capacitors connect to the RF coil and the transmitter/receiver; adjustment of the tune and match capacitors changes the capacitance of the circuit, allowing for a better match to the frequency of the the sample and better power transfer from the load.

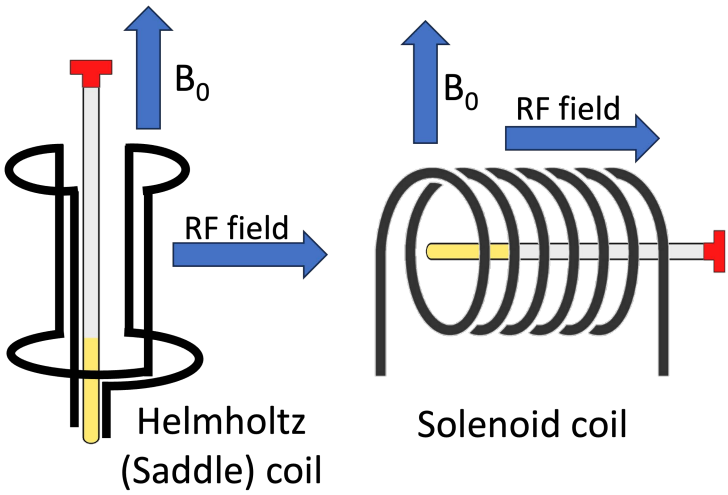


Figure 2.12: A Helmholtz (saddle) RF coil configuration (left), and the traditional solenoid coil (right). Geometries like the saddle and birdcage allow for vertical sample access, an important necessity for most modern NMR experiments.

These configurations include saddle and birdcage coils, the former depicted in Figure 2.12, left [90]. Both offer vertical access for more versatile sample insertion and geometry.

Gradient and Shim Coils

The gradient coils allow for a magnetic field with a well-calibrated linear variation in magnitude. Specific configurations of wound wires on cylindrical shells, or more commonly in recent decades, etched copper cylindrical shells, can create these fields [90]. Layered shells create a spectrometer with potentially linear variations in all three spatial dimensions (x, y, and z), either selectively or simultaneously applied by turning current on or off to each [90]. This capability sets dynamic NMR measurements apart from traditional spectroscopy, as it enables images and motion measurements through spin phase tracking [37].

Shim coils (or "shims") homogenize the B_0 magnetic field. Like gradient coils, they exist as cylindrical, current-carrying shells within the spectrometer, but unlike gradient coils which produce purposeful variations by the geometric configuration of the shell, shims cancel out field inhomogeneities by the application of specific, spatially-oriented current to the shells [90]. Two types of shims exist: permanent shims and room-temperature shims (the former sometimes called the "shim stack", or "passive" shims; the latter often just referred to as "shims", or "active" shims) [168]. A skilled technician must physically manipulate the spectrometer to access and change the permanent shims, which generally occurs during initial set-up [67, 168]. The computer program that controls the spectrometer enables manipulation of the smaller, more precise room-temperature shims. The program can examine the spherical harmonics which make up the inhomogeneities in the field, and then (at the user's prompting) apply an equal and opposite current in specific spatial orientations (such as x, y, z, x^2, y^2, etc.) to cancel the inhomogeneities [67]. This provides a rigorously homogeneous field adaptable to changes in the surrounding magnetic environment.

The Transmitter and the Receiver

The transmitter generates controlled RF pulses with several components [90]. These components include a frequency synthesizer, a gate, an attenuator, and an amplifier. The frequency synthesizer serves to produce a low-power, stable frequency with precise control, which an experimenter can manipulate with a computer, and can also phase-shift as necessary. The gate creates clean pulses with controlled lengths and timing through communication with a computer. The attenuator can then shape this pulse with the application of a programmed electronic signal. Finally, the amplifier, naturally, amplifies the weak, low-power pulse signal so that it translates sufficient power to the sample.

The receiver exists to amplify the signal which originates from the probe (sample). Such signals have a very small voltage (on the order of microvolts) [90]. Thus, to effectively amplify the signal with reasonable fidelity, the receiver must sit in very close physical proximity to the probe. The distance a signal travels between its origin and its amplification contributes to noise, because the signal samples an increasing number of electronic environments through wires, which will inevitably corrupt the pure signal [90]. Thus, the "pre-amplifier" device commonly seen in NMR labs will necessarily have a seat at the base of the spectrometer. The complex nature of the sample probe receiver signal means that the receiver probe does not need two separate coils to obtain $x-$ and $y-$ components of the magnetization [90]. If one splits the receiver signal and applies a 90° phase shift to one path, one path will have the real portion of the signal (x-component), and the other, the imaginary portion (y-component). This clever "trick", termed *quadrature detection*, avoids the use of excess hardware that would complicate and severely limit sample size and geometry [90].

The transmitter and the receiver both feed into the *diplexer*, which serves to separate the signals [90]. To limit the likelihood of destroying the very sensitive receiver, the diplexer will ground either the transmitter or the receiver when it connects to the other using photodiodes, based on expected voltage limits.

Rheo-NMR: Drive-shafts

Rheo-NMR, detailed in later sections, combines rheometry and nuclear magnetic resonance techniques to probe fluid flow [37]. This combined technique relies on the use of magneto-compatible *drive-shafts*, home-built experimental devices which act as rheometers within an NMR spectrometer bore. Drive-shafts shear fluids at specified rotation rates with a motor, a microcontroller, and a small external computer [29]. Figure 2.13 (left) shows the general configuration of a Rheo-NMR drive-shaft, while Figure 2.13 (right) shows the drive-shaft and direction of insertion to a spectrometer. The Rheo-NMR systems used in this research were built by Dr. Timothy Brox during his PhD in Professor Petrik Galvosas's Lab at Victoria University in Wellington, NZ, and are summarized below [29].

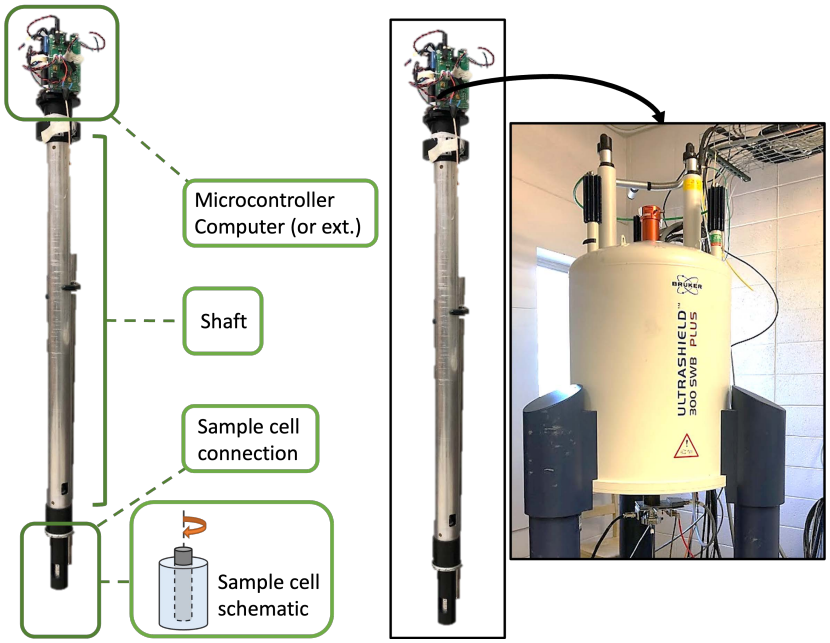


Figure 2.13: Left: A picture of a Rheo-NMR drive-shaft which indicates the most important components. Right: A demonstration of how the drive-shaft inserts into the top of the NMR spectrometer, such that the sample cell will sit directly within the homogeneous magnetic field of the spectrometer bore [29]. Pictures of the Rheo-NMR drive-shaft and 300 MHz Bruker NMR spectrometer are from the Magnetic Resonance (MR) Lab at Montana State University, operated by Dr. Joseph Seymour and Dr. Sarah Codd.

Sample cell Various types of sample cells compatible with Rheo-NMR drive-shafts exist, but the general configuration consists of a concentric cylinder geometry known as a Couette cell (shown in Figure 2.14). This geometry uses a glass outer cell (the "stator"), acting as a cup which holds the fluid, and an inner PEEK (polyether ether ketone) cylinder (the "rotor") inserted into the fluid. To satisfy necessary geometry-related fluid flow assumptions, explained in further detail elsewhere in this manuscript, the cylinder configuration remains the same regardless of the sample cell type. However, based on the experiment requirements, different rotors with different ends can serve as analogs to traditional rheometer geometries, such as parallel plate and cone and plate.

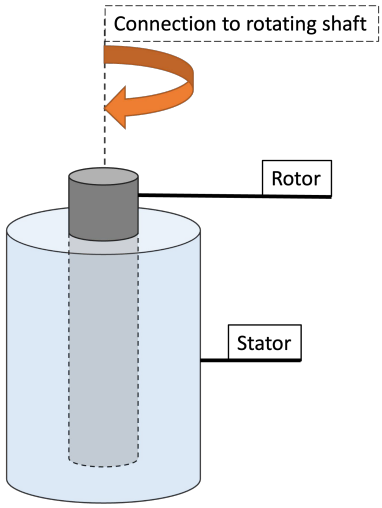


Figure 2.14: A schematic of a Rheo-NMR sample cell, which connects to the rotating inner shaft of the Rheo-NMR drive-shaft and allows for fluid shearing in an elongated Couette cell geometry.

Motor The motor, situated at the top of the drive-shaft, turns the inner shaft at a specified rotation rate. This inner shaft connects to the rotor of the sample cell through a series of couplings, and shears the fluid. It receives commands from the microcontroller [29].

Microcontroller The microcontroller serves as the bridge between the computer and the motor. It receives electronic signals from the computer that command a physical function (e.g., rotate at $\dot{\gamma} = 3\ s^{-1}$), and then translates this command to the motor as a voltage.

Computer The computer, generally a Raspberry Pi chip, houses the scripts and data files that allow for the operation of the drive-shaft. An external computer connects to the Raspberry Pi such that the drive-shaft operator can call the programs and operate the drive-shaft through a graphic user interface (GUI). It can also store information in an SD card for later retrieval.

Torque-sensing drive-shaft With simple modifications, a Rheo-NMR drive-shaft can not only shear fluids (generating flow which the spectrometer images), but also measure the resistance of the fluid to flow. This modified drive-shaft, called a *torque-sensing drive-shaft*, shares some of the same main components with a basic drive-shaft, but it also contains some specialized ones that facilitate its torque-sensing capability. These include an optical encoder, transducer, and torque-specific printed circuit boards (PCB's) [29].

Optical Encoder

The optical encoder exists as part of a stepper motor (Evodrive stepper servo motor package, EVA Robotics). The optical encoder consists of an LED light beam, a disc with holes, and a photodetector. The LED light beam passes through the holes of the disc, and the photodetector detects the light and responds with an electronic pulse train that indicates whether the light is on or off [29]. In this way, the optical encoder encodes the position of the rotating shaft, which ultimately tells the shear rate of the shaft [29].

Transducer

The transducer (TQ Mini 5.0, Vibrac), connected in-line along the shaft, measures the

torque resulting from the fluid's flow. As the fluid flows in the sample cell, it will resist the rotation of the rotor, and cause an angular displacement of the torsion bar within the transducer. The transducer contains an "encoder-type" disc that then measures this displacement and sends a current signal proportional to the torque (similar to how the optical encoder detects the shaft position with a laser, disc, and photodetector) [29].

Torque-specific PCB's

Two specific PCB's, one from the torque transducer manufacturer (Vibrac) and one custom-built, allow for communication between the transducer, the microcontroller, and the computer. They collectively have ±15 V of power and perform ADC and DAC (digital-to-analog converter) functions [29].

NMR and Complex Motion

The Complex Motion Motivation

As discussed in the prior sections, NMR magnetic field gradients allow for static imaging as well as motion encoding. Originally, motions of interest to NMR researchers consisted of unrestricted self-diffusion (Brownian motion) and steady, laminar flow [37]. Soon after, however, the capability of NMR to resolve complex forms of motion was realized.

Various types of complex motion exist, and Figures 2.15 and 2.16 depict some common examples. Those of particular interest to NMR include restricted diffusion, incoherent or periodic flow, spatially heterogeneous dynamics, and fluid dispersion [37]. Restricted diffusion occurs often in systems where fluid particles (spin-species) encounter the walls of their container; a specific example would involve micro-scale pore systems where particles will exhibit motional behavior characteristic of the size of the pore which contains them. Incoherent flow broadly describes turbulent, chaotic systems; periodic flow may involve

vorticial behavior as exhibited by Taylor vortices, or slip-stick behavior of gel and polymer systems. Spatially heterogeneous dynamics can result from susceptibility effects, which occur due to differences in magnetic susceptibility across a sample [37]. They also may occur in the movement of fluids with heterogeneous microstructure, such as shear-banding fluids [35]. Additionally, NMR finds utility in the analysis of fluid dispersion, often in the case of packed porous beds [37].

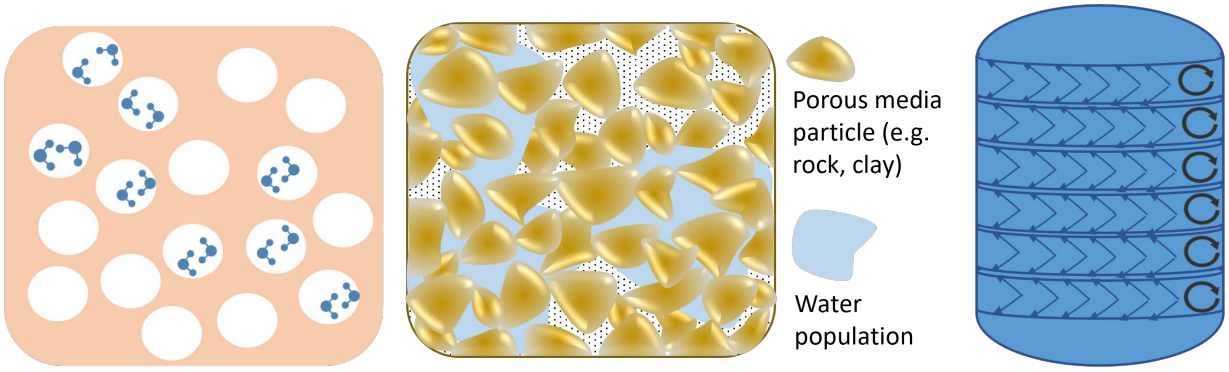


Figure 2.15: Examples of complex motion. Left: A schematic which shows restricted motion in closed pores of a porous bed. Middle: Depiction of a porous bed with interconnected pores. Right: A schematic which demonstrates the vortices from instabilities in Taylor-Couette flow, a type of complex motion.

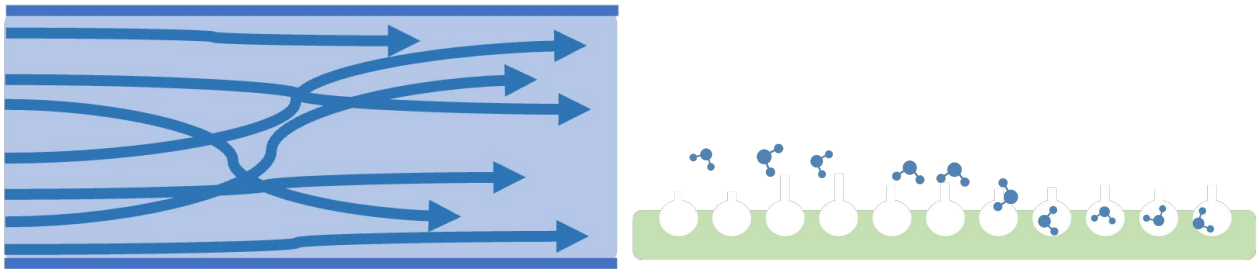


Figure 2.16: Examples of complex motion. Left: A depiction of the flow lines for turbulent flow through a pipe. Right: A figure demonstrating the restricted motion of molecules against a wall.

The motivation for employing NMR for these forms of complex motion ranges from practical measures of structure and motion to the advancement of fundamental knowledge.

For example, the enhancement of fundamental physics knowledge regarding molecular flow behavior in the multiphase flow of porous media is an ongoing topic of research for which NMR is well-suited [93]. On the other hand, finding simple, quantitative measures of water content in natural media like biomass serves a particularly useful role in biomass conversion, and involves the study of relaxation behavior as a result of restricted diffusion [175]. Additionally, studying the heterogeneous flow of complex fluids with NMR can advance fundamental rheologic understanding, while offering useful metrics for application in the industrial manufacturing of complex fluids [34].

To facilitate the discussion of NMR and complex motion, we will express magnetization in terms of the phase evolution under a time-varying gradient. This will involve defining an effective gradient; exploring three special cases of this magnetization expression; evaluating the effect of diffusive motion on signal attenuation; and examining the Bloch Torrey analysis for diffusion and flow [36, 37]. In addition, we will discuss the Stejskal-Tanner experiment and the Carr-Purcell analysis, the role of background gradients, the narrow gradient pulse approximation, the low-q limit, and the propagator formalism for magnetization in q-space [36, 37]. Finally, we will address the use of double PGSE and NMR velocimetry techni$q$ues to study mean flow and fluctuations [36, 37].

The Effective Gradient

A simplification in the analysis to define an effective gradient, $\mathbf{g}^*(t)$, because RF pulses alter the sign of the spin phases [37]. This effective gradient will account for the effect of RF pulses on the spin phases, and rests on two ideas: first, that the initial effective gradient has been, by convention, "historically inverted" by a 180° RF pulse (such that it is a negative sign gradient); and second, that the gradients applied when spins are not in the transverse plane are not effective - that is, only the transverse magnetization phase is altered [37]. Figure 2.17 displays a useful example: the stimulated spin echo sequence.

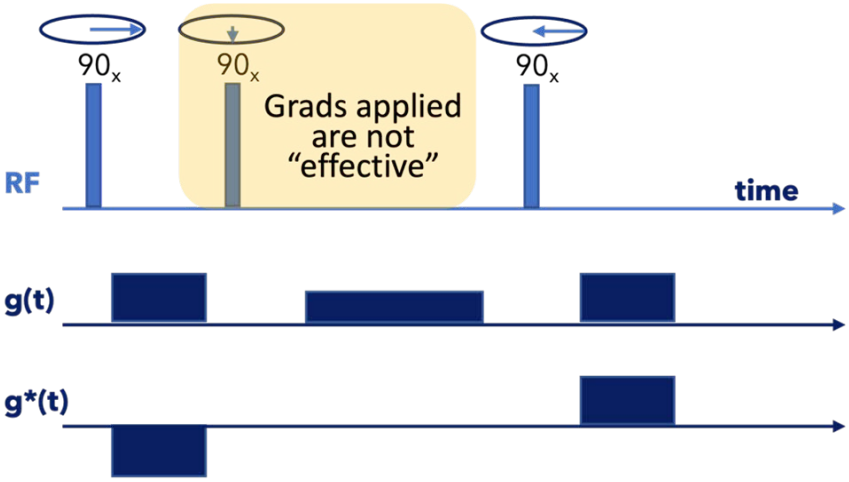


Figure 2.17: A stimulated Pulsed Gradient Spin Echo (PGStE) sequence which depicts the effect of effective gradients. The gradient applied after the second 90° RF pulse is not part of the effective gradient, since the spin magnetization is not in the transverse plane.

In this sequence, a 90° RF pulse initiates the spin transition to the transverse plane. The gradient applied afterwards can be considered an effective gradient because our spins are detectable, and as it is the first gradient pulse, it will be depicted as historically inverted – that is, negative in sign. The next 90° RF pulse subsequently places our spins in the longitudinal direction, where the magnetization does not generate a signal in the RF coil. The next gradient applied is not “effective”, and does not encode phase, so our effective gradient is zero. A final 90° RF pulse has the same effect as the first to place our spins back into the transverse plane, and the resulting gradient pulse is again effective. With the effective gradient defined, we can now broach the magnetization expression in terms of phase evolution under a time-varying gradient. To begin this discussion, one can imagine a spin translating under a time-varying gradient with a position vector, $\mathbf{r}$, and a starting position vector, $\mathbf{r_0}$, as depicted in Figure 2.18. We can then express the signal contribution in terms of transverse magnetization from a collection of such spins as the following [36, 37]:

$$M_+(\mathbf{r_0}, t) = M_+(\mathbf{r_0}, 0) \exp\left(i\gamma \int_0^t \mathbf{g}^*(t') \cdot \mathbf{r}(t') dt'\right) \tag{2.27}$$

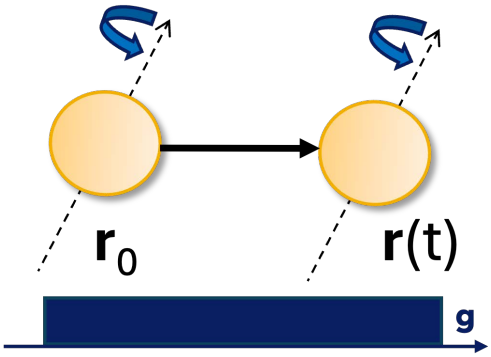


Figure 2.18: A depiction of a spin translating with an initial position, $\mathbf{r}_0$, and a position vector, $\mathbf{r}_(t)$, in the presence of a magnetic field gradient, $\mathbf{g}$.

However, we must also consider the range of starting positions of the spins, and the distribution of possible molecular trajectories which arise from these starting positions. This gives rise to the requirement of an ensemble average, which we may describe as [37]:

$$M_+(t) = \int d\mathbf{r_0} M_{+j}(\mathbf{r_0}, 0) \left\langle \exp\left(i\gamma \int_0^t \mathbf{g}^*(t') \cdot \mathbf{r}(t') dt'\right) \right\rangle_{j-ensemble} \tag{2.28}$$

It is worth noting that the resulting signal expression no longer depends on the spin starting positions, $\mathbf{r_0}$, but only on time.

Now we may examine three special cases of this magnetization expression [37].

Case 1: No spin motion In the instance of no spin motion, we consider our j^{th} position vector, $\mathbf{r_j}(t)$, as equal to our starting position vector, $\mathbf{r_0}$. The integrand will no longer include the position vector now since our starting position does not depend on time. Equation 2.29 depicts the resulting expression.

$$M_+(t) = \int d\mathbf{r_0} M_{+j}(\mathbf{r_0}, 0) \exp\left(i\gamma \int_0^t \mathbf{g}^*(t') \cdot \mathbf{r}(t') dt'\right) \tag{2.29}$$

An especially important condition arises from this expression, in which $\int_0^t \mathbf{g}^*(t')dt' = 0$. A simple inspection of Equation 2.29 with this condition will present its significance: when the effective gradient over the observed time duration equals zero, the magnetization signal equals the initial magnetization [37]. Recall that this constitutes the condition for an echo! Equation 2.30 demonstrates the result of this condition [37].

$$M_+(t) = M_+(0) \tag{2.30}$$

Before moving on to the next case for this expression, we will discuss normalizing our signal. Currently, our expression sums over our starting positions with the term $\int d\mathbf{r_0} M_+(\mathbf{r_0}, 0)$. In doing so, we allow for non-uniform spin density over our sample [37]. We can also easily add in relaxation effects, simply multiplying our expression with the associated exponential decay terms for T_1 and T_2. However, often, our interest may lie strictly in the role of the gradients in the phase evolution; in such a case, it becomes more convenient to normalize our signal with respect to the magnetization at the echo condition [37]. This results in a normalized echo amplitude, $E(t)$, defined in Equation 2.31.

$$\text{Normalized echo amplitude} \equiv E(t) = \frac{M_+(t)_{\mathbf{g}^*(t')\neq 0}}{M_+(t)_{\mathbf{g}^*(t')=0}} \tag{2.31}$$

This normalization presents an important caveat, which is that we must assume our sample has uniform relaxation. By this assumption, we state that spin position does not correlate to relaxation. This, at first glance, may seem an unreasonable assumption for heterogeneous materials, however, on the time scales of gradient flow encoding times, generally on the order of milliseconds, the effects of relaxation on position may not have a serious effect on the spin phase [37]. Of course, the judicious experimenter must consider this and the sample in question when planning gradient pulse sequences.

Case 2: Common motional behavior The case of common motional behavior indicates that a force imparts some flow on the sample which dominates the motion, such as a constant velocity or acceleration (indicated in our position vector notation with Equations 2.32 and 2.33). This necessarily excludes the case of thermal diffusive Brownian motion. We may then rewrite the phase for the cases of constant velocity or acceleration, expressed in Equation 2.34 [37].

Kinematics:

$$\mathbf{r}_j(t') = \mathbf{r}_0 + \mathbf{v}t' \tag{2.32}$$

$$\mathbf{r}_j(t') = \mathbf{r}_0 + \mathbf{v}t' + \frac{1}{2}at'^2 \tag{2.33}$$

Phase description:

$$\phi_j(t) = \gamma \int_0^t \mathbf{g}^*(t') \cdot \mathbf{r}(t')dt') = \gamma\mathbf{v} \cdot \int_0^t t'\mathbf{g}^*(t')dt' + i\gamma\mathbf{a} \cdot \int_0^t t'^2\mathbf{g}^*(t')dt' + ... \tag{2.34}$$

This new expression describes the moment expansion of the effective gradient as a function of time [37]. Here we can note that the first moment of the gradient, indicated by the term with the first power of time (t^1), represents the velocity, while the second moment (t^2) represents acceleration. The zeroth moment, not shown, equates to the instance where t^0, described as $\mathbf{r}_0 \int_0^t \mathbf{g}^*(t)dt$ – which encodes position [37].

This moment expansion presents a powerful perspective on how to design gradient pulse sequences, which Figure 2.19 demonstrates. Both pulse sequences begin with a 90° RF pulse, rendering spins in the transverse plane. They both also depict the graph of the effective gradient, along with its first and second moments. One should also note that they both meet the echo condition since the effective gradient over the course of the experiment sums to zero [37].

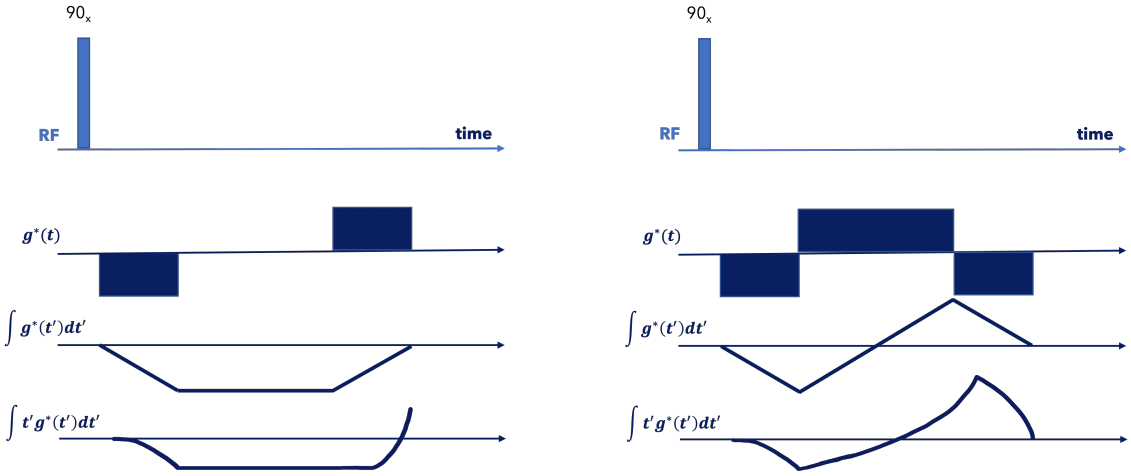


Figure 2.19: Gradient pulse sequences and the plots of their successive gradient moments. Left: Nonzero first moment gradient pulse sequence; a pulse sequence with gradient pulses such that the first moment of the gradient, $\int_0^t t'\mathbf{g}^*(t')dt'$, is not equal to zero. Right: Nonzero second moment gradient pulse sequence; a pulse sequence with gradient pulses such that the second moment of the gradient, $\int_0^t t'^2\mathbf{g}^*(t')dt'$, is not equal to zero [37].

The pulse sequence in Figure 2.19, left shows a gradient echo and the resulting plots of the moments (the *Phase Encoding: The PGSE and Gradient Echo Sequences* section discussed the importance of gradient echo). We know that this encodes for displacement, providing velocity, since the first gradient moment dominates the magnetization phase. In this pulse sequence, the phase is "wound up" and encoded in a magnetization helix, corresponding to a "ramp" in the first moment [37]. The first moment of the gradient then remains constant even after the removal of the gradient pulse, until the inverted pulse "unwinds" the helix and causes a reverse "ramp" of the first moment [37]. In the pulse sequence represented in Figure 2.19, right, the phase helix winds up and "ramps" in the first moment; then, the inverted, longer duration gradient "unwinds" and then "winds" to encode in the opposite direction, and then "unwinds" again to render no net phase encoding. During this period, the first moment ramps, then inverts, and then ramps again in the

opposite direction. In this pulse sequence, we note that there is no net change of phase for the first moment, but it instead sums to zero over the experiment. The signal phase, then, has sensitivity to the second moment, the spin acceleration, as opposed to velocity [36].

Our ability to selectively examine different types of common motional behavior with NMR hinges on the ability to properly design gradient pulses. This includes both pulse arrangement as well as duration and timing.

Case 3: Brownian motion In the case of Brownian motion, or thermal self-diffusion, a characteristic dephasing of the NMR signal occurs. In 1954, Herman Carr and Edward Purcell sought to understand this motion and the resulting signal effect in terms of piece-wise time-varying gradients [40]. In doing so, they imagined this self-diffusive motion to occur in discrete "hops", as indicated in Figure 2.20. One could then resolve the effective displacement, ξ, of these hops in the direction of the gradient by summing as done in the Pythagorean Theorem [37]. Equation 2.35 describes the result [37].

$$Z(n\tau_s) = \sum_{i}^{n} \xi a_i \tag{2.35}$$

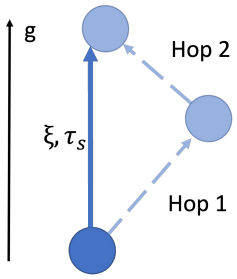


Figure 2.20: A depiction of the displacement for a spin undergoing diffusion, where the total displacement of hops can be equated to the Pythagorean Theorem. Adapted from [37].

In the equation $Z(t) = z(t) - z(0)$, z indicates the total displacement after n hops which have an average duration of τ_s, where a_i represents a random number $+1$ or -1. This number

indicates one direction or the other in a mode of motion, e.g., left, or right. Squaring both sides of this expression and taking the ensemble average of the a_i's simplifies the expression. Equations 2.36-2.38 demonstrate this process [37].

$$\overline{Z^2(n\tau_s)} = \sum_i^n \tag{2.36}$$

$$\overline{a_i a_j} = 0, \quad \text{unless} \quad i = j \tag{2.37}$$

$$\overline{Z^2(n\tau_s)} = \sum_i^n \xi^2 \overline{a_i^2} = \xi^2 \sum_i^n 1 = n\xi^2 \tag{2.38}$$

At this point, we can also define a diffusion coefficient in terms of our effective displacement and average duration over a series of hops, expressed in Equation 2.39 [37].

$$D = \frac{\xi^2/2}{2\tau_s} \tag{2.39}$$

This expression has units, squared length per time, expected of diffusion. We can then equate the above equation to Equation 2.38 and obtain our mean squared displacement in terms of the diffusion coefficient and time, t. Equations 2.40 and 2.41 show the results for one dimension and three dimensions.

$$\overline{Z^2(t)} = 2Dt \tag{2.40}$$

$$\overline{R^2(t)} = 6Dt \tag{2.41}$$

A natural connection to the Einstein relation arises since this method also defines thermal diffusion as a stochastic process [37]. No difference between the two exists, as they model the same behavior. Carr and Purcell simply went through their derivation from the perspective of NMR to explain how one should model thermal diffusive motion under a piece-wise time-varying gradient, as in a discreet random walk.

Signal Attenuation

The Carr-Purcell method also gives rise to a convenient description for signal dephasing. While the complete derivation does not concern us here (though the reader may seek out [37] for the relevant details), the resulting phase change and its impact on the transverse magnetization offers an informative expression. Since we know that the phase change must vary randomly across the ensemble for Brownian motion, we can express the phase change in terms of a probability distribution [37]. We also know that a Gaussian function appropriately models random Brownian motion, and as a result, we can substitute it for our probability distribution and simplify. Equations 2.42 and 2.43 below represent the average phase change in this description [37].

$$\overline{\exp(i\Delta\phi)} = \int_{-\infty}^{+\infty} P(\Delta\phi)\exp(i\Delta\phi)d(\Delta\phi) \tag{2.42}$$

$$\overline{(\exp i\Delta\phi)} = \exp(\frac{1}{3}\gamma^2 g^2 D t^3) \tag{2.43}$$

Since we also know that our spins exhibit a *distribution* of starting positions across the gradient axis, z, we need to represent this effect with a *spin density* function, $\rho(z)$. This then allows us to write the total phase as dictated by Equation 2.44 [37].

$$\overline{exp(i\phi)} = \Big(\int_{-\infty}^{+\infty} \rho(z)\exp(i\gamma g z t)dz\Big)\overline{\exp(i\Delta\phi)} \tag{2.44}$$

This result elegantly provides two important pieces of information. The first term, $\int_{-\infty}^{+\infty} \rho(z)\exp(i\gamma g z t)dz$, represents the cumulative phase information of the inhomogeneities present in the magnetic field, $g = \Delta B_0$ if present, or in the spin density $\rho(z)$. In the context of a relaxation experiment, this quantity represents the phase changes that give rise to a T_2^* decay measurement if g is inhomogeneous [37]. The second term, $\exp(-\frac{1}{3}\gamma^2 g^2 D t^3)$, describes the *actual signal attenuation* due to diffusion (represented by the diffusion coefficient, D) in a

homogeneous gradient field g [37]. In other words, this term describes the signal attenuation which results from the random dephasing of spin phases caused by Brownian motion. When performing diffusion measurements, the use of the spin echo allows us to refocus the phase information from the inhomogeneities in the magnetic field, effectively removing it from the transverse magnetization signal. This then leaves us with the actual signal attenuation due to diffusion, from which we can calculate a diffusion coefficient.

The Stejskal-Tanner Experiment

The Stejskal-Tanner experiment, performed in 1965 by Edward Stejskal and John Tanner [152], involves an application of the Carr-Purcell method to the PGSE pulse sequence (described earlier in the *Phase Encoding: The PGSE and Gradient Echo Sequences* section). This experiment allows for the measurement of diffusion. We can write a description for the normalized echo signal, $E(g)$, using the total phase change resulting from diffusion, described above for the Carr-Purcell method, in terms of the timing for a PGSE pulse sequence [37]:

$$E(g) = S(g)/S(0) = \exp\left(\gamma^2 g^2 \delta^2 D(\Delta - \frac{\delta}{3})\right). \tag{2.45}$$

Here one should recall the pulse timing variables defined previously: Δ, the gradient flow encoding time, also referred to as the displacement observation time, and δ, the gradient pulse duration time. This equation describes how the echo signal depends only on the gradient amplitude, g, as all other quantities are fixed. Increased values of the gradient amplitude will cause more signal attenuation. Carefully manipulating this value while simultaneously measuring the signal attenuation allows for the measurement of a diffusion coefficient [37]. Therefore, performing a diffusion experiment involves repeatedly changing the gradient amplitude, measuring the signal attenuation, and fitting the result to obtain a diffusion coefficient [37]. This process results in a plot with a linear decay for constant diffusion coefficient, with a slope representing the diffusion coefficient, as shown in Figure

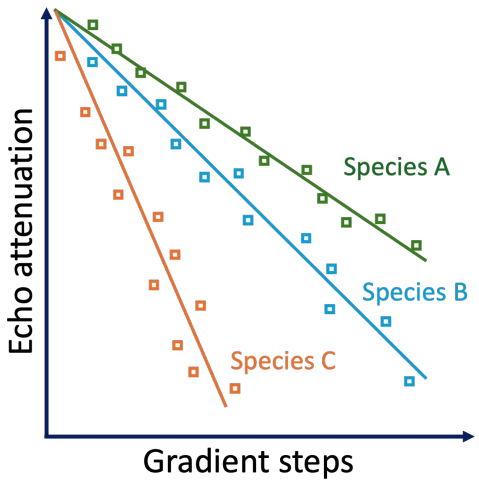


Figure 2.21: Hypothetical data which shows the effect of plotting the signal attenuation as a function of increasing gradient steps for three species with different diffusion constants. The slope of each line corresponds to the diffusion coefficient for the respective species, with $D_C > D_B > D_A$.

2.21.

Expressing Echo Signal in Terms of Velocity

We can also model the normalized echo attenuation which results from diffusive behavior including a uniform velocity, $\mathbf{v}$, shown below in Equation 2.46 [37]:

$$E(\mathbf{g}) = \exp\left(i\gamma\delta\mathbf{g}\cdot\mathbf{v}\Delta - \gamma^2 g^2\delta^2(\Delta - \frac{\delta}{3})\right) \tag{2.46}$$

This equation resembles Equation 2.45 but includes velocity phase modulation term in addition to the diffusive attenuation. Both the Carr-Purcell method and the Bloch-Torrey analysis, discussed in the *The Bloch-Torrey Analysis of Diffusion and Flow* section, can be used to derive this expression. However, this expression idealizes our signal behavior because it does not account for the time it takes for gradient pulses to rise and fall [37]. These gradient rise and fall times, which we will now discuss, have the potential to significantly influence our signal.

The Effect of Gradient Rise and Fall Times

To this point, we have pictured gradients as rectangular pulses of finite width. However, in practice, NMR experiments do not include perfectly rectangular pulses. Two reasons exist for this fact. Firstly, a spectrometer cannot physically turn a gradient pulse on, instantaneously, in time; the physical world requires a certain duration of time over which the pulse "ramps up" to its full amplitude. In this way, a trapezoid - where a gradient linearly increases over time until it reaches the designated amplitude - represents the realistic form for all "rectangular"-modeled pulses [37].

Secondly, an important reason for this controlled ramping consists of a phenomenon known as *eddy currents*. Much like the motion of eddy currents typically found in a stream (depicted in Figure 2.22a), the eddy currents in NMR spectrometers comprise swirling-like changes in the current in conductive materials, and they result from Faraday's Law [37]. When very rapid applications of electric current, such as a steep gradient pulse, occur, it induces a rapid change in the magnetic field. The resulting change in the magnetic field includes the large and expected change, but it also includes secondary, smaller changes in the field. These induce smaller changes in the electrical fields (currents) of the conductive materials in the magnet hardware.

This means, in practice, that rapid changes in applied electric current can induce eddy currents, which will then – by Faraday's Law – induce changes in the magnetic field. This can alter the expected magnetic field and cause unwanted gradient artifacts. As a result, NMR experimenters must carefully control the ramping of gradient pulses to limit the possibility of detrimental eddy currents [37].

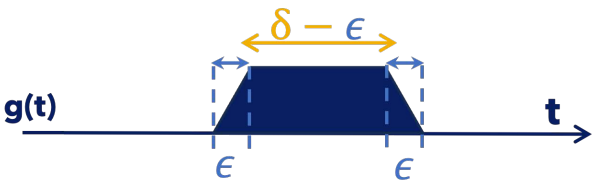
We can append the normalized echo attenuation expression with a correction factor that depends on the time to ramp, ϵ, demonstrated for the trapezoidal gradient in Figure 2.22b, to account for gradient ramp times. Equation 2.47 depicts the echo attenuation expression with this correction factor. For many experiments, neglecting this correction makes little

difference since it is on the order of a tenth of a percentage [37]; but in the case of very precise diffusion measurements, for example, the experimenter may find utility in calculating it.

$$E(\mathbf{g}) = \exp\left(i\gamma\delta\mathbf{g}\cdot\mathbf{v} - \gamma^2 D g^2 \gamma^2 (\Delta - \frac{\delta}{3})\left[1 + \frac{\epsilon}{\Delta - \frac{\delta}{3}}\left(\frac{\epsilon^2}{30\delta^2} - \frac{\epsilon}{\delta}\right)\right]\right) \tag{2.47}$$



(a) A picture of an eddy current in a stream. © Nigel /Adobe Stock



(b) A schematic showing a trapezoidal-shaped gradient with a value, ϵ, which can correct for the change from rectangular to trapezoidal. Adapted from [37].

The Pulsed Gradient Stimulated Echo Sequence

We can also reduce the effect of gradient artifacts with a modified PGSE sequence, known as the *pulsed gradient stimulated echo sequence* (PGStE), shown in Figure 2.23 below. This sequence serves the same purpose of motional phase encoding as the PGSE, but it does so by storing the magnetization along the longitudinal axis rather than in the transverse plane [37]. This occurs because the first 90° pulse places the spins in the transverse plane, the first gradient pulse phase encodes the spins, and then the second 90° pulse tips the now phase-encoded spins along the longitudinal axis during the observation time Δ. Near the end of the observation time, another 90° pulse recalls the spins to the transverse plane so as

to allow for their detection, and a final gradient pulse de-encodes the spins to determine the motion [37].

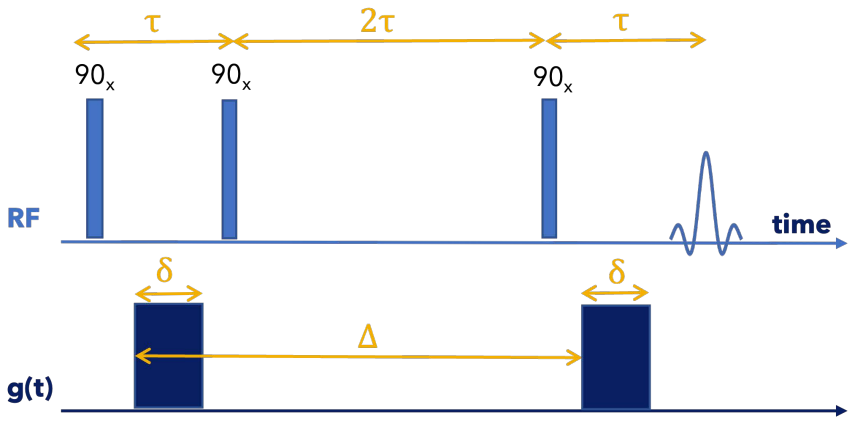


Figure 2.23: The Pulsed Gradient Stimulated Echo sequence, which encodes spin phases after the first 90° RF pulse and stores the resulting phase information in the longitudinal plane after the second 90° RF pulse. The remaining RF pulse recalls the magnetization to the transverse plane and the second gradient pulse encodes for the motion over the gradient observation time, Δ. Since T_1 of longitudinal magnetization decays slower than T_2 of transverse magnetization, PGStE can allow for the imaging of faster decaying species.

This storage of magnetization requires a loss of magnetization signal amplitude of 1/2, due to the projection of the longitudinal signal onto the transverse plane [37]. However, the advantage of the PGStE lies in the ability to not only reduce the effect of gradient artifacts (like those that may result from eddy currents, as described earlier), but also to better image fast T_2 relaxing samples. For samples which exhibit fast T_2 relaxation, substantial dephasing can occur in a standard PGSE sequence before the gradient flow encoding time Δ has passed, such that phase encoding is essentially lost. In contrast, for the PGStE experiment, the storage of magnetization along the longitudinal axis during the gradient flow encoding time ensures that T_2 relaxation does not impact the spins, but rather T_1 relaxation, which, in general, has a much slower rate than T_2 [37]. As a result, the gradients can properly phase encode for motion without substantial dephasing from T_2.

The Bloch-Torrey Analysis of Diffusion and Flow

The Bloch-Torrey analysis illustrates yet another useful perspective to analyze motion under the influence of a gradient in NMR [158]. This perspective finds utility in situations where we have non-piece-wise gradients and the Carr-Purcell analysis necessarily fails [37]. Situations like these include when our system contains gradient artifacts, or sine-shaped gradient pulses [37]. Previously, we briefly encountered the Bloch-Torrey equations, a set of three ordinary differential equations which represent magnetization in an Eulerian perspective as a transport conservatino equation. From this magnetization transport mechanism perspective in the context of a PGSE experiment, we can form integrals related to the first and second orders of the gradient magnetization and solve them to derive the same result as from the Carr Purcell method [37]. Doing so provides an illuminating look at the gradient moments and signal sensitivity to position, velocity, and diffusion.

The integrals in Equations 2.48-2.50, when evaluated across each time interval during a typical PGSE sequence, result in three relevant expressions. The first expression, Equation 2.48, denotes the *condition for echo formation*, which indicates the *sensitivity of our signal to position* [37]. The second expression, Equation 2.49, demonstrates the *sensitivity to velocity through a velocity-induced phase shift* [37]. Finally, Equation 2.50, the last expression, represents the *sensitivity to phase spread associated with diffusion* – in other words, the diffusion-induced echo attenuation [37].

$$\int_0^{2\tau} \mathbf{g}^*(\mathbf{t}')dt' = 0 \tag{2.48}$$

$$\begin{aligned}
&\int_0^t \int_0^{t'} \mathbf{g}^*(t'')dt''dt' \\
&= -\int \mathbf{g}(t'-t_1)\delta dt' + \int_{t_1}^{t_1+\delta} \mathbf{g}\delta dt' + \int_{t_1+\delta}^{t_1+\Delta} [-\mathbf{g}\delta + \mathbf{g}(t'-t_1-\Delta)]dt' \\
&\quad + \int_{t_1+\Delta+\delta}^{2\tau} [-\mathbf{g}\delta + \mathbf{g}\delta]dt' = -\mathbf{g}\delta\Delta
\end{aligned} \tag{2.49}$$

$$\begin{aligned}
&\int_0^t \left(\int_0^{t'} \mathbf{g}^*(t'')dt'' \right)^2 dt' \\
&= -\int_{t_1}^{t_1+\delta} g^2(t'-t_1)^2 dt' - \int_{t_1+\delta}^{t_1+\Delta} g^2\delta^2 dt' \\
&+ \int_{t_1+\Delta}^{t_1+\Delta+\delta} [g^2\delta^2 - 2g^2(t'-t_1+\Delta) + g^2(t'-t_1-\Delta)^2]dt' \\
&= g^2\delta^2(\Delta - \frac{\delta}{3})
\end{aligned} \tag{2.50}$$

These results, of course, very closely resemble the terms in our result from Carr-Purcell, shown in Equation 2.51 below:

$$E(g) = \exp\left[(i\gamma\delta\mathbf{g}\cdot\mathbf{v}\Delta)\left(\gamma^2 g^2 \delta^2 D(\Delta - \frac{\delta}{3}) \right) \right] \tag{2.51}$$

Examining General Motion with the PGSE Using Propagator Formalism

The Carr-Purcell method and the Bloch-Torrey analysis have thus far demonstrated the echo attenuation for *diffusion* and *velocity flow*. However, other more general forms of motion exist, such as the forms of *complex motion* described earlier, which we may want to model. For these general forms of motion, no closed form for the echo amplitude exists with the Bloch-Torrey analysis [37].

The Narrow Gradient Pulse Approximation Although no closed form for the echo amplitude exists with the Bloch-Torrey approach, if we choose to use idealized *narrow*

gradient pulses, we can obtain general analytic expressions [37]. These narrow gradient pulses necessitate that we make the assumption that $\delta \to 0$. Why does this assumption work? Simply because we can neglect motion during the time of the gradient, and this greatly simplifies the expressions needed to solve for the magnetization [37]. It also allows for a description called *propagator formalism* that will describe our dynamics.

In practice, a $\delta \to 0$ assumption must consider the characteristic times of motion present in the sample. Since a gradient pulse length of zero cannot exist realistically, and limitations in hardware dictate the smallest attainable gradient pulse lengths, narrow gradient pulse approximation can only be that: an approximation [37]. But the approximation serves us well in situations where the sample exhibits characteristic times of motion reasonably longer than the gradient pulse time. This allows for the reasonable assumption that little motion will have occurred over the period of the "narrow" gradient pulse. Therefore, the quality of this approximation comes down to the NMR experimenter's judicious choice of a δ in consideration of their sample [37].

Under the narrow gradient pulse approximation, we can conveniently describe our echo attenuation in terms of probabilities of motion [37]. This perspective requires the use of *propagator formalism*; for a more detailed treatment of this formalism, the reader may consult source [37] or any introductory quantum mechanics text. For the purposes of this work, the propagator formalism presents an intuitive way of understanding our signal in terms of q-space and the probabilities associated with motion.

Figure 2.24 describes the echo attenuation equation in this perspective. The signal depends on the gradient amplitude, $\mathbf{g}$ and the observation time, Δ, and it expresses the relationship between the molecular density of the spins $\rho(\mathbf{r})$, the probability of a spin moving from position state $\mathbf{r}$ to $\mathbf{r}'$, and the phase shift associated with a spin moving from the change in position due to translation from $\mathbf{r}$ to $\mathbf{r}'$. These each contribute as an ensemble average over all of the individual spins (denoted by the integration over both $\mathbf{r}$ and $\mathbf{r}'$). In essence, the

expression explains how spins which may be non-uniformly dispersed throughout a system exhibit a phase shift due to their motion under the influence of a gradient, and accounts for the fact that this motion depends on the collective probable tendency for these spins to translate [37].

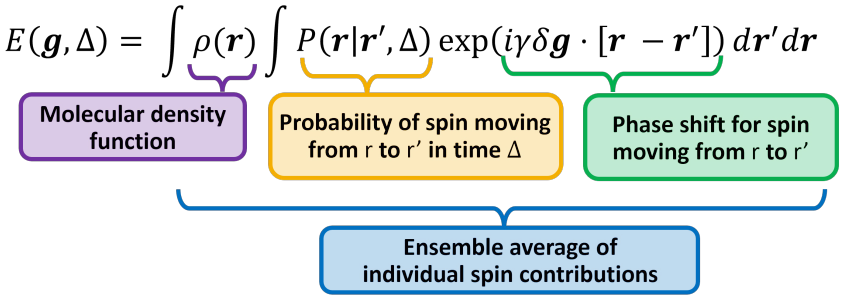


Figure 2.24: The propagator formalism for the PGSE signal depicted with labels indicating each term.

As described previously, q-space provides a convenient way to describe motion in the NMR perspective because it facilitates the use of the Fourier transform. Here, we will provide the definition of the q-vector again and substitute it into our echo attenuation. This will simplify our expression, as it expresses the signal in terms of our q-vector, the Fourier reciprocal wave length to displacement instead of the gradient amplitude [37].

$$\mathbf{q} = \frac{1}{2\pi}\gamma\delta\mathbf{g}, \left[\frac{\text{rad}}{\text{m}}\right] \quad \text{(angular spatial frequency)} \tag{2.52}$$

$$E(\mathbf{q},t) = \int \rho(\mathbf{r}) \int P(\mathbf{r}|\mathbf{r}',t) \exp\left(i\mathbf{q}\cdot[\mathbf{r}'-\mathbf{r}]\right) d\mathbf{r}'d\mathbf{r} \tag{2.53}$$

We may now write an averaged propagator to describe our motion. First, we will define a dynamic displacement vector, $\mathbf{R}$, which expresses the translation of our spins,

$$\mathbf{R} = \mathbf{r}' - \mathbf{r}. \tag{2.54}$$

Then, the averaged propagator can be written as [37]

$$\overline{P}(\mathbf{R},t) = \int \rho(\mathbf{r}) P(\mathbf{r}|\mathbf{r}'+\mathbf{R},t) d\mathbf{r}. \tag{2.55}$$

We may then rewrite the signal:

$$E(\mathbf{q},\Delta) = \int \overline{P}(\mathbf{R},\Delta) \exp\left(i\mathbf{q}\cdot\mathbf{R}\right) d\mathbf{R}. \tag{2.56}$$

Such that we now express our signal in terms of the average propagator, $\overline{P}(\mathbf{R},\Delta)$, which contains the information for spin density and the probability of spin displacement, and an exponential term in the inverse q-space. One might recognize the Fourier relationship between the real-space propagator and the q-space signal. This relationship means that motional imaging, much like static imaging with k-space, relies on a Fourier relationship between real and inverse space [37]. However, in static imaging we measure the density of spins when we Fourier transform our k-space signal, but here we measure the *probability of motion of spins, weighted by their density* [37]. This nuance – that what the spectrometer really measures represents a probability of translation within a segment of q-space – often remains unspoken in discussions of diffusion measurements or velocity profiles. Taking the probability as a true value and "ignoring" this nuance requires the proper application of the narrow pulse approximation and a strong understanding of the spectrometer's resolution capabilities.

This expression describes the general motion of spins, but if we wished to express diffusion or flow specifically in the perspective of the narrow pulse approximation we could

do so with the following expressions for the phase-shift term [37]:

$$E(q,\Delta) = \exp\left(-q^2 D\Delta\right); \quad \text{Diffusion} \tag{2.57}$$

$$E(q,\Delta) = \exp\left(i\mathbf{q}\cdot\mathbf{v}\Delta\right); \quad \text{Flow} \tag{2.58}$$

Restricted Diffusion

Restricted diffusion often arises in systems with complex, heterogeneous structures. For systems where molecular species experience limits on their free diffusive behavior from the constraints of their surroundings, the typical free diffusion coefficient will no longer describe the motion, and instead an *effective diffusion coefficient*, D_{eff} can be used [37]. The most usual case of restricted diffusion results from "walls" which impede molecular motion, and often these occur in porous systems.

In NMR studies, the measurement of diffusion in a restricted environment depends on gradient strength, the gradient displacement encoding time, and the echo time [37]. The value of D_{eff} will also depend on the length of the time of displacement observation. At short displacement observation times relative to the diffusive timescale to sample a pore of size a, $\Delta \ll \frac{a^2}{D}$, $D_{eff} \approx D$, the diffusion coefficient for free diffusion, as the molecular species will not have yet collided with the pore walls. As a molecular species diffuses over a longer period of time $\Delta \gg \frac{a^2}{D}$, it will collide with the walls of its surrounding pore. In an interconnected porous system, it will eventually "hop" between pores and sample the surrounding environment. For this reason, the value of D_{eff} depends strongly on the observation time [37].

PGSE experiments performed at varying values of the gradient displacement encoding time, Δ, can provide a means to determine the time and length-scale when a system exhibits restricted diffusion. This length-scale can also serve as an estimate for the characteristic pore-size of the system [37]. Figure 2.25 depicts such an experiment.

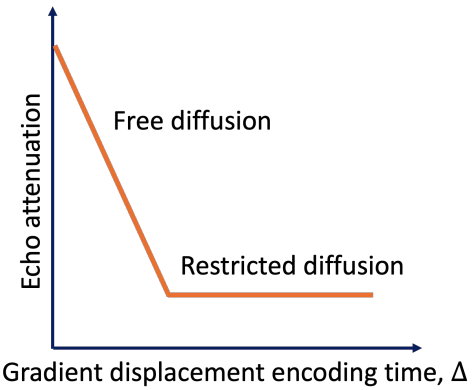


Figure 2.25: Hypothetical data showing the change in the slope of the echo signal as a function of altering the gradient flow encoding time, Δ. As Δ is increased, the window of time to observe the motion of the spin species increases. For a spin species in an area of restricted mobility, e.g. a pore, at short times it will appear to move freely but there will be a critical time that indicates the size of the pore. This critical time is the value of Δ where the slope of the signal becomes zero.

Hydrodynamic Dispersion

Another form of complex motion which NMR is well-positioned to study is hydrodynamic, or Taylor, *dispersion* [37]. Dispersion, like diffusion, represents a form of mass transfer which, macroscopically, transfers along a negative concentration gradient according to Fick's Law $J = -E\frac{dc}{dt}$ [37]. However, dispersion differs from free diffusion in that the motion itself is not inherently random (though it arises from random motions). Like turbulence, dispersive forms of motion often contain pattern structures which indicate a form of order. In the case of dispersion, this order often corresponds to the geometry of the system. NMR experiments can then provide useful information about the sample structure where dispersion occurs.

Dispersion generally arises in porous media systems and along streamlines of flow (such as in Taylor dispersion, depicted in Figure 2.26) [12]. Two geometrical cases of dispersion – mechanical and hold-up – are depicted in Figures 2.27. Mechanical dispersion occurs from the stochastic variations in velocity due to flow bifurcations, while hold-up occurs from

dead-end pores [37].

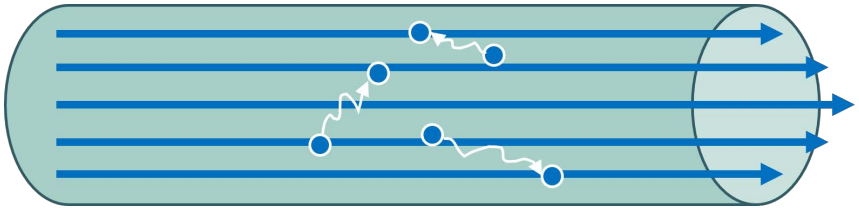


Figure 2.26: A schematic which depicts Taylor dispersion along stream-lines in laminar pipe flow.

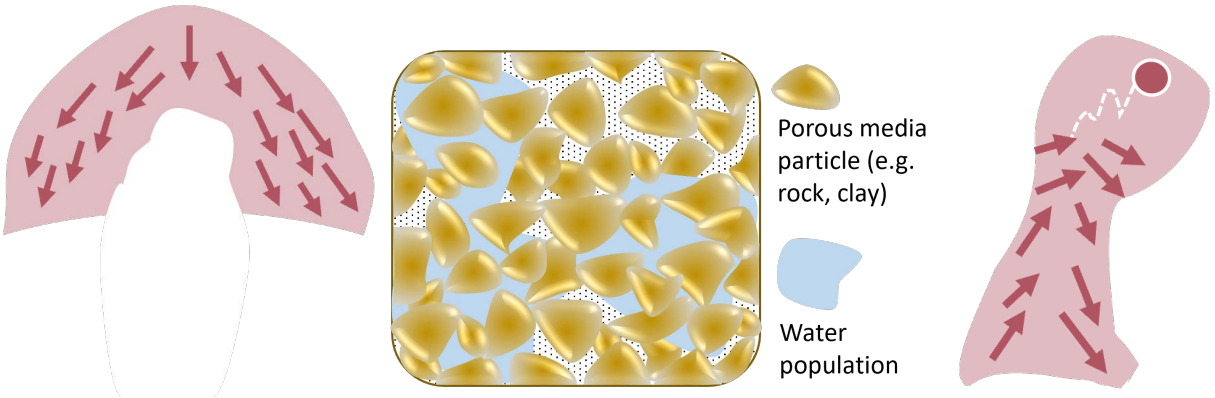


Figure 2.27: Examples of fluid dispersion. Left: Mechanical dispersion; a depiction of mechanical dispersion, which occurs as a result of bifurcation in the geometry of the system, adapted from [37]. Middle: Porous flow; a depiction of flow in a porous bed. Right: Hold-up dispersion; a depiction of hold-up dispersion, which occurs as a result of a dead-end in a porous system, adapted from [37].

Dispersion generally occurs as an anisotropic form of motion, described by the dispersion tensor, $\underline{\underline{\mathbf{D}^*}}$. However, by taking the trace of the dispersion tensor, we can obtain a steady-state dispersion coefficient, D^*, (Equation 2.59) which considers the change in the mean-squared displacements at long time scales [37]. NMR can measure this effective dispersion coefficient, D^*, to describe dispersion in a system [37].

$$D^* = Tr(\underline{\underline{D^*}}) = \lim_{t\to\infty} \frac{1}{2}\frac{d\sigma^2(t)}{dt} \tag{2.59}$$

We may also represent this dispersive behavior from the perspective of averaged transport with Reynold's decomposition. In this perspective, we express the total dispersive motion as the sum of an average velocity and a fluctuation term. The following section describes the importance of NMR experiments to the study of fluctuating motions.

Velocity Fluctuations

Velocity fluctuations occur in a variety of systems and at different length and time scales. In some systems, these fluctuations do not impact the overall macroscopic flow behavior of the system to first order. However, in turbulent systems, complex fluids, and porous media – among other systems - fluctuations can induce large changes in flow [37]. This might occur through a cascade of energy dissipation that can cause self-similar flow patterns (such as in turbulence); it could also occur through successive microstructural rearrangements in complex fluids, which cause radical changes in fluid effective viscosity.

NMR offers several options for measuring fluctuations in fluids. These include rapid velocimetry techniques (discussed in the *Rapid Velocimetry Techniques* subsection), propagator measurements, and measurements of the velocity autocorrelation function. The double PGSE sequence, described below, offers a particularly powerful option for measuring the velocity of fluctuations [37].

Double PGSE

The double PGSE pulse sequence, as the name implies, effectively combines two PGSE sequences. Double PGSE cancels mean velocity flow effects due to the sequence of gradients used. As described in *NMR and Complex Motion*, strategically applying gradient pulses allows for the manipulation of the higher moments of the gradient waveform; in this case, the first moment of the gradient waveform does not meet the echo condition, but the second moment does. The first moment contains information about the mean velocity, while the second moment contains the fluctuating behavior [37]. This provides a convenient way to

obtain information about velocity fluctuations within the flow field.

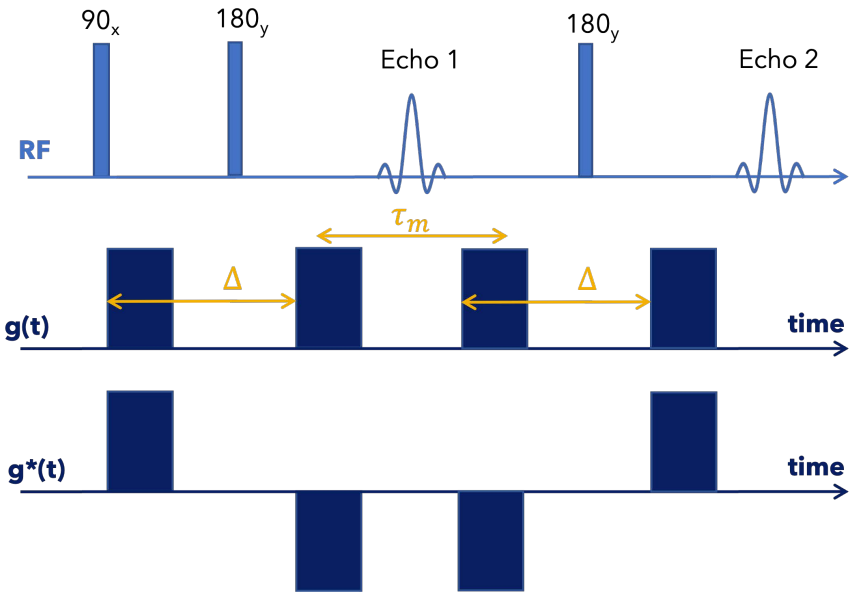


Figure 2.28: The mean velocity compensated double PGSE sequence shown with gradient pulses, $\mathbf{g}(t)$ and effective gradient pulses, $\mathbf{g}^*(t)$.

Figure 2.28 describes the flow *compensated* version of the sequence, showing the RF pulses, gradient pulses, and effective gradients. An *uncompensated* version of the sequence can serve as a control; here, the uncompensated sequence contains both information about the mean and fluctuations, similar to a standard PGSE, but since the pulse sequence is equivalent to the compensated double PGSE sequence it can be more readily compared. The second echo in the sequence contains the fluctuating flow information from the time between the two gradient pulse pairs – often called the *mixing time*, τ_m, while the first echo contains information from a typical single PGSE, and simply occurs due to the pulse sequence design [37].

Equation 2.60 expresses the normalized echo signal for a double PGSE sequence as an

ensemble average [37]. Equation 2.61 shows the corresponding propagator description.

$$E(\mathbf{q}) = \langle \exp\left(i\mathbf{q} \cdot [\mathbf{r}(2\Delta + \tau_m) - \mathbf{r}(\Delta) + \mathbf{r}(0)]\right)\rangle \tag{2.60}$$

$$\begin{aligned} E(\mathbf{q}) = &\int d\mathbf{r}\rho(\mathbf{r}) \int d\mathbf{r}' P(\mathbf{r}|\mathbf{r}', \Delta) \int d\mathbf{r}'' P(\mathbf{r}'|\mathbf{r}'', \tau_m) \\ &\cdot \int d\mathbf{r}''' P(\mathbf{r}''|\mathbf{r}''', \Delta) \exp\left(i\mathbf{q} \cdot [\mathbf{r}''' - \mathbf{r}'' - \mathbf{r}' + \mathbf{r}]\right) \end{aligned} \tag{2.61}$$

In the ensemble average description, each successive $\mathbf{r}$ term denotes the position at the time of a gradient pulse (or, in the case of $\mathbf{r}(0)$, the initial position), with times expressed in terms of Δ and τ_m. The propagator description expresses the cumulative probabilities of moving from a particular state in a given time, which weight the initial spin density, $\rho(\mathbf{r})$. This signal for a single PGSE sequence can also be expressed in terms of the Reynolds decomposition $v = V + u(t)$ of the mean velocity, V, and fluctuations about the mean, $u(t)$ as [37]:

$$E_S(\mathbf{q}) = \exp\left(i\mathbf{q} \cdot \mathbf{V}\Delta\right) \left\langle \exp\left(i\mathbf{q} \cdot \int_0^{\Delta} \mathbf{u}(t)dt\right) \right\rangle. \tag{2.62}$$

But, since the mean flow cancels in the double PGSE sequence for the even echo, the following expression describes the signal in terms of fluctuations only [37]:

$$E_D(\mathbf{q}) = \left\langle \exp\left(i\mathbf{q} \cdot \int_0^{\Delta} \mathbf{u}(t)dt\right) \cdot \exp\left(-i\mathbf{q} \cdot \int_{\tau_m+\Delta}^{\tau_m+2\Delta} \mathbf{u}(t)dt\right) \right\rangle \tag{2.63}$$

The measurement in the low-q limit, using a Taylor series expansion and an assumption of stationarity and zero mean $< u(t) >= 0$ for the fluctuations results in the following equation [37]:

$$E_D(\mathbf{q}) \approx 1 - \frac{1}{2}q^2 \left[2\int_0^{\Delta} \int_0^{\Delta} \langle \mathbf{u}(t)\mathbf{u}(t')\rangle dtdt' - 2\int_0^{\Delta} \int_{\tau_m}^{\tau_m+\Delta} \langle \mathbf{u}(t)\mathbf{u}(t')\rangle dtdt' \right]. \tag{2.64}$$

If we consider that $\tau_m \gg \tau_v$, where τ_v represents the correlation time of the fluctuations, then

the displacements between the two successive encoding intervals for the gradient pulse pairs are completely uncorrelated. In that case, the second integral in the sum from Equation 2.64 equals zero. The new expression for the signal is shown in the equation below [37].

$$E_D(\mathbf{q}) \approx 1 - \frac{1}{2}q^2\left[2\int_0^{\Delta}\int_0^{\Delta}\langle \mathbf{u}(t)\mathbf{u}(t')\rangle dtdt'\right] \tag{2.65}$$

If we would prefer to measure the velocity autocorrelation function (VACF) of the fluctuations, we can consider the situation where $\Delta \ll \tau_v$, such that the observation time is much less than the time of fluctuations [37]. In this case, the fluctuations become essentially constant over Δ. In the limit of $q^2 \to 0$, and assuming a low-q^2 slope, the resulting equation provides the VACF [37]:

$$-\frac{1}{\Delta}\lim_{q_\alpha \to 0}\frac{\partial^2}{\partial q_\alpha^2}\ln|E_D(q_\alpha)| = \langle u_\alpha^2\rangle\Delta - \langle u_\alpha(0)u_\alpha(\tau_m)\rangle\Delta. \tag{2.66}$$

Alternatively, we can also measure the effective dispersion coefficient as a function of varying τ_m to provide the normalized VACF [37]:

$$\frac{\langle u_\alpha(0)u_\alpha(\tau_m)\rangle}{\langle u_\alpha^2\rangle} = \frac{D_{eff}(\infty) - D_{eff}(\tau_m)}{D_{eff}(\infty)}. \tag{2.67}$$

Velocimetry

While PGSE techniques can provide important information about the average flow behavior of a system, certain systems benefit from techniques that offer *spatially resolved* flow measurements. NMR velocimetry techniques allow for the imaging of motion. This is done through a combination of k-space imaging and PGSE techniques to encode for both position and velocity. In this way, each pixel or voxel of an image provides information about the signal propagator, and thus the average velocity of a spatially localized volume element [37]. Velocimetry techniques can provide spatial information about flow down to the

$\sim$10 µm scale. This technique offers an incredibly powerful method for examining spatial flow profiles and heterogeneous systems under flow. It also provides advantages over other techniques such as light scattering in terms of non-invasiveness and opacity requirements [34].

The overall goal of velocimetry involves the measurement of the local velocity field in a fluid sample. We must assume that the spin density, $\rho(\mathbf{r})$, remains constant. In fluid dynamic terms, we require incompressibility of our fluid sample [37]. Various methods of NMR velocimetry exist, including steady state recovery, time of flight, and phase shift (PGSE) methods. Steady state recovery involves the rapid repetition of RF and gradient pulses such that saturation recovery signal depends on the spin motion [37]. Time of flight, on the other hand, involves tagging a section of spins in spatial regions using RF excitation, then taking an image at two separate times, and comparing the displacement of the spatial domains to determine motion [37]. Phase shift methods rely on the phase encoding process described previously in the PGSE pulse sequence techniques. Since phase shift methods form the basis for the experiments described in the manuscripts which follow, our discussion will focus solely on these.

As we noted above, our goal is to measure the velocity field, $\mathbf{v}(\mathbf{r}, t)$. This measurement relies on the phase shifts of our spins, and it also requires a mixed perspective in terms of fluid mechanics. Our desired local velocity field represents a Eulerian perspective; here, we imagine a stationary spatial frame which our fluid flows through to provide a velocity profile or other flow information. However, NMR inherently operates from a Lagrangian perspective, since NMR pulses excite and phase encode individual spins, which become ensemble averaged in our signal analysis methods [37]. This ensemble average of the fluid's spin behavior informs each individual "piece" of our Eulerian perspective. Though this mixed perspective may seem like a pedantic detail, it represents a fundamental strength of NMR in the study of fluid mechanics. Other techniques often exhibit limitations in the

ability to probe *both* the "microscopic" and the macroscopic behavior of a fluid. However, as NMR not only detects individual spin behavior, but can also shift through a wide range of averaging of length and time scales of motion with pulse sequence design, it provides an incredible ability to resolve complex molecular behavior which may otherwise go unnoticed with other techniques.

Physical constraints - Capillary flow Of course, physical constraints which limit our measurable maximum and minimum velocities exist. The maximum measurable velocity is fundamentally limited by the receiver coil length for flow through experiments, l, and the observational timescale encoding displacements [37]. The receiver coil limitation exists because the RF coil can only encode and detect a given spin-bearing molecule while within the length of the coil. Similarly, there is a certain minimum amount of time needed to encode displacements, which corresponds to the echo time, TE [37]. In this way, we can define the maximum measurable velocity for flow through experiments as [37]:

$$v_{max} = \frac{l}{TE}, \quad \left[\frac{\mathrm{m}}{\mathrm{s}}\right] \tag{2.68}$$

Self-diffusion of the fluid species limits the minimum measurable velocity. Since the longest observable time-scale we might expect, under a stimulated echo sequence, would be T_1, our minimum measurable velocity could be defined as [37]:

$$v_{min} = \sqrt{\frac{D}{T_1}}, \left[\frac{\mathrm{m}}{\mathrm{s}}\right] \tag{2.69}$$

These definitions represent a minimum measurable velocity of about 50 µm/s for water, and about 1 µm/s for larger molecules based on the RF coils used in this research.

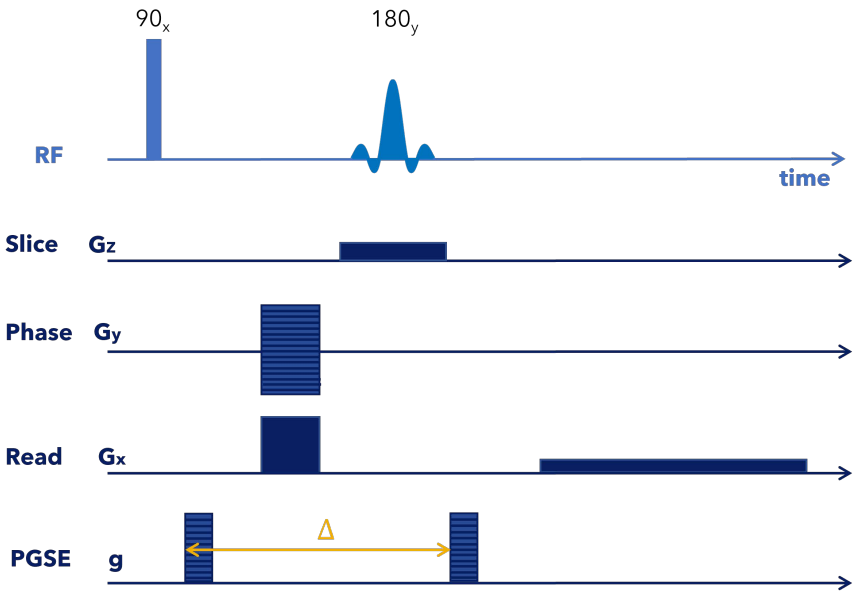


Figure 2.29: The basic velocimetry pulse sequence, which includes both q- and k-space encoding for imaging a full propagator in each pixel.

The basic velocimetry pulse sequence, signal, Fourier analysis, and propagator As was mentioned previously, to perform velocimetry experiments we must image in both k-space and q-space. The basic version of a velocimetry pulse sequence, depicted in Figure 2.29, involves a PGSE portion incorporated with a k-space imaging scheme. In this sequence, the typical phase encoding from a pair of stepped PGSE gradients encodes for motion during the time of the gradient flow encoding time, Δ, while the k-space imaging scheme traverses through k-space with the use of a stepped phase-encoding gradient, and a readout gradient applied during the echo acquisition. This efficiently encodes for both motion and position within a sample and forms the basis for a variety of other motion-encoding schemes.

We can represent the signal obtained from such a sequence with the narrow gradient pulse approximation. The equation below depicts this signal [37].

$$E(q, \Delta, \mathbf{r}) = E(0, \Delta, \mathbf{r}) \exp(iqv\Delta) \exp(-q^2 D\Delta) \tag{2.70}$$

In this expression, $\exp[iqv\Delta]$ represents an oscillating term that corresponds to the velocity induced phase modulation behavior of the signal, whereas $\exp(-q^2D\Delta)$ denotes a damping term associated with the diffusive behavior [37]. Due to using quadrature detection, our signal contains both real and imaginary components which can be used to calculate phase shift and amplitude. Sampling in both k-space and q-space also necessitates two sets of Fourier transforms to process the data. After this analysis, we can obtain a propagator expression for each pixel within the image, Equation 2.71, with characteristics described by Equations 2.72-2.74 [37]. These expressions consider a digital perspective, where N is the total number of points over which the propagator is defined, k_v is the digital shift of the pixel resolved propagator (not to be confused with the spatial encoding k), n_D is the current value of the stepped gradient, and g_m is the maximum value of the gradient [37].

$$\overline{P}\left(\frac{k_v}{N},\Delta\right) = \left(\frac{\pi n_D^2}{\gamma^2\delta^2 g_m^2 D\Delta}\right)^{1/2} \exp\left[-\frac{\pi^2 k_v^2 n_D^2}{\gamma^2\delta^2 g_m^2 N^2 D\Delta}\right] \otimes \delta\left(\frac{k_v}{N} - \frac{\gamma\delta v\Delta g_m}{2\pi n_D}\right) \tag{2.71}$$

$$k_v = \frac{N\gamma\delta v\Delta g_m}{2\pi n_D} \tag{2.72}$$

$$v = \frac{2\pi n_D k_v}{N\gamma\delta v\Delta g_m} \tag{2.73}$$

$$k_{\mathrm{FWHM}} = \left(\frac{2}{\pi}\right)[\ln(2)]^{1/2} N\gamma\delta\left(\frac{g_m}{n_D}\right)(D\Delta)^{1/2} \tag{2.74}$$

$$D = \frac{(n_D k_{\mathrm{FWHM}})^2}{\left[\left(\frac{4\ln(2)}{\pi^2}\right)\gamma^2\delta^2 g_m^2 N^2\Delta\right]} = \frac{3.56(n_D k_{\mathrm{FWHM}})^2}{[\gamma^2\delta^2 g_m^2 N^2\Delta]} \tag{2.75}$$

In these expressions, k_v defines the position of the propagator peak center along the $\frac{g_m}{n_D}$ gradient steps, v defines the velocity (located at the peak center), k_{FWHM} defines the full-width-half-max of the assumed Gaussian propagator, and D describes the diffusion constant obtained from the propagator. Since the propagator describes the distribution of velocities within the pixel, the center of the Gaussian peak logically indicates the average velocity within that pixel [37]. The "spread" or width of the peak naturally relates to the diffusion

coefficient.

The Two q-step Method It is worth noting that, in practice, there is often little reason to obtain an entire propagator for each individual pixel. To obtain a well-resolved full propagator requires many q-steps, which take a great deal of valuable experimental time, and may offer little benefit. A reasonable alternative which can offer the mean flow at a pixel utilizes only two q-steps: a positive and negative of the same magnitude. Such a sequence, depicted in Figure 2.30, forms the basic sequence used in most of the velocimetry experiments within the manuscripts of this document [37].

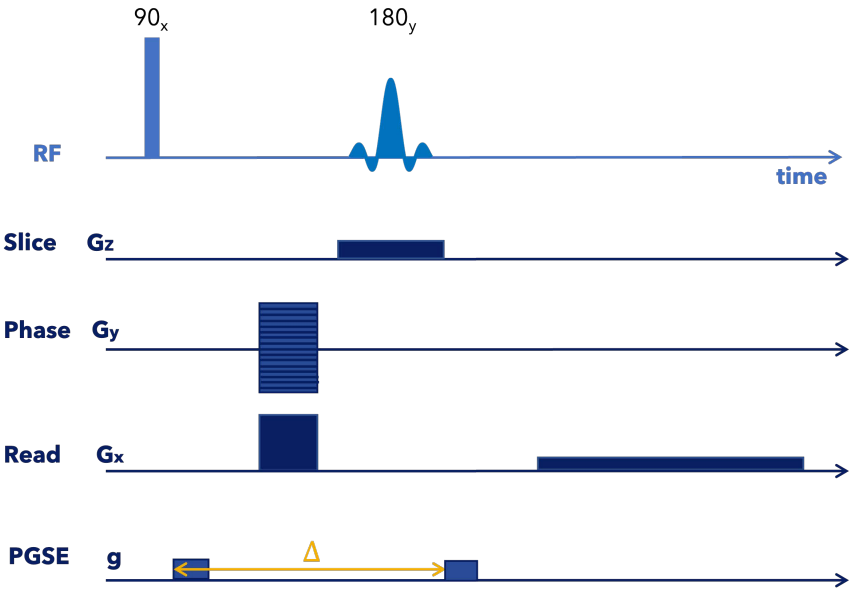


Figure 2.30: The two q-step velocimetry pulse sequence, which uses 2 q-steps instead of obtaining the full propagator (shown in Figure 2.29).

The signal in this case lends itself to a more direct form of data analysis. Equations 2.76-2.77 represent expressions for the two q-steps. To determine the phase shift which represents the mean velocity change, one can exploit the phase relationship between the oscillating real and imaginary signals [37]. Equations 2.78-2.82 show the process of obtaining the velocity

from this relationship.

$$q_1 = \gamma\delta(-g_{max}) \tag{2.76}$$

$$q_2 = \gamma\delta(+g_{max}) \tag{2.77}$$

$$\tan\phi = \frac{\mathrm{Im}(S)}{\mathrm{Re}(S)} \tag{2.78}$$

$$\phi_1 = \arctan\left(\frac{\mathrm{Im}(S_1)}{\mathrm{Re}(S_1)}\right), \quad \phi_2 = \arctan\left(\frac{\mathrm{Im}(S_2)}{\mathrm{Re}(S_2)}\right) \tag{2.79}$$

$$\phi_2 - \phi_1 = (q_2 - q_1)v\Delta = \gamma\delta v\Delta(+g_{max} - (-g_{max})) \tag{2.80}$$

$$\phi_2 - \phi_1 = 2\gamma\delta v\Delta g_{max} \tag{2.81}$$

$$v = \frac{\phi_2 - \phi_1}{2\gamma\delta\Delta g_{max}}, \quad [\mathrm{m/s}] \tag{2.82}$$

Fourier Analysis of the Two q-step Method The advantage of the two q-step method becomes clear when considering the power of *zero-filling* the q-domain images before Fourier transforming the q-space data. The zero-filling process changes our q-domain from q_1 and q_2 to $0 < n < N-1$ [37]. The Fourier analysis for this process involves a propagator represented by Equation 2.83 [37]:

$$\overline{P}\left(\frac{k_v}{N}\right) = 1 + \exp\left(\frac{i2\pi k_v}{N} - i\phi\right) \tag{2.83}$$

Where the steps in our q-domain range from $0 < n < N-1$, and the steps in the propagator domain range from $-N/2 < k_v < N/2 - 1$. A zero-fill of the q-domain (digitally in k_v) offers the ability to "create" a propagator from the two q-step data so that the data can then provide the same information obtained from the full propagator experiment. Although one might assume that the zero-fill process inserts uncertainty into the measurements, an analysis of error [37] demonstrates that both the phase method and Fourier analysis method have equivalent magnitudes of uncertainty. The two q-step method with Fourier analysis provides an efficient means to obtain velocimetry information without the need for sampling

a large range of q-space [37].

The Reference Phase Processing Method In a similar fashion to the two q-step method, another option to determine velocity which does not require the full propagator uses a reference $q = 0$ step along with a $q = q_1$ step.

To determine the phase angle in this situation, we exploit the following relationship between the signal from the $q = 0$ step and the $q = q_1$ step [37]:

$$\frac{E(q_1, \Delta, \mathbf{r})}{E(0, \Delta, \mathbf{r})} = A \exp(i\phi) \tag{2.84}$$

Where $\phi = q_1 v \Delta$, and $A \leq 1$ represents the attenuation factor from diffusive effects. However, this method suffers from low signal-to-noise, and in practice the two q-step method provides superior experimental information [37].

Rapid Velocimetry Techniques

Various rapid velocimetry sequences which build upon the basic sequence represented in Figure 2.30 exist, with different levels of efficiency and robustness to artifacts. Such sequences may prove especially valuable when attempting to capture fast dynamics that a typical velocimetry sequence cannot resolve. Typically, these sequences sacrifice spatial resolution $\sim$100 µm (often partly from the occurrence of artifacts) in favor of speed, providing full images on the order of 100 ms. One sequence of interest to the experiments described in this document, Rapid Acquisition Relaxation Enhanced imaging (RARE), provides a balance between speed and resilience to artifacts [37].

RARE utilizes a symmetric k-space sampling scheme, as well as a multiple spin-echo train to refocus unwanted background phase shifts [37]. Both prevent ghosting artifacts, which flow and gradients can amplify. Two modifications often used to prevent ghosting artifacts include soft 180°; RF pulses (as opposed to hard) and the use of even echoes in the

pulse sequence, since odd and even echoes alternate in amplitude due to pulse imperfections (this phenomenon also becomes exacerbated by flow) [37].

Velocimetry Applications

Rheo-NMR Chapter 3 introduces the field of rheology, defined as the *study of the flow and deformation of matter*, which the reader may find helpful in understanding this section. Rheo-NMR – which constitutes the use of NMR techniques to provide rheological information about a sample – provides a useful complement to standard rheometry techniques. These techniques may consist of relaxometry, diffusometry, and velocimetry. Rheo-NMR velocimetry can provide a very useful complement to visualize flow induced by deformation. The ability to spatially resolve flows offers utility in instances where fluids exhibit wall-slip, shear-banding, or sample fracture [35]. These behaviors are all typical of *complex fluids*. Complex fluids encompass a wide variety of materials and have increasingly piqued both academic and industrial interest for their strange and useful properties (complex fluids are also described in more detail in Chapter 3). There is a growing need to understand the flow profiles of these fluids, as other rheometric techniques cannot always describe their motion.

Rheo-NMR provides particular advantages over other techniques for obtaining flow information. Many other techniques, such as particle image velocimetry (PIV), Rheo-SANS (small-angle-neutron-scattering) and Rheo-SAXS (small-angle-x-ray-scattering), among others, rely on optical methods to image velocity. These methods necessarily come with constraints. In the case of PIV, it is required to imbibe the fluid with tracer particles, which can interfere with the natural mechanical deformation of the fluid [34]. For Rheo-SANS or Rheo-SAXS, transparency requirements dictate the type of samples which can be accurately imaged. Additionally, most techniques have significant constraints on the geometry of the sample that can be imaged. In the case of Rheo-NMR, there are no transparency constraints,

no geometry constraints (provided the sample can fit into the active region of the RF coil), and there is no risk of sample destruction since it is noninvasive [34, 37].

NMR also offers a broad range of length and time scales to measure motion. Many other techniques have high precision and sensitivity but can only measure within narrow length and time ranges [34, 37]. The ability to design pulse sequences is powerful because it allows NMR to robustly measure many types of dynamic motion; and, as hardware advances, this power increases. The research demonstrated in this document utilizes this particular advantage of NMR to study the flow of nanocolloidal suspensions, a class of complex fluids.

RHEOLOGY AND COMPLEX FLUIDS

Rheology

Introduction

Rheology is the study of the flow and deformation of matter [110]. The techniques used to measure this flow and deformation fall under the term rheometry, and possibly the most quintessential, powerful, and widely used instrument at the rheologist's disposal is the rheometer itself. Rheometers measure rotational and oscillatory deformation based on the principle of constant shear [110], and can operate in controlled stress or controlled shear rate mode. A material sandwiched between two flat plates spanning a height h, where the top plate moves with a velocity $\vec{v}$ and the bottom remains stationary, will experience a deforming force over the area in contact with the top plate, known as *shear stress* (Fig. 3.1). The shear rate $\dot{\gamma} = d\vec{v}/dh$ will not vary, but the velocity will change at a constant (linear) rate [110]. Rheometers operate on this powerful principle, which we call the *viscometric assumption*: a linear velocity profile guarantees a constant shear rate across the entire fluid [10]. In the most typical mode, this allows a rheometer to control shear across a sample and measure the resulting stress. Unfortunately, it is precisely this assumption that limits its capabilities.

The limitation arises because the rheometer requires that dh, a differential element of the fluid height, is constant and thus represents the entire fluid [110]. Simple fluids with homogeneous structure easily satisfy this requirement. Many complex fluids do not. Often the most interesting and technologically useful fluids do not, which leaves the scientist hoping to study or make use of such fluids without a satisfying technique to probe their behavior. Our advancing, growing society demands superior products, and the design and manufacture of such products necessitates techniques to more fully characterize these fluids. Often fluids that defy simple behavior are categorized generally as *complex fluids*.

The rheometer can measure fluids by deforming them in two primary ways: rotation

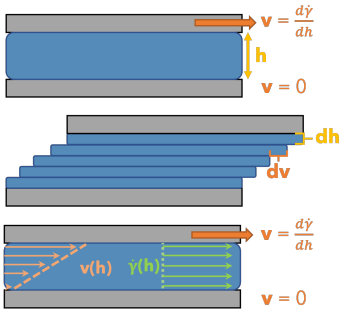


Figure 3.1: Top: The Couette flow two-plate model, where the top plate moves with velocity v and the bottom plate is stationary. The plates are separated by a fluid sample with a height, h. Middle: The discretized version of the two-plates model, showing fluid layers with constant height and velocity differentials. Bottom: The two-plate model showing the linear velocity profile and constant shear, demonstrating the viscometric assumption.

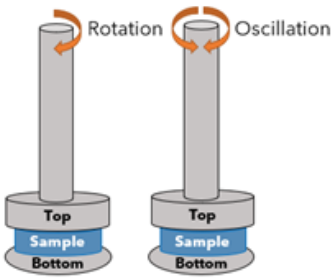


Figure 3.2: Rheometers have two main modes of deforming fluids: rotation and oscillation. Rotation probes the resistance to flow, while oscillation probes the balance between viscous and elastic forces, and how this influences flow.

and oscillation (Fig. 3.2). Measurement of stress under controlled shear, or shear rate under controlled stress during rotational deformation provides information about the *fluid flow response*, like the flow between two plates (imagine that the top plate rotates in a circle rather than dragging the fluid in a linear path) [110]. Oscillatory deformation provides information about the *molecular structure* which produces the flow response [20]. While rotating our fluid in a consistent way will measure how the fluid resists flow (its *viscosity*), oscillating the fluid will question how closely the fluid "harmonizes" with the disturbance [20]. Fluids will always oscillate at the same frequency as the rheometer's oscillation in the

linear regime (where the deformation is not enough to damage the internal structure) but how closely this matches the rheometer input indicates the molecular details.

Fluids which respond and harmonize very quickly, i.e. for which the input strain and stress are nearly in phase, are deemed *elastic*: they bounce back, like a ball of Silly Putty®. They also have stronger internal molecular interactions, where energy can be stored and quickly dissipated without loss of structure or unnecessary friction. Fluids which respond more slowly are called *viscous* and have a larger phase difference between input strain and stress response; the molecules in these fluids are not structured, but must flow past each other, expending energy as they sample each other's energetic states and lose kinetic energy through close-range electron interactions. Viscoelastic fluids, which have elastic and viscous

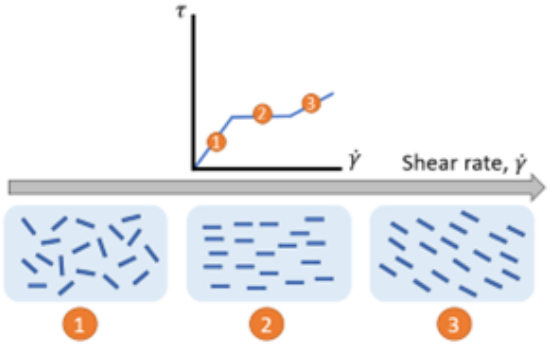


Figure 3.3: Schematic depicting shear-banding phenomenon in a nanorod suspension. Shear-banding is a process that causes microscale restructuring as the fluid adjusts to the imposed shear and acts to dissipate it. (1) Rest state structure response; (2) Characteristic "stress plateau"; (3) Further restructuring due to shear.

forces both significantly contribute to their mechanical behavior, are commonly studied with oscillatory rheometry because of this ability to differentiate between the two forces. Many viscoelastic fluids are also *shear-banding*, meaning they exhibit a re-ordering of their structural components under shear [96]. This is characteristically seen as "bands" in a plot of shear stress against strain for a shear-banding material, where an obvious stress plateau signifies the presence of this reordering effect. (Fig. 3.3) Shear-banding is of particular

interest because it originates from non-linear behavior as described earlier, and rheometers are limited in their ability to characterize fluids that exhibit this phenomenon.

Rheological Models

Numerous macroscale models exist to describe fluid behavior by relating stress and shear rate. These are primarily separated into the Newtonian fluid model, non-Newtonian models, viscoelastic models, yield stress models, time-dependent models, and empirical models. Although it is beyond the scope of this document to describe all models, a select few of importance are explained below.

The Newtonian Fluid Model

The Newtonian fluid model describes the shear stress, σ, of a fluid with constant viscosity independent of the shear rate, $\dot{\gamma}$. Equation 3.1 below describes the constitutive equation for a Newtonian fluid [19].

$$\sigma = \mu \frac{du}{dy} = \mu \dot{\gamma} \tag{3.1}$$

Common Newtonian fluids include water, honey, and motor oil, among others [109].

The Power-Law (Ostwald-de Waele) Model

The Power-Law fluid model defines a fluid with either shear-thinning (often called pseudoplastic) or shear-thickening (often called dilatant) behavior, and as the name suggests, uses a power-law relationship to do so [10].

$$\sigma = K \dot{\gamma}^n \tag{3.2}$$

Here, K represents the consistency index while n describes the shear-thinning or shear-thickening behavior. When $n > 1$, the fluid is shear-thickening, whereas when $n < 1$,

the fluid is shear-thinning. For $n = 1$, the fluid exhibits Newtonian behavior. Numerous fluids in consumer products exhibit shear-thinning or shear-thickening properties. Common examples are paint, ketchup, and hair gel (all shear-thinning), and the shear-dependent material response offers a challenge in industrial applications like pumping paper or fruit pulp or other industrial slurries.

The Bingham Plastic Model

The ideal Bingham Plastic Model requires the shear stress to surpass a characteristic yield stress for flow to occur [10]. Once the flow occurs, the fluid otherwise exhibits the linear relationship between stress and shear rate of a Newtonian fluid. Equation 3.3 below demonstrates this relationship [10].

$$\sigma = \sigma_y + \mu_p \dot{\gamma} \tag{3.3}$$

In this equation, σ_y indicates the yield stress, while μ_p describes the plastic viscosity, which is the viscosity after yielding. Some fluids that exhibit Bingham plastic behavior include drilling muds/slurries and concrete.

The Herschel-Bulkley Model

The Herschel-Bulkley (H-B) model combines the Power-Law and Bingham models [10] and finds common use in clay or sand suspensions and drilling applications. Recent research has incorporated microscale fluidization concepts into the transient behavior of the H-B power law scaling and shear banding [14].

$$\sigma = \sigma_y + K\dot{\gamma}^n \tag{3.4}$$

Examples of common fluids with behavior modeled by H-B include ketchup, toothpaste, and mayonnaise.

The Maxwell and Kelvin-Voigt Models

The Maxwell and Kelvin-Voigt models describe the behavior of viscoelastic fluids. The representation of a Maxwell fluid includes an elastic spring and a viscous "dashpot" (or dampening force), connected in series [110]. The damper describes a Newtonian fluid behavior, while the spring describes an idealized elastic force with Hooke's Law. This model describes solid-like behavior at short timescales, but as a constant strain is applied, the dissipation of the stress through the viscous element causes liquid-like behavior at long timescales. Equation 3.5 below describes the Maxwell fluid model, where E indicates the elastic modulus and γ the strain [110].

$$\frac{1}{E}\frac{d\sigma}{dt} + \frac{\sigma}{\mu} = \frac{d\gamma}{dt} \tag{3.5}$$

The Kelvin-Voigt model uses the same representation of springs and dashpots as the Maxwell model, but instead of a series connection, the model connects them in parallel [110]. This configuration describes solid-like materials which exhibit creep behavior when exposed to a constant stress. Rather than a rapid deformation when exposed to stress, the strain of the material increases more slowly over time and does not relax due to the elastic spring element. Equation 3.6 describes the Kelvin-Voigt behavior [110].

$$\sigma = E\varepsilon + \mu\frac{d\gamma}{dt} \tag{3.6}$$

Rheometer Basics

The most widely used instrument to perform rheometry experiments is the *rheometer*. A rheometer is capable of deforming fluids through compression, shear, and oscillatory shearing experiments [109]. A variety of different useful experiments exist in these categories. A

description for three such experiments of interest in this work follows.

Shear experiments involve a fluid sample fit between a stationary bottom plate and an upper plate which rotates (depicted earlier in Figure 3.2) and can involve steady or oscillatory motion. The experiments described below all constitute shearing tests.

A **flow sweep** provides a measure of the fluid's stress response, σ, in response to the shear rate $\dot{\gamma}$. This data provides information about shear-thinning, shear-thickening, and can be used to judge similarity to the behavior of known fluids [109] (Figure 3.4).

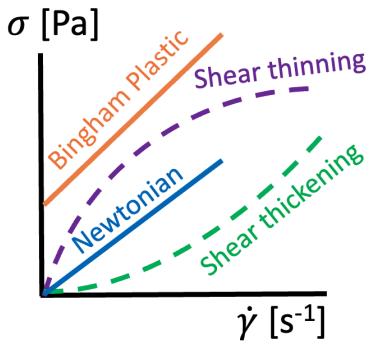


Figure 3.4: A depiction of idealized stress σ and shear rate $\dot{\gamma}$ relationships for several common rheological models. The deviation from Newtonian behavior helps to identify what type of rheological model may best describe a given fluid.

A **strain sweep** applies a range of oscillation strain values, γ (often expressed as a percentage), to the fluid, and measures the viscosity, μ, as well as the storage modulus, G', and loss modulus, G'' (G' and G'' are explained in more detail below) [109]. From this experiment, the linear viscoelastic region (LVR), where the material has a linear stress response to the imposed shear, can be obtained. Beyond the LVR, the material experiences a critical stress which irreversibly destroys its elastic nature at a microscale. The oscillation strain value for an oscillatory shear experiment must be within the LVR to ensure that the measurements reliably measure the elastic nature of the material [109].

Frequency sweeps involve rotationally shearing the material to a specified strain angle, γ, within the LVR at different frequencies of rotation [109]. This type of experiment

provides information about the material's *viscoelasticity*. This oscillatory motion probes the frequencies of motion within the molecular bonds and particulate interactions of the material [20]. The variables G' and G'' are often plotted against ω, and they represent the *elastic modulus* and *loss modulus* of the material, respectively. The elastic component, G', relates

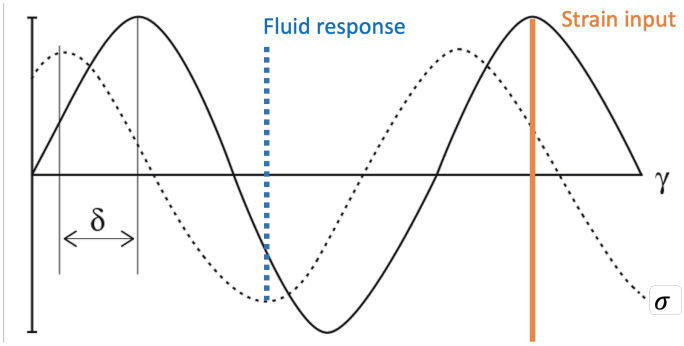


Figure 3.5: A plot which demonstrates how the stress response of the fluid, σ, to a given strain, γ, results in a "lag" between the phases of the waveforms. This phase difference is defined as δ and describes the viscoelasticity of the fluid.

to the energy stored within the molecular bonds of the material when measured in the LVR, which can be "stretched" and distorted, but not broken (reversible energy). Viscous response indicated by the loss modulus G'', relate to the frictional behavior of the molecules as they slide past one another in flow (irreversible, or lost energy). The variables G' and G'' are often combined to describe the complex modulus, $G^* = G' + iG'' = \frac{\tau}{\gamma}$, and relate to the phase shift (δ) between the frequency of the applied strain (γ) and the fluid's stress response σ [109]. (Figure 3.5). Viscoelastic solids and gels will generally have a constant value of G', and $G' > G''$, while viscoelastic liquids may have $G'' > G'$ and switch to $G'' < G'$ at a specified "crossover" frequency known as the gel point [110]. Equation 3.7 below expresses

these relationships and shows δ can describe the deviation from an ideal elastic solid [109].

$$G^* = \frac{|\tau|}{|\gamma|} = G^{'} + iG^{''} \tag{3.7}$$

$\delta = 0°$, ideal elastic solid

$45° < \delta \leq 90°$, viscoelastic fluids

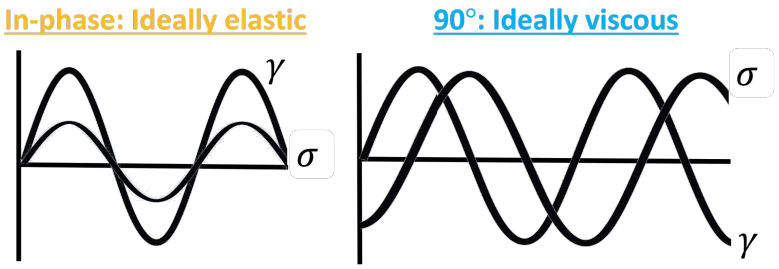


Figure 3.6: The plots above demonstrate the relationships between imposed strain, γ, and responding fluid stress, σ, for an ideally viscous fluid and an ideally elastic material.

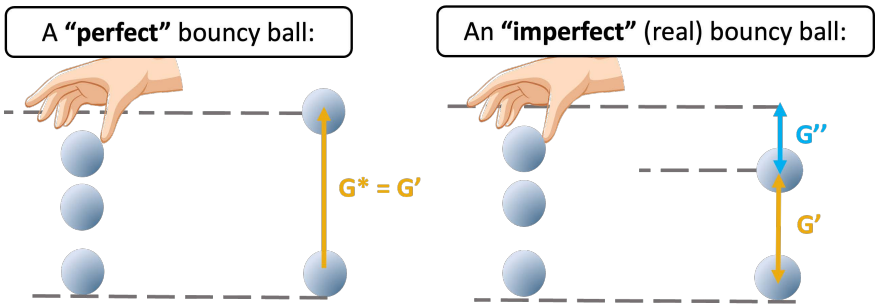


Figure 3.7: A depiction of an ideal and a real bouncy ball to describe the relationship between G^*, $G^{'}$, and $G^{''}$ in terms of elastic and viscous forces. An ideal bouncy ball will bounce back to its original height with no loss of energy due to frictional viscous forces; a real bouncy ball will instead lose height due to the frictional viscous forces, and that loss of height can be related to $G^{'}$ and $G^{''}$ through δ, the phase difference.

Figure 3.6 shows the stress and strain relationships for an ideally elastic material and an

ideally viscous material. Figure 3.7 provides an analogy for viscous and elastic components with a "bouncy ball" [129]. A perfectly elastic ball will return to the same height that it was dropped, as no energy was lost due to internal or external friction. A realistic ball, which contains friction, will not return to the same height. The difference between the height the ball was dropped from and the height after bouncing (i.e. akin to the phase shift δ) can give information about the viscous component. To perform these tests, various

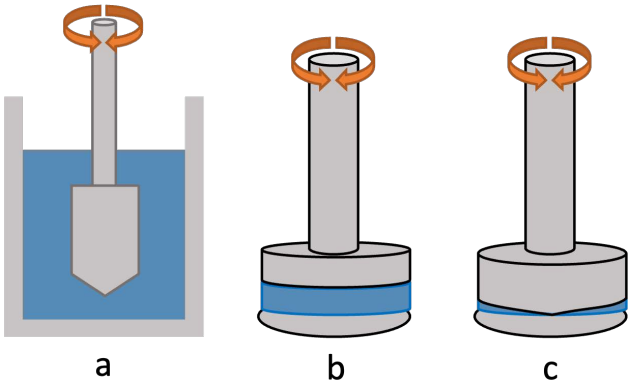


Figure 3.8: A comparison of three different common rheometer geometries. Geometry a) depicts a "cup and bob" or Couette cell geometry, often used for low to medium viscosity samples; geometry b) depicts a parallel plate, well-suited for medium viscosity samples and gels; and geometry c) shows a cone and plate geometry, commonly used for low to medium viscosity samples.

types of geometries may be inserted onto the rheometer, such as cone and plate, cup and bob (Couette cell), and parallel plate, which Figure 3.8 demonstrates. The choice of which geometry to use lies with the sample's characteristics; low to medium viscosity samples may benefit from the use of a Couette cell or a cone and plate, while medium viscosity samples and gels find utility with a parallel plate geometry [109].

Complex Fluids

Introduction

The surprise of grabbing a ketchup bottle and winding up with a giant mess is hard to forget. Complex fluids, like ketchup which is a suspension of tomato cell fibers in a suspending fluid, flow in strange and often surprising ways. They are also ubiquitous in daily life. Complex fluids encompass everything from the food we consume to the personal care products we rely on for our health and comfort [96, 110]. They comprise materials that have revolutionized our quality of life in the past half century, like the polymers in plastics and the liquid crystals in electronics. Even critical healthcare products, like gel capsules, skin grafts, and joint replacements, rely on complex fluids. Modern life without them would be near impossible. They are used in the way we obtain fuel for travel, in myriad industrial settings underpinning the economy, and within our bodies, as we are all filled with complex fluids like blood, mucus, and synovial fluid, to name only a few [110].

Complex fluid behavior and applications vary greatly, but they share certain commonalities. Complex fluids have macroscale mechanical properties that lay on a continuum between a liquid and solid [6, 96]. A complex fluid's macroscale behavior is dominated by structural features at the microscale (a term that, in this document, refers to a range of length scales between 10^{-9} and 10^{-3} m). Disorder or order in the structure of the fluid controls the way the fluid flows, but also dynamically changes with the flow and deformation of the fluid itself. This property is what makes complex fluids incredibly versatile, but also difficult to study and quantitatively model. Fluids are studied with a rheometer, which deforms them by compression or shear, and records how they respond allowing researchers to classify fluids and their applications based on this response [110].

A primary challenge with complex fluids is that rheometers measuring stress-strain response are subject to the viscometric flow assumption, which assumes that the fluid flows

with a linear laminar velocity profile [11]. The internal structures of complex fluids impact velocity profiles and defy this critical assumption. This means experiments with rheometers on complex fluids require care in interpreting stress-strain responses to characterize their behavior [107]. Given how integrated our lives are with complex fluids, these limitations constitute a striking problem in manufacturing and processing.

This challenge can be addressed with NMR, which can differentiate between molecules moving at different velocities and track their motion at a variety of length and time scales [34, 37]. This means that NMR can measure the microscale velocity profiles in flow cells that rheometers cannot. It is this ability to manipulate and detect changes in spins that allows for the powerful molecular tracking of displacements on various scales (see Chapter 2, Basics of Nuclear Magnetic Resonance, for more details) [36, 37].

Colloid Theory

Basics A colloidal suspension contains a dispersion medium, a solvent, and a colloidal particle solute phase [99]. These particles constitute a collection of atoms or molecules, which normally exceed 1 nm in length. Due to the small size of these particles, thermal fluctuations on the order of k_BT (where k_B indicates the Boltzmann constant, 1.38×10^{-23} J/K) cause them to undergo Brownian motion due to solvent-particle collisions. For an ideal spherical particle, this causes a standard diffusivity which depends on the dynamic viscosity of the dispersion medium, μ, as well as the colloid radius, R, and the thermal energy k_BT [99, 108]. The expression for the Stokes-Einstein-Sutherland diffusivity is

$$D = \frac{k_BT}{6\pi\mu R}. \tag{3.8}$$

Surface forces, rather than body forces, dominate colloids because of their very large surface area to volume ratio ($S/V \gg 1$) [99]. These surface forces contribute to the

complicated properties colloids exhibit compared to pure small molecule liquids. Surface forces such as electrostatic interactions and steric behavior of the colloids and the dispersion medium, as well as interactions with the container walls, dictate the type of material properties colloids demonstrate [96, 99]. They also control whether a colloidal suspension is stable or unstable. Unstable suspensions lead to aggregation and sedimentation of the colloid phase [96, 99].

Stability of Colloids Colloids remain stable in suspension when the density of the particles remain lower than the density of the solvent [99]. Instability of a colloidal suspension occurs because of attractive forces that cause particles to initially couple and then group into aggregates, which eventually exceed the density of the solvent, and cause gravitational settling [108]. Three main mechanisms prevent aggregation: *electrostatic stabilization*, *steric stabilization*, and *electrosteric stabilization* [99]. All three mechanisms function by ensuring a repulsive force exists to counteract the attractive force that causes aggregation.

Electrostatic stabilization prevents aggregation by ensuring that the colloid particles have like charges [99, 108]. Because like charges repel, this acts as a barrier to the attractive forces which cause particles to stick and aggregate. Steric stabilization involves coating particles with a polymer layer, which generates a repulsive force between polymer layers from approaching coated colloids, again preventing aggregation [99, 108]. Electrosteric stabilization uses a polyelectrolyte layer to generate a repulsive force that stabilizes coated colloids [99, 108].

Various parameters exist that influence whether a colloid suspension remains stable or unstable. These parameters, when tuned or altered, affect the colloidal interactions and thus the rheological properties of the suspension. Examples of such parameters include colloid size, shape, or volume fraction, solvent composition (pH, ionic strength, and dielectric properties), and the presence of additional species such as polymers or polyelectrolytes [99, 108]. The

following equation describes the total interactions of a colloidal suspension [99]:

$$\Phi_{Total} = \Sigma\Phi_{Attractive} + \Sigma\Phi_{Repulsive} \tag{3.9}$$

The variable Φ_{Total} refers to the total interaction electric potential energy, which includes the summation of all attractive forces and all repulsive forces. Attractive forces originate from the van der Waals interactions. Repulsive forces originate from electrostatic interactions and steric forces. In general, to ensure a stable suspension, one should require $\left|\Sigma\Phi_{Repulsive}\right| \geq \left|\Sigma\Phi_{Attractive}\right|$ [99, 108].

Van der Waals Interactions Van der Waals interactions in colloids originate from permanent dipole forces as well as London dispersion forces [96, 99, 108]. Permanent dipole forces occur in charged species. London dispersion forces cause temporary induced dipole moments in atoms; for example, two helium atoms in close vicinity to one another will arrange the polarity of their electron clouds such that they will each become a dipole with a partial positive electric charge, δ^+ on one side, and a partial negative charge, δ^-, on the other [99]. At the atomic level, the van der Waals potential between two atoms separated by a distance h can be described as [99]:

$$V(h) = -\frac{c}{h^6} \tag{3.10}$$

Where V describes the electric potential energy and c indicates a proportionality constant. For microscopic particles, long range interactions also occur; long range interactions are important in liquid crystal colloids and are described in the Nanocrystalline Cellulose subsection below. To obtain a pair potential for microscopic bodies, such as two colloidal spheres, one can integrate the electric potentials over all atoms within the two interacting bodies [99]. The van der Waal's attraction force between two spherical bodies of radius R

can be expressed as [99]

$$V(h) = -\frac{A}{6}\left[\frac{2R^2}{h(2R+h)} + \ln\left(1+\frac{h}{2R}\right)\right], \tag{3.11}$$

where A represents the Hamaker constant, described in more detail in the following section. If one assumes a small distance h relative to the radius of the spheres, R, such that $R \gg h$, then the first term in the brackets dominates, and the expression simplifies to [99]:

$$V(h) = -\frac{AR}{12h} \tag{3.12}$$

Which includes a geometric factor of 1/2. For the interaction between a sphere and a wall, the formula is instead $V(h) = -AR/6h$. This indicates that the attraction between a sphere and nearby wall is twice that of the attraction between two spheres. Additionally, it is important to note that the van der Waal's interaction between two identical bodies in suspension is always attractive, whereas the interaction between bodies could be attractive or repulsive, depending on the value of the Hamaker constant [99, 107].

The Hamaker Constant The Hamaker constant relates the primary absorption frequency of the system, ν_e, with the dielectric constants, ε_i, and refractive indices, n_i, of the particles and the dispersion medium. The equation for the Hamaker constant, where the subscript of 1 refers to both colloids and 2 refers to the dispersion medium, is shown below [99].

$$A_{121} = \frac{3}{4}k_BT\left(\frac{\varepsilon_1-\varepsilon_2}{\varepsilon_1+\varepsilon_2}\right) + \frac{2h\nu_e}{16\sqrt{2}}\frac{(n_1^2-n_2^2)^2}{(n_1^2+n_2^2)^{3/2}} \tag{3.13}$$

Another form to express Hamaker constant emphasizes the energy contributions [99]

$$A_{121} = A_{\nu=0} + A_{\nu>0}. \tag{3.14}$$

In this expression, the first term indicates the zero-frequency term, which describes purely entropic energy contributions. These cannot exceed approximately $(3/4)k_BT$ (or 3×10^{-21} J mol^{-1}) at room temperature [99]. The second term, $A_{\nu>0}$, describes attractive dispersion energy contributions arising from London dispersion forces. The Hamaker constant can be used below 5 nm, but a form dependent on h must be used in cases where distances exceed 5 nm [99]. Van der Waals interactions are proportional to the Hamaker constant regardless of the geometry, so the sign and magnitude of the Hamaker constant has a large influence on electrostatic interactions. Van der Waals interactions are always attractive unless the Hamaker constant is negative [80, 99, 108]. For similar particles, the Hamaker constant is always positive (such that van der Waals interactions are always attractive), while for dissimilar particles the Hamaker constant can be positive or negative, depending on the values of the terms in Equation 3.13 [80, 99, 108].

Rigid (Stern) and Diffuse Layers Colloids exist in suspension with a double layer charge configuration that includes the rigid (Stern) layer and the diffuse layer [96, 99]. The rigid layer is tightly bound to the surface of the particle and contains permanently adsorbed ions. These tightly packed counter ions heavily screen the potential on the particle surface and move with the particle during Brownian motion. In the diffuse layer, the counter ion concentration decays exponentially, obeying the Debye-Huckel model [99],

$$\Psi(x) = \Psi_0 \exp(-\kappa x), \tag{3.15}$$

where Ψ_0 is the surface potential, κ the inverse Debye length, and x indicates the

distance from the surface of the particle. The diffuse layer does not move with the particle as it undergoes Brownian motion [99].

Debye Screening Length and Zeta Potential The Debye screening length, the inverse of which is described in Equation 3.16 below, defines the distance away from the particle surface at which the potential has decreased to Ψ_0/e. It depends solely on the properties of the liquid suspending medium and often defines the diffuse layer thickness [1, 99, 138].

$$\kappa = \sqrt{\frac{e^2 \Sigma_i C_i Z_i^2}{D \varepsilon_0 \kappa T}} \tag{3.16}$$

In the equation above, Z_i indicates the ion valence, C_i the concentration of the particles, e the electric charge, and ε the dielectric constant. For a suspension which contains electrolyte cations and anions at a 1:1 ratio (e.g. NaCl), the Debye length can be calculated as [99]

$$\kappa^{-1} = \frac{0.304}{[\mathrm{C}]_{salt}^{1/2}}, \tag{3.17}$$

where the salt concentration is used in moles. Regardless of the salt, the Debye length is inversely proportional to the concentration, such that the less salt present, the greater the distance it takes for the electric potential to decrease to Ψ_0/e [99].

The Zeta potential ζ is a measure of the electric potential on the particle surface [99, 108]. An actual measurement at the surface of the particle is not possible, but is possible at the *slip plane*, which occurs at the outer edge of the diffuse layer [99]. The Zeta potential can inform whether particle surfaces are attracted to or repulsed by one another. Large magnitudes of the Zeta potential, e.g. $|\zeta| > 25$ mV, indicate stable particles with repulsive interactions; lower magnitudes indicate unstable suspensions [96, 99].

Particle surfaces can be charged by ionization or dissociation of surface groups, or adsorption of ions from the suspending medium onto the surface [80, 99, 108]. In suspensions

with a low pH, excess protons are available to protonate surface groups, which leads to a positive Zeta potential. In high pH, excess hydroxide ions deprotonate surface groups, and lead to a negative Zeta potential. When $\zeta = 0$, called the *isoelectric point* (which is not necessarily pH 7, but depends on the colloid/suspension system), there is no net charge, and no electrophoretic mobility [96, 99].

DLVO Theory For spherical colloids of radius, R, in a suspending medium of dielectric constant ε, the electrostatic interactions can be expressed by [96, 99]:

$$V_{elect} = 2\pi\varepsilon R\Psi_0^2 \ln\left(1 + \exp\left(-\kappa x\right)\right), \tag{3.18}$$

which is valid when $\kappa R > 10$. The central theory to describe colloid interactions in water, known as DLVO (Derjaguin-Landau-Verwey-Overbeek) theory, combines van der Waals attractive forces with the electric potential forces expressed in equation 3.18 [96, 99]. The combination of these forces gives rise to a total potential.

$$V_{total} = V_{vDW} + V_{elect} \tag{3.19}$$

Combining the expression for the van der Waals potential (Equation 3.12) and the electrostatic interactions (Equation 3.18), the total potential can be written as [99]

$$V_{total} = -\frac{AR}{12h} + 2\pi\varepsilon R\Psi_0^2 \ln\left(1 + \exp\left(-\kappa x\right)\right). \tag{3.20}$$

Figure 3.9 demonstrates the relationship between the van der Waal's interaction at the electrostatic interaction in defining an interaction energy. Attractive forces that cause aggregation and settling must overcome a repulsive barrier [99]. In general, the repulsive barrier decreases as the Hamaker constant, A, increases, and it increases as the surface

potential, Ψ_0, increases [99]. Additionally, the repulsive barrier can be decreased by adding salt or changing pH. A critical coagulation concentration, or *ccc*, indicates the salt content required to induce flocculation of the colloids, eventually resulting in settling [96, 99].

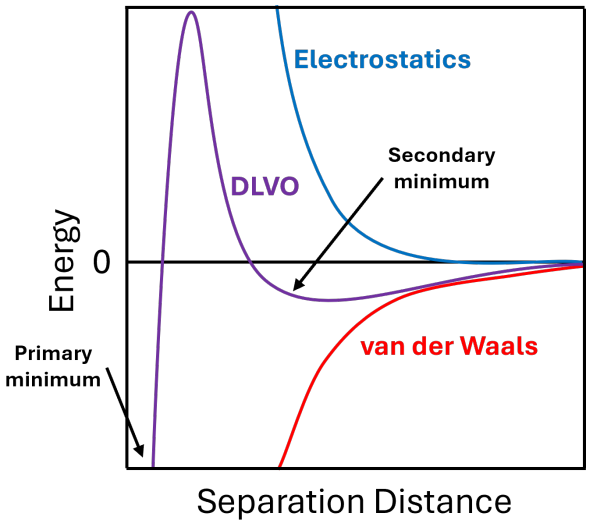


Figure 3.9: The plot above demonstrates the relationship between electrostatic repulsion and van der Waals attraction, and shows how DLVO theory combines them to explain colloidal stability. The primary minimum describes colloids which are completely repulsive. The maximum shows the barrier which must be overcome for attractive interactions to dominate. The secondary minimum defines a stable state where the system has a balance between repulsive and attractive forces interactions.

Stable and Unstable Colloidal Suspensions A kinetically stable colloidal suspension occurs at the primary minimum shown in Figure 3.9. The stability ratio demonstrates the relationship between the parameters that stabilize a colloidal system [99]

$$W = \frac{k_0}{k} = \exp\left(\frac{\frac{V_{max}}{k_B T}}{2kR}\right). \tag{3.21}$$

Here, k_0 represents the ideal rate constant for aggregation under ideal conditions, and k describes the real rate constant dictated by the repulsive barrier, V_{max}.

Unstable colloidal suspensions occur when the repulsive barrier has been surpassed. Initially, doublets of particles begin to form, then clusters. After cluster formation, the suspension can either continue aggregation and settling, or form a sample spanning cluster, a gel, depending on colloid density and charges [80, 96, 99, 108].

Reversible flocculation can occur when the repulsive barrier is small and there is active association/disassociation; often the suspension can redisperse through agitation like shaking or stirring [96, 99]. Irreversible flocculation occurs when the repulsive barrier is high, often making redispersion impossible [99].

Spatially Resolved Rheometry As mentioned previously, the *viscometric assumption* underlies the interpretation of stress-strain measurements made with traditional rheometers. Due to this assumption, rheometer data often does not capture the true complexity of behavior of non-Newtonian materials. Other rheometric methods provide a useful complement to traditional rheometer measurements [34, 88]. Generally, these methods provide information about the micro- or mesostructure of fluids related to spatial variations in velocity to inform how they flow.

Spatially resolved methods often utilize optical techniques to determine structural information of fluids [34]. Examples of such techniques include SANS (small-angle neutron scattering) and SAXS (small-angle x-ray scattering), DLS (dynamic light scattering), laser doppler velocimetry, particle image velocimetry (PIV), optical coherence tomography (OCT), Raman/Brillouin scattering, optical tweezer rheometry, and flow birefringence [88, 96]. An in-depth description of these methods is outside the scope of this document, but a few generalizations can be made. In general, these methods provide either a velocity flow profile or information, e.g. scattering wave-vectors, from which the fluid structure, and potentially the relationship between the velocity distribution and the material structure can be determined. Many of these methods can obtain precise information about the flow but

are restricted to probing only a small range of time/length scales [88]. In addition, many techniques also require transparent samples or specific sample geometries that limit the variety of samples which can be measured [34].

Rheo-NMR, discussed in Chapter 2, provides a method with the potential to precisely probe wide ranges of molecular motions (ranging from femtoseconds to minutes) and structures (nm to mm) and can correlate these motions with velocity profiles [34, 35]. Two Rheo-NMR techniques are used in this research: velocimetry and relaxometry. Rheo-NMR velocimetry provides spatially resolved velocity profiles at a resolution on the order of tens of microns [34, 37]. Rheo-NMR relaxometry offers information about fluid structure and molecular scale dynamics over time [37, 175]. This research utilizes the power of NMR to provide data which complements that from a traditional rheometer for complex fluids of interest.

Nanocrystalline Cellulose (NCC)

Cellulose, a biological polymer formed by glucose monomers, composes plant cell walls [17]. It has been heralded as the most abundant renewable compound. A relatively new process involves bundling cellulose chains and separating them into nanoparticles or nanofibers, collectively termed nanocrystalline cellulose (NCC) [159]. NCC has been regarded as "futuristic" owing to its chemical and physical properties. Such properties include impressive stiffness and strength, chemical inertness, tunable mechanics, and modifiable surface chemistry, among others [159]. These advantages enable a wide variety of industrial applications, from capacitors and food products to fibers and cement, and a growing research interest to inform such pursuits [73, 74, 117, 144, 146, 159]. Current challenges stem from the inability to accurately predict NCC macroscale properties from modifications of traditional physical polymer models such as Doi-Edwards (D-E) theory for rod-like molecules, and to reliably verify models experimentally as many techniques lack

mesoscale resolution [55].

Doi-Edwards and Leslie-Ericksen Theories for Modeling NCC's NCC suspensions exhibit complex behavior which according to D-E theory can be classified into three regimes based on concentration (volume fraction, ϕ): dilute, semi-dilute, and concentrated [55]. A rigid rod in a dilute system which moves only due to Brownian motion can be described with two motional modes: rotation and translation. Lagrange equations of motion can be combined with the Smoluchowski equation to account for randomness in translation as well as orientation [147]. In shear flows, this random translation is replaced by a shear-imposed velocity. As the suspension reaches higher concentrations and moves into a semi-dilute regime, hydrodynamic interactions become important and excluded volume principles apply [96]. The dynamics of motion, however, are not entirely different from the dilute case.

Once within the concentrated nematic regime, the excluded volume principles begin to greatly influence behavior, and nanorods undergo spontaneous bulk orientational rearrangements to limit repulsion [133]. These nanorod suspensions can be labeled as "liquid crystal", as they show anisotropic, parallel ordering of rods, where rods may be randomly distributed through the solution as liquid rod-like molecules are but show orientational ordering like solid crystals. Under shear, different regions of ordering can occur, and small perturbations to the system may cause a dramatic re-orientation effect [133]. This results in microstructural changes with severe consequences to macroscale stress-strain, velocity profile, and fluctuation behavior.

Many models since Doi and Edwards' original treatment [55] have sought to introduce details which better describe rod-like polymer suspensions. These include a large amount of work dedicated specifically to worm-like micelles (WLM) and similar complex materials, many of which are relevant to NCC solutions [57, 68, 79, 97, 122, 156, 171]. Modifications to these models involve introducing deviations from the ideal rod that have been motivated

by experimental observations. Examples of these deviations include a dependence on aspect ratio, ellipsoid shapes, and semi-flexible (not ideally rigid) rods which can bend [97, 115, 162]. Other models have sought to account for the implicit monodomain assumption of the D-E theory, where all rods are aligned with the same orientation across a sample. It is known from optical birefringence and dynamic light scattering experiments that there are regions of discrete orientation [122, 133], sometimes called "polydomains" in liquid crystal nomenclature. Models derived from continuum mechanics such those related to Leslie Ericksen (L-E) theory seek to describe the mesostructural changes associated with re-orientation (sometimes called "texture effects") by modeling microscopic orientation changes. Yet, a particular issue arises with this family of theories. They were originally designed to model low molecular weight species, and often fail in the case of liquid crystalline polymers, where D-E theory relatives are better suited [133].

Use of NMR to Understand NCC Mesostructure As mentioned in previous sections (see Section 3 from this chapter and Section 2 from Chapter 2), NMR offers a powerful yet noninvasive way to probe the dynamics and mesoscale structure of materials. This conveniently complements other rheometric techniques. It can also provide necessary data to inform mathematical models like those described above.

In the case of NCC, the use of velocimetry and diffusometry enables the alteration of time scales when determining velocity and diffusive behavior. This change in time scales allows for a determination of the length scale of dynamics such as velocity fluctuations induced by rod orientation dynamics [133], which is explored in Chapter 4. Additionally, NMR relaxometry performed during hydration of high concentration NCC samples provides information about structural changes which occur in an NCC porous media system. The differences observed with changes in ionic concentrations offers insight into the impact of electrostatic interactions on the diffusion of water in NCC porous media systems.

Laponite®

Nanoclay suspensions have broad potential in applications as varied as medicine, agriculture, and oil and gas production [50, 51, 106, 134, 151], but they can be difficult to process and handle. Laponite® ($Na_{0.7}Si_8Mg_{5.5}Li_{0.3}O_{20}(OH)_4$) is a synthetic, layered, smectite nanoclay which is of particular technological interest. Laponite® serves as a model natural clay in research [124]. It also finds uses in cosmetics [31, 166], pharmaceuticals [31, 91, 151], food packaging [9, 38, 101, 143], paints and coatings [31, 161], and nanocomposites [31, 89]. However, Laponite® forms unstable nanoscale structures and exhibits "peculiar properties" [47] which makes it the subject of both scientific debate and industrial processing interest.

Unstable nanoscale structures commonly undergo attractive or repulsive energetic restructuring over time which may be induced by perturbations from temperature or shear changes. This restructuring gives rise to observed behaviors, like aging and thixotropy, in many nanoclays including Laponite®. The connection between microstructure and rheological behavior is still an open area of research for many nanoparticulate materials of which nanoclays are no exception. Shear forces during processing of nanoparticulate materials interact with the microstructure and generate complex fluid behavior, which must be understood to control the microstructure for various applications.

As the industrial relevance and application of Laponite® continues to grow, there is an increasing need to settle the contentious debate about the microstructural arrangement of aqueous Laponite® dispersions. Numerous studies [4, 5, 7, 26, 27, 86, 95, 126, 127, 130, 131, 157, 169] have been performed and commentaries published [26, 87] to elucidate the relationship between Laponite® flow and microstructure, but a widespread consensus still does not exist. The debate revolves around the existence of a repulsive, double-layer Wigner glass state at concentrations above 4% w/v as opposed to an attractive gel network, or "house-of-cards" structure [87]. Figure 3.10 depicts these two structural states.

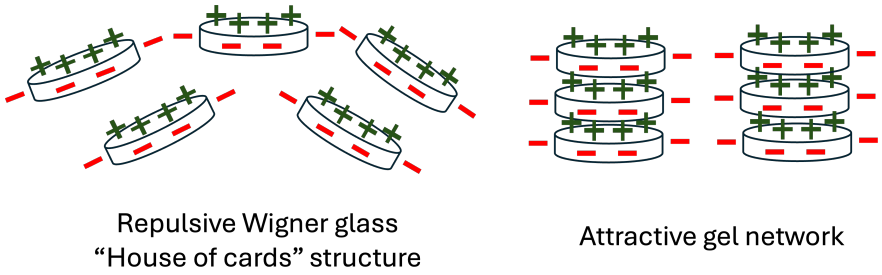


Figure 3.10: Schematics describing the two primary structures theorized for Laponite® at 4% w/v. Left: the repulsive Wigner glass or “house of cards” structure. Right: the attractive gel network structure.

While the NMR experiments presented in this work do not intend to settle the structure debate, they provide useful information about the aging behavior and velocity fluctuations and wall slip exhibited by Laponite® clays under shear. This information, when coupled with other experimental methods, can elucidate important details about the behavior of Laponite® at concentrations above 4% w/v. This would inform processing conditions for industrial applications or further research pursuits into nanocolloidal fluids.

RHEO-NMR VELOCIMETRY OF NANOCRYSTALLINE CELLULOSE SUSPENSIONS

Contribution of Authors and Co-Authors

Manuscript in Chapter 4

Author: Maribelle A. Stanley

Contributions: Designed and performed experiments and formal analysis, wrote the initial manuscript, conceived concept, curated data, and reviewed/edited the manuscript.

Co-author: Jayesha S. Jayaratne

Contributions: Involved with data curation/analysis.

Co-author: Sarah L. Codd

Contributions: Performed data curation/analysis, supervised work, reviewed/edited the manuscript.

Co-author: Dilpreet S. Bajwa

Contributions: Provided samples and reviewed/edited manuscript.

Co-author: James N. Wilking

Contributions: Provided funding, data analysis assistance and reviewed/edited manuscript.

Co-author: Joseph D. Seymour

Contributions: Wrote initial manuscript, conceived concept, designed experiments, curated data, performed analysis, supervised work, reviewed/edited manuscript.

Manuscript Information

Maribelle A. Stanley, Jayesha S. Jayaratne, Sarah L. Codd, Dilpreet S. Bajwa, James N. Wilking, Joseph D. Seymour

Applied Rheology

Status of Manuscript:
____ Prepared for submission to a peer-reviewed journal
____ Officially submitted to a peer-reviewed journal
____ Accepted by a peer-reviewed journal
_X_ Published in a peer-reviewed journal

De Gruyter
Vol. 34 Issue 1
10.1515/arh-2024-0026

DE GRUYTER Applied Rheology 2024; 34: 20240026

Research Article

Maribelle A. Stanley, Jayesha S. Jayaratne, Sarah L. Codd, Dilpreet S. Bajwa, James N. Wilking, and Joseph D. Seymour*

Rheo-NMR velocimetry of nanocrystalline cellulose suspensions

https://doi.org/10.1515/arh-2024-0026
received September 23, 2024; accepted December 10, 2024

Abstract: The velocity data presented demonstrate the complicated flow behavior of nanocrystalline cellulose (NCC) suspensions even when standard rheometry shows only subtle effects. Rheo-nuclear magnetic resonance (NMR) velocimetry with spatial and temporal resolution indicates that NCC suspensions undergo varying flow behavior, which correlates with bulk rheology and includes wall-slip, shear banding, and yielding. Large-velocity fluctuations in a chiral nematic liquid crystal-phase suspension (5% w/v) indicate particle director orientation tumbling and flow. The results provide details of the mesoscale velocity distributions in space and time, which can be used to inform the interpretation of rheology data, as well as processing flow conditions to control NCC suspension microstructure and impact properties of composite and other materials.

Keywords: nanocrystalline cellulose, complex fluids, colloidal suspensions, shear-banding, velocity fluctuations

Abbreviations

NCC	nanocrystalline cellulose
NMR	nuclear magnetic resonance
PGSE	pulsed gradient spin echo

*** Corresponding author: Joseph D. Seymour**, Chemical and Biological Engineering Department, Montana State University, Bozeman, MT, United States of America, e-mail: jseymour@montana.edu
Maribelle A. Stanley, Jayesha S. Jayaratne: Chemical and Biological Engineering Department, Montana State University, Bozeman, MT, United States of America
Sarah L. Codd, Dilpreet S. Bajwa: Mechanical and Industrial Engineering Department, Montana State University, Bozeman, MT, United States of America
James N. Wilking: Chemical and Biological Engineering Department, Montana State University, Bozeman, MT, United States of America; Department of Physiology and Biomedical Engineering, Mayo Clinic, Rochester, MN, United States of America

1 Introduction

Cellulose is the main component of plant cell walls [1]. It is a biological polymer of glucose monomers [2] that has been heralded as the most abundant renewable compound [3]. Numerous processes seek to utilize it as a replacement for traditional feedstocks [4–6]. A relatively new process for this purpose involves bundling cellulose chains and separating them into nanoparticles or nanofibers called *nanocrystalline cellulose (NCC)* [7]. Materials formed with NCC have been regarded as "futuristic" owing to NCC's impressive chemical and physical properties. Such properties include stiffness and strength, chemical inertness, tunable mechanics, optical birefringence, and modifiable surface chemistry, among others [7]. These advantages enable a wide variety of applications, from capacitors and food products to fibers, cement, and biomedical tissues [7–12], and a growing research interest to inform such pursuits.

To fully maximize the industrial relevance of NCCs, their flow mechanics must be understood to optimize processing conditions. NCCs form colloidal aqueous suspensions that exhibit a wide range of complex rheological behaviors [13]. This behavior depends on particle concentration, salt concentration, sonication energy, and applied shear stress [14,15]. Concentration dependence prompts changes from shear-thinning viscoelastic to liquid crystal three-region and shear-thinning polymeric gel behavior [14–16]. This broad material response in concentration-dependent behavior results from differences in phase microstructure. NCC particles are rod-like of aspect ratio $\frac{L}{d} \sim 10$ with sulfate half-ester groups that generate electrostatic repulsion [17]. The interaction free energy is a combination of geometric excluded volume and electrostatic effects [17,18]. The electrostatic repulsion generates an equilibrium-phase isotropic-nematic system at a lower critical concentration than pure geometric kinetic arrest [17,18]. As the particle concentration increases above the critical concentration, the system enters a liquid crystal chiral nematic phase and then typically isotropic gel phase, which can, however, maintain the nematic structure [17].

Open Access. © 2024 the author(s), published by De Gruyter. This work is licensed under the Creative Commons Attribution 4.0 International License.

Sonication disperses aggregates, while shearing can disperse, break apart, and re-assemble aggregates [19,20]. Such varied behavior is a current limit to the use of NCC's capabilities on an industrial scale.

Like many complex fluids, bulk rheological measurements provide a challenge because of microscale heterogeneity unresolvable with traditional torque-based rheological measurements. Previous studies have sought to overcome these challenges in NCCs by complementing bulk rheological measurements with optical and spectroscopic techniques [13,21]. Nuclear magnetic resonance (NMR) velocimetry is particularly suited to this challenge because of its ability to resolve heterogeneous flow behavior down to the micron scale, and pinpoint flow dynamics occurring at multiple length and time scales [22–30]. Rheo-NMR velocimetry couples the ability to shear fluids at controlled shear rates with direct observations of the spatial velocity occurring in real time [22,23,28–30]. To date, Rheo-NMR studies have focused on hydroxypropyl cellulose, a separate and somewhat less versatile cellulose liquid crystal derivative, with mainly deuterated spectral studies as opposed to NMR velocity imaging [21,31,32]. The authors are not aware of any Rheo-NMR velocimetry studies that focus specifically on NCC suspensions as pointed out in the review from Kadar and coworkers [13].

In this work, Rheo-NMR velocimetry was used to obtain transient and steady-state 1D velocity profiles of NCC suspensions in the fluid gap of a home-built, NMR-compatible concentric cylinder shear cell [29]. From these velocity distributions, the flow evolution is observed at several shear rates for a range of concentrations. Traditional bulk rheology measurement with strain-controlled measurements for the same samples complements the results. The data demonstrate four distinct regimes of flow behavior as a function of particle concentration that offer a more detailed picture of the material response to shear of NCC suspensions.

2 Materials and methods

2.1 Sample preparation

The NCC systems investigated in this work are a series of aqueous suspensions ranging from 3 to 12% w/v. Cellulose nanocrystals in the form of nanorods with dimensions 10–15 nm in width and 80–100 nm in length were obtained from the U.S. Department of Agriculture, Forest Products Laboratory (Madison, WI) [33]. The samples were prepared by weighing the cellulose nanocrystals as a freeze-dried powder and then adding the appropriate amount of reverse osmosis/deionized water with stirring. The resulting suspensions were homogenized by applying ultrasound energy from a 2510 Branson sonication ice water bath (130 W power output, 40 kHz frequency, 2.81 L bath volume); ice water (~12°C) was used in the bath to prevent the degradation of the NCC particles due to sensitive surface charges, which may cause de-esterification of sulfate groups [14,34,35]. Samples were sonicated and periodically vortexed until visually homogeneous, such that the total sonication energy for each sample was ~300 J/g of NCC, where <1,000 J/g is found to be sufficient to break aggregates and disperse the nanorods [14]. All suspensions were stored in a refrigerator (3°C) before and after measurements.

2.2 Rheometry

Linear rheological measurements were performed with an AR-G2 rheometer (TA Instruments) equipped with either a 60 mm diameter and 2° angle cone-and-plate geometry for 3% w/v suspensions or a 20 mm diameter parallel plate for 5, 7, and 12% w/v suspensions. All experiments were run at 25°C with a controlled strain rate. The viscosity and shear stress measurements (Figure 1) are in agreement with reported data for NCC suspensions with no salt and sonication levels of 300 J/g, relative to non-sonicated and 1,000 J/g sonicated samples [14].

2.3 Rheo-NMR velocimetry

Velocimetry experiments were performed with a portable, home-built Rheo-NMR experimental system and methodology with well-established fluid flow measurement capabilities across a variety of length and time scales [22,36–38]. The system includes an NMR-compatible, motor-powered driveshaft, which rotates the inner rotor of a Couette shear cell, depicted in Figure 2. The shear cell has a 9 mm outer radius glass cylinder stator and 8 mm inner radius PEEK rotor. The dimensions approach a narrow gap system with fluid gap width ($d = R_o - R_i$) of 1 mm, a radius ratio $\left(\kappa = \frac{R_i}{R_o}\right)$ of 0.89, and a q value $\left(q = \frac{d}{R_i}\right)$ of 0.143, so stress inhomogeneity is small but nonzero. Thus, as the shear rate inhomogeneity is also small but nonzero, the shear rate, $\dot{\gamma}$, refers to an effective shear rate. Samples were loaded into the shear cell and the 7 and 12% w/v samples were put under

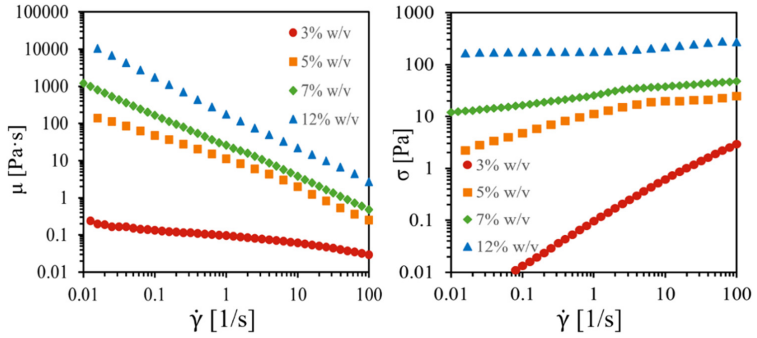


Figure 1: Left: viscosity vs. applied shear rate from bulk rheometry experiments on NCC suspensions, for a 3% w/v sample, which demonstrates slightly nonlinear shear-thinning behavior; a 5% w/v sample, which demonstrates a higher viscosity at low shear rates, and slight deviation from a linear decrease as shear rate is increased; a 7% w/v sample, which shows a much higher viscosity at low shear rates and a linear decrease; and a 12% w/v sample, which also shows a much higher viscosity and a linear decrease. Right: shear stress vs. applied shear rate from bulk rheometry experiments on NCC suspensions, for a 3% w/v sample demonstrating mostly Newtonian behavior and slight shear thinning; a 5% w/v sample, which exhibits the stress plateau that characterizes shear banding fluids, extending from γ = 6.3 to 40/s; a 7% w/v sample, which shows a slight stress plateau and shear thinning; and a 12% w/v sample, showing slight shear thinning. The data were measured at 25°C with a 60 mm, 2° cone-and-plate for 3% w/v suspensions, and a 20 mm parallel plate geometry for 5, 7, and 12% w/v suspensions.

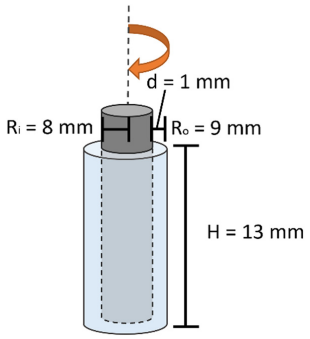


Figure 2: Schematic that depicts the Rheo-NMR sample Couette cell dimensions.

vacuum for 30 min to eliminate air bubbles. All samples were pre-sheared to remove air bubbles and provide a uniform microstructure initialization prior to measurements, using an applied shear rate of $\dot{\gamma}$ = 4.6/s for 30 min to 1 h. The samples were allowed 3 h to relax before measurements were taken. Shear rates of $\dot{\gamma}$ = 0.9, 2.8, and 4.6/s were applied with a calibration fluid silicone oil (10,000 cSt) used to measure the actual velocity at the rotor to experimentally determine $\dot{\gamma}$ for each motor set point.

NMR measurements were taken with a Bruker AVANCE 300 MHz spectrometer and 7 T superconducting super wide bore magnet equipped with a 25 mm ^{1}H birdcage resonator coil and a Micro-2.5 gradient system (providing a maximum gradient of 1.5 T/m at 60 A). Bruker TopSpin 3.5pl7 software was used to acquire data with the spectrometer, while MATLAB (MathWorks, Inc., Natick, MA) and Prospa software (Magritek, Wellington, NZ) were used to analyze the data. A pulsed gradient spin echo (PGSE) pulse sequence (Figure 3) was used to acquire 1D velocity profiles of the liquid phase from the protons of the fluid molecules. The PGSE pulse sequence encodes for magnetization phase, ϕ, where $\phi = \gamma v \int g(t')t'dt' = \gamma g \delta \Delta \cdot v$. Here, γ refers to the magnetogyric ratio (a material property), g refers to the gradient amplitude, δ refers to the gradient pulse duration, and Δ refers to the displacement observation time. The PGSE pulse sequence was employed with double slice selection [23,29]. The slices used were a 1 mm thick slice in the flow direction (y) to eliminate curvature and provide $v_\theta(r)$ azimuthal radius-dependent velocity directly over a 10 mm slice in the vertical direction (z) to provide and average more ^{1}H spins over the vorticity direction of the flow and increase signal to noise for two average 8 s acquisitions. Two gradient steps of equal duration (δ = 1 ms) and magnitude but opposite sign were used as flow-encoding gradients with amplitude ranging from 0.178 to 0.889 T/m dependent on shear rate-induced velocity, which were separated by a displacement observation time of Δ = 11 ms. The lateral direction (x) "read" gradients imaged the velocity with a 30 mm field of view using 512 points (58.6 μm resolution) across the diameter of the flow cell providing directly the velocity as a function of gap distance $v(x)$.

Steady-state experiments used 16 scans (repetitions) of gradient flow-encoding steps over a total acquisition time of 1 min and 12 s, with the velocity measured representing

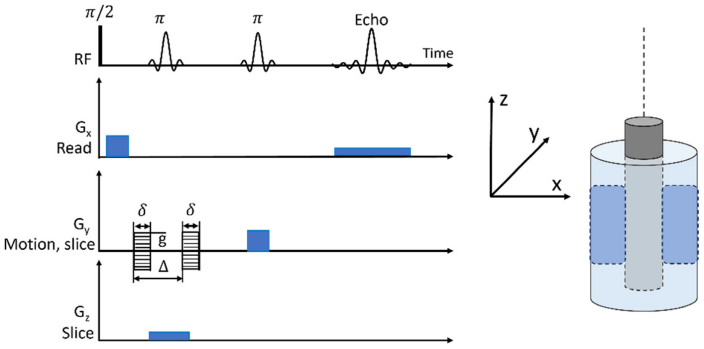


Figure 3: The PGSE pulse sequence with double slice selection used to acquire 1D velocity profiles and an adjacent depiction of the imaged region of the Couette flow cell. Data were acquired from a 10 mm slice in the vorticity direction (*z*-axis) and a 1 mm thick slice along the velocity direction (*y*-axis) as shown in the shaded section of the Couette schematic. The 1D profile was acquired across the fluid gap in the read gradient direction (*x*-axis) with a spatial resolution of 58.6 μm/pixel.

an average velocity over this time. Unsteady-state (start-up) experiments used 2 scans for a faster acquisition and acquired 75 independent velocity profiles averaged over 8.11 s for a total duration of approximately 10 min and 12 s. This transient measurement minimizes the velocity averaging time but lowers the acquired voltage signal-to-noise ratio. Velocimetry experiments were performed with shear and without shear for each shear rate to provide a no-flow control. This control allows for the removal of phase shifts from background magnetization during data analysis. All results shown represent the difference in the phase between flow and no-flow velocity profiles. The velocity-induced phase shifts map $\pm V_{max}$ to $\pm\pi$ in phase. Velocities larger than the velocity maximum with phase $\phi_{max} = \pi + \delta$ result in a phase wrap to $-\pi + \delta$, and standard-phase unwrapping methods are used [39]. This ensures that imperfections from magnetic gradient fields do not affect the result.

3 Results and discussion

3.1 Rheometry

The viscosity and shear stress behavior of the NCC suspensions shown in Figure 1 is in agreement with published data [14,15]. The 3% w/v sample exhibits isotropic fluid behavior with a near-constant viscosity at low shear rate, $\dot{\gamma}$, and linear increase in shear stress. At 5% w/v, the classic 3-region behavior of nematic chiral liquid crystals [40,41] is evident with shear thinning at low $\dot{\gamma}$ up to ~1/s, followed by a slight plateau from 1 to 10/s and stronger shear thinning at high $\dot{\gamma}$ greater than 10/s [14,15]. The shear stress exhibits a plateau and slight decrease in the region from 1 to 10/s, which is consistent with shear banding and flow instability phenomenon [40,41]. When the concentration reaches 7% w/v, a near-constant shear-thinning behavior of viscosity, which is consistent with a gel-like phase, is initiated, while the shear stress shows a slight plateau in the 1–10/s region. By 12% w/v, the viscosity exhibits a constant shear-thinning behavior over the entire $\dot{\gamma}$ range with near-constant shear stress.

3.2 Rheo-NMR velocimetry

The Rheo-NMR velocimetry results provide insight into the spatial and time dependence of the shear-induced motion. The lowest concentration (3% w/v) exhibits nearly Newtonian behavior in both start-up and steady-state experiments, depicted by a near-linear flow profile with no slip at the stator and less than 3% at the rotor (Figure 4a and b, Table 1). The linear velocity distribution reflects the near-isotropic fluid behavior exhibited in the rheology at the $\dot{\gamma}$ = 0.9, 2.8, and 4.6 s^{-1} examined. The viscosity data indicate a slight shear-thinning behavior; however, for the narrow gap flow cell geometry, the deviation from linearity of the velocity distribution is small even for Ostwald de Waele power law indices of $0.5 < n < 1.0$ [38]. In Figure 4c, the time-dependent velocities at the stator, gap center, and rotor are shown. The fluctuations in velocity are consistent with the noise of the stepper motor, as indicated by the Newtonian calibration silicone oil. Mean, $\mu = \langle v \rangle$, and standard deviation of velocity, $\sigma = \langle v'^2 \rangle^{1/2}$, are shown in Table 2 for all three gap positions and shear rates. The flow cell-

induced velocity fluctuations as measured by the standard deviation increase with $\dot{\gamma}$ and decrease from rotor to stator with decreasing velocity across the gap.

At 5% w/v for the chiral nematic phase, the steady-state velocity distributions (Figure 5a) remain linear, which is consistent with a shear-thinning fluid flow. The suspension begins to exhibit a significant slip at the stator and rotor, with the stator slip decreasing with increasing shear rate. The rotor slip as a percentage of the Newtonian no-slip velocity of silicone oil, defined as $\left(1 - \frac{v_{NCC}}{v_{SiOil}}\right) \cdot 100\%$, provides a measure of the slip by comparing the velocity of the NCC sample at the pixel closest to the rotor compared to that of the no-slip silicone oil, which indicates the actual

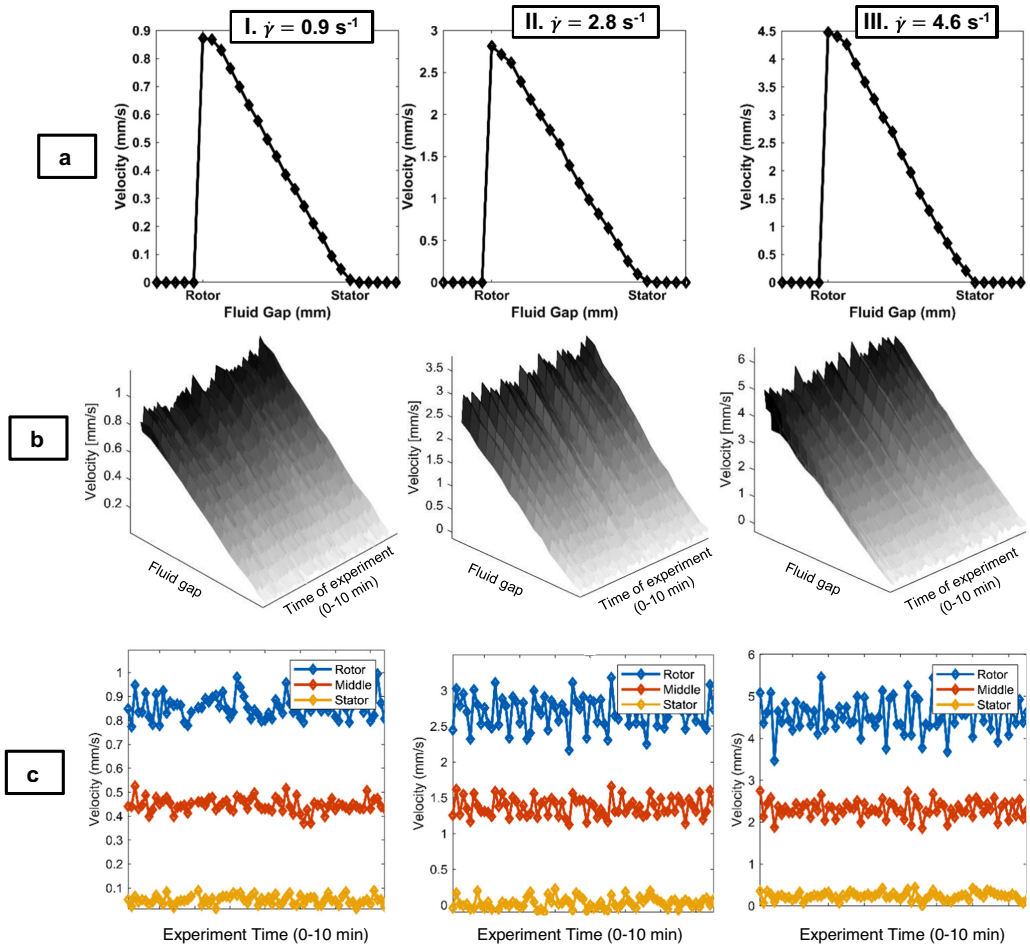


Figure 4: Rows a and b, columns I–III. 1D NMR velocimetry experiments for NCC2, 3% w/v suspension. Rows (a) steady-state, 1D velocity profiles, with 16 scans and total time of acquisition of 1 min and 12 s, and a pixel resolution of approximately 65 µm; (b) surface plots for 1D velocity profiles during an unsteady-state experiment with 75 experiments averaged over 2 scans and total time of acquisition of approximately 10 min and 12 s; (c) velocity profiles from the same unsteady-state experiment as (b), but displayed at three discrete positions across the 1 mm sample Couette cell fluid gap (rotor, middle, and stator) for all time points, which demonstrate the velocity changes across the experiment time and the fluid gap. Columns I: shear rate of $\dot{\gamma}$ = 0.9/s; II: shear rate of $\dot{\gamma}$ = 2.8/s; III: shear rate of $\dot{\gamma}$ = 4.6/s. The data present nearly Newtonian behavior for this concentration. Rotor and stator data points are approximately 58.6 µm from the physical walls.

Table 1: Rotor slip percentage and localized shear rates at rotor ($\dot{\gamma}_H$) and stator ($\dot{\gamma}_L$)

Shear rate [/s]	Variable	3% w/v	5% w/v	7% w/v	12% w/v
0.9	Rotor slip %	3.07	15.63	−1.10	4.17
	$\dot{\gamma}_H$			0.82	0.60
	$\dot{\gamma}_L$			0.11	(−0.07)
2.8	Rotor slip %	−0.44	−0.44	7.04	15.08
	$\dot{\gamma}_H$			4.01	5.32
	$\dot{\gamma}_L$			0.81	(−0.12)
4.6	Rotor slip %	2.69	15.89	2.12	16.40
	$\dot{\gamma}_H$			5.31	2.95
	$\dot{\gamma}_L$			1.63	0.26

rotor velocity. Rotor slip values for 5% w/v (Table 1) are large at $\dot{\gamma}$= 0.9 and 4.6/s, but not 2.8/s. The transient velocity distributions (Figure 5b) indicate significant spatial variations with shearing time for all $\dot{\gamma}$. In Figure 5c, the time-dependent velocity across the gap indicates significant fluctuations greater than for the Newtonian standard. The largest fluctuations in Figure 5b and c increase in frequency during the shearing time with increasing $\dot{\gamma}$. The standard deviations show a large increase in σ across the gap from stator to rotor, and we will return to a detailed discussion of this large fluctuation behavior in the context of liquid crystal flow instabilities below [39,42,43].

Increasing the NCC concentration to 7% w/v into the gel phase generates strong spatial dependence of the steady-state velocity distributions (Figure 6a). There is a significant stator slip decreasing with increasing $\dot{\gamma}$ and rotor slip decreasing from 10% of Newtonian fluid velocity at $\dot{\gamma}$ = 0.9/s to 2% of Newtonian, which is similar to the 3% w/v sample at $\dot{\gamma}$ = 4.6/s. The decrease in slip at the highest $\dot{\gamma}$ indicates the microstructural disruption of the gel phase by the higher shear rate. Coupled effects of apparent wall slip and shear localization in shear banding and yield stress materials is a well-established phenomenon, which occurs in particulate dispersions [44]. Apparent wall slip in particle dispersions occurs in a thin layer of the suspending fluid [45]. The data indicate that apparent slip occurs in a single pixel, meaning the slip-layer thickness is much less than the 58.6 μm pixel resolution. The steady-state velocity distributions indicate shear banding or shear localization [22–29]. Coussot and co-workers have defined shear localization as a progressive continuous decrease in $\dot{\gamma}$ across a gap in contrast to a shear rate discontinuity for shear banding [25]. The measured steady-state velocity distributions (Figure 6a) have a continuous variation of $\dot{\gamma}$ but can be characterized by a region of high shear rate, $\dot{\gamma}_H$, near the rotor and constant low shear rate, $\dot{\gamma}_L$, near the stator (Table 1). At applied shear rate $\dot{\gamma}$ = 0.9/s, the $\dot{\gamma}_H$ is lower than the applied shear due to the 10% wall slip and $\dot{\gamma}_L$ occupies the majority of the fluid gap. The behavior at $\dot{\gamma}$ = 2.8/s with smaller rotor slip demonstrates an increase in $\dot{\gamma}_H$ over the applied shear rate and a smaller gap $\dot{\gamma}_L$ region, indicating a greater disruption of the microstructure with the shear overcoming the particle negative surface charge repulsions. By applied $\dot{\gamma}$ = 4.6/s, $\dot{\gamma}_H$ is larger than the applied shear and occupies over half the gap (Table 3) and the low shear region is undergoing significant shear. The transient velocity distributions (Figure 6b and c) exhibit no large fluctuations in contrast to the 5% w/v sample despite a slight indication of a small plateau in the rheology data (Figure 1), and the standard deviation is similar to the Newtonian calibration fluid.

The 12% w/v gel exhibits yield stress behavior. The slip at the rotor (Figure 7a) is comparable to 5% w/v, and at the stator, it is largest of all samples for all $\dot{\gamma}$. The steady-state velocity distributions (Figure 7a) exhibit an increasing region of shearing into the gap with increasing $\dot{\gamma}$. Of note is the increasing velocity with increasing distance across the gap (Table 3) in the no-shear region at $\dot{\gamma}$ = 0.9 and 2.8/s (Figure 7a I and II), which indicates the solid body rotation [36,38]. At

Table 2: Mean (μ) and standard deviation (σ) of velocity at three gap positions for transient data

Shear rate [/s]	Position	3% w/v		5% w/v		7% w/v		12% w/v		10k cSt Si Oil	
		μ [mm/s]	σ [mm/s]	μ [mm/s]	σ [mm/s]	μ [mm/s]	σ [mm/s]	μ [mm/s]	σ [mm/s]	μ [mm/s]	σ [mm/s]
0.9	Rotor	0.86	0.05	0.80	0.22	0.88	0.05	0.86	0.05	0.88	0.04
	Middle	0.45	0.03	0.41	0.12	0.63	0.03	0.75	0.05	0.46	0.02
	Stator	0.05	0.02	0.16	0.05	0.58	0.05	0.77	0.05	0.04	0.01
2.8	Rotor	2.71	0.23	2.51	0.82	2.63	0.24	2.42	0.20	2.75	0.23
	Middle	1.37	0.13	1.23	0.31	1.23	0.10	0.95	0.09	1.44	0.12
	Stator	0.03	0.08	0.29	0.08	0.81	0.04	0.91	0.08	0.13	0.03
4.6	Rotor	4.55	0.40	4.17	1.34	4.06	0.25	3.91	0.26	4.62	0.32
	Middle	2.31	0.20	2.10	0.59	1.79	0.13	1.06	0.12	2.42	0.17
	Stator	0.23	0.09	0.35	0.12	0.92	0.06	0.93	0.10	0.20	0.07

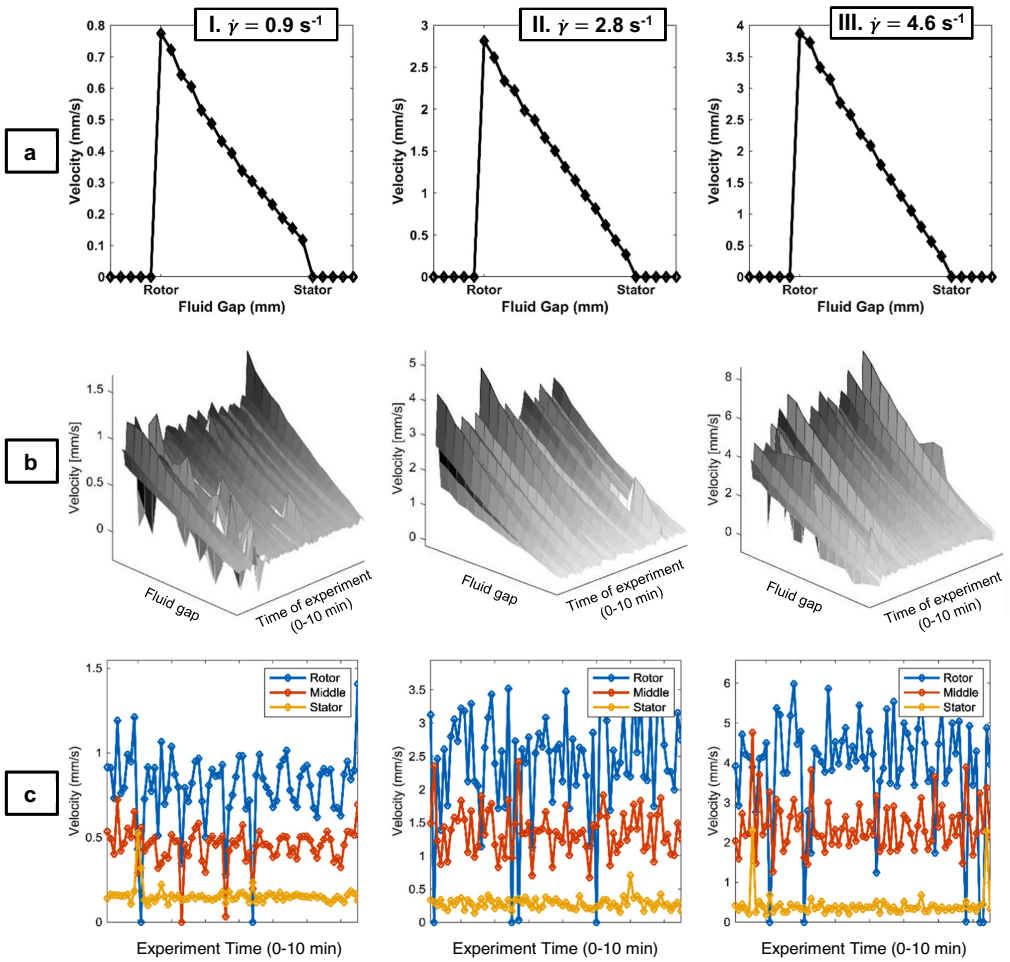


Figure 5: Rows a and b, columns I–III. 1D NMR velocimetry experiments for NCC3, 5% w/v suspension, a liquid crystal. Rows (a) steady-state, 1D velocity profiles, with 16 scans and total time of acquisition of 1 min, 12 s, and a pixel resolution of approximately 65 μm; (b) surface plots for 1D velocity profiles during an unsteady-state experiment with 75 experiments averaged over 2 scans and total time of acquisition of approximately 10 min and 12 s, which demonstrate velocity fluctuations; (c) velocity profiles from the same unsteady-state experiment as (b), but displayed at three discrete positions across the 1 mm sample Couette cell fluid gap (rotor, middle, and stator) for all time points, which demonstrate the velocity changes across the experiment time and the fluid gap; significant velocity fluctuations exist for this concentration. Columns I: shear rate of $\dot{\gamma}$ = 0.9/s; II: shear rate of $\dot{\gamma}$ = 2.8/s; III: shear rate of $\dot{\gamma}$ = 4.6/s. Rotor and stator data points are approximately 58.6 μm from the physical walls.

$\dot{\gamma}$ = 4.6/s (Figure 7a III), the shear rate in the near solid-like region is positive with $\dot{\gamma}_L$ = 0.26/s, indicating a disruption of the solid microstructure, which is present in the $\dot{\gamma}$ = 0.9 and 2.8/s applied shear rates as evidenced by the $\dot{\gamma}$ sign changes, where in Table 1 we define $\dot{\gamma}$ relative to the gap so that decreasing velocity across the gap is listed as positive $\dot{\gamma}$ and increasing velocity as negative $\dot{\gamma}$. The transient data for $\dot{\gamma}$ = 0.9 and 2.8/s (Figure 7b I and II and 7c I and II) show a longer timescale transient not present at lower concentrations or at $\dot{\gamma}$ = 4.6/s. This manifests as the clear progression of the velocity spatial distributions, for $\dot{\gamma}$ = 0.9/s (Figure 7b I) to larger slip at both rotor and stator and in the time-dependent data

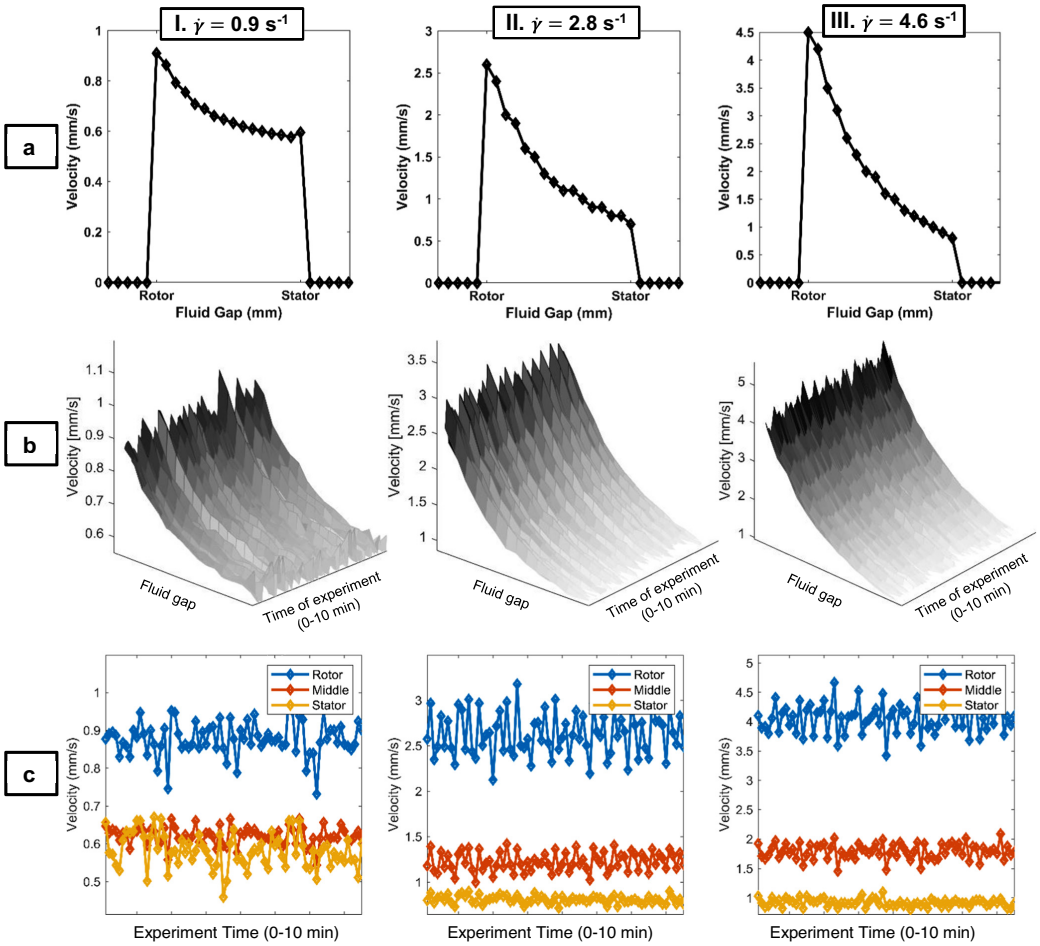


Figure 6: Rows a and b, Columns I–III. 1D NMR velocimetry experiments for NCC1, 7% w/v suspension, a gel. Rows (a) steady-state, 1D velocity profiles, with 16 scans and total time of acquisition of 1 min, 12 s, and a pixel resolution of approximately 65 μm; (b) surface plots for 1D velocity profiles during an unsteady-state experiment with 75 experiments averaged over 2 scans and total time of acquisition of approximately 10 min and 12 s; (c) velocity profiles from the same unsteady-state experiment as (b), but displayed at three discrete positions across the 1 mm sample Couette cell fluid gap (rotor, middle, and stator) for all time points, which demonstrate velocity changes across the experiment time and the fluid gap. Columns I: shear rate of $\dot{\gamma}$ = 0.9/s; II: shear rate of $\dot{\gamma}$ = 2.8/s; III: shear rate of $\dot{\gamma}$ = 4.6/s. The data present wall-slip and yielding behavior representative of a yield-stress gel. Rotor and stator data points are approximately 58.6 μm from the physical walls.

(Figure 7c I) as a drift to lower velocities over the 10 min shearing times. These effects are also present in the solid body flow region at $\dot{\gamma}$ = 2.8/s (Figure 7b II and 7c II). The temporal velocity fluctuation amplitudes as measured by the standard deviation are of order of the Newtonian calibration, indicating that the gel structure damps fluctuations relative to the 5% w/v sample.

3.3 Large-velocity fluctuations

The large fluctuations in transient velocity near the rotor generate large-velocity values greater than the rotor speed that (Figure 5c) are highly reproducible in the 5% w/v sample, which exhibits nematic liquid crystal-type rheology. Large fluctuations in velocity have been predicted for nematic

Table 3: Gap positions (mm), where $\dot{\gamma}_H$ and $\dot{\gamma}_L$ intersect or solid body rotation initiates for gel concentrations

Shear rate [/s]		7% w/v		12% w/v
0.9	Intersection	0.39	Solid body	0.19
2.8	Intersection	0.41	Solid body	0.31
4.6	Intersection	0.53	Intersection	0.49

liquid crystals in the simulations of Kupferman et al. using a long-range elastic correlation [43], for Ericksen numbers $\mathrm{Er} = \frac{\eta\dot{\gamma}_{\mathrm{eff}}}{\frac{K}{d^2}} \sim 400$ and Deborah number $\mathrm{De} = \frac{\dot{\gamma}}{D_R} \sim 1$. Er is the ratio of viscous stress $\eta\dot{\gamma}_{\mathrm{eff}}$, with η a characteristic Leslie viscosity $\dot{\gamma}_{\mathrm{eff}} = v/d$, to the Frank elastic stress, where $K \sim \frac{u}{a}$ is the Frank constant proportional to the nematic interaction

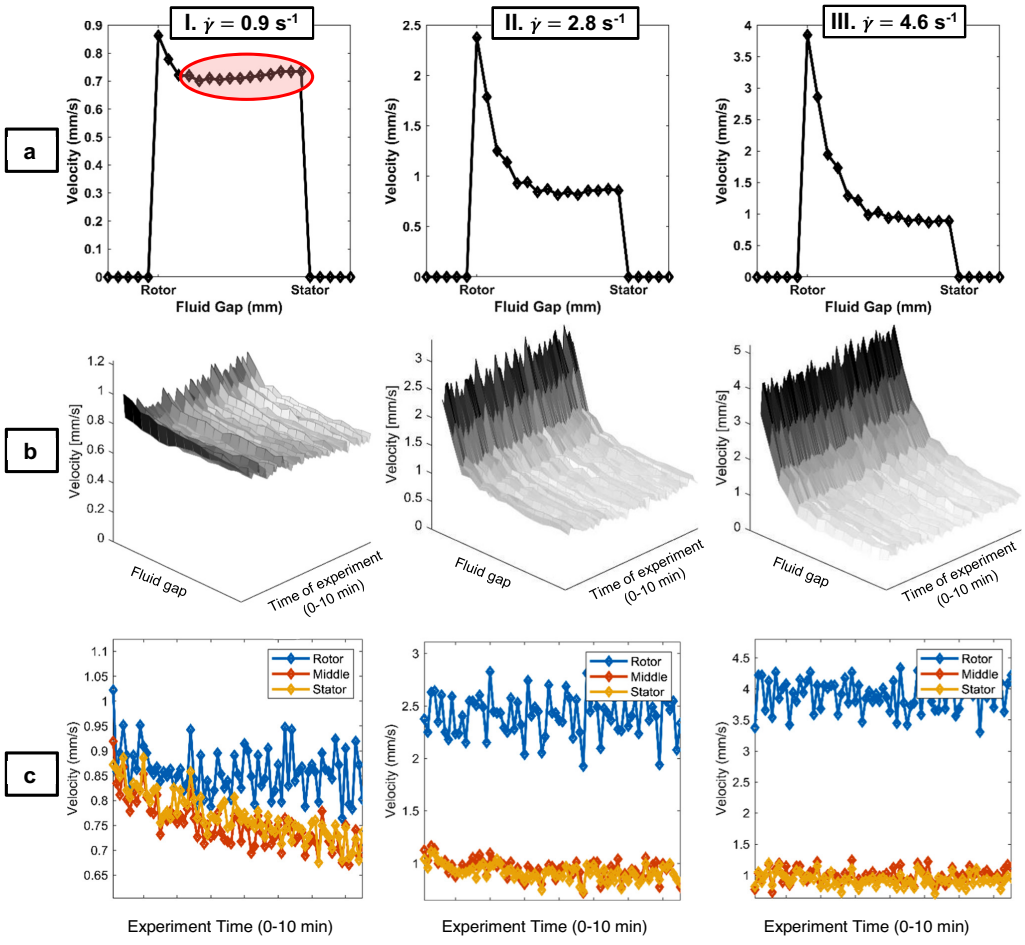


Figure 7: Rows a and b, Columns I–III. 1D NMR velocimetry experiments for NCC4, 12% w/v suspension, a very thick gel. Rows (a) steady-state, 1D velocity profiles, with 16 scans and total time of acquisition of 1 min, 12 s, and a pixel resolution of approximately 65 μm; (b) surface plots for 1D velocity profiles during an unsteady-state experiment with 75 experiments averaged over 2 scans and total time of acquisition of approximately 10 min and 12 s; (c) velocity profiles from the same unsteady-state experiment as (b), but displayed at three discrete positions across the 1 mm sample Couette cell fluid gap (rotor, middle, and stator) for all time points, which demonstrate velocity changes across the experiment time and the fluid gap. Columns I: shear rate of $\dot{\gamma}$ = 0.9/s; II: shear rate of $\dot{\gamma}$ = 2.8/s; III: shear rate of $\dot{\gamma}$ = 4.6/s. The data present wall-slip, shear-banding, and yielding representative of a thick yield-stress gel. The red shaded region indicates a region of solid-body-like rotation. Rotor and stator data points are approximately 58.6 μm from the physical walls.

energy u and a the nematic length scale [40]. De is the ratio of the experimental rate of shear $\dot{\gamma}$ to the rate of relaxation of the nematic director $\underline{n}$, which is $1/D_R$, with D_R being the nematic rotational diffusivity [40]. The nematic length scale a can be either the molecular or particle length scale or a supermolecular scale of microdomains of oriented nematics, which for the NCC particles is a ~ 10 μm, while the dimensionless interaction potential of the order of the Doi rigid rod model is u ~ 10, and the rotational diffusivity is D_R ~ 10^2/s [40,43,46]. For the NCC particles in this work and the d = 1 mm flow gap, the data in Figure 5 are in the De ~ 10^{-2} and Er ~ 10^3 regime for which tumbling of the particles occurs [40,42,43]. In the simulations of Kupferman et al. at De ~ 1 and Er ~ 400, intense vortex structures are formed due to large elastic energy release from the destruction of defect lines generated by rod tumbling, which result in large positive and negative velocities exceeding the wall velocity [43]. The frequency and amplitude of the large-velocity fluctuations (Figure 5c) scales with $\dot{\gamma}$, increasing with increasing $\dot{\gamma}$. In addition, chiral nematic liquid crystal mesophases are known to exhibit positional, orientational, and coupled positional–orientational slip at various length scales [40,42]. These modes contribute to the dynamic flow instabilities exhibited as velocity fluctuations in the velocimetry data. Ongoing research aims to determine the impact of each of these modes by applying PGSE NMR methods to characterize the length and timescale of these fluctuations as has been done in turbulent and granular flows [39,47].

Velocimetry methods have not previously been applied to study the rheological flows of NCC suspensions [13]. Novel Rheo-NMR velocimetry data with spatial and temporal resolution indicate that NCC suspensions undergo strongly varying flow deviations from linear in a Couette cell, which correlates with subtle variations in steady bulk rheology and includes wall-slip, shear banding, and yielding. The data indicate large-velocity fluctuations in the liquid crystal-phase suspension (5% w/v), seen for the first time in NCCs, due to particle director orientation tumbling and flow instability not clearly discernible in the bulk rheology. The results provide the details of the mesoscale velocity distributions on the order of 10's μm, which allows the integration of the observed wall-slip and shear banding phenomena to model NCC rheology. This data is also relevant to the design of processing flow conditions where stress inhomogeneity can cause significant material microstructure change over scales of the order of 10's μm that alter material properties. The data also clearly demonstrate the utility of using magnetic resonance velocimetry to study a range of processing flows of NCC.

Acknowledgement: M. Stanley would like to thank Matthew C. Young for MATLAB scripts and assistance.

Funding information: M. Stanley acknowledged the MSU ChBE for support from the Benjamin Fellowship and the Noble Family Fellowship. J. Seymour and S. Codd acknowledged the M.J. Murdock Charitable Trust and the NSF MRI program for instrument funding. J. Wilking acknowledged the Army Research Office (Grant #W911NF-19-1-0288) and the NIH (Grant # R01 GM131408-01). Research reported in this publication was supported in part by the National Institute of General Medical Sciences of the National Institutes of Health under Award Number P20GM103474. The content is solely the responsibility of the authors and does not necessarily represent the official views of the National Institutes of Health.

Author contributions: MAS and JDS wrote the initial manuscript, conceived of the concept of the work, designed experiments, curated data, and performed analysis. MAS performed experiments and performed formal analysis. JDS, JNW, and SLC supervised the work. JNW provided funding and assisted data analysis. SLC performed data curation and analysis. JSJ was involved with data curation and analysis. DB aided with sample acquisition. All authors reviewed and edited the manuscript.

Conflict of interest: The authors state no conflict of interest.

Ethical approval: The conducted research is not related to either human or animal use.

Data availability statement: All data generated or analyzed during this study are included in this published article.

References

[1] Rongpipi S, Ye D, Gomez ED, Gomez EW. Progress and opportunities in the characterization of cellulose – an important regulator of cell wall growth and mechanics. Front Plant Sci. 2019;9:1894.
[2] McNamara JT, Morgan JL, Zimmer J. A molecular description of cellulose biosynthesis. Annu Rev Biochem. 2015;84:895–921.
[3] Bhatia SK, Jagtap SS, Bedekar AA, Bhatia RK, Patel AK, Pant D, et al. Recent developments in pretreatment technologies on lignocellulosic biomass: Effect of key parameters, technological improvements, and challenges. Bioresour Technol. 2020;300:122724.
[4] Carolin CF, Kamalesh T, Kumar PS, Hemavathy RV, Rangasamy G. A critical review on sustainable cellulose materials and its multifaceted applications. Ind Crop Prod. 2023;203:117221.
[5] Delidovich I, Hausoul PJC, Deng L, Pfützenreuter R, Rose M, Palkovits R. Alternative monomers based on lignocellulose and their use for polymer production. Chem Rev. 2016;116(3):1540–99.
[6] Raj T, Chandrasekhar K, Naresh Kumar A, Kim S-H. Lignocellulosic biomass as renewable feedstock for biodegradable and recyclable plastics production: A sustainable approach. Renew Sustain Energy Rev. 2022;158:112130.

[7] Trache D, Tarchoun AF, Derradji M, Hamidon TS, Masruchin N, Brosse N, et al. Nanocellulose: From fundamentals to advanced applications. Front Chem. 2020;8:392.
[8] Ong X-R, Chen AX, Li N, Yang YY, Luo HK. Nanocellulose: Recent advances toward biomedical applications. Small Sci. 2023;3(2):2200076.
[9] Ghilan A, Nicu R, Ciolacu DE, Ciolacu F. Insight into the latest medical applications of nanocellulose. Materials (Basel). 2023;16(12):15–27.
[10] Shojaeiarani J, Bajwa DS, Chanda S. Cellulose nanocrystal based composites: A review. Compos Part C: Open Access. 2021;5:100164.
[11] George J, Sabapathi SN. Cellulose nanocrystals: synthesis, functional properties, and applications. Nanotechnol Sci Appl. 2015;8:45–54.
[12] Singh S, Bhardwaj S, Tiwari P, Dev K, Ghosh K, Maji PK. Recent advances in cellulose nanocrystals-based sensors: a review. Mater Adv. 2024;5(7):2622–54.
[13] Kadar R, Spirk S, Nypelo T. Cellulose nanocrystal liquid crystal phases: Progress and challenges in characterization using rheology coupled to optics, scattering, and spectroscopy. ACS Nano. 2021;15(5):7931–45.
[14] Shafiei-Sabet S, Hamad WY, Hatzikiriakos SG. Rheology of nanocrystalline cellulose aqueous suspensions. Langmuir. 2012;28(49):17124–33.
[15] Liao J, Pham KA, Breedveld V. Rheological characterization and modeling of cellulose nanocrystal and TEMPO-oxidized cellulose nanofibril suspensions. Cellulose. 2020;27(7):3741–57.
[16] Cainglet HE, Tanner J, Nasiri N, Browne C, Garnier G, Batchelor W. Rapid cellulose nanomaterial characterisation by rheology. Cellulose. 2023;30(8):4971–82.
[17] Gray DG. Order and gelation of cellulose nanocrystal suspensions: an overview of some issues. Philos Trans R Soc A: Math, Phys Eng Sci. 2018;376(2112):20170038.
[18] Stroobants A, Lekkerkerker HNW, Odijk T. Effect of electrostatic interaction on the liquid crystal phase transition in solutions of rodlike polyelectrolytes. Macromolecules. 1986;19(8):2232–8.
[19] Xu Y, Atrens AD, Stokes JR. Rheology and microstructure of aqueous suspensions of nanocrystalline cellulose rods. J Colloid Interface Sci. 2017;496:130–40.
[20] Zakani B, Grecov D. Effect of ultrasonic treatment on yield stress of highly concentrated cellulose nano-crystalline (CNC) aqueous suspensions. Carbohydr Polym. 2022;291:119651.
[21] Echeverria C, Almeida PL, Feio G, Figueirinhas JL, Rey AD, Godinho MH. Rheo-NMR study of water-based cellulose liquid crystal system at high shear rates. Polymer. 2015;65:18–25.
[22] Callaghan PT. Rheo-NMR and velocity imaging. Curr Opin Colloid Interface Sci. 2006;11(1):13–8.
[23] Rogers SA, Vlassopoulos D, Callaghan PT. Aging, yielding, and shear banding in soft colloidal glasses. Phys Rev Lett. 2008;100(12):128304.
[24] Holmes WM, Lopez-Gonzalez MR, Callaghan PT. Fluctuations in shear-banded flow seen by NMR velocimetry. Europhys Lett. 2003;64(2):274–80.
[25] Ovarlez G, Rodts S, Chateau X, Coussot P. Phenomenology and physical origin of shear localization and shear banding in complex fluids. Rheol Acta. 2009;48(8):831–44.
[26] Britton MM, Callaghan PT. Two-phase shear band structures at uniform stress. Phys Rev Lett. 1997;78(26):4930–3.
[27] Coussot P. Progress in rheology and hydrodynamics allowed by NMR or MRI techniques. Exp Fluids. 2020;61(9):6–8.
[28] Al-kaby RN, Codd SL, Seymour JD, Brown JR. Characterization of velocity fluctuations and the transition from transient to steady state shear banding with and without pre-shear in a wormlike micelle solution under shear startup by Rheo-NMR. Appl Rheol. 2020;30(1):1–13.
[29] Brox TI, Douglass B, Galvosas P, Brown JR. Observations of the influence of Taylor-Couette geometry on the onset of shear-banding in surfactant wormlike micelles. J Rheol. 2016;60(5):973–82.
[30] Davies CJ, Sederman AJ, Pipe CJ, McKinley GH, Gladden LF, Johns ML. Rapid measurement of transient velocity evolution using GERVAIS. J Magn Reson. 2010;202(1):93–101.
[31] Siebert H, Grabowski DA, Schmidt C. Rheo-NMR study of a non-flow-aligning side-chain liquid crystal polymer in nematic solution. Rheol Acta. 1997;36(6):618–27.
[32] Geng Y, Almeida PL, Feio GM, Figueirinhas JL, Godinho MH. Water-based cellulose liquid crystal system investigated by Rheo-NMR. Macromolecules. 2013;46(11):4296–302.
[33] Chanda S, Bajwa DS, Holt GA, Stark N, Bajwa SG, Quadir M. Silane compatibilization to improve the dispersion, thermal and mechanical properties of cellulose nanocrystals in poly (ethylene oxide). Nanocomposites. 2021;7(1):87–96.
[34] Beck-Candanedo S, Roman M, Gray DG. Effect of reaction conditions on the properties and behavior of wood cellulose nanocrystal suspensions. Biomacromolecules. 2005;6(2):1048–54.
[35] Casado U, Mucci VL, Aranguren MI. Cellulose nanocrystals suspensions: Liquid crystal anisotropy, rheology and films iridescence. Carbohydr Polym. 2021;261:117848.
[36] Callaghan PT. Rheo NMR and shear banding. Rheol Acta. 2008;47(3):243–55.
[37] Al-kaby RN, Jayaratne JS, Brox TI, Codd SL, Seymour JD, Brown JR. Rheo-NMR of transient and steady state shear banding under shear startup. J Rheol. 2018;62(5):1125–34.
[38] Jayaratne JS, Codd SL, Al-Kaby RN, Maley J, Brox TI, Galvosas P, et al. Large amplitude oscillatory shear rheo-NMR velocimetry. Phys Fluids. 2023;35(9):093105.
[39] Callaghan PT. Translational dynamics and magnetic resonance: principles of pulsed gradient spin echo NMR. Oxford, England: Oxford University Press; 2011.
[40] Larson RG. The structure and rheology of complex fluids. Oxford, England: Oxford University Press; 1999.
[41] Onogi S, Asada T. Rheology and rheo-optics of polymer liquid crystals. In: Astarita G, Marrucci G, Nicolais L, editors. Rheology: Volume 1: Principles. Boston, MA: Springer US; 1980. p. 127–47.
[42] Rey AD, Denn MM. Dynamical phenomena in liquid-crystalline materials. Annu Rev Fluid Mech. 2002;34:233–66.
[43] Kupferman R, Kawaguchi MN, Denn MM. Emergence of structure in a model of liquid crystalline polymers with elastic coupling. J Non-Newton Fluid. 2000;91(2–3):255–71.
[44] Cloître M, Bonnecaze RT. A review on wall slip in high solid dispersions. Rheol Acta. 2017;56:283–305.
[45] Buscall R. Letter to the Editor: Wall slip in dispersion rheometry. J Rheol. 2010;54(6):1177–83.
[46] Van Rie J, Schütz C, Gençer A, Lombardo S, Gasser U, Kumar S, et al. Anisotropic diffusion and phase behavior of cellulose nanocrystal suspensions. Langmuir. 2019;35(6):2289–302.
[47] Seymour JD, Caprihan A, Altobelli SA, Fukushima E. Pulsed gradient spin echo nuclear magnetic resonance imaging of diffusion in granular flow. Phys Rev Lett. 2000;84(2):266–9.

RHEO-NMR VELOCIMETRY OF NANOCRYSTALLINE CELLULOSE SUSPENSIONS IN SODIUM CHLORIDE

Contribution of Authors and Co-Authors

Manuscript in Chapter 5

Author: Maribelle A. Stanley

Contributions: Designed and performed experiments and formal analysis, wrote the initial manuscript, conceived concept, curated data, and reviewed/edited the manuscript.

Co-author: Jayesha S. Jayaratne

Contributions: Involved with data curation/analysis.

Co-author: Sarah L. Codd

Contributions: Performed data curation/analysis, supervised work, reviewed/edited the manuscript.

Co-author: James N. Wilking

Contributions: Provided funding, data analysis assistance and reviewed/edited manuscript.

Co-author: Joseph D. Seymour

Contributions: Wrote initial manuscript, conceived concept, designed experiments, curated data, performed analysis, supervised work, reviewed/edited manuscript.

Manuscript Information

Maribelle A. Stanley, Jayesha S. Jayaratne, Sarah L. Codd, James N. Wilking, Joseph D. Seymour

Status of Manuscript:
_X_ Prepared for submission to a peer-reviewed journal
____ Officially submitted to a peer-reviewed journal
____ Accepted by a peer-reviewed journal
____ Published in a peer-reviewed journal

Abstract

The data demonstrate NMR velocimetry and standard rheometry of nanocrystalline cellulose (NCC) suspensions with NaCl mediated particle interactions. Velocity profiles with 50 µm spatial and temporal resolution demonstrate complex flow behavior which correlates with standard rheometry but provides clear evidence of wall-slip, yielding, shear-banding, and velocity fluctuations associated with solid to liquid phase transitions. Addition of NaCl for higher concentration suspensions generate coherent velocity fluctuations for 5%, 7%, and 12% w/v with 0.1 M NaCl. These fluctuations and variation in spatial velocity distributions can be correlated to glass and gel phase transitions. The results provide mesoscale data complementary to published rheology data with potential to tune particle interactions to control processing flow conditions of NCC suspensions.

Introduction

Nanocrystalline cellulose (NCC) is a renewable material of nanorod structure formed from acid hydrolysis of cellulose [8, 39, 77, 92, 137, 142, 144, 174]. NCC nanorods are characterized by high aspect ratios $L/D > 10$ [16, 92, 159] and generate colloidal suspensions when dispersed in water, which are stabilized by electrostatic repulsion from sulfate groups formed during acid hydrolysis [16, 142, 174]. NCC exhibits impressive properties, including both strength and elasticity, optical birefringence, adaptable and adjustable mechanics, and alterable surface chemistry, among others, which have earned it a classification as a "next-generation" material [159]. These properties have garnered interest in using NCC for a variety of applications such as tissue engineering, biomedical devices, bioremediation, cement, food products, and electric sensors [74, 84, 117, 144, 146, 159].

Nanocrystalline cellulose (NCC) rheology and colloidal behavior have been studied extensively in the last three decades to understand NCC flow behavior and its correlation

to microstructure [16, 41, 88, 141, 142, 160, 172, 174, 176]. NCC exhibits phase change behavior that is concentration-dependent [16, 88, 141, 142, 149, 172, 174], time-dependent [149, 174], temperature-dependent [141, 159, 167, 174], shear-dependent [16, 141, 172, 174], and charge-dependent [16, 43, 44, 58, 59, 81, 112, 116, 123, 142, 172–174]. NCC suspensions vary in behavior with concentration on a continuum spanning from an isotropic Newtonian-like viscous liquid, to a viscoelastic liquid anisotropic nematic liquid crystal, and a shear-thinning isotropic gel [16, 88, 141, 142, 172, 174, 174]. It has been reported that the influence of ionic species can induce liquid crystal phase changes, gelation, and complete irreversible aggregation [16, 58, 59, 142, 172, 174]. Understanding the impact of such variables on NCC microstructure and flow can enhance controlled design of NCC based materials and processing conditions.

Traditional rheometry provides characterization of NCC suspensions, however, like other complex fluids, NCC exhibits a heterogeneous microstructure and concomitant yield and shear banding flow, which cannot be resolved with bulk-scale measurements [49, 149]. It is necessary to employ methods that complement traditional rheometers by providing velocity distribution data to properly evaluate flow and structure. This has been done with a variety of optical methods by numerous groups [44, 88, 118, 141, 142, 174]. Rheo-NMR velocimetry, only recently applied to study NCC, utilizes ^{1}H nuclear magnetic resonance (NMR) imaging methods to visualize flow on the micron scale with time resolution on the order of seconds [34, 35, 37, 149]. Rheo-NMR has long been shown to provide useful flow and structural information for complex fluids [2, 3, 28, 30, 34, 35, 49, 52, 82, 85, 149] that is inaccessible with traditional torque-based measurements. In addition, there are no transparency or sample size constraints, and invasive tracer particles are not needed [34, 37]. Previously, our group has evaluated the effect of concentration-dependence on NCC with Rheo-NMR and found non-viscometric flow in homogeneous velocity distributions across the flow cell, i.e. yield stress and shear banding [149]. In addition, we observed velocity

fluctuations associated with a known liquid crystal phase concentration of 5% w/v [149]. To the authors' knowledge, this is the only other work on nanocrystalline cellulose utilizing Rheo-NMR velocity imaging techniques [88], while previous Rheo-NMR studies have focused on hydroxypropyl cellulose (HPC), a less commonly used derivative, with ^{2}H deuterium spectroscopy under shear [64, 72, 145].

In this work, we use Rheo-NMR velocity imaging to evaluate the impact of NCC concentration and added NaCl on the flow behavior of NCC suspensions, with a different material source from our previous work [149]. This is done by generating transient and steady-state velocity profiles for NCC concentrations which span the liquid solid phase transition at three shear rates using a home-built Rheo-NMR device with a 1 mm fluid gap Couette flow cell. In addition, torque-based and strain-controlled rheometry measurements are employed to inform and complement Rheo-NMR observations. The spatial velocity data demonstrate the correlation between the phase transitions and significant variations in flow behavior.

Theory

Colloidal behavior is modeled by Derjaguin–Landau–Verwey–Overbeek (DLVO) theory, which describes the potential enthalpic energy between colloid particles interacting through repulsive and attractive electrostatic interactions [80, 96, 108]. Colloid particles are stabilized in a potential energy well by the repulsive double layer. Identical surface forces from like colloids generate this repulsive double layer, which causes an increased excluded volume effect and either dominates or balances the van der Waals forces that attract particles [1, 80, 138]. When the repulsive double layer is shortened, as generally occurs with interparticle screening from added ionic species, van der Waals forces can dominate and cause aggregation. If the van der Waals forces are large enough, a completely unstable colloidal suspension may occur which separates into two distinct phases of separate concentrations [80, 96, 108].

It has been reported that the addition of monovalent and divalent salts to NCC generates altered microstructures and flow behaviors [16, 43, 44, 81, 112, 116, 123, 142, 172–174]. DLVO theory is hypothesized as the main mechanism for the alterations in structure [16, 44, 112, 116, 123, 172]. The reduced Debye length of the repulsive double layer can enable closer packing of nanorods and can also affect the helical pitch of nematic domains in liquid crystals [59, 81, 142], the degree to which will vary with both the concentration of NCC and salt. However, the dynamics of nematic NCC liquid crystals with added ionic species is also thought to be governed by Onsager theory [16, 119, 174]. Onsager theory describes the ordering of hard rods in liquid crystals as an entropy-driven process, where a critical packing fraction, $\phi_c \sim 4L/D$, allows for a transition from isotropic to nematic ordering [119, 174]. This transition increases translational entropy but preferentially reduces the free energy by lowering orientational entropy [56, 119, 162, 170]. As the change in enthalpy from addition of salt will, according to DLVO theory, affect the excluded volume, it is thought that it will also affect the orientation of rods and may contribute to the formation of nematic liquid crystal domains at NCC concentrations which are typically isotropic, giving rise to a competing effect between enthalpy and entropy in some NCC systems [174].

Materials and Methods

Sample Preparation

The nanocrystalline cellulose systems investigated in this work are aqueous suspensions ranging from 3% w/v to 12% w/v with and without 0.05 – 0.1 M NaCl. Cellulose nanocrystals in the form of nanorods with dimensions 3-5 nm in diameter and 85-95 nm in length were obtained from CelluForce NCC® NCV100-NASD90 (Windsor, QC, Canada). The samples were prepared as directed by CelluForce NCC® by weighing the cellulose nanocrystals as a spray-dried powder and then adding the appropriate amount of RO/DI water or NaCl aqueous solution (NaCl dissolved in RO/DI water) with stirring. Ultrasound

energy was applied to the resulting suspensions to homogenize them with a Fisher Scientific ultrasonication ice water bath (160 W power output, 40 kHz frequency, 1.9 L bath volume, model 15337402); ice water (∼12 °C) was used in the bath to prevent NCC particle degradation from de-esterification of sulfate groups [13, 41, 141]. Samples were sonicated and periodically vortexed until visually homogeneous, such that the total sonication energy for each sample was ∼300 J/g of NCC, where < 1000 J/g is found to be sufficient to break aggregates and disperse the nanorods [141]. All suspensions were stored in a refrigerator (3 °C) before and after measurements.

Rheometry

Linear rheological measurements were performed with an AR-G2 rheometer (TA Instruments) equipped with either a 60 mm diameter, 2° angle cone-and-plate geometry for 3%, 5%, 7% w/v suspensions without NaCl, and all samples with NaCl, or a 20 mm diameter parallel plate for the 12% w/v and 12% w/v with NaCl suspensions. All experiments were run at 25 °C with a controlled strain rate analogous to the Rheo-NMR control.

Rheo-NMR Velocimetry

The methods described here follow those detailed in Stanley et. al. 2024 [149]. A home-built and portable Rheo-NMR experimental system, coupled with a methodology for well-established fluid flow measurement capabilities across a variety of length and time scales, was employed for velocimetry experiments [2, 34, 35, 85]. The experimental system involves an NMR-compatible stepper motor-powered driveshaft which rotates the inner rotor of a Couette shear cell. The inner cylinder is 8 mm in diameter and composed of PEEK, while the outer 9 mm diameter cylinder is composed of glass (Figure 5.1). These dimensions approach a narrow gap system with a fluid gap width ($d = R_o - R_i$) of 1 mm, a radius ratio ($\kappa = R_i/R_o$) of 0.89, and a q value ($q = d/R_i$) of 0.143, resulting in a small but nonzero stress inhomogeneity [61]. After loading the samples into the shear cell, they were

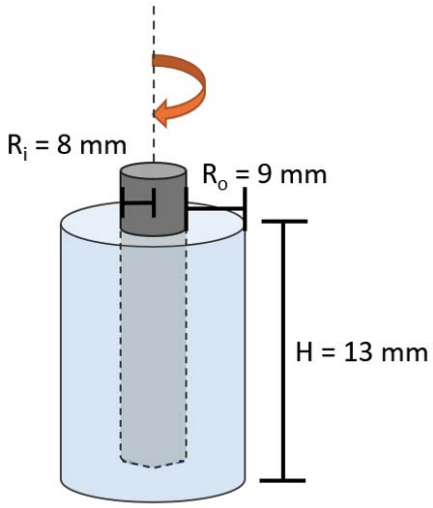


Figure 5.1: A schematic that depicts the Rheo-NMR sample Couette cell dimensions.

placed under vacuum for 30 minutes to eliminate air bubbles, and subsequently pre-sheared to remove remaining air bubbles and provide a uniform microstructure initialization before measurements. Pre-shearing was done using an applied shear rate of $\dot{\gamma} = 4.6$ s^{-1} for 30 minutes to 1 hour, and samples were allowed to relax for 3 hours before measurements. A Newtonian silicone oil calibration fluid (10,000 cSt) was used to measure the actual velocity at the rotor to determine $\dot{\gamma}$, with shear rates of $\dot{\gamma} = 0.9$, 2.8, and 4.6 s^{-1}, obtained for set points of 1, 3, and 5 s^{-1}.

Measurements were performed with a Bruker AVANCE 300 spectrometer and 7 T superconducting super wide bore magnet equipped with a 25 mm birdcage resonator coil and Micro-2.5 gradient system (providing a maximum gradient of 1.5 T/m at 60 A). Bruker TopSpin 3.5pl7 software was used to acquire data with the spectrometer, and the data was subsequently analyzed with MATLAB (MathWorks, Inc., Natick, MA). A modified pulsed gradient spin echo (PGSE) pulse sequence (Figure 5.2) was used to acquire 1D velocity profiles [136]. The PGSE pulse sequence encodes the water protons velocity in magnetization phase, ϕ, where $\phi = \gamma v \int g(t')t'dt' = \gamma g \delta \Delta$. Here, γ refers to the magnetogyric ratio (which is

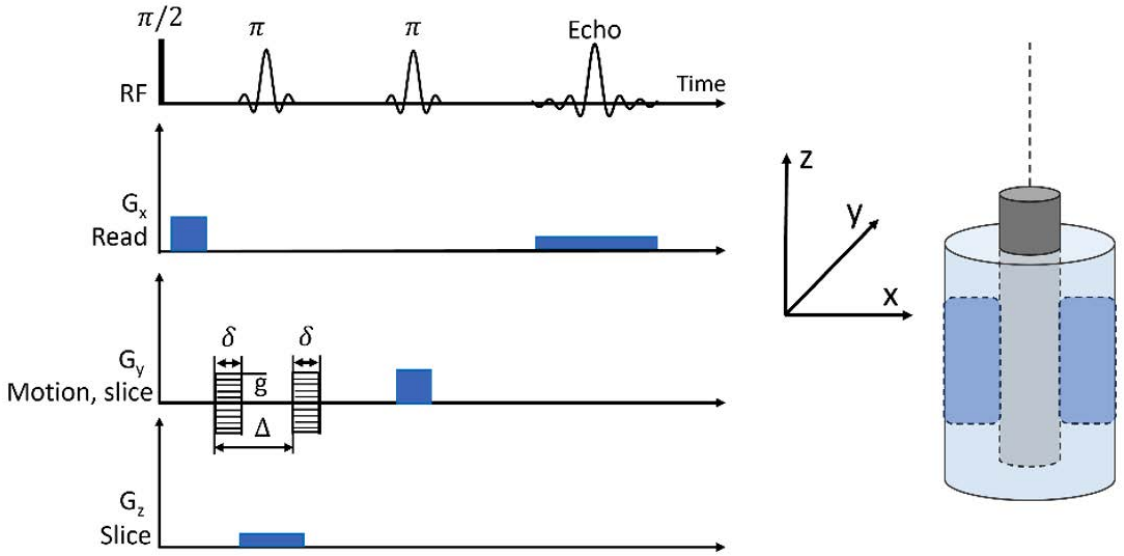


Figure 5.2: The PGSE pulse sequence with double slice selection used to acquired 1D velocity profiles and an adjacent depiction of the imaged region of the Couette flow cell. Data was acquired from a 10 mm slice in the vorticity direction (z-axis) and a 1 mm thick slice along the velocity direction (y-axis) as shown in the shaded section of the Couette schematic. The 1D profile was acquired across the fluid gap in the read gradient direction (x-axis) with a spatial resolution of 58.6 µm/pixel.

a material property of the ^{1}H spin), g the gradient amplitude, δ the gradient pulse duration, Δ the displacement observation time, and v the velocity encoded. Double slice selection was employed with the PGSE pulse sequence [29, 136]. A 1 mm thick slice in the flow direction (y) was used to eliminate curvature and provide $v_\theta(r)$ azimuthal radius dependent velocity directly, averaged over a 10 mm slice in the vertical vorticity direction (z) to provide more ^{1}H spins and increase signal to noise for two average 8 s acquisitions. Two gradient steps of equal duration ($\delta = 1$ ms) and magnitude but opposite sign, separated by a displacement observation time of $\Delta = 11$ ms, were used as flow encoding gradients with amplitude ranging from 0.178 to 0.889 T/m dependent on shear rate induced velocity. The velocity was imaged with a 30 mm field of view using 512 points (58.6 µm resolution) across the diameter of the flow cell using the lateral direction (x) "read" gradients, which provides the velocity directly as a function of gap distance $v(x)$.

Steady state experiments used 16 scans (repetitions) of gradient flow encoding steps over a total acquisition time of 1 minute and 12 seconds; the velocity measured thus represents an average velocity over this time. Unsteady state (transient, or start-up) experiments used 2 scans for a faster acquisition and acquired 75 independent velocity profiles averaged over 8.11 seconds for a total duration of approximately 10 minutes and 12 seconds. This transient measurement minimizes the velocity averaging time but lowers the acquired voltage signal to noise ratio. Velocimetry experiments were performed both with shear and without shear for each shear rate to provide a no flow control. This control allows for the removal of phase shifts from background and imaging magnetic field gradients during data analysis [37]. All results shown represent the difference in the phase between flow and no flow velocity profiles. The velocity induced phase shifts map $\pm V_{max}$ to $\pm\pi$ in phase. Velocities larger than the velocity maximum with phase $\phi_{max} = \pi + \delta$ result in a phase wrap to $-\pi + \delta$ and standard phase unwrapping methods are used [37]. This ensures that imperfections from magnetic field gradients do not affect the result.

Results

Rheometry

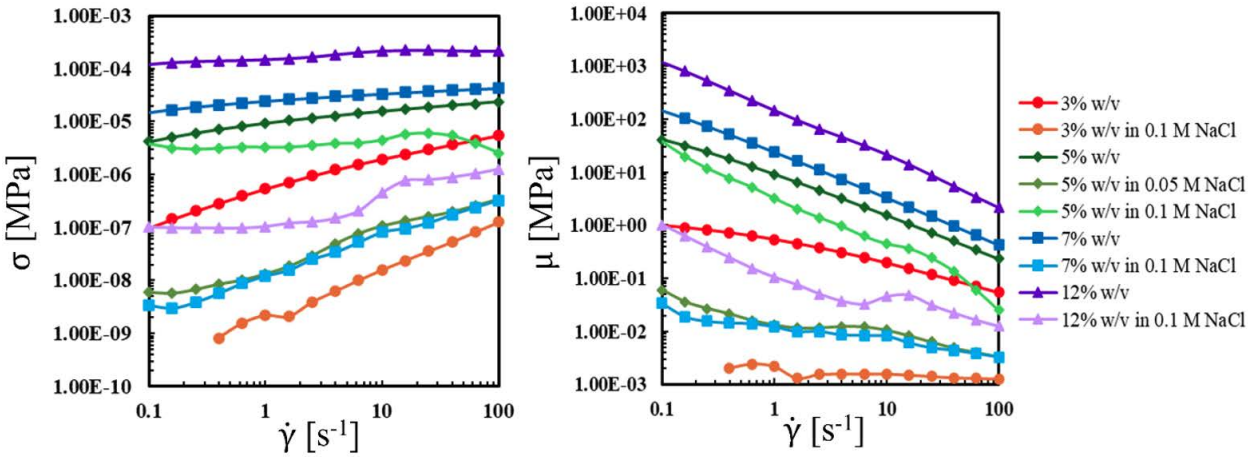


Figure 5.3: Shear stress vs. applied shear rate (left) and viscosity vs. applied shear rate (right) from bulk rheometry experiments on NCC. As expected and noted in the literature [100, 141], shear stress and viscosity increase as the concentration of NCC increases for all non-salt samples. Notably, all samples show a significant decrease ($\mathcal{O} \sim 3$) in shear stress and viscosity with the addition of salt, and salt samples generally show non-monotonic behavior. The liquid crystal concentration, 5% w/v, shows a decrease in shear stress and viscosity at 0.05 M NaCl, but an increase in both quantities at 0.1 M NaCl, which has been observed in the literature [172].

As expected and noted in the literature [100, 141], shear stress and viscosity increase as the concentration of NCC increases for all non-salt samples (Figure 5.3). Notably, all samples show a significant decrease ($\mathcal{O} \sim 3$) in shear stress and viscosity with the addition of salt, and salt samples generally show non-monotonic behavior. The liquid crystal concentration, 5% w/v, shows a decrease in shear stress and viscosity at 0.05 M NaCl, but an increase in both quantities at 0.1 M NaCl, which has been observed in the literature [172, 173]. Shear stress and viscosity data is notably different from that previously reported by us for a different NCC source material [149], with the most significant difference being the magnitude of shear stress and viscosity, which is at least $\mathcal{O} \sim 6$ lower for the material reported here. This is a

common challenge with NCC that arises from the variety of NCC sources and their impact on NCC synthesis, which has been reported [174].

Shear stress and viscosity data for the 3% w/v sample without NaCl demonstrates mostly Newtonian behavior and slight shear thinning, while the 3% w/v sample with 0.1 M NaCl demonstrates non-monotonic behavior at shear rates below 2 s^{-1} but Newtonian behavior at higher shear rates (Figure 5.3). The 5% w/v sample without NaCl exhibits mostly shear thinning behavior, while the 5% w/v sample with 0.05 M NaCl shows a slight stress plateau spanning from approximately 1 to 10 s^{-1} shear rate, and the 5% w/v sample with 0.1 M NaCl shows shear thinning behavior until around 10 s^{-1}, where it then exhibits shear thinning behavior. The 7% w/v sample without NaCl shows slight shear thinning while the 7% w/v sample with 0.1 M NaCl shows a slight stress plateau spanning from approximately 1 to 10 s^{-1} shear rate. The 12% w/v sample without NaCl shows slight shear thinning, while the 12% w/v sample with 0.1 M NaCl shows a short but dramatic stress plateau spanning from approximately 3 to 11 s^{-1} shear rate.

Rheo-NMR Velocimetry

Steady state 1D velocity profiles depicted in Figure 5.4 demonstrate the effects of shear and salt content on the flow behavior of NCC suspensions ranging from 3% w/v to 12% w/v. The 3% w/v sample shows a Newtonian-like linear flow profile across the gap with no dependence on shear or salt content. The 5% w/v sample, a known liquid crystal phase [88, 141, 149, 172], demonstrates a dramatic change in profile curvature with addition of salt at 0.05 M NaCl for $\dot{\gamma} = 0.9$ s^{-1}, and a notable shear banding or yield stress behavior with addition of salt at 0.1 M NaCl. At 7% w/v, a nearly Newtonian flow profile is observed for $\dot{\gamma} = 0.9$ and 4.6 s^{-1}, with some slip observed at the stator for $\dot{\gamma} = 2.8$ s^{-1} in an otherwise linear profile. Addition of salt at 0.1 M NaCl results in a dramatic change in the velocity profile, where $\dot{\gamma} = 0.9$ s^{-1} depicts a near solid body flow which then yields in increasing

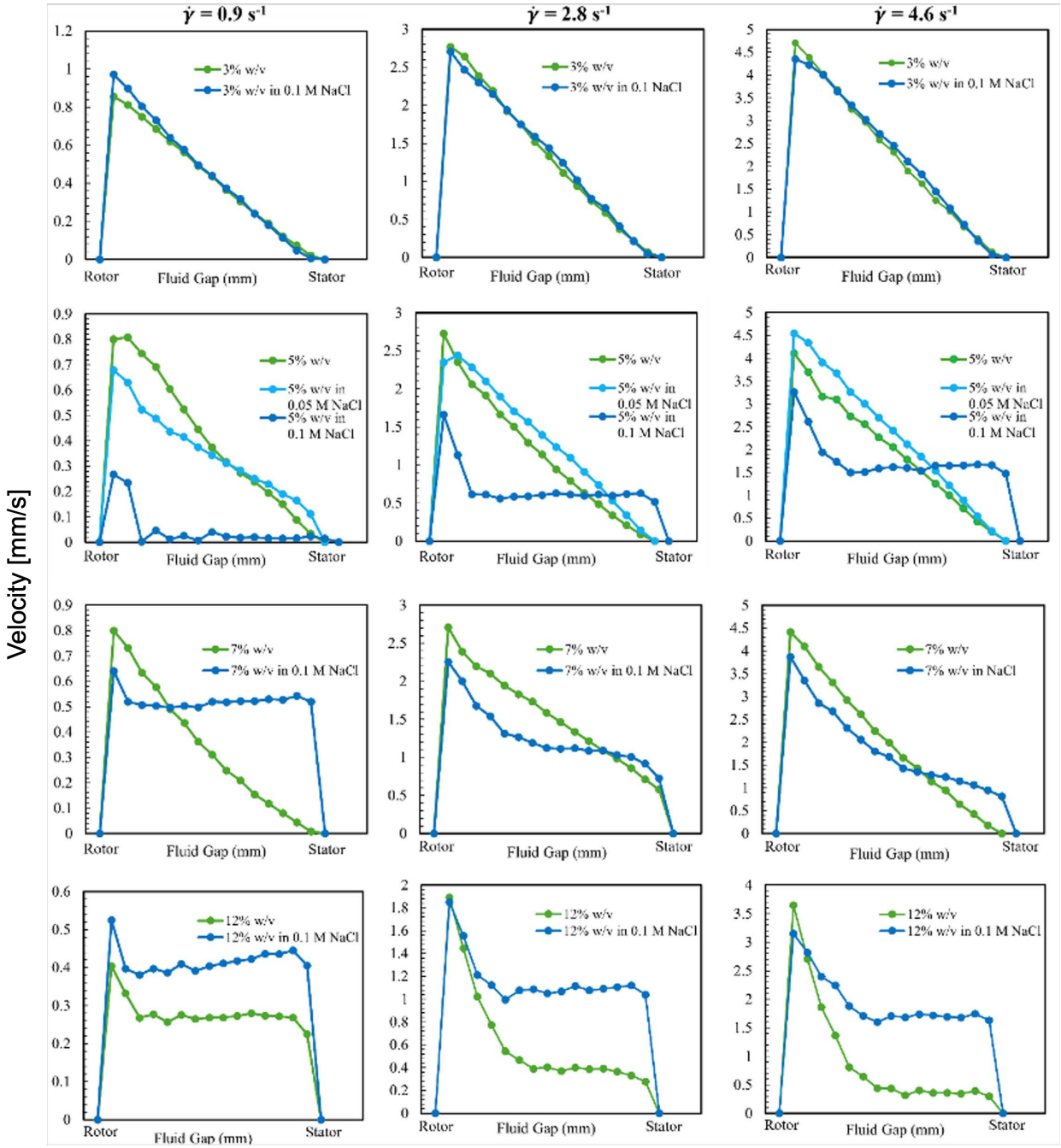


Figure 5.4: 1D NMR velocimetry experiments for 3%, 5%, 7%, and 12% w/v with and without added salt at $\dot{\gamma}$ = 0.9, 2.8, and 4.6 s^{-1}. Steady state, 1D velocity profiles were obtained with 16 scans and total acquisition time of 1 minute, 12 seconds and a pixel resolution of approximately 65 µm. Rotor and stator data points are approximately 58.6 µm from the physical walls.

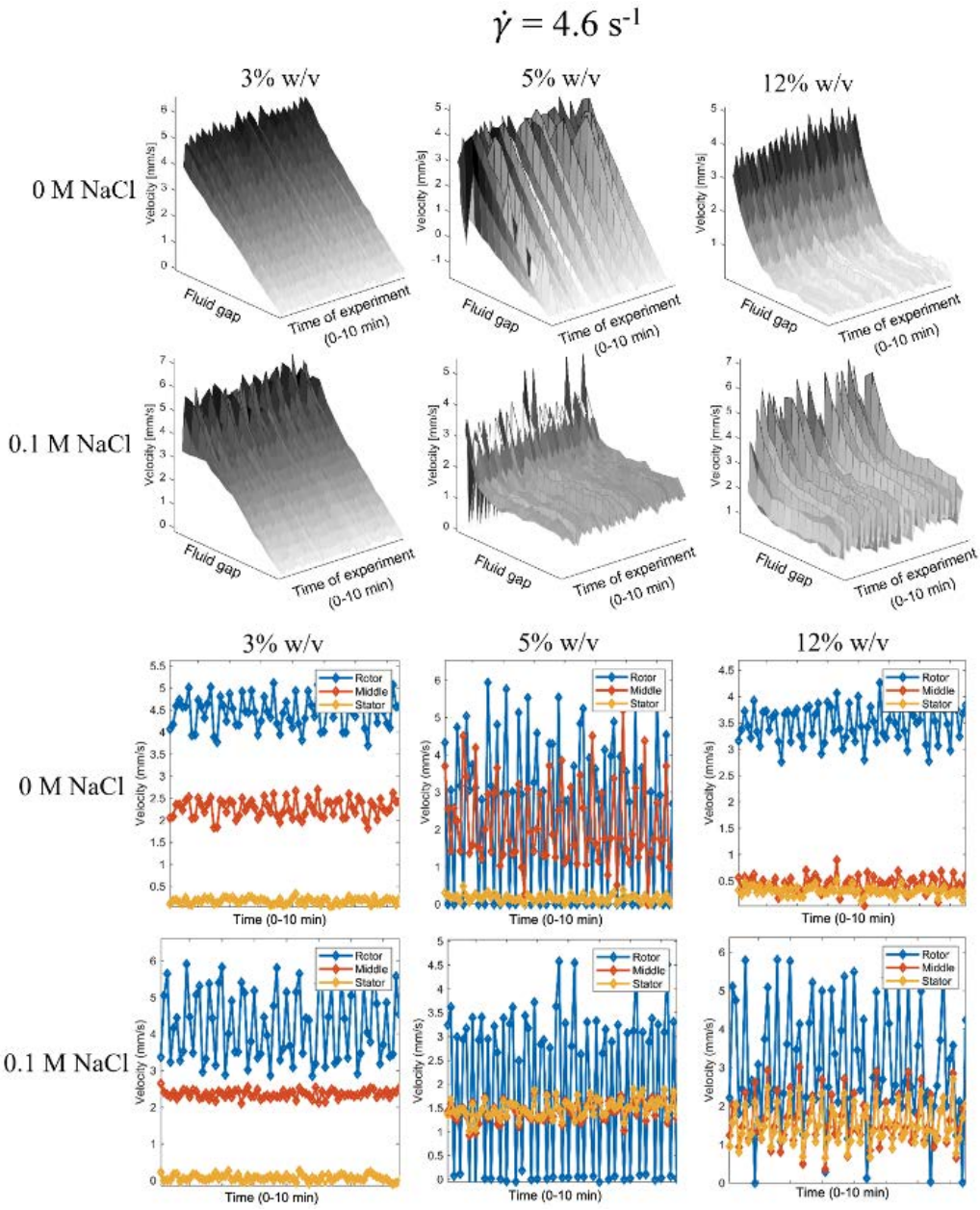


Figure 5.5: Select transient data plots from 1D NMR velocimetry experiments for 3%, 5%, and 12% w/v with and without added salt at $\dot{\gamma} = 4.6\ s^{-1}$. Top: Surface plots for 1D velocity profiles from unsteady-state experiments with 75 experiments averaged over 2 scans and total time acquisition of approximately 10 minutes, 12 seconds. Bottom: Velocity profiles from the same unsteady-state experiments as in Top, but displayed at three discrete points across the 1 mm sample Couette cell fluid gap (rotor, middle, stator) for all time points, which demonstrate velocity changes across the experiment time and fluid gap. Pixel resolution of approximately 65 µm. Rotor and stator data points are approximately 58.6 µm from physical walls. Detailed transient data is available in SI, Figures A.1-A.9

.

regions of the gap at $\dot{\gamma} = 2.8$ and 4.6 s^{-1} and demonstrates shear-banding. At the highest concentration of 12% w/v, a solid body velocity profile is observed at $\dot{\gamma} = 0.9$ s^{-1}, which gives way to a larger yielded flow region and shear-banding at $\dot{\gamma} = 2.8$ and 4.6 s^{-1}, while the addition of 0.1 M NaCl causes a stronger solid body like flow with increased slip and strong bands of high and low shear.

Select transient velocity surface plots (Figure 5.5, top) and plots showing velocity at three positions across the gap (Figure 5.5, bottom) provide insight into the effect of 0.1 M NaCl salt on velocity fluctuations for 3%, 5%, and 12% w/v NCC suspensions at $\dot{\gamma} = 4.6$ s^{-1}. The addition of salt causes an increase in rotor velocity fluctuations for 3%, 5%, and 12% w/v. For 5% and 12% w/v, an increase in slip at the stator is also observed. Additionally, fluctuations at the middle of the fluid gap for 5% w/v appear to be damped in the suspension with 0.1 M NaCl. A significant increase in velocity fluctuations at the middle and the stator is also observed for 12% w/v with added salt. Additional transient data is available in the supplementary information in the Appendix, Figures A.1-A.9.

Discussion

Steady State Velocity Profiles

The steady state velocity data correlates with the NCC concentration and NaCl concentration phase transition diagram proposed by Stokes and co-workers [172–174]. The 3% w/v NCC data is in a viscous liquid phase for NaCl concentrations below 0.03 M and a viscoelastic liquid at higher salt concentrations [173]. The velocity data for 3% w/v NCC exhibits viscous liquid state velocity profiles at all shear rates and 0 and 0.1 M salt concentrations (Figure 5.4). At 5% w/v NCC and salt concentrations < 0.02 M a viscoelastic liquid phase is predicted [173] and slightly non-linear velocity profiles are observed. Addition of salt at 0.05 M is predicted to be on the boundary of a viscoelastic liquid to gel phase transition and at 0.1 M to be in a gel phase [173]. These phase transitions are evident in

the transition from a linear velocity profile for 0 M salt to a strong viscoelastic non-linear velocity profile at 0.05 M salt at $\dot{\gamma} = 0.9$ s^{-1}, which shear thins to a more linear velocity profile at higher shear rates $\dot{\gamma} = 2.8$ and 4.6 s^{-1}. At 0.1 M the velocity profiles exhibit yield stress behavior with an increasing sheared region near the rotor and enhanced stator slip as $\dot{\gamma}$ increases. The solid-like flow spatial region has increasing velocity with increasing radius across the gap at $\dot{\gamma} = 2.8$ and 4.6 s^{-1} consistent with solid body rotation and gel phase behavior (Figure 5.4). The 7% w/v NCC system is a viscoelastic liquid with no salt and a gel phase at 0.1 M NaCl [173]. The velocity profile data correlates exactly with this phase transition for all $\dot{\gamma}$. The 7% w/v NCC with 0.1 M salt data exhibits a transition with $\dot{\gamma}$ from a yield stress response at $\dot{\gamma} = 0.9$ s^{-1}, with a non-sheared solid body rotation region. As $\dot{\gamma}$ increases a shear banding behavior is observed with the higher shear region near the rotor having similar shear rate at 2.8 and 4.6 s^{-1} and a low shear region which occupies less of the gap and has a higher shear rate in the low shear region at $\dot{\gamma} = 4.6$ s^{-1}. At 12% w/v NCC glass phases are predicted with a repulsive glass with no salt and an attractive glass with 0.1 M NaCl [173]. The velocity data for 12% w/v NCC show regions of high shear near the rotor with the high shear region occupying more of the gap as $\dot{\gamma}$ increases, consistent with a glass phase under shear. The 0.1 M salt system exhibits greater stator slip and solid body rotation in comparison to the no salt sample in which a low shear rate band is formed. This is consistent with the no salt sample being a repulsive glass in which particles move relative to one another in cage breaking in the low shear region while the 0.1 M salt sample with attractive particle interactions has a particle network which is less disrupted.

As discussed earlier, Derjaguin–Landau–Verwey–Overbeek (DLVO) theory describes colloidal suspension physics and provides the basis for understanding NCC nanorod behavior, particularly in the presence of ionic species. From DLVO theory, it is known that the repulsive double layer associated with a colloid is shortened due to the screening effect of an oppositely charged ion (in this study, Na^+) on a colloidal particle (an NCC nanorod) [56,

80, 96, 108, 162]. This repulsive double layer is responsible for counteracting the attractive van der Waals forces which promote particle aggregation. The NCC nanorods in this study have sulfate groups (SO_4^{2-}) which impart a negative charge to the surface; when screened by positively charged Na^+) ions, the repulsive double layer will shorten and may allow van der Waals forces to increase particle attraction. This particle attraction causes closer groupings of nanorods [16, 174] and could exhibit an electrostatically stable, metastable, or time-dependent structure change from the conjugate non-ionic concentration. It has been reported that addition of salt can cause changes in helical structure of NCC liquid crystals [16, 58, 59, 174], alter the microstructure of NCC gel [16, 112, 172, 174], increase viscosity [16, 172, 174], decrease viscosity [16, 81, 112], cause complete aggregation with settling [81, 112, 172], and promote gelation from intermediate aggregation [16, 112, 172, 174], depending on the concentration and source of the NCC material as well as the concentration and valency of ionic species.

In this study, both rheometer and velocimetry experiments demonstrate a notable difference in samples with NaCl compared to their non-salt counterparts. An overall decreased viscosity is observed in rheometry data (Figure 5.3, right) with the addition of salt, indicating a loss of structure of the fluid and perhaps more liquid-like behavior. However, the velocimetry data tells a more nuanced story, as a significant increase in stator wall slip and regions of shear-banding can be seen for 5%, 7%, and 12% w/v at 0.1 M NaCl, indicating solid phase gel or glass-like flow behavior as discussed above. Additionally, the fluctuations in transient data (Figure 5.5, top and bottom) for 3%, 5%, and 12% w/v with added 0.1 M NaCl shows stick-slip behavior at $\dot{\gamma} = 4.6\ s^{-1}$ which also indicates gel or glass-like phase.

Velocity Fluctuations

Previously, Rheo-NMR velocimetry experiments on NCC from a different material source showed significant velocity fluctuations for a 5% w/v sample [149]. The details of these

findings and the discussion can be read elsewhere [149]. In brief, these velocity fluctuations are hypothesized to occur because of director fluctuations within the nematic liquid crystal structure, as the 5% w/v concentration is known to be a liquid crystal [88, 141, 149, 172]. For the purposes of this manuscript, it is useful to acknowledge that though the source material varies, the 5% w/v sample does indeed show significant velocity fluctuations similar to previous observations [149].

Of additional note, several other concentrations (3% w/v in 0.1 M NaCl, 5% w/v in 0.05 M NaCl, 5% w/v in 0.1 M NaCl, 7% w/v in 0.1 M NaCl, 12% w/v, and 12% w/v in 0.1 M NaCl) in this study exhibit velocity fluctuations with varied character. The fluctuations vary from only affecting the rotor, or the stator, or by affecting the entire fluid gap. Particularly curious is the periodic nature of the fluctuations, some of which appear to have strong correlation across the gap and throughout time (the full breadth of these can be observed in the Appendix, Figures A.1-A.9).

To summarize, velocity fluctuations occur with the 5% w/v liquid crystal concentration, the 12% w/v gel concentration, and all concentrations with salt. The addition of salt can have important effects on the stability of NCC suspensions and has been reported to change the measured viscosity and observed structure of NCC suspensions [16, 44, 58, 59, 81, 112, 123, 172, 174]. These fluctuations may indicate dynamic restructuring phenomenon and/or stick-slip behavior, depending on the time-scale, length-scale, and frequencies with which they occur. Further analysis of the data and future experiments including NMR diffusometry may help to elucidate such features of these fluctuations and the underlying microstructural behaviors which give rise to them.

Conclusion and Future Directions

This work has demonstrated that Rheo-NMR velocimetry correlates to NCC suspension liquid-solid phase transition behavior. Concentration-dependent phase-transitions have been

observed, along with fluctuations for the known 5% w/v liquid crystal concentration. Both phenomena are consistent with a previous study from our group [149], with other variations in behavior that can likely be attributed to the difference in source material [174]. Changes in liquid to solid phase, which have been theorized and observed [16, 81, 112, 123, 172] for the addition of ionic species to NCC suspensions have also been observed in this work, with signature changes in velocity profiles accompanied by velocity fluctuations with notable patterned frequencies.

Future works will focus on evaluating the timescale and correlation of velocities. Frequencies of correlation may provide insight into the microstructure of NCC suspensions [3, 28, 82], which could verify theorized structural phase transitions [172] for varying degrees of NCC and salt concentrations.

Acknowledgments

M.A.S. acknowledges the MSU ChBE for support from the Benjamin Fellowship and the Noble Family Fellowship. J.D.S. and S.L.C. acknowledge the M.J. Murdock Charitable Trust and the NSF MRI program for instrument funding. J.N.W. acknowledges the Army Research Office (Grant #W911NF-19-1-0288) and the NIH (Grant #R01 GM131408-01). Research reported in this publication was supported in part by the National Institute of General Medical Sciences of the National Institutes of Health under Award Number P20GM103474. The content is solely the responsibility of the authors and does not necessarily represent the official views of the National Institutes of Health.

RHEO-NMR VELOCIMETRY OF LAPONITE® NANOPARTICLE SUSPENSIONS

Contribution of Authors and Co-Authors

Manuscript in Chapter 6

Author: Maribelle A. Stanley

Contributions: Designed and performed experiments and formal analysis, wrote the initial manuscript, conceived concept, curated data, and reviewed/edited the manuscript.

Co-author: Jayesha S. Jayaratne

Contributions: Involved with data curation/analysis.

Co-author: Sarah L. Codd

Contributions: Performed data curation/analysis, supervised work, reviewed/edited the manuscript.

Co-author: James N. Wilking

Contributions: Provided funding, data analysis assistance and reviewed/edited manuscript.

Co-author: Joseph D. Seymour

Contributions: Wrote initial manuscript, conceived concept, designed experiments, curated data, performed analysis, supervised work, reviewed/edited manuscript.

Manuscript Information

Maribelle A. Stanley, Jayesha S. Jayaratne, Sarah L. Codd, James N. Wilking, Joseph D. Seymour

Status of Manuscript:
_X_ Prepared for submission to a peer-reviewed journal
____ Officially submitted to a peer-reviewed journal
____ Accepted by a peer-reviewed journal
____ Published in a peer-reviewed journal

Abstract

Laponite® ($Na_{0.7}Si_8Mg_{5.5}Li_{0.3}O_{20}(OH)_4$) is a synthetic, layered, smectite nanoclay which serves as a model for natural clay in research [124] and finds use in cosmetics, pharmaceuticals, food packaging, paints and coatings, and nanocomposites [9, 31, 38, 89, 91, 101, 143, 151, 161, 166]. Laponite® also forms unstable nanoscale structures which commonly undergo attractive or repulsive energetic restructuring, giving rise to aging and thixotropy. As the industrial relevance and application of Laponite® continues to grow, there is an increasing need to settle the contentious debate about the microstructural arrangement of aqueous Laponite®. This debate revolves around the existence of repulsive, double-layer Wigner glass state at concentrations near 4% w/v as opposed to an attractive gel network, or "house-of-cards" structure [87]. In this study, spatially resolved RheoNMR (nuclear magnetic resonance) velocimetry is used to probe the relationship between flow and microstructure for 2%, 3.2%, 4%, and 5% w/v aqueous Laponite® RD suspensions over the course of several days. The results demonstrate shear localization, stress fluctuations, and thixotropic behavior. They also provide insight into concentration and shear-dependent behavior, the aging process, and a structural transition occurring between 3-4% w/v. Future NMR diffusion experiments are discussed to provide more insight into the microstructure debate.

Introduction

Nanoclay suspensions have broad potential in applications as varied as medicine, agriculture, and oil and gas [50, 51, 106, 134, 151], but they can be difficult to process and handle. Laponite® ($Na_{0.7}Si_8Mg_{5.5}Li_{0.3}O_{20}(OH)_4$) is a synthetic, layered, smectite nanoclay of technological interest. Laponite® serves as a model for natural clay in research [124]. It also finds uses in cosmetics [31, 166], pharmaceuticals [31, 91, 151], food packaging

[9, 38, 101, 143], paints and coatings [31, 161], and nanocomposites [31, 89]. However, Laponite® forms unstable nanoscale structures and exhibits "peculiar properties" [47] which makes it the subject of both scientific debate and industrial processing interest.

Unstable nanoscale structures commonly undergo attractive or repulsive energetic restructuring over time which may be induced by perturbations from temperature or shear changes. This restructuring gives rise to observed behaviors, like aging and thixotropy, in many nanoclays including Laponite®. The connection between microstructure and rheological behavior is still an open area of research for many nanoparticulate materials of which nanoclays are no exception. Shear forces during processing of nanoparticulate materials interact with the microstructure and generate complex fluid behavior, which must be understood to control the microstructure for various applications.

As the industrial relevance and application of Laponite® continues to grow, there is an increasing need for more data to inform the debate about the glass and gel states and microstructural arrangement of aqueous Laponite® dispersions. Numerous studies [4, 5, 7, 26, 27, 86, 95, 126, 127, 130, 131, 157, 169] have been performed and commentaries published [26, 87] to elucidate the relationship between Laponite flow and microstructure, but a widespread consensus still does not exist. The debate revolves around the existence of a repulsive, double-layer Wigner glass state at concentrations above 4% w/v as opposed to an attractive gel network, or "house-of-cards" structure [87].

Spatially resolved velocimetry experiments using MRI have previously proved useful in elucidating the relationship between flow and microstructure in complex fluids [3, 29, 34, 35, 85]. MRI velocimetry experiments have been applied to bentonite clay suspensions [48] and to a 3.5% w/v Laponite® clay suspension in a steady state flow [25], but there lacks a comprehensive MRI velocimetry study during both transient and steady-state flows as a function of concentration and aging. Previous MRI velocimetry studies [25] have been performed in Couette sample cells of 2 cm gap size with a 50 mT/m gradient strength

providing hundreds of μm of spatial resolution. The data reported here was obtained with a Couette flow sample cell of 1 mm gap size and 1.5 T/m magnetic field gradients which provide spatial resolution of 58.6 μm. The sample cell provides a close approximation to a narrow gap, and the MRI spatial resolution offers the ability to observe shear localization, banding, and velocity fluctuations. Herein we present detailed MRI velocimetry data of salt-free Laponite® RD for transient and steady-state shear flows as a function of concentration and short-term aging over the timescale of days. Transient and steady-state 1D spatially-resolved velocity profiles indicate significant microstructure variation associated with varying levels of shear during aging in 3.2%, 4%, and 5% w/v aqueous Laponite® RD suspensions undergoing shear.

Rheometry with Laponite® RD suspensions

Traditional bulk rheometry techniques are problematic for nanoclays, like most complex fluids, because of the microscale heterogeneities associated with their layered and often unstable structures. These heterogeneities violate the viscometric assumption and make traditional rheological measurements unresolvable. Measurements of nanoclays with optical and spectroscopic techniques have provided complementary information to rheological measurements to characterize nanoclay behavior and couple it to microstructure [124, 126]. In particular, NMR relaxometry and diffusion has been used as a technique to characterize the structure of various nanoclays, including Laponite®, by analyzing water population distributions and transport [63, 70, 95]. Interest and contention about Laponite® rheology has existed for close to four decades, while interest about clay structure and flow has been of interest at least since the 1950s [163]. Bulk rheometry shows evidence for both an attractive gel [87] as well as a repulsive "glassy" state [4, 5, 26]; light-scattering techniques which have aimed to elucidate microstructure have similarly shown evidence for both potential structures [5, 131]. Various contradictory studies exist [4, 5, 7, 86, 87, 130, 131]. The general

consensus is that below 3% w/v, Laponite® dispersions form attractive, shear-thinning gels [87]. However, above 4% w/v, dispersions have been classified as either attractive gels or repulsive Wigner glasses [87]. There appears to be a structural transition point occurring between 3-4% w/v [4, 5, 87], which the MRI velocimetry data presented here supports. Reports of shear localization and shear-banding [25, 125], as well as fluctuations in stress [25, 46], have also been reported in various concentrations of aqueous Laponite® dispersions. The MRI velocimetry data presented here also demonstrates evidence to support shear localization, stress fluctuations, and the known thixotropic behavior of Laponite®.

Materials and Methods

Sample Preparation

The Laponite® RD systems investigated in this work are a series of aqueous suspensions ranging from 2.0% w/v to 5.0% w/v. Laponite® RD material was obtained from BYZ, Inc. (Gonzalez, TX). The samples were prepared by weighing the Laponite® RD powder and then gradually adding it to the appropriate amount of RO/DI water while stirring for approximately one hour until the suspension was clear. All suspensions were stored in a refrigerator (3 °C) before and after measurements.

Rheo-NMR Velocimetry

Velocimetry experiments were performed with a portable, home-built Rheo-NMR experimental system and methodology with well-established fluid flow measurement capabilities across a variety of length and time scales [3, 34, 35, 85]. The system includes an NMR-compatible, motor-powered driveshaft which rotates the inner rotor of a Couette shear cell, depicted in Figure 6. The shear cell has a 9 mm outer radius glass cylinder stator and 8 mm inner radius PEEK rotor, resulting in a fluid gap of 1 mm, and a radius ratio of 0.89. Samples were loaded into the shear cell and either briefly put under vacuum or sheared to eliminate

air bubbles. Pre-sheared samples were allowed at least 3 hours to relax before measurements were taken. Shear rates of $\dot{\gamma} = 0.9$, 2.8 and 4.6 s^{-1} were applied with a calibration fluid silicon oil (10,000 cSt) used to measure the actual velocity at the rotor to determine $\dot{\gamma}$.

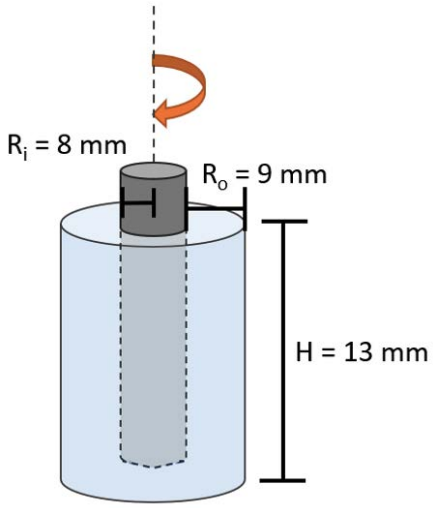


Figure 6.1: A schematic that depicts the Rheo-NMR sample Couette cell dimensions.

NMR measurements were taken with a Bruker AVANCE 300 spectrometer and 7 T superconducting super wide bore magnet equipped with a 25 mm birdcage resonator coil and a Micro-2.5 gradient system (providing a maximum gradient of 1.5 T/m at 60A). Bruker TopSpin 3.5pl7 software was used to acquire data with the spectrometer, while MATLAB (MathWorks, Inc., Natick, MA) and Prospa software (Magritek, Wellington, NZ) was used to analyze the data. A pulsed gradient spin echo (PGSE) pulse sequence (Figure 6.1) was used to acquire 1D velocity profiles. The PGSE pulse sequence encodes for magnetization phase, ϕ, where $\phi = \gamma \int g(t')t'dt' = \gamma g \delta \Delta$. Here, γ refers to the magnetogyric ratio (a material property), g the gradient amplitude, δ the gradient pulse durations and Δ the displacement observation time. The change in magnetization phases relate linearly to the change in spin positions, since the applied magnetic field gradient causes a linear spatial variation in the magnetic field, $\boldsymbol{G} = \nabla \boldsymbol{B}$, and a resulting change in the Larmor frequency

(or phase), $\omega_0 = \gamma\big[|\boldsymbol{B}| + \boldsymbol{r} \cdot \boldsymbol{G}\big]$. The PGSE pulse sequence was employed with double slice selection [29, 136].The slices used were a 1 mm thick slice in the flow direction (y) to eliminate curvature and provide $v_\theta(r)$ azimuthal radius dependent velocity directly over a 10 mm slice in the vertical direction (z) to provide and average more ^{1}H spins over the vorticity direction of the flow and increase signal to noise for two average 8 s acquisitions. Two gradient steps of equal duration ($\delta = 1$ ms) and magnitude but opposite sign were used as flow encoding gradients with amplitude ranging from 0.178 to 0.889 T/m dependent on shear rate induced velocity, which were separated by a displacement observation time of $\Delta = 11$ ms. The lateral direction (x) "read" gradients imaged the velocity with a 30 mm field of view using 512 points (58.6 µm resolution) across the diameter of the flow cell.

Steady state experiments used 16 scans (repetitions) of the two gradient flow encoding steps over a total acquisition time of 1 minute and 12 seconds, with the velocity measured representing an average velocity over this time. Unsteady state (start-up) experiments used 2 scans for a faster acquisition and acquired 75 independent velocity profiles averaged over 8.11 seconds each for a total shear duration of approximately 10 minutes and 12 seconds. This transient measurement minimizes the velocity averaging time but lowers the acquired voltage signal to noise ratio. Velocimetry experiments were performed with shear and without shear for each shear rate to provide a no flow control. This control allows for removal of phase shifts from background magnetization during data analysis. All results shown represent the difference in the phase between flow and no flow velocity profiles. This ensures that imperfections from magnetic gradient fields do not affect the result.

Results and Discussion

Results

Table 6.1: Rotor slip percentages for all $\dot{\gamma}$, days, and Laponite® concentrations

Shear rate [s^{-1}]	Day	2% w/v	3.2% w/v	4% w/v	5% w/v
0.9	1	2.55	-2.60	33.34	79.68
	2	-2.60	63.00	15.63	79.68
	3	6.20		8.34	1.51
	4			2.09	-7.87
	5		69.27		
2.8	1	1.57	0.51	65.35	72.36
	2	-1.44	55.78	64.34	83.42
	3	-2.51		51.79	60.81
	4			54.80	54.27
	5		50.28		
4.6	1	-0.88	0.65	68.92	64.32
	2	-0.37	41.88	63.83	84.20
	3	-0.94		72.47	72.47
	4			57.71	69.41
	5		38.86		

Table 6.2: Mean and % RMS of velocity at three gap positions for transient data, Day 1

Red font for standard deviation indicates greater than 20% over the respective Si oil value.

		2% w/v		3.2% w/v		4% w/v		5% w/v		10k cSt Si oil	
		μ [mm/s]	σ [mm/s]	μ [mm/s]	σ [mm/s]	μ [mm/s]	σ [mm/s]	μ [mm/s]	σ [mm/s]	μ [mm/s]	σ [mm/s]
Shear rate [s^{-1}]	Position										
0.9	Rotor	0.89	0.04	0.92	0.06	0.58	0.05	0.07	0.09	0.88	0.04
	Middle	0.46	0.02	0.45	0.05	0.61	0.05	0.01	0.03	0.46	0.02
	Stator	0.00	0.01	0.01	0.02	0.64	0.05	0.01	0.02	0.04	0.01
2.8	Rotor	2.78	0.22	2.83	0.25	0.72	0.11	0.34	0.57	2.75	0.23
	Middle	1.42	0.06	1.28	0.16	0.68	0.08	-0.30	0.93	1.44	0.12
	Stator	0.00	0.02	-0.03	0.07	0.75	0.07	0.03	0.14	0.13	0.03
4.6	Rotor	4.66	0.29	4.66	0.31	0.78	0.15	0.50	0.13	4.62	0.32
	Middle	2.43	0.09	2.43	0.20	0.82	0.12	0.11	0.11	2.42	0.17
	Stator	0.00	0.03	0.29	0.06	0.81	0.12	0.08	0.09	0.20	0.07

Table 6.3: Mean and % RMS of velocity at three gap positions for transient data, Day 2

Red font for standard deviation indicates greater than 20% over the respective Si Oil value.

		2% w/v		3.2% w/v		4% w/v		5% w/v		10k cSt Si oil	
		μ [mm/s]	σ [mm/s]	μ [mm/s]	σ [mm/s]	μ [mm/s]	σ [mm/s]	μ [mm/s]	σ [mm/s]	μ [mm/s]	σ [mm/s]
Shear rate [s^{-1}]	Position										
0.9	Rotor	0.88	0.05	0.07	0.05	0.71	0.04	0.17	0.04	0.88	0.04
	Middle	0.45	0.02	-0.01	0.03	0.75	0.03	0.14	0.03	0.46	0.02
	Stator	0.04	0.02	0.00	0.01	0.79	0.03	0.15	0.02	0.04	0.01
2.8	Rotor	2.88	0.30	0.28	0.12	0.91	0.10	0.48	0.10	2.75	0.23
	Middle	1.38	0.08	-0.02	0.08	0.86	0.09	0.32	0.08	1.44	0.12
	Stator	0.01	0.08	0.01	0.07	0.94	0.08	0.34	0.07	0.13	0.03
4.6	Rotor	4.54	0.27	0.80	0.17	1.12	0.15	0.74	0.14	4.62	0.32
	Middle	2.35	0.10	0.00	0.11	1.03	0.13	0.48	0.10	2.42	0.17
	Stator	0.20	0.09	0.04	0.11	1.03	0.12	0.60	0.11	0.20	0.07

Table 6.4: Mean and % RMS of velocity at three gap positions for transient data, Day 3

Red font for standard deviation indicates greater than 20% over the respective Si oil value.

		2% w/v		4% w/v		5% w/v		10k cSt Si oil	
		μ [mm/s]	σ [mm/s]	μ [mm/s]	σ [mm/s]	μ [mm/s]	σ [mm/s]	μ [mm/s]	σ [mm/s]
Shear rate [s^{-1}]	Position								
0.9	Rotor	0.87	0.05	0.77	0.05	0.80	0.05	0.88	0.04
	Middle	0.43	0.02	0.81	0.04	0.84	0.04	0.46	0.02
	Stator	0.03	0.01	0.86	0.03	0.89	0.04	0.04	0.01
2.8	Rotor	2.72	0.24	1.04	0.10	1.15	0.11	2.75	0.23
	Middle	1.36	0.10	1.01	0.08	1.10	0.12	1.44	0.12
	Stator	0.10	0.05	1.06	0.08	1.16	0.12	0.13	0.03
4.6	Rotor	4.56	0.30	1.30	0.15	1.25	0.14	4.62	0.32
	Middle	2.32	0.13	1.02	0.11	1.21	0.13	2.42	0.17
	Stator	0.19	0.09	1.17	0.11	1.27	0.16	0.20	0.07

Table 6.5: Mean and % RMS of velocity at three gap positions for transient data, Day 4

Red font for standard deviation indicates greater than 20% over the respective Si oil value.

		4% w/v		5% w/v		10k cSt Si oil	
		μ [mm/s]	σ [mm/s]	μ [mm/s]	σ [mm/s]	μ [mm/s]	σ [mm/s]
Shear rate [s^{-1}]	Position						
0.9	Rotor	0.81	0.05	0.90	0.05	0.88	0.04
	Middle	0.85	0.04	0.95	0.04	0.46	0.02
	Stator	0.89	0.03	1.00	0.04	0.04	0.01
2.8	Rotor	1.09	0.10	1.38	0.15	2.75	0.23
	Middle	1.03	0.09	1.34	0.16	1.44	0.12
	Stator	1.12	0.08	1.36	0.16	0.13	0.03
4.6	Rotor	1.44	0.14	1.55	0.16	4.62	0.32
	Middle	0.96	0.12	1.35	0.12	2.42	0.17
	Stator	1.20	0.11	1.45	0.12	0.20	0.07

Table 6.6: Mean and % RMS of velocity at three gap positions for transient data, Day 5

Red font for standard deviation indicates greater than 20% over the respective Si oil value.

		3.2% w/v		10k cSt Si oil	
		μ [mm/s]	σ [mm/s]	μ [mm/s]	σ [mm/s]
Shear rate [s^{-1}]	Position				
0.9	Rotor	0.08	0.05	0.88	0.04
	Middle	0.02	0.03	0.46	0.02
	Stator	0.02	0.02	0.04	0.01
2.8	Rotor	0.93	0.34	2.75	0.23
	Middle	0.05	0.07	1.44	0.12
	Stator	0.03	0.06	0.13	0.03
4.6	Rotor	0.89	0.18	4.62	0.32
	Middle	0.12	0.09	2.42	0.17
	Stator	0.04	0.10	0.20	0.07

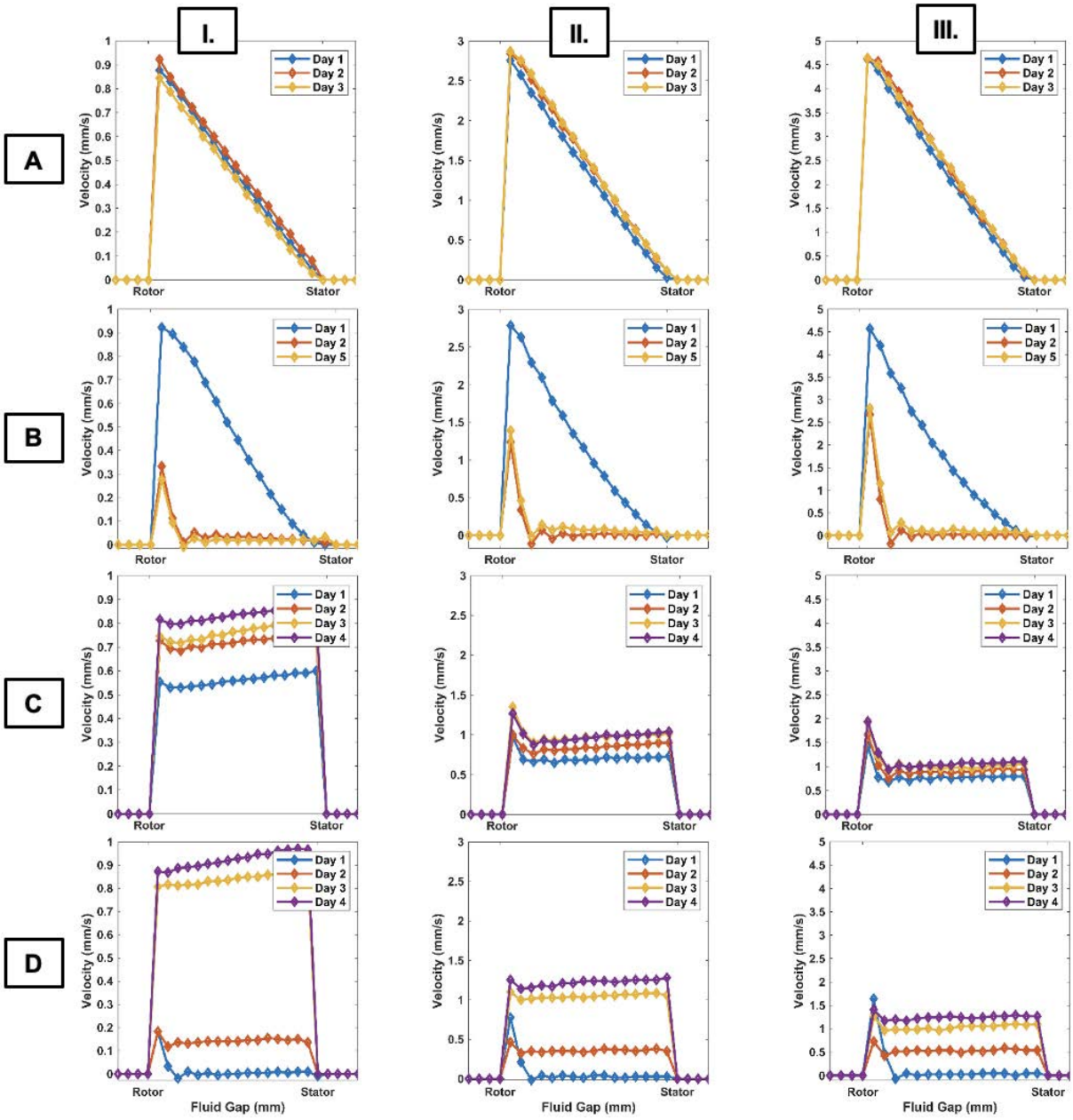


Figure 6.2: Rows A-D, Columns I-III. 1D NMR steady-state velocimetry experiments for several concentrations of Laponite® RD suspensions over multiple days, with 16 scans and total time of acquisition of 1 minute, 12 seconds and a pixel resolution of 58.6 µm. Rows A: 2% w/v; B: 3.2% w/v; C: 4% w/v; D: 5% w/v. Columns I. Shear rate of $\dot{\gamma} = 0.9$ s^{-1}; II. Shear rate of $\dot{\gamma} = 2.8$ s^{-1}; III. Shear rate of $\dot{\gamma} = 4.6$ s^{-1}. Rotor and stator data points are approximately 58.6 µm from the physical walls.

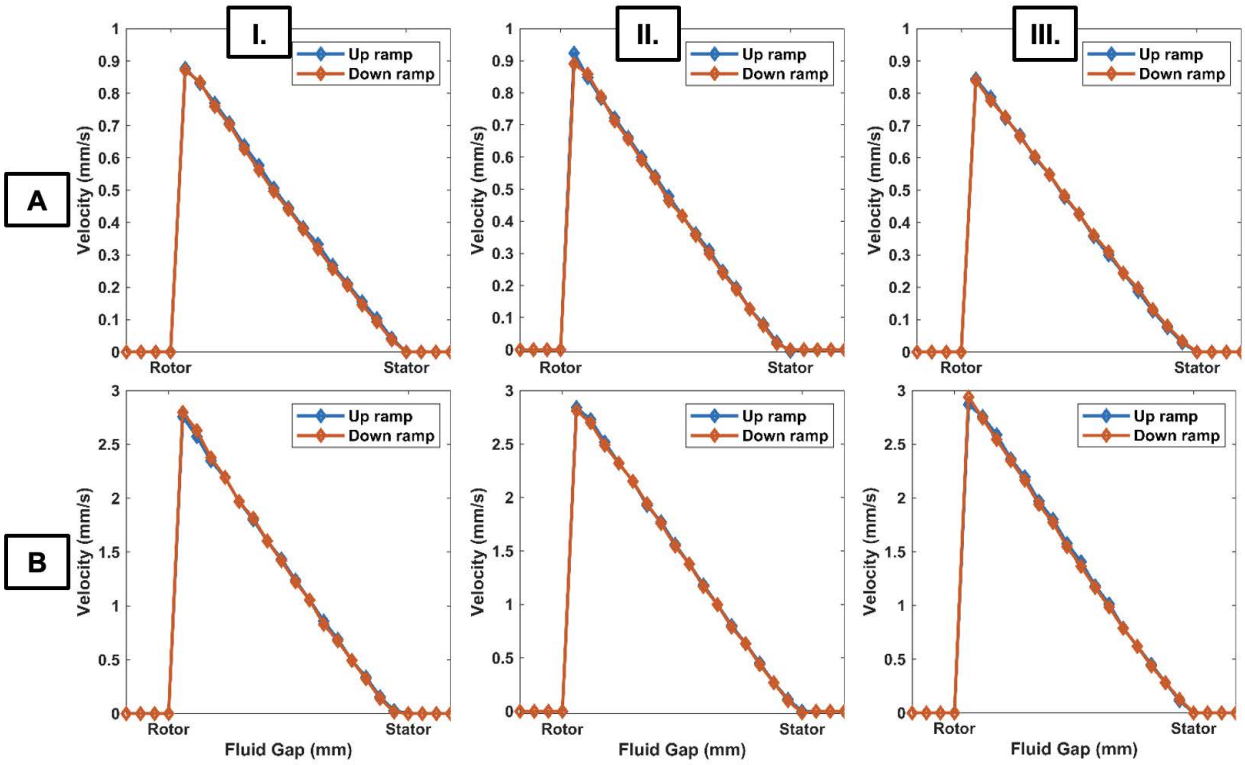


Figure 6.3: Rows A-B, Columns I-III. 1D NMR velocimetry experiments for 2.0% w/v Laponite® RD, with 16 scans and total time of acquisition of 1 minute, 12 seconds and a pixel resolution of 58.6 µm, shown with up ramp and down ramp overlaid for shear rates of $\dot{\gamma} = 0.9$ s^{-1} and $\dot{\gamma} = 2.8$ s^{-1} for multiple days. Rows A: Shear rate of $\dot{\gamma} = 0.9$ s^{-1}; B: Shear rate of $\dot{\gamma} = 2.8$ s^{-1}. Columns I. Day 1; II. Day 2; III. Day 3. Rotor and stator data points are approximately 58.6 µm from the physical walls. The data shows no hysteresis for the 2.0% w/v suspension.

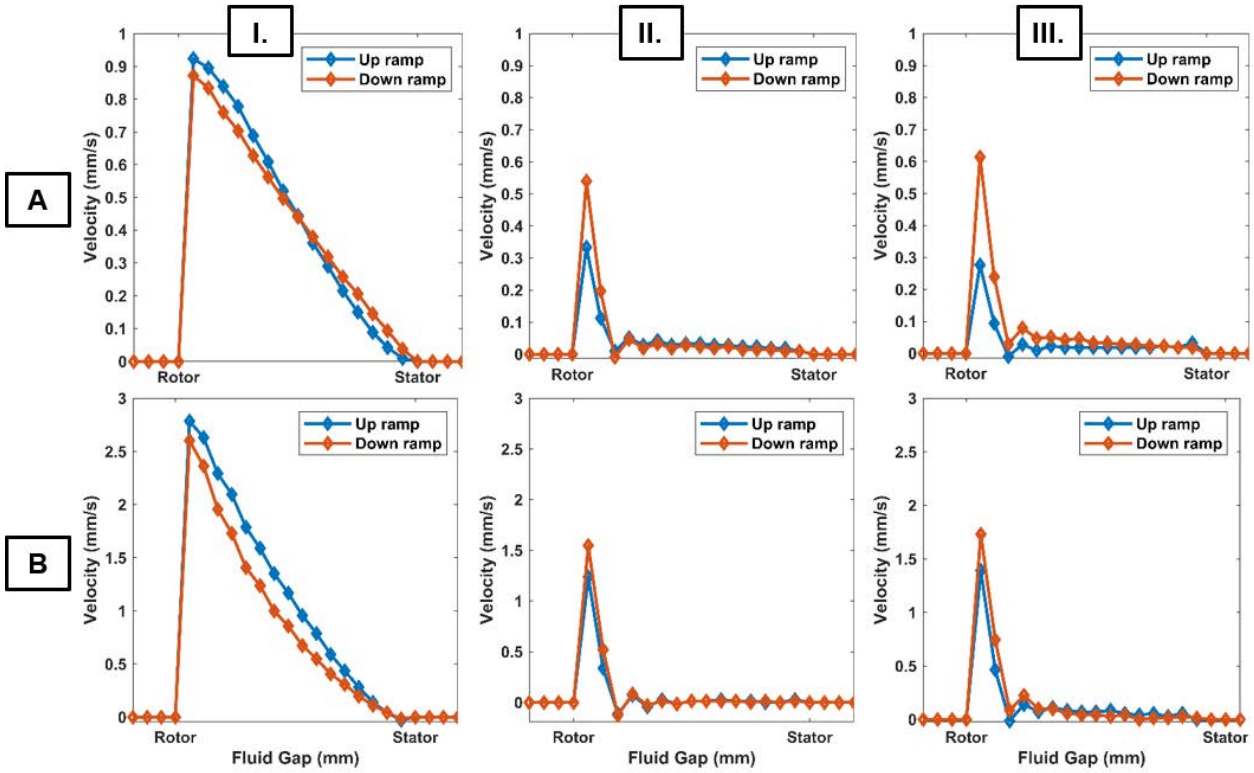


Figure 6.4: Rows A-B, Columns I-III. 1D NMR velocimetry experiments for 3.2% w/v Laponite® RD, with 16 scans and total time of acquisition of 1 minute, 12 seconds and a pixel resolution of 58.6 µm, shown with up ramp and down ramp overlaid for shear rates of $\dot{\gamma} = 0.9$ s^{-1} and $\dot{\gamma} = 2.8$ s^{-1} for multiple days. Rows A: Shear rate of $\dot{\gamma} = 0.9$ s^{-1}; B: Shear rate of $\dot{\gamma} = 2.8$ s^{-1}. Columns I. Day 1; II. Day 2; III. Day 5. Rotor and stator data points are approximately 58.6 µm from the physical walls. The data shows obvious hysteresis on day 1 at $\dot{\gamma} = 0.9$ and 2.8 s^{-1} by the change in curvature of the velocity profiles, as well as a reduction in slip for the down-ramp at $\dot{\gamma} = 0.9$ s^{-1} on days 2 and 3.

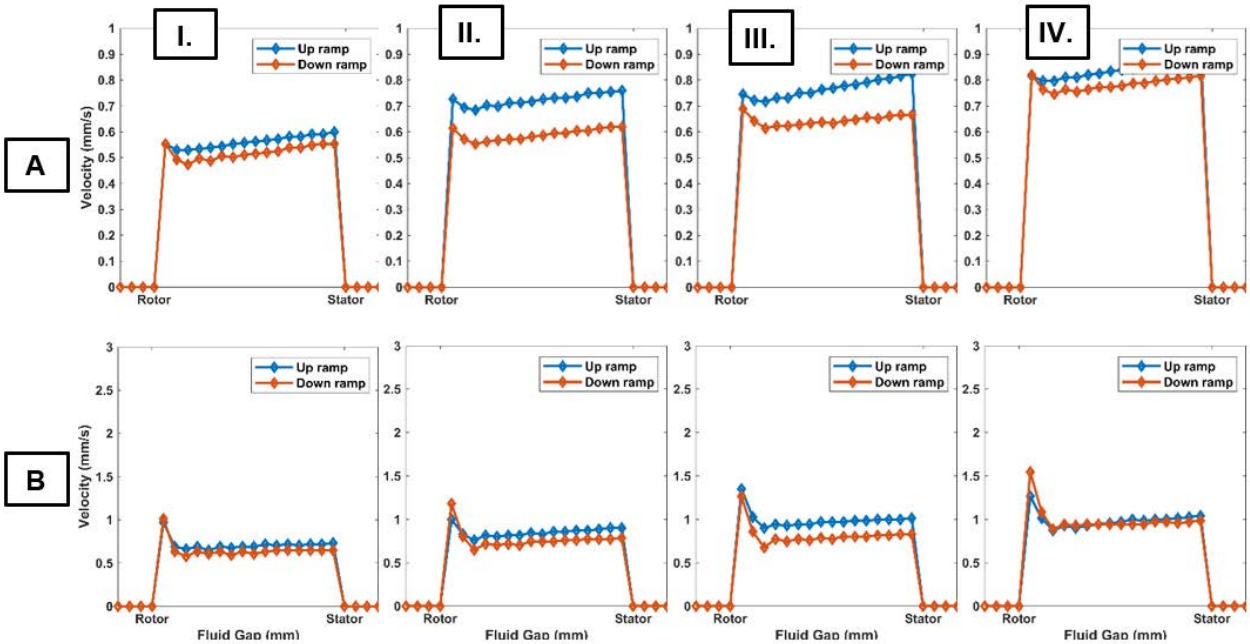


Figure 6.5: Rows A-B, Columns I-IV. 1D NMR velocimetry experiments for 4.0% w/v Laponite® RD, with 16 scans and total time of acquisition of 1 minute, 12 seconds and a pixel resolution of 58.6 µm, shown with up ramp and down ramp overlaid for shear rates of $\dot{\gamma} = 0.9\ s^{-1}$ and $\dot{\gamma} = 2.8\ s^{-1}$ for multiple days. Rows A: Shear rate of $\dot{\gamma} = 0.9\ s^{-1}$; B: Shear rate of $\dot{\gamma} = 2.8\ s^{-1}$. Columns I. Day 1; II. Day 2; III. Day 3; IV. Day 4. Rotor and stator data points are approximately 58.6 µm from the physical walls. The data shows a notable increase in slip during the down ramp relative to the up ramp for all days at $\dot{\gamma} = 0.9\ s^{-1}$, which is most drastic on day 2 and narrows by day 4. A similar phenomenon is seen for $\dot{\gamma} = 3\ s^{-1}$, where an increase in slip is observed in the down ramp; the slip continues to increase until day 4, where then minimal hysteresis is observed.

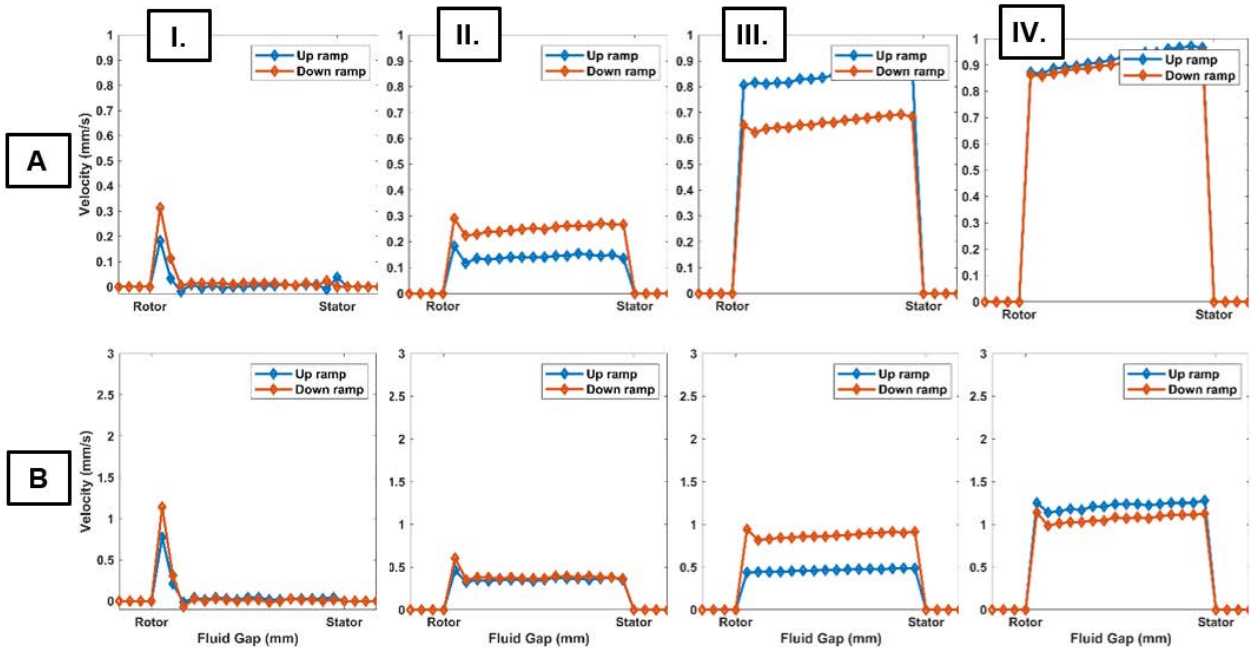


Figure 6.6: Rows A-B, Columns I-IV. 1D NMR velocimetry experiments for 5.0% w/v Laponite® RD, with 16 scans and total time of acquisition of 1 minute, 12 seconds and a pixel resolution of approximately 58.6 µm, shown with up ramp and down ramp overlaid for shear rates of $\dot{\gamma} = 0.9$ s^{-1} and $\dot{\gamma} = 2.8$ s^{-1} for multiple days. Rows A: Shear rate of $\dot{\gamma} = 0.9$ s^{-1}; B: Shear rate of $\dot{\gamma} = 2.8$ s^{-1}. Columns I. Day 1; II. Day 2; III. Day 3; IV. Day 4. Rotor and stator data points are approximately 58.6 µm from the physical walls. The data shows a decrease in slip during the down ramp relative to the up ramp for days 1 and 2 at $\dot{\gamma} = 0.9$ s^{-1}, a trend which is reversed for day 3, with no hysteresis observed on day 4. Little to no hysteresis is observed for days 1 and 2 at $\dot{\gamma} = 2.8$ s^{-1}, but a decrease in slip is observed on day 3 for the down ramp relative to the up ramp, which contradicts the phenomenon seen at $\dot{\gamma} = 0.9$ s^{-1} on day 3. The trend reverses for day 4 at $\dot{\gamma} = 2.8$ s^{-1}, where the down ramp exhibits a slight increase in slip.

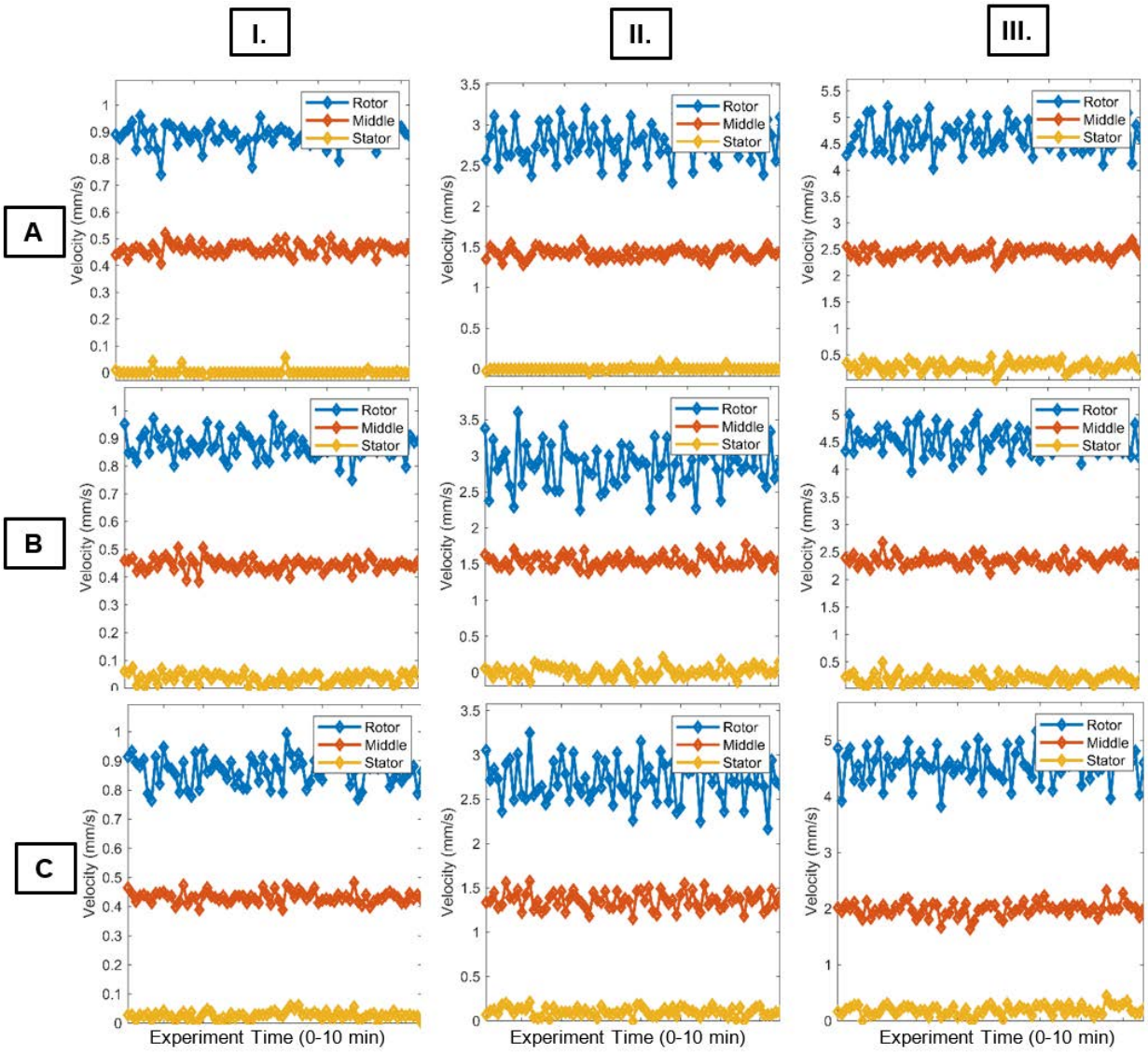


Figure 6.7: Rows A-C, Columns I-III. 1D NMR velocity profiles from unsteady-state experiments over several days for 2% w/v Laponite® RD with 75 experiments averaged over 2 scans and total time of acquisition of approximately 10 minutes, 12 seconds. The data is displayed at three discrete positions across the 1 mm sample Couette cell fluid gap (rotor, middle, and stator) for all time points, which demonstrates velocity changes across the experiment time and the fluid gap. Rows A: Day 1; B: Day 2; C: Day 3. Columns I: Shear rate of $\dot{\gamma} = 0.9$ s^{-1}. II: Shear rate of $\dot{\gamma} = 2.8$ s^{-1}. III. Shear rate of $\dot{\gamma} = 4.6$ s^{-1}. Rotor and stator data points are 58.6 µm from the physical walls. The data presents an equal separation of velocities across the gap, with relative standard deviations for each position similar to what is expected for instrument noise with a silicone oil control, indicating Newtonian-like behavior.

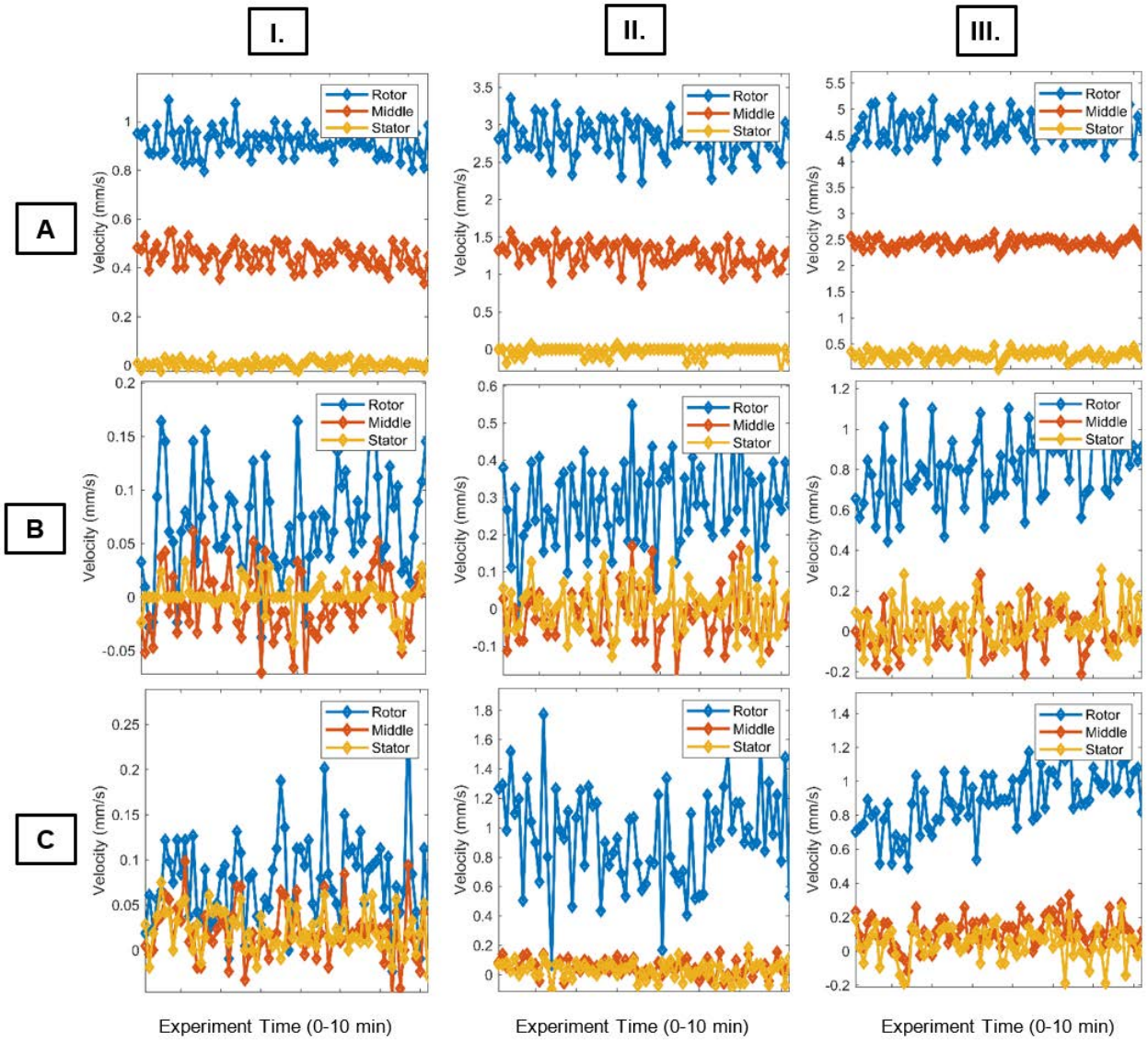


Figure 6.8: Rows A-C, Columns I-III. 1D NMR velocity profiles from unsteady-state experiments over several days for 3.2% w/v Laponite® RD with 75 experiments averaged over 2 scans and total time of acquisition of approximately 10 minutes, 12 seconds. The data is displayed at three discrete positions across the 1 mm sample Couette cell fluid gap (rotor, middle, and stator) for all time points, which demonstrates velocity changes across the experiment time and the fluid gap. Rows A: Day 1; B: Day 2; C: Day 5. Columns I: Shear rate of $\dot{\gamma} = 0.9\ s^{-1}$. II: Shear rate of $\dot{\gamma} = 2.8\ s^{-1}$. III. Shear rate of $\dot{\gamma} = 4.6\ s^{-1}$. Rotor and stator data points are 58.6 µm from the physical walls. The data demonstrates long-term temporal changes, where day 1 exhibits Newtonian-like behavior, and successive days indicate dynamic restructuring with extreme slip and standard deviations at each fluid gap position larger than expected for instrument noise.

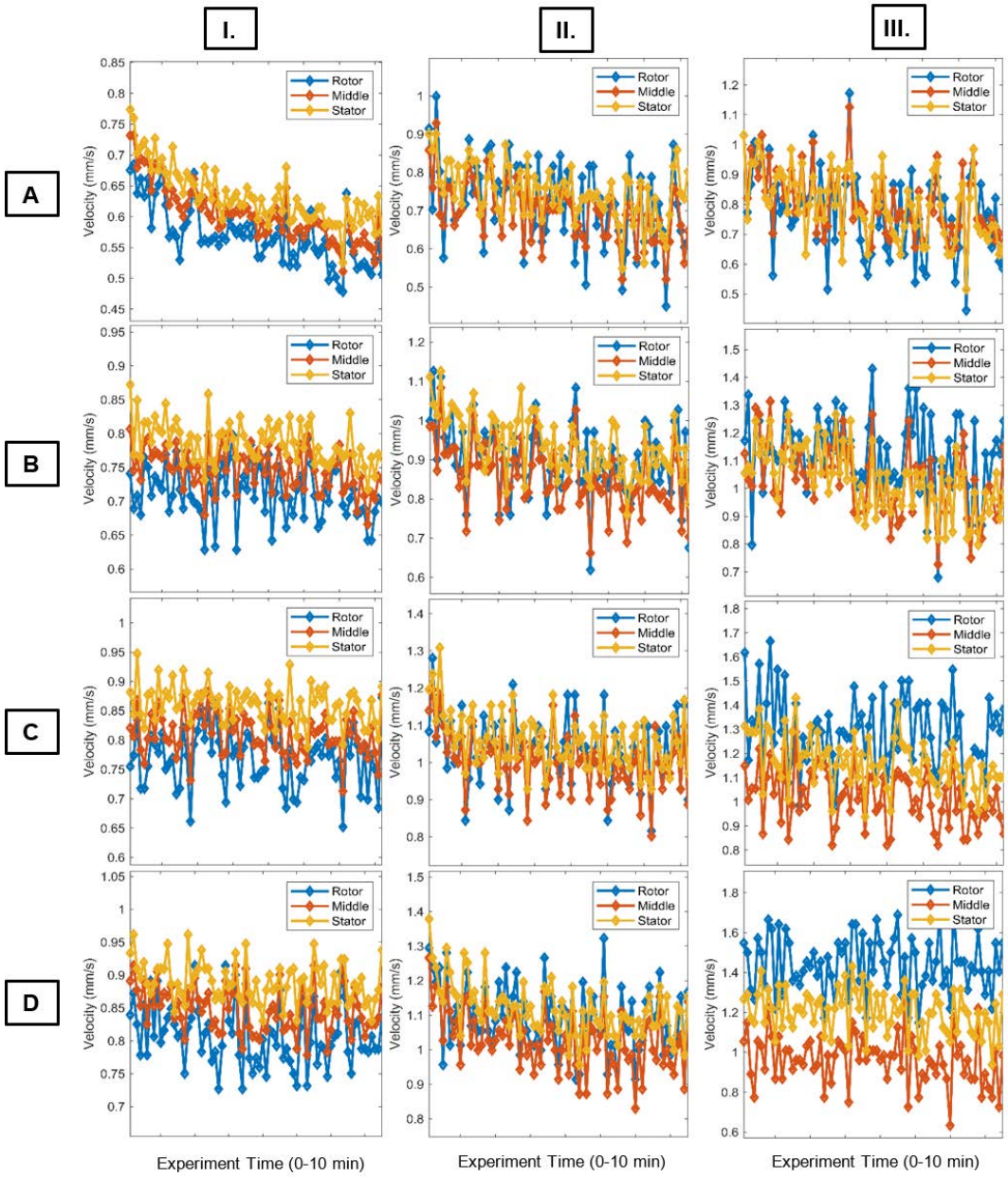


Figure 6.9: Rows A-D, Columns I-III. 1D NMR velocity profiles from unsteady-state experiments over several days for 4.0% w/v Laponite® RD with 75 experiments averaged over 2 scans and total time of acquisition of approximately 10 minutes, 12 seconds. The data is displayed at three discrete positions across the 1 mm sample Couette cell fluid gap (rotor, middle, and stator) for all time points, which demonstrates velocity changes across the experiment time and the fluid gap. Rows A: Day 1; B: Day 2; C: Day 4; D: Day 5. Columns I: Shear rate of $\dot{\gamma} = 0.9$ s^{-1}. II: Shear rate of $\dot{\gamma} = 2.8$ s^{-1}. III. Shear rate of $\dot{\gamma} = 4.6$ s^{-1}. Rotor and stator data points are 58.6 µm from the physical walls. The data demonstrates extreme slip and solid-body rotation indicative of a gel structure for all days, with velocity fluctuations greater than expected for instrument noise.

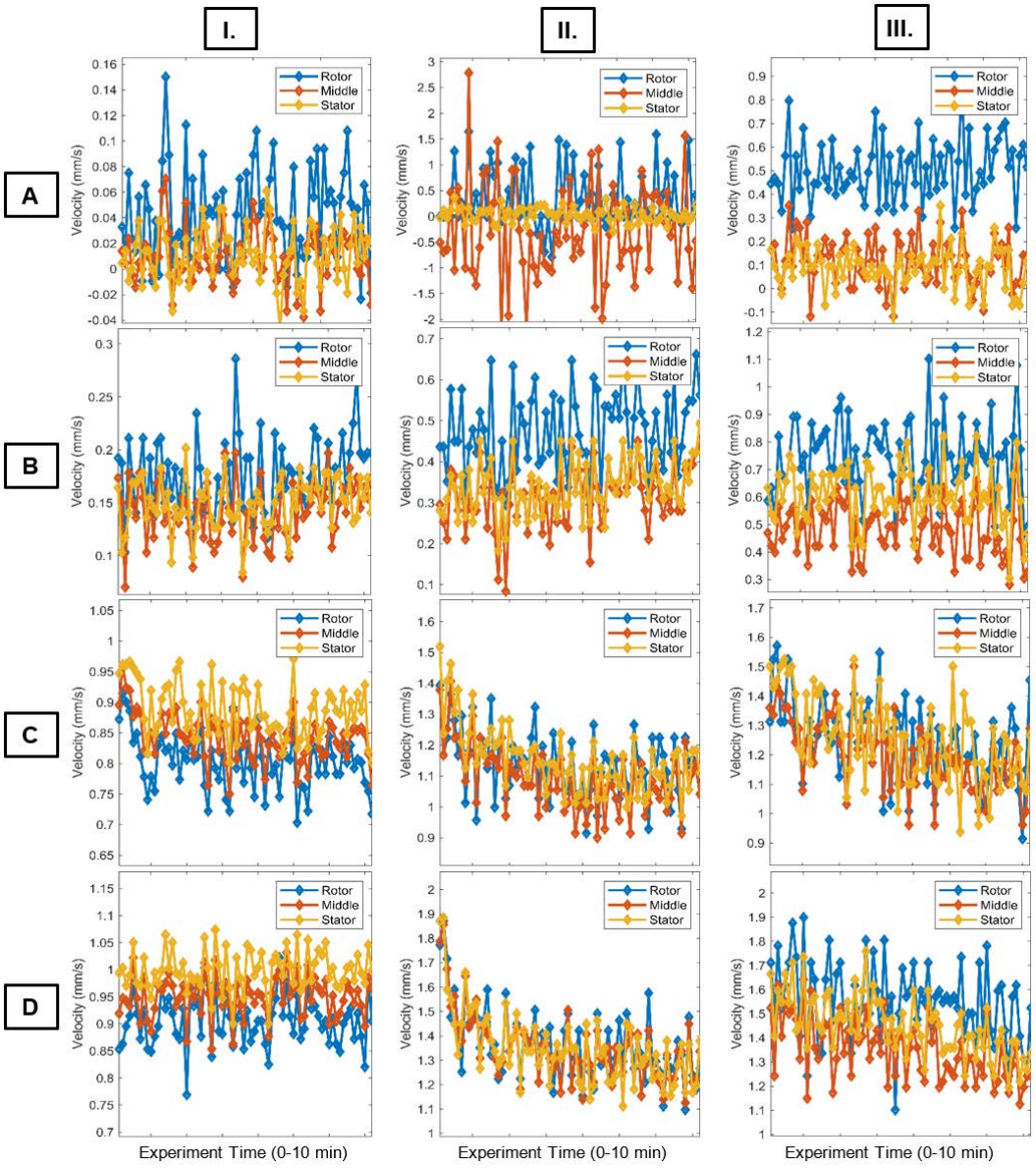


Figure 6.10: Rows A-D, Columns I-III. 1D NMR velocity profiles from unsteady-state experiments over several days for 5.0% w/v Laponite® RD with 75 experiments averaged over 2 scans and total time of acquisition of approximately 10 minutes, 12 seconds. The data is displayed at three discrete positions across the 1 mm sample Couette cell fluid gap (rotor, middle, and stator) for all time points, which demonstrates velocity changes across the experiment time and the fluid gap. Rows A: Day 1; B: Day 2; C: Day 4; D: Day 5. Columns I: Shear rate of $\dot{\gamma} = 0.9\ s^{-1}$. II: Shear rate of $\dot{\gamma} = 2.8\ s^{-1}$. III. Shear rate of $\dot{\gamma} = 4.6\ s^{-1}$. Rotor and stator data points are 58.6 µm from the physical walls. The data demonstrates long-term temporal changes, where day 1 exhibits Newtonian-like behavior, and successive days indicate dynamic restructuring with extreme slip and standard deviations at each fluid gap position larger than expected for instrument noise.

The 2% w/v sample depicts near-perfect Newtonian behavior, as evidenced by the linear velocity profiles without slip in the steady-state experiments (Figure 6.2) and the constant velocities across the Couette cell gap in transient experiments (6.7) for all shear rates $\dot{\gamma}$ = 0.9, 2.8, 4.6 s^{-1}. Mean, $\mu = \langle v \rangle$, and standard deviation of velocity, $\sigma = \langle v'^2 \rangle^{1/2}$ are shown in Tables 6-8 for all three gap positions and shear rates. The standard deviations for transient experiments (Figure 6.7) also align with that of silicone oil, a standard Newtonian control (Tables 6.2-6.6) for day 1, with minimal deviation for days 2 and 3. This indicates no velocity fluctuations beyond that expected as instrument noise. Additionally, hysteresis experiments for the 2% w/v indicate that the sample does not exhibit thixotropy (Figure 6.3).

The 3.2% w/v sample exhibits a marked transition between day 1 and day 2 in both steady-state (Figure 6.2) and transient experiments (Figure 6.8). This observation is in line with recent experiments which indicate a glass-glass transition around 3% w/v [4, 5]. Steady-state experiments (Figure 6.2) show a slightly nonlinear velocity profile on day 1 across $\dot{\gamma}$ = 0.9, 2.8, 4.6 s^{-1} that indicates potential shear-thinning viscoelastic behavior. This behavior is expected at this concentration prior to aging [87]. Day 2 and 5 steady-state experiments show a dramatic change in the velocity profile, with a localized region of shearing and extreme slip at the rotor for all shear rates $\dot{\gamma}$ = 0.9, 2.8, 3.6 s^{-1}, and slip velocity relative to rotor velocity decreasing with increasing $\dot{\gamma}$. The data shows an extreme slip combined with a severely decreasing slope over a 100-200 µm region near the rotor that is sheared. This behavior has been observed in bentonite clay suspensions and a 3.5% w/v Laponite® clay suspension aged for 3 hours [25, 48] in a large gap system with spatial resolution approximately an order of magnitude less than here. The steady-state variations with position occurring at low velocity values, which have not been seen in other studies, may be visible because of the increased resolution for the experiments performed in this study. Such spatial variations across the gap have also been seen for a foam system [135] which is also considered a "soft glassy material".

The extreme slip (slip % = $\frac{V_{measurd}-V_{rotor}}{V_{rotor}} \times 100\%$) and change in slope accompanied by oscillations at low velocities indicate shear localization and stick-slip behavior across the gap. The transient data (Figure 6.8) indicates nearly Newtonian behavior for day 1 at all shear rates $\dot{\gamma} = 0.9, 2.8, 4.6\ s^{-1}$, evidenced by the constant velocity values across the gap and values of velocity standard deviation σ only slightly greater than expected for Newtonian standard velocity values. Days 2 and 5 show erratic velocity behavior at all shear rates. At $\dot{\gamma} = 0.9\ s^{-1}$, rotor, middle, and stator positions exhibit closer mean values (Day 2: 0.07, -0.01, 0.00 mm/s respectively; Day 5: 0.08, 0.02, 0.02 mm/s) relative to each other than day 1 (0.92, 0.45, 0.01 mm/s and standard deviations (Day 2: 0.05, 0.03, 0.01 mm/s; Day 5 0.05, 0.03, 0.02 mm/s) larger than those expected from instrument noise (0.04, 0.02, 0.01 mm/s). Shear rates of $\dot{\gamma} = 2.8$ and $4.6\ s^{-1}$ begin to show a separation of the mean value for the rotor from those of the middle and stator, which corresponds to the observation in steady-state experiments (Figure 6.2) that the slip decreases as shear rate increases. The increased transient velocity standard deviations for days 2 and 5 are indicative of velocity fluctuations. Such fluctuations could explain the microstructural arrangements occurring during the so-called "glass-glass transition", wherein the attractive gel configuration restructures to form either an attractive gel with more repulsive interactions ("attractive glass"), or a repulsive Wigner glass. Hysteresis experiments (Figure 6.4) depict thixotropy at all shear rates $\dot{\gamma} = 0.9, 2.8, 4.6\ s^{-1}$ for all days examined, where the curve of the velocity profile is altered in the down ramp profile (Figure 6.4AI-II, Figure 5.3AI-II and 6.4BI-II) or otherwise slip has decreased (6.4AII and 6.4AIII). The thixotropic effect is less apparent for days 2 and 5 at $\dot{\gamma} = 2.8\ s^{-1}$ than for day 1 at $\dot{\gamma} = 2.8\ s^{-1}$, and all days at $\dot{\gamma} = 0.9\ s^{-1}$.

The steady-state data for the 4% w/v sample (Figure 6.2C) shows solid-body rotation, indicated by increasing velocity with increasing gap position, with significant slip for the lowest shear rate $\dot{\gamma} = 0.9\ s^{-1}$, and slip decreasing (average velocity increasing) as aging progresses from day 1 to day 4. Higher shear rates, $\dot{\gamma} = 2.8$ and $4.6\ s^{-1}$, show shear

localization as the plug-like flow separates into a faster flowing band of 100-200 µm thickness as in the 3.2 % w/v system and a solid-body rotation region. The effect is more dramatic at the highest shear rate. The solid-body rotation indicates that the sample formed a solid structure, and the change in profile shape signifies yielding and restructuring behavior. The transient data for the 4% w/v sample shows a progressive increase in slip for most days and shear rates as overall velocity decreases at all positions along the gap (Figure 6.9). There are obvious fluctuations with velocity standard deviation (Tables 6.2-6.5) above that expected from instrument noise, indicating restructuring behavior at the timescale of the transient experiments. For days 3 and 4 at $\dot{\gamma} = 4.6$ s^{-1} (Figures 6.9CIII and 6.9DIII), although steady-state experiments do not appear to have changed from the solid-body rotation at the previous shear rate $\dot{\gamma} = 2.8$ s^{-1}, the transient experiments show the velocity values which coincided at all three positions across the gap begin to vary from one another. This behavior is most dramatic for day 4, $\dot{\gamma} = 4.6$ s^{-1}. Hysteresis data for the 4.0% w/v sample shows thixotropic behavior for all days and both shear rates $\dot{\gamma} = 0.9$ and 2.8 s^{-1}, with greater slip for the down ramp relative to the up ramp, and slip decreasing overall from days 1-4. Days 1 and 4 exhibit the least thixotropy for both $\dot{\gamma} = 0.9$ and 2.8 s^{-1}, with nearly no thixotropic effect observed for $\dot{\gamma} = 2.8$ s^{-1}.

The 5% w/v steady-state profiles exhibit significant slip velocity for days 1 and 2 at all shear rates, $\dot{\gamma} = 0.9$, 2.8, 4.6 s^{-1} (Figure 6.2D). Interestingly, day 1 shows strong shear localization in a high velocity band of 100-200 µm thickness near the rotor, similar to the 3.2% w/v sample on days 2 and 5 (Figure 6.2B). Additionally, like the 3.2% w/v sample, the 5% w/v sample also experiences an increase in banding as the shear rate is increased. The 5% w/v sample shows oscillations at lower velocity values, though less dramatic than the 3.2% w/v sample. Day 2 exhibits large slip velocity but shows a transition to solid-body rotation at all shear rates $\dot{\gamma} = 0.9$, 2.8, 4.6 s^{-1} (Figure 6.10B). Slip decreases overall as aging progresses, and days 3 and 4 display a solid-body rotation behavior (Figure 6.10C and D) for

all three shear rates $\dot{\gamma} = 0.9, 2.8, 4.6\ s^{-1}$. Though little slip is observed at $\dot{\gamma} = 0.9\ s^{-1}$ (Figure 6.10I), higher shear rates, $\dot{\gamma} = 2.8$ and $4.6\ s^{-1}$, show large slip velocity (Figure 6.10II and 6.10III). This slip is not accompanied by yielding or shear localization, in contrast to what was observed for the 4% w/v sample at the same shear rates (Figure 6.9II and 6.9III). The transient data for day 1 at $\dot{\gamma} = 0.9\ s^{-1}$ (Figure 6.10AI) exhibits dramatic velocity fluctuations ($\sigma = 0.09, 0.03, 0.02$ mm/s) predominantly at the rotor. This behavior, which corresponds to the steady-state velocity profile in Figure 6.2D, shows that fast restructuring dynamics underlay the solid body rotation. Shear rates of $\dot{\gamma} = 2.8$ and $4.6\ s^{-1}$ (Figures 6.10II and 6.10III) also exhibit velocity fluctuations which are notably larger in the middle of the gap. Solid-body rotation and yielding behavior are both apparent in transient profiles, while an increase in slip at later times is observed at higher shear rates, $\dot{\gamma} = 2.8$ and $4.6\ s^{-1}$, for days 3 and 4 (Figures 6.10CII-III and 6.10DI-III). Hysteresis data for 5% w/v (Figure 6.6) shows very slight thixotropy on day 1 for $\dot{\gamma} = 0.9$ and $2.8\ s^{-1}$ (Figures 6.6AI and 6.6BI), and day 2 for $\dot{\gamma} = 2.8\ s^{-1}$ (Figure 6.6BII), but later days show large changes in slip velocity which alternate in time between up and down ramp. Day 2 at $\dot{\gamma} = 0.9\ s^{-1}$ shows a decrease in slip for the down ramp (higher average velocity), while day 3 at $\dot{\gamma} = 0.9\ s^{-1}$ shows an increase in slip for the down ramp (lower average velocity). Day 4 at $\dot{\gamma} = 0.9\ s^{-1}$ shows minimal thixotropy. At $\dot{\gamma} = 2.8\ s^{-1}$ on day 3, the down ramp shows an increase in slip (lower average velocity), while by day 4 the down ramp now shows a decrease in slip (higher average velocity) relative to the up ramp. Although a 3% w/v concentration has been noted as a transition point in the literature for Laponite® restructuring behavior [86, 87], the data presented here for 5% w/v obviously demonstrates significant transient fluctuations associated with microstructural changes even without long periods of aging (Figure 6.10, $\dot{\gamma} = 0.9\ s^{-1}$) which are averaged out over minute timescale in steady-state experiments.

Discussion

The velocity data indicate that a significant transition in material behavior occurs near 3.2% w/v, which is observed on day 2 of both steady-state and transient data and has been reported in literature. Another transition is observed for 5% w/v, where it appears to have similar behavior to 3.2% w/v for day 1. These transitions are accompanied by intense yielding resulting in shear localization, solid body rotation 100-200 µm from the rotor, as well as velocity fluctuations in the transient data. From this current data, it is not possible to conjecture on the type of electrostatic configuration (repulsive Wigner glass, attractive glass, or attractive gel network) which gives rise to the velocity fluctuations and indicate microstructural changes; however, future Rheo-NMR diffusion experiments which elucidate the correlation length and time of fluctuations as a function of observation time and displacement wave-vector, $\boldsymbol{q}$, may give better insight. Since repulsive glasses, attractive gels, and so-called "repulsive gels" or "attractive glasses" should each have different characteristic lengths of structure [155] it should in theory be possible to differentiate between such structures using diffusion experiments to obtain a characteristic length scale [37]. Altering the electrostatic screening with ionic species can provide a straightforward way to explore changes in structure.

Acknowledgments

M.A.S. acknowledges the MSU ChBE for support from the Benjamin Fellowship and the Noble Family Fellowship. J.D.S. and S.L.C. acknowledge the M.J. Murdock Charitable Trust and the NSF MRI program for instrument funding. J.N.W. acknowledges the Army Research Office (Grant #W911NF-19-1-0288) and the NIH (Grant #R01 GM131408-01). Research reported in this publication was supported in part by the National Institute of General Medical Sciences of the National Institutes of Health under Award Number P20GM103474.

The content is solely the responsibility of the authors and does not necessarily represent the official views of the National Institutes of Health.

NMR RELAXOMETRY OF NANOCRYSTALLINE CELLULOSE POROUS MEDIA

Contribution of Authors and Co-Authors

Manuscript in Chapter 7

Author: Maribelle A. Stanley

Contributions: Designed and performed experiments and formal analysis, wrote the initial manuscript, conceived concept, curated data, and reviewed/edited the manuscript.

Co-author: Matthew C. Young

Contributions: Involved with data curation/analysis.

Co-author: Sarah L. Codd

Contributions: Performed data curation/analysis, supervised work, reviewed/edited the manuscript.

Co-author: James N. Wilking

Contributions: Provided funding, data analysis assistance and reviewed/edited manuscript.

Co-author: Joseph D. Seymour

Contributions: Wrote initial manuscript, conceived concept, designed experiments, curated data, performed analysis, supervised work, reviewed/edited manuscript.

Manuscript Information

Maribelle A. Stanley, Matthew C. Young, Sarah L. Codd, James N. Wilking, Joseph D. Seymour

Status of Manuscript:
_X_ Prepared for submission to a peer-reviewed journal
____ Officially submitted to a peer-reviewed journal
____ Accepted by a peer-reviewed journal
____ Published in a peer-reviewed journal

Abstract

Nanocrystalline cellulose (NCC) is often supplied as a dried powder and hydrated before use in applications ranging from thin film and pharmaceutical composites to tissue engineering [74, 74, 84, 144, 159]. Enhanced understanding of NCC hydration dynamics will allow greater control of processing conditions. NCC systems are known to undergo structural phase changes due to NCC concentration [141, 149, 172], shear [64, 88, 141, 149, 172], sonication [141, 176], ion concentration [44, 112, 123, 150], aging [54], and temperature [71]; however, the hydration of unmodified NCC from a dried state has not been significantly studied. This work uses nuclear magnetic resonance (NMR) relaxometry to measure the mobility of water molecules during hydration at 30%, 50%, and 70% NCC with 0, 0.05, and 0.1 M NaCl added, providing a measure of the redistribution of water and changes in particle packing structure as a function of water concentration as well as ion concentration. The results demonstrate clear changes in NMR T_2 relaxation time values due to both NCC and ion concentration, and provide a guide for future studies using a greater range of NCC concentrations, ion concentrations, and ion valencies.

Introduction

Nanocrystalline cellulose (NCC) is a derivative of cellulose, which is the primary component of plant cell walls [137] and the most abundant renewable compound in the world [17]. Formed by the acid hydrolysis of cellulose [17, 73, 144, 159], NCC nanorods range in size from $\mathcal{O} \sim 10$ nm in length and $\mathcal{O} \sim 100$ nm in diameter [73]. NCC has found use in many applications due to its material properties, including but not limited to high strength, stiffness, tunable mechanics, optical birefringence, modifiable surface chemistry, electrical conductivity, and biocompatibility [88, 159]. Such applications include thin films and composites for next-generation materials [144, 159], optical sensors [146], biosensors

[146], tissue engineering [74, 84], pharmaceutical composite development [74], and others.

Consumer-available NCC is often offered as a spray-dried or freeze-dried powder (such as NCC from CelluForce® (Windsor, QC, CA) and USDA Forest Products Laboratory (Madison, WI)). To allow for adequate processing of NCC materials in various applications, the hydration of dried NCC must be understood. Aqueous NCC suspensions are increasingly studied, with evidence to indicate that they are sensitive to concentration [141, 149, 172], shear [64, 88, 141, 149, 172], sonication [141, 176], temperature [71], as well as ion concentration [44, 112, 123, 150], and time [54]. However, to the authors' knowledge, no studies exist which solely focus on the dynamics of hydration for non-modified NCC (only one study exists on hydration of NCC films and carboxylated NCC, performed by Garg et. al. 2021 [71]), which are important to control in applications that use dried forms of NCC to prepare liquid dispersion materials and in processes such as thin film casting where drying is involved.

NCC as a dried, partially dried or hydrated material constitutes a nanoparticulate fiber porous media. A porous medium is defined as a solid matrix and an inter-connected pore space [12, 37, 62, 65]. Pore networks can exhibit complicated hydrodynamic behavior, including capillary pressure, cavitation of pores, and various forms of hydrodynamic dispersion in the presence of advective motion [12, 37, 62, 65]. Porous media are also often opaque, making them a challenge to image with optical methods [37]. Average pore size distribution and average interparticle distances within the network can impact the imbibition of fluids and the dynamics that occur. Knowing the degree of restriction of water molecules within the system provides an indirect measurement of pore size within the network [37] and offer insight into the pore structure of the system.

NMR offers a useful, non-invasive and non-destructive way to evaluate porous media dynamics which does not require transparent samples [37]. In particular, NMR relaxometry allows measurement of the degree of rotational mobility restriction of water molecules within

a porous media network, and can be performed rapidly, with high precision, and over long periods of time [37]. Relaxometry allows for a qualitative analysis of the porous media network dynamics and can provide insight into the structural changes during dynamic events such as hydration.

In this study, we measure the hydration of NCC using NMR relaxometry techniques. NCC is hydrated at 30% w/v NCC (70% H_2O), 50% w/v NCC (50% H_2O), and 70% w/v NCC (30% H_2O) with 0, 0.05 M, or 0.1 M concentrations of NaCl. Measurements with 1D-T_2 relaxometry are taken over the course of approximately 110 hours. Two main methods of data analysis of the time domain data – a modified inverse Laplace transform using a Tikhonov regularized non-negative least squares solution to the Fredholm integral [165], allowing for a 1D-T_2 distribution of relaxation populations, and a mono-exponential fit to the time-domain data, allowing for the observation of the average T_2 data variation over hydration time – are used to inform discussion. The data provides the water dynamic behavior during hydration of NCC, highlighting the usefulness of NMR and the need for more thorough studies to be performed on NCC hydration to understand water distribution and dynamics and their role in particle network structure.

Materials and Methods

Sample Preparation

The nanocrystalline cellulose systems investigated in this work are porous media hydrated with water at 30%, 50%, and 70% w/v NCC, with 0, 0.05 or 0.1 M NaCl. Cellulose nanorods with dimensions 3-5 nm diameter and 85-95 nm length were obtained from CelluForce NCC® NCV100-NASD90 (Windsor, QC, CA). The samples were prepared by weighing the cellulose nanocrystals as a spray-dried powder and then adding the appropriate amount of RO/DI water or NaCl aqueous solution (NaCl dissolved in RO/DI water) with manual mixing to distribute the fluid. The resulting material was then packed into a 5 mm

glass NMR tube with moderate manual pressure to reduce the presence of air bubbles. The tubes are sealed to avoid water loss.

Methods

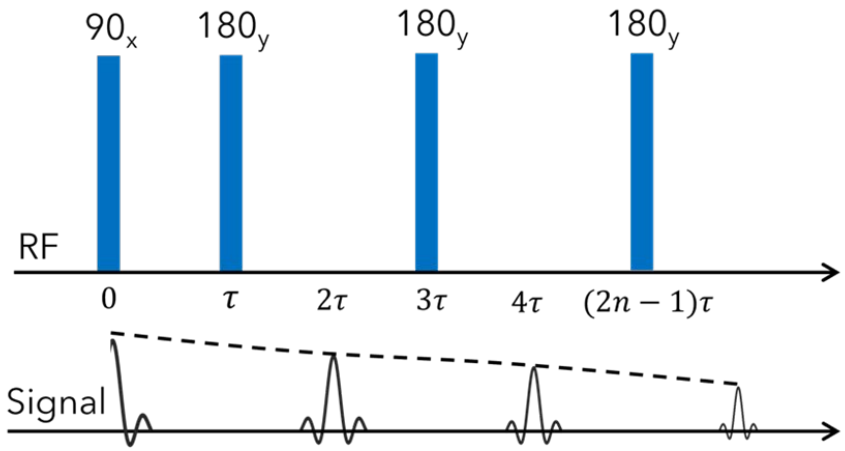


Figure 7.1: The Carr-Purcell-Meiboom-Gill (CPMG) pulse sequence and depiction of the resulting RF echo signal. A 90° pulse in the x direction causes the hydrogen atoms to tip into the transverse plane to allow for detection of signal. A subsequent 180° pulse (twice the duration of the 90° pulse) in y refocuses the spins when they lose coherence from T_2 relaxation after time τ, resulting in a spin echo. A 16 step phase cycle is used. The process of refocusing is repeated multiple times until the signal has sufficiently decayed, and a fit is applied to the exponentially decaying signal to obtain the rate constant of decay, T_2.

Relaxation Measurements

NMR relaxation experiments were conducted in a manner previously published elsewhere [175], which is paraphrased here for completeness. The experiments were conducted with a Bruker 250 MHz superconducting magnet equipped with an Avance III spectrometer and a 5 mm custom high-power RF probe. All T_2 measurements were made using a Carr-Purcell Meiboom Gill (CPMG) pulse sequence [40, 105], shown in Figure 7.1. The CPMG pulse sequence involves the generation of a free induction decay (FID) by using a 90° RF pulse, and consistent refocusing of the FID into spin echoes using a series of 180° RF pulses at each odd integer multiple of the 90°-180° interval time τ. The total experiment time is equal

to $2n\tau$, where n represents the number of echoes acquired. Each echo maximum is plotted against the total experiment time to produce the T_2 decay envelope. CPMG experiments were conducted using 60 W RF pulses of 3.2-3.5 µs for 90° and double for 180°, an inter-experiment delay of 60 s and 16 averages. Temperature control at 20 °C is used to minimize sample heating due to RF power deposition. CPMG experiments for each sample utilized a sweep width of 0.5 MHz for 1 µs acquisition dwell time, a τ time of 12 µs, and ran for 10,000-20,000 echoes.

Data Processing for Relaxation Measurements

The resulting time domain voltage signal from CPMG experiments was either inverse Laplace transformed using a Tikhonov regularized non-negative least squares solution to the Fredholm integral [165] to obtain a T_2 distribution, or was fitted using a mono-exponential function to obtain T_2 values. For the inverse Laplace transform method, the best smoothing parameter to maximize curvature, minimize the residual, and thus uphold parsimony was chosen for each data inversion [37]. Population distributions for 1D-T_2 were produced by normalizing the resulting probability distributions by the area under the curve [148].

Results and Discussion

1D-T_2 Distributions from ILT Analysis

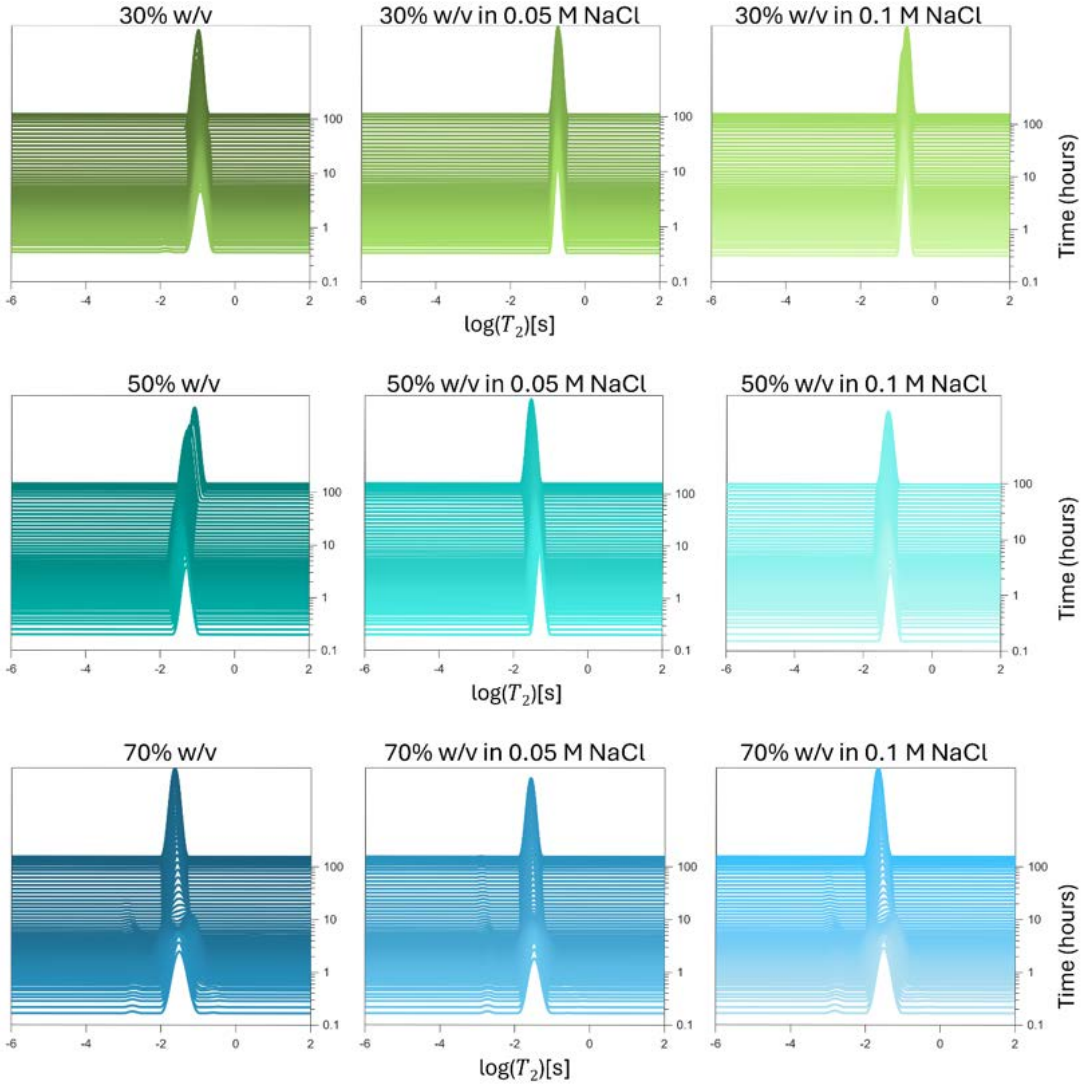


Figure 7.2: 1D T_2 probability distributions for 30%, 50%, and 70% w/v NCC with 0 M, 0.05 M, and 0.1 M NaCl, over approximately 110 hydration hours. The data was obtained with an inverse Laplace transform using a Tikhonov regularized non-negative least squares approach to measurements from 1D T_2 relaxation experiments. Top, left: 30% w/v; Top, center: 30% w/v with 0.05 M NaCl; Top, right: 30% w/v with 0.1 M NaCl; Middle, left: 50% w/v; Middle, center: 50% w/v with 0.05 M NaCl; Middle, right: 50% w/v in 0.1 M NaCl; Bottom, left: 70% w/v; Bottom, center: 70% w/v with 0.05 M NaCl; Bottom, right: 70% w/v with 0.1 M NaCl.

Table 7.1: T_2 values from 1D-T_2 distributions at 0, 10, and 100 hours for 30% w/v NCC

30% w/v NCC		**0 M NaCl**	**0.05 M NaCl**	**0.1 M NaCl**
	Hydration time [h]	T_2 **[s]**	T_2 **[s]**	T_2 **[s]**
Primary peak	0	0.1140	0.1866	0.1650
	10	0.1072	0.1754	0.1371
	100	0.0948	0.1754	0.1754

Table 7.2: T_2 values from 1D-T_2 distributions at 0, 10, and 100 hours for 50% w/v NCC

50% w/v NCC		**0 M NaCl**	**0.05 M NaCl**	**0.1 M NaCl**
	Hydration time [h]	T_2 **[s]**	T_2 **[s]**	T_2 **[s]**
Primary peak	0	0.0512	0.0544	0.0579
	10	0.0333	0.0376	0.0544
	100	0.0838	0.0294	0.0512

Table 7.3: T_2 values from 1D-T_2 distributions at 0, 10, and 100 hours for 70% w/v NCC

70% w/v NCC		**0 M NaCl**	**0.05 M NaCl**	**0.1 M NaCl**
	Hydration time [h]	T_2 **[s]**	T_2 **[s]**	T_2 **[s]**
Primary peak	0	0.02939	0.03126	0.02939
	10	0.02899	0.03126	0.03325
	100	0.02297	0.02764	0.02031
Secondary peak	0	0.00162	0.00195	0.00153
	10	0.00127	0.00144	0.00106
	100	-	-	-

Figure 7.2 shows 1D-T_2 probability distributions for 30, 50, and 70% w/v NCC without salt, with 0.05 M NaCl, and with 0.1 M NaCl over approximately 110 hours of hydration, obtained from inverse Laplace transforms on 1D T_2 measurements, using a Tikhonov regularized non-negative least squares solution to the Fredholm integral [165]. Tables 7.1, 7.2, and 7.3 show T_2 values of primary and secondary peaks for 1D-T_2 distributions at 0, 10, and 100 hour time-points for 30, 50, and 70% w/v NCC concentrations, respectively, at all concentrations of salt.

For the 30% w/v sample, one major population is observed at $T_2 = 0.1140$ s for $t = 0$ (Table 7.1), which shifts slightly to shorter T_2 as time progresses. The 30% w/v with 0.05 M NaCl sample exhibits one major population at $T_2 = 0.1866$ s at $t = 0$, which remains mostly stationary as time progresses. For the 30% w/v with 0.1 M NaCl sample, one major population is observed at $T_2 = 0.1650$ s at $t = 0$, which appears to shift to slightly towards longer T_2 values past $t = 100$ hours.

The 50% w/v exhibits one major population at $T_2 = 0.0512$ s at $t = 0$, which initially shifts to shorter T_2 values at short times, then longer T_2 values (0.0838 s) at $t > 10$ hours (Table 7.2). For the 50% w/v with 0.05 M NaCl, again one primary population is observed at $T_2 = 0.0544$ s at $t = 0$, which shifts slightly to lower values representative of greater restricted mobility as hydration time progresses. The 50% w/v in 0.1 M NaCl shows one major population at $T_2 = 0.0579$ s at $t = 0$, which initially shifts to shorter T_2 values (0.0512 s) at $t > 10$ hours, then longer T_2 values at $t > 10$ hours.

The 70% w/v sample exhibits two populations with a population at $T_2 = 0.02939$ s at $t = 0$ and a smaller secondary, more rotational mobility restricted population at $T_2 = 0.00162$ s at $t = 0$ (Table 7.3). The major population splits into two populations around $t = 3$ hours, which then merge shortly thereafter into a single peak that moves to more restricted mobility, lower T_2 values as time progresses, while the secondary population shifts to less restricted mobility, higher T_2, then a lower T_2 more motional restricted relaxation

around $t = 3$ hours, and subsequently disappears around $t = 10$ hours. For the 70% w/v with 0.05 M NaCl sample, two populations are observed, one at $T_2 = 0.03126$ s at $t = 0$ and a smaller, secondary, more restricted mobility peak at lower $T_2 = 0.00195$ s. The longer relaxation time population decreases in amplitude and the probability distribution broadens around $t = 3$ hours, and shifts very slightly to lower T_2 values representative of greater restricted rotational mobility as time progresses, while the secondary peak exhibits behavior identical to the secondary peak of 70% w/v no salt. The 70% w/v with 0.1 M NaCl shows two populations: a population at $T_2 = 0.02939$ s at $t = 0$ and a smaller, secondary, more restricted mobility population at $T_2 = 0.00153$ s. The major and secondary populations both exhibit nearly identical behavior to that of 70% w/v without salt.

An important aspect of the data is that only one major water mobility population exists for all probability distributions (one small secondary population is observed for 70% w/v no salt, 70% w/v with 0.05 M NaCl, and 70% w/v with 0.1 M NaCl). The lack of additional large peaks allows for the appropriate use of a mono-exponential fit to further analyze the relaxation data, which is shown in Figure 7.3 and discussed below.

Mono-Exponential Fits to 1D-T_2 Experiments

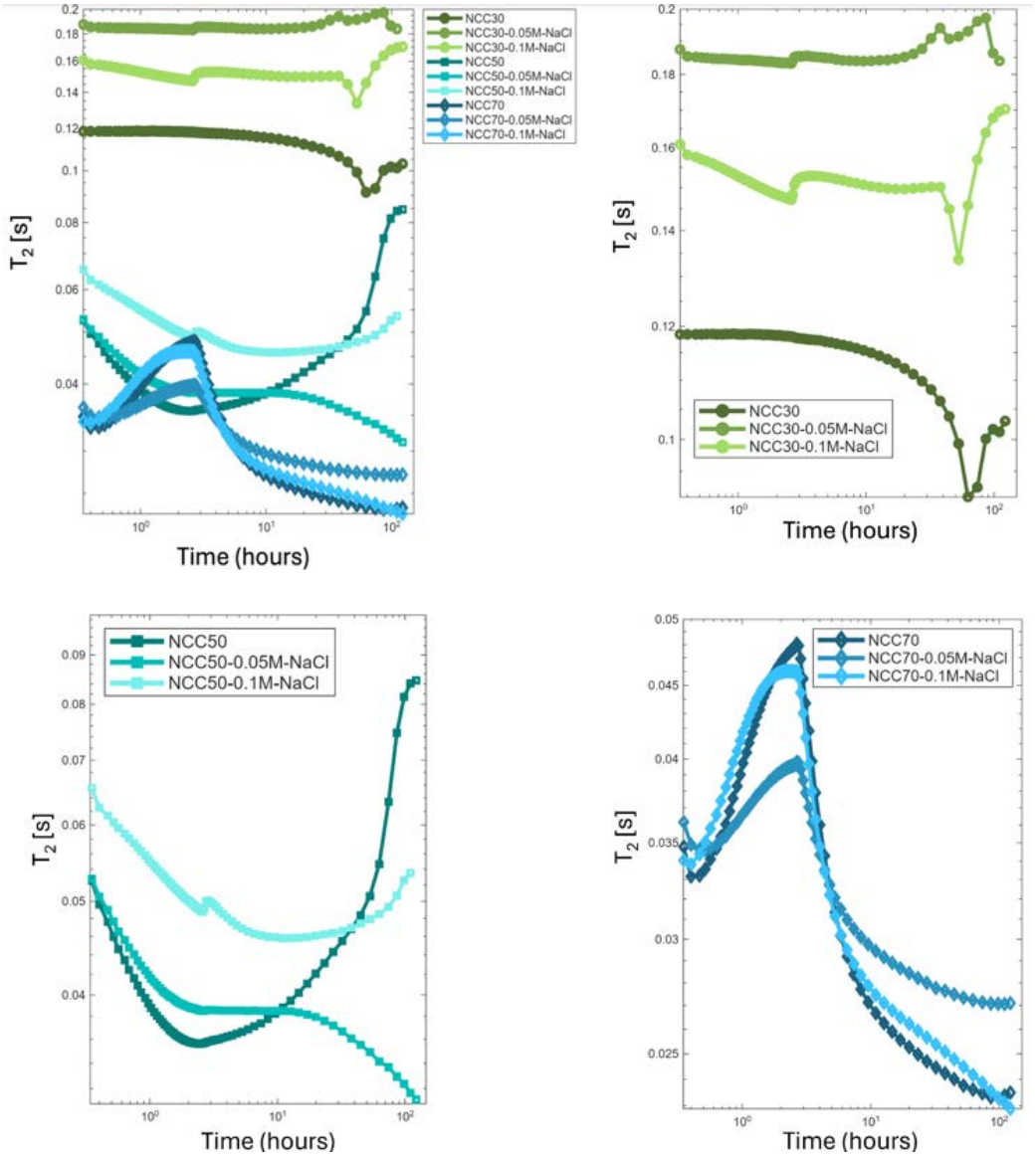


Figure 7.3: Average T_2 values for 30%, 50%, and 70% w/v NCC with 0, 0.05, and 0.1 M NaCl, over approximately 110 hydration hours. The data was obtained with a mono-exponential fit to measurements from 1D T_2 relaxation experiments (the same experiments as Figure 7.2). Top left: All NCC and salt concentrations overlaid; Top right: 30% w/v NCC sample at 0 M, 0.05 M, and 0.1 M NaCl; Bottom left: 50% w/v NCC sample at 0 M, 0.05 M, and 0.1 M NaCl; Bottom right: 70% w/v NCC sample at 0 M, 0.05 M, and 0.1 M NaCl. All samples depict non-monotonic behavior over time, indicating dynamic temporal changes in the surrounding environments of the major water population.

Figure 7.3 depicts average T_2 values for 30%, 50%, and 70% w/v NCC without salt, with 0.05 M NaCl, and with 0.1 M NaCl, over approximately 110 hours of hydration. The data was obtained from mono-exponential fits to 1D T_2 relaxation data, a complementary form of analysis on the same experimental data analyzed and displayed in Figure 7.2.

The plot which shows all NCC and salt concentrations overlaid (top left) demonstrates expected behavior overall for the concentrations of NCC. The most concentrated, 70% w/v, which contains the least water, displays the most water rotational mobility restricted behavior with the lowest T_2 values, and overall T_2 values increase with lower NCC concentration, indicating greater water molecular mobility with higher water content.

The plot which shows 30% w/v NCC with no NaCl, 0.05 M NaCl, and 0.1 M NaCl (top right) demonstrates an increase in T_2 from approximately 0.12 to 0.185 s at $t = 0 - 11$ hours for the 0.05 M NaCl sample, while a decrease in T_2 is shown for 0.1 M NaCl, which starts at approximately 0.16 s at $t = 0$ hours and steadily decreases.

The plot showing 50% w/v NCC with no NaCl, 0.05 M NaCl, and 0.1 M NaCl (bottom left) exhibits an overall increase in T_2 as salt content is increased. It depicts similar characteristics for all salt levels until approximately 11 hours, where contrasting behavior is then observed.

For the 70% w/v NCC sample with no NaCl, 0.05 M NaCl, and 0.1 M NaCl (bottom right), the plot shows similar behavior for all salt levels, with a significant decrease in maximum T_2 for 0.05 M NaCl, but an increase for 0.1 M NaCl that approaches the no salt data. All samples depict non-monotonic behavior over time, indicating dynamic temporal changes in the mobility and water particle interaction environments of the major water population.

Discussion

A few key points about the data are of particular interest. One curious aspect is the division and recombination of the major peak for 70% w/v without salt and with 0.1 M NaCl, and the broadening and lowering of amplitude for the 70% with 0.05 M NaCl, all of which occur around $t = 3$ hours. Additionally, the 70% w/v samples with and without salt are the only samples which show a very small, more restricted secondary peak, with identical character between them, and which vanishes at long times.

Another interesting aspect of the data, observed in the mono-exponential fits (Figure 7.3), is the complex and non-monotonic behavior of the average T_2 values which not only varies as expected with NCC concentration, but also varies over the time of hydration and as salt concentration is changed. Nearly all concentrations of NCC, with and without salt (excluding 30%, no salt), show a noticeable change in curvature at approximately 11 hours, which is most dramatic in the 50% w/v and 70% w/v samples. Particularly interesting is the dramatic change in 50% with 0.05 M NaCl from concave to convex, which is a strong departure from the curvature that is relatively similar between 50% and 50% with 0.1 M NaCl. For the 50% samples, an overall increase in mobility is seen with increased salt content.

Also of interest is the pronounced change in average T_2 values for 30% w/v samples between 12-15 hours, where a severe change to more restricted behavior occurs for 30% without salt and 30% with 0.1 M NaCl. Both exhibit very similar patterns, while a moderate change to a less restricted behavior occurs for 30% with 0.05 M NaCl. Additionally, 30% with 0.05 M NaCl is the least restricted and most mobile of the samples, while 30% with 0.1 M is less restricted than 30% without salt.

For the 70% w/v samples, the samples all show considerably similar behavior; however, the no salt and 0.1 M samples show the most similarity, while 0.5 M exhibits a marked decrease in T_2 amplitude around 12 hours compared to the other two 70% w/v samples. Overall, 70% w/v with 0.05 M NaCl seems to show a much less dramatic change in behavior

than the 70% w/v no salt and 70% w/v with 0.1 M NaCl, as at times $t > 10$ hours, it has less restricted mobility where both 70% w/v and 70% w/v with 0.1 M NaCl have similarly decreased mobility.

In summary, it appears that while no salt and 0.1 M NaCl samples seem to show similar behavior for a given concentration of NCC, the 0.05 M NaCl seems to show divergent behavior in comparison, regardless of the concentration of NCC. Along with the fact that the amount of salt changes average T_2 behavior, this indicates that microstructure of the material is controlled by electrostatic interactions. The electrostatic interaction between the sodium ions and the negatively charged NCC nanorods is known to be ion-concentration dependent [173] and affects the mobility of water molecules and the structuring of the NCC porous media. Rheological studies of lower particle concentration NCC systems ($< 12\%$ w/v) have indicated that 0.05 M salt induces a liquid to solid phase transition due to electrostatic screening effects, a finding consistent with the changes observed here at the higher NCC concentrations [173]. The 30% NCC sample exhibits a large increase in T_2 and hence water mobility upon addition of 0.05 M NaCl indicating less water binding to particles due to electrostatic screening of water from the particles by the ions [173]. This effect is still present in 30% w/v NCC with 0.1 M NaCl however this larger ion concentration results in lower T_2 and water mobility than the 0.05 M sample, yet higher than no salt. These findings indicate the impact of changing the electrostatic Debye length scale for which $\kappa^{-1} \sim \sqrt{I}$, where I is the monovalent ion concentration and κ^{-1} is of the order of nanometers [173]. This charge-mediated effect during hydration impacts water mobility and possibly aging in the material, which has been reported to occur for NCC [54]. Further studies with a range of salt concentrations are required to quantify this phenomena.

Conclusion

The experiments described here are an exploration into the structural behavior of high concentration NCC. They provide insight into the impacts of hydration, ion concentration, and aging on the dynamic structure of NCC. As NCC use in novel materials applications continues to grow, it is increasingly important to understand the effects of water content on NCC processing behavior. Further NMR measurements with NCC can provide insight. Future works may consider a more thorough survey of ion-dependence, including experiments with various sizes of monovalent ions as well as divalent ions; additionally, altering the surface molecules of NCC with ligands of various charges could provide useful insight. Additional experiments with other nanoparticulate geometries – e.g., discoids as in Laponite® RD, spheres, or different aspect ratios of nanorods - might offer useful data on the impact of geometric and steric factors to restructuring phenomenon.

Acknowledgments

M.A.S. acknowledges the MSU ChBE for support from the Benjamin Fellowship and the Noble Family Fellowship. J.D.S. and S.L.C. acknowledge the M.J. Murdock Charitable Trust and the NSF MRI program for instrument funding. J.N.W. acknowledges the Army Research Office (Grant #W911NF-19-1-0288) and the NIH (Grant #R01 GM131408-01). Research reported in this publication was supported in part by the National Institute of General Medical Sciences of the National Institutes of Health under Award Number P20GM103474. The content is solely the responsibility of the authors and does not necessarily represent the official views of the National Institutes of Health.

CONCLUSION

In this dissertation, we have introduced concepts related to NMR and rheometry (Chapters 2 and 3) to inform the analysis of material properties of two useful nanoparticulate complex fluids, NCC and Laponite®. These fluids find great application in a variety of fields but require a better understanding of mesoscale structures and particle interaction dynamics to properly predict macroscale flow behavior. The following is a brief overview of the research performed as well as a discussion of future directions.

In Chapter 4, standard rheometry and NMR velocimetry of aqueous suspensions of nanocrystalline cellulose at various concentrations (3%, 5%, 7%, and 12% w/v) and shear rates ($\dot{\gamma} = 0.9$, 2.8, and 4.6 s^{-1}) are explored [149]. The NMR data provide mesoscale velocity distributions across the gap of a Couette flow cell with spatial and temporal resolution and demonstrate large velocity fluctuations for the chiral nematic liquid-crystal phase suspension (5% w/v) despite only subtle effects observed in the standard bulk rheometry. These fluctuations indicate particle director orientation tumbling and flow. Velocity fluctuations are further investigated through velocimetry with a different NCC material source and the addition of ionic species, which alters the mesoscale velocity behavior, in Chapter 5.

In Chapter 5, standard rheometry and NMR velocimetry for 3%, 5%, 7%, and 12% w/v NCC concentrations with the addition of NaCl provide novel data on the mesoscale velocity changes associated with electrostatic screening. Complex flow behavior is seen in velocity profiles, which correlates with bulk standard rheometry but provides additional detail on wall-slip, yielding, shear-banding, and velocity fluctuations during liquid to solid phase changes induced by particle and ion concentration. An overall change towards more complex and gel-like behavior is noted with the addition of 0.1 M NaCl for most suspensions; in particular, an increase in distinct, patterned velocity fluctuations are observed for 5% w/v in 0.1 M NaCl, 7% w/v in 0.1 M NaCl, and 12% w/v in 0.1 M NaCl. Large velocity

fluctuations are also noted in the chiral nematic liquid crystal phase at 5% w/v suspension without salt, which aligns with observations from a different NCC material (see Chapter 5) [149].

Chapter 6 describes NMR velocimetry experiments on Laponite® RD at varying concentrations (2%, 3.2%, 4%, and 5% w/v) and shear rates ($\dot{\gamma}$ = 0.9, 2.8, and 4.6 s^{-1}) as a function of aging over the course of several days. As Laponite® forms unstable nanoscale structures which undergo attractive or repulsive energetic restructuring, it exhibits complex flow behavior and changes in mesoscale structure on the timescale of days. The velocity profiles demonstrate these long time-dependent changes in flow as well as shear localization, velocity fluctuations, and thixotropic behavior, and additionally provide insight into the heavily debated structural transition occurring between 3-4% w/v.

In Chapter 7, a study of hydration dynamics using 1D-T_2 NMR relaxometry on highly concentrated aqueous NCC (30%, 50%, 70% w/v) with two concentrations of NaCl (0.05 and 0.1 M) over approximately 5 days demonstrates the effects of both time and electrostatic screening on NCC as water redistributes during hydration. Notably, 30%, 50%, and 70% w/v show an expected decrease in average T_2 with increase in particle concentration, but most samples show an unexpected but significant change in T_2 around t = 11 hours which requires further study. Other features of average T_2 changes demonstrate clear differences between 0, 0.05 and 0.1 M NaCl, indicating a significant effect of electrostatic screening on mobility of water and thus mesoscale structure of NCC. The results demonstrate changes in T_2 values due to both NCC and ion concentration, and suggest future studies which use a greater range of NCC concentrations, ion concentrations and ion valencies.

Future Directions

Many possible directions exist for NCC velocimetry experiments. A broader scope of concentrations of NCC could provide more information on the flow and structural dependence

with interparticle interactions, and the altering of the screening ion species in salt studies would provide detailed information about the role of electrostatic interactions on liquid to solid phase transition impacts on velocity.

In addition to these, the use of NMR diffusometry experiments can help to elucidate the time and length-scale of the chiral nematic liquid crystal phase velocity fluctuations, which may help inform mathematical modeling efforts on liquid crystal director fluctuations.

Other possible extensions of these studies would be the addition of either neutral (or charged), inert spheres of various radii into the NCC suspension or the embedding of such spheres on the rotor surface. The addition of spheres at various sizes would likely alter flow behavior, and the size-dependence might provide insight into the mesoscale structural features (a clear and dramatic change in flow behavior may indicate disruption of the structure at a critical sphere size, and could help bound the network structure length scale).

Future Laponite® velocimetry experiments should be performed with rotors and/or stators that provide no-slip conditions. Options include sand-blasted, hatched/cross-hatched, or otherwise roughened surfaces that will provide increased surface area that limits slip. Such conditions are necessary to ensure that velocity fluctuations like those observed in Chapter 6 occur solely due to microstructural dynamics as opposed to slick-slip events.

Other Laponite® experiments of interest would be the addition of ionic species. Determining the effect of ionic species on the flow behavior of Laponite®, both immediate and as a function of aging, may provide insight into electrostatic screening effects on mesoscale structure. In addition, Laponite® would benefit from NMR diffusometry experiments that could provide more detail on the time and length-scale of fluctuating behavior. This type of experiment would require no-slip conditions like those noted above.

Future studies for highly concentrated NCC should be conducted at a greater range of NCC concentrations, ion concentrations, ion radii size, and ion valencies (e.g. divalent, trivalent). Although lower concentrations of NCC ($> 10\%$, $< 30\%$ w/v) can be challenging to

load into 5 mm NMR tubes, observing concentrations below 30% w/v may provide valuable insight into the dependence on concentration, as it is possible that the increased presence of water could promote faster or more dramatic structural changes. Probing the effects of other ion concentrations may offer insight into trends associated with screening. Since 0.05 M seems to have an interesting and unexpected behavior for NCC samples as opposed to 0.1 M NaCl based on the data in Chapter 7, measuring T_2 for concentrations between 0.05 and 0.1 M could inform as to whether a significant electrostatic induced structural transition occurs within this range. A change in ion radii size while maintaining the same valency may offer insight into the effect of excluded volume in the electrostatic screening for NCC during hydration. Also, different ion valencies are known to influence NCC structure when in lower aqueous concentrations ($\leq 10\%$), so it is likely that given the significant T_2 changes with NaCl, a difference will be obtained by changing the screening ion valence, which could provide information about the dependence of NCC hydration structure on valency.

In addition, to extend on the studies, neutral and charged ligands could be appended to the surface of NCC nanorods to determine the effects of excluded volume due to steric versus electrostatic screening and how this factor may impact the structural changes during hydration.

An interesting extension of NCC hydration studies would be to monitor NCC drying with T_2 relaxometry. This could provide insight into the energetic driving factors of the structural changes by determining whether the hydration is a reversible or irreversible process. Since this will likely change with the addition of electrostatic screening and increased interparticle interactions, a suite of ion concentrations and NCC concentrations could also be probed with this extension.

Finally, the experimental work for the project in Chapter 7 also included Laponite®, although it was not shown for brevity and due to the lack of changes observed between 30%, 50%, and 70% w/v Laponite®. Since Laponite® is a discoid and NCC a rod, there remains

a question as to whether the nanoscale geometry affects the ability to restructure during hydration. Future experiments could probe this by performing identical experiments with nanoscale spheres or ellipsoids of various aspect ratios. Overall, these experiments could provide important insight into how highly concentrated NCC responds to ionic species and what physical effects (excluded volume, electrostatic screening, sterics, particle geometry) are important. Such information can inform how best to design and process NCC in highly concentrated materials applications.

REFERENCES CITED

[1] Arthur Adamson. *A Textbook of Physical Chemistry*. Elsevier, 2012. ISBN 032314070X.

[2] R. N. Al-kaby, J. S. Jayaratne, T. I. Brox, S. L. Codd, J. D. Seymour, and J. R. Brown. Rheo-nmr of transient and steady state shear banding under shear startup. *Journal of Rheology*, 62(5):1125–1134, 2018. ISSN 0148-6055. doi: 10.1122/1.5037594.

[3] R. N. Al-kaby, S. L. Codd, J. D. Seymour, and J. R. Brown. Characterization of velocity fluctuations and the transition from transient to steady state shear banding with and without pre-shear in a wormlike micelle solution under shear startup by rheo-nmr. *Applied Rheology*, 30(1):1–13, 2020. ISSN 1430-6395. doi: 10.1515/arh-2020-0001.

[4] Roberta Angelini, Emanuela Zaccarelli, Flavio Augusto de Melo Marques, Michael Sztucki, Andrei Fluerasu, Giancarlo Ruocco, and Barbara Ruzicka. Glass–glass transition during aging of a colloidal clay. *Nature Communications*, 5(1):4049, 2014. ISSN 2041-1723. doi: 10.1038/ncomms5049.

[5] Roberta Angelini, Domenico Larobina, Barbara Ruzicka, Francesco Greco, and Raffaele Pastore. Rheological signatures of a glass-glass transition in an aging colloidal clay. *Journal of Rheology*, 67(4):811–811, 2023. ISSN 0148-6055. doi: 10.1122/8.0000592.

[6] Paulo Arratia. Complex fluids at work. *Physics*, 4, 2011. ISSN 1943-2879. doi: 10.1103/Physics.4.9.

[7] R. G. Avery and J. D. F. Ramsay. Colloidal properties of synthetic hectorite clay dispersions: Ii. light and small angle neutron scattering. *Journal of Colloid and Interface Science*, 109(2):448–454, 1986. ISSN 0021-9797. doi: https://doi.org/10.1016/0021-9797(86)90322-X.

[8] My Ahmed Said Azizi Samir, Fannie Alloin, and Alain Dufresne. Review of recent research into cellulosic whiskers, their properties and their application in nanocomposite field. *Biomacromolecules*, 6(2):612–626, 2005. ISSN 1525-7797. doi: 10.1021/bm0493685. URL `https://doi.org/10.1021/bm0493685`. doi: 10.1021/bm0493685.

[9] M. L. Barbosa, L. M. Oliveira, R. Paiva, A. C. Dametto, D. D. S. Dias, C. A. Ribeiro, M. Wrona, C. Nerín, H. D. S. Barud, and S. A. Cruz. Evaluation the potential of onion/laponite composites films for sustainable food packaging with enhanced uv protection and antioxidant capacity. *Molecules*, 28(19), 2023. ISSN 1420-3049. doi: 10.3390/molecules28196829.

[10] H.A. Barnes, Institute of Non-Newtonian, and Fluid Mechanics. *A Handbook of Elementary Rheology*. University of Wales, Institute of Non-Newtonian Fluid Mechanics, 2000. ISBN 9780953803200.

[11] Howard A. Barnes, John Fletcher Hutton, and Kenneth Walters. *An introduction to rheology*. Rheology series. Elsevier : Distributors for the U.S. and Canada, Elsevier Science Pub. Co., Amsterdam, New York, 2005. ISBN 0444871403; 9780444871404.

[12] Jacob Bear. *Dynamics of fluids in porous media*. Courier Corporation, 2013. ISBN 0486131807.

[13] Stephanie Beck-Candanedo, Maren Roman, and Derek G. Gray. Effect of reaction conditions on the properties and behavior of wood cellulose nanocrystal suspensions. *Biomacromolecules*, 6(2):1048–1054, 2005. ISSN 1525-7797. doi: 10.1021/bm049300p.

[14] Roberto Benzi, Thibaut Divoux, Catherine Barentin, Sébastien Manneville, Mauro Sbragaglia, and Federico Toschi. Unified theoretical and experimental view on transient shear banding. *Physical Review Letters*, 123(24):248001, 2019. doi: 10.1103/PhysRevLett.123.248001.

[15] Daniel Bernoulli. *Hydrodynamica, sive de viribus et motibus fluidorum commentarii*. (in Latin, source ETH-Bibliothek Zürich, Rar 5503), 1738.

[16] Pascal Bertsch, Stéphane Isabettini, and Peter Fischer. Ion-induced hydrogel formation and nematic ordering of nanocrystalline cellulose suspensions. *Biomacromolecules*, 18(12):4060–4066, 2017. ISSN 1525-7797. doi: 10.1021/acs.biomac.7b01119. URL `https://doi.org/10.1021/acs.biomac.7b01119`. doi: 10.1021/acs.biomac.7b01119.

[17] Shashi Kant Bhatia, Sujit Sadashiv Jagtap, Ashwini Ashok Bedekar, Ravi Kant Bhatia, Anil Kumar Patel, Deepak Pant, J. Rajesh Banu, Christopher V. Rao, Yun-Gon Kim, and Yung-Hun Yang. Recent developments in pretreatment technologies on lignocellulosic biomass: Effect of key parameters, technological improvements, and challenges. *Bioresource Technology*, 300:122724, 2020. ISSN 0960-8524. doi: 10.1016/j.biortech.2019.122724.

[18] Eugene C. Bingham. The history of the society of rheology from 1922 - 1944. *Society of Rheology*, 1944.

[19] R.B. Bird, W.E. Stewart, and E.N. Lightfoot. *Transport Phenomena*. Wiley, 2006. ISBN 9780470115398.

[20] Robert Byron Bird, Robert Calvin Armstrong, and Ole Hassager. *Dynamics of polymeric liquids. Vol. 1: Fluid mechanics*. John Wiley and Sons Inc., New York, NY, 1987.

[21] F. Bloch. Nuclear induction. *Physical Review*, 70(7-8):460–474, 1946. doi: 10.1103/PhysRev.70.460. PR.

[22] B. Blümich. *Essential NMR: for Scientists and Engineers*. Springer Berlin Heidelberg, 2005. ISBN 9783540271932.

[23] Ludwig Boltzmann. *Further Studies on the Thermal Equilibrium of Gas Molecules*, pages 262–349. 1872. doi: 10.1142/9781848161337_0015.

[24] Ludwig Boltzmann. *The Second Law of Thermodynamics*, pages 13–32. Springer Netherlands, Dordrecht, 1974. doi: 10.1007/978-94-010-2091-6_2.

[25] D. Bonn, P. Coussot, H. T. Huynh, F. Bertrand, and G. Debrégeas. Rheology of soft glassy materials. *Europhysics Letters*, 59(5):786, 2002. ISSN 0295-5075. doi: 10.1209/epl/i2002-00195-4.

[26] Daniel Bonn, Hamid Kellay, Hajime Tanaka, Gerard Wegdam, and Jacques Meunier. Laponite: What is the difference between a gel and a glass? *Langmuir*, 15(22):7534–7536, 1999. ISSN 0743-7463. doi: 10.1021/la990167+. doi: 10.1021/la990167+.

[27] Daniel Bonn, Sorin Tanase, Bérengère Abou, Hajime Tanaka, and Jacques Meunier. Laponite: Aging and shear rejuvenation of a colloidal glass. *Physical Review Letters*, 89(1):015701, 2002. doi: 10.1103/PhysRevLett.89.015701.

[28] Melanie M. Britton and Paul T. Callaghan. Two-phase shear band structures at uniform stress. *Physical Review Letters*, 78(26):4930–4933, 1997. doi: 10.1103/PhysRevLett.78.4930.

[29] Timothy Brox. *New Methods for Studying Materials Under Shear with Nuclear Magnetic Resonance*. Thesis, Te Herenga Waka-Victoria University of Wellington, 2016.

[30] Timothy I. Brox, Bradley Douglass, Petrik Galvosas, and Jennifer R. Brown. Observations of the influence of taylor-couette geometry on the onset of shear-banding in surfactant wormlike micelles. *Journal of Rheology*, 60(5):973–982, 2016. ISSN 0148-6055. doi: 10.1122/1.4961478.

[31] Cristina-Eliza Brunchi and Simona Morariu. Laponite®—from dispersion to gel—structure, properties, and applications, 2024.

[32] Richard Buscall. Letter to the editor: Wall slip in dispersion rheometry. *Journal of Rheology*, 54(6):1177–1183, 2010. ISSN 0148-6055. doi: 10.1122/1.3495981.

[33] Hans Estrella Cainglet, Joanne Tanner, Naghmeh Nasiri, Christine Browne, Gil Garnier, and Warren Batchelor. Rapid cellulose nanomaterial characterisation by rheology. *Cellulose*, 30(8):4971–4982, 2023. ISSN 1572-882X. doi: 10.1007/s10570-023-05180-1.

[34] P. T. Callaghan. Rheo-nmr and velocity imaging. *Current Opinion in Colloid & Interface Science*, 11(1):13–18, 2006. ISSN 1359-0294. doi: 10.1016/j.cocis.2005.10.003.

[35] P. T. Callaghan. Rheo nmr and shear banding. *Rheologica Acta*, 47(3):243–255, 2008. ISSN 0035-4511. doi: 10.1007/s00397-007-0251-2.

[36] P.T. Callaghan. *Principles of Nuclear Magnetic Resonance Microscopy*. Clarendon Press, 1991.

[37] P.T. Callaghan. *Translational Dynamics and Magnetic Resonance: Principles of Pulsed Gradient Spin Echo NMR*. Oxford University Press, 2011.

[38] Cristiane Capello, Gabriel Coelho Leandro, Talita Ribeiro Gagliardi, and Germán Ayala Valencia. Intelligent films from chitosan and biohybrids based on anthocyanins and laponite®: Physicochemical properties and food packaging applications. *Journal of Polymers and the Environment*, 29(12):3988–3999, 2021. ISSN 1572-8919. doi: 10.1007/s10924-021-02168-5.

[39] Femina Carolin C, T. Kamalesh, P. Senthil Kumar, R. V. Hemavathy, and Gayathri Rangasamy. A critical review on sustainable cellulose materials and its multifaceted applications. *Industrial Crops and Products*, 203:117221, 2023. doi: 10.1016/j.indcrop.2023.117221.

[40] H.Y. Carr and E.M. Purcell. Effects of diffusion on free precession in nuclear magnetic resonance experiments. *Physical Review*, 94(3):630–638, 1954. doi: 10.1103/PhysRev.94.630. PR.

[41] Ulises Casado, Verónica L. Mucci, and Mirta I. Aranguren. Cellulose nanocrystals suspensions: Liquid crystal anisotropy, rheology and films iridescence. *Carbohydrate Polymers*, 261:117848, 2021. doi: 10.1016/j.carbpol.2021.117848.

[42] Saptaparni Chanda, Dilpreet S. Bajwa, Greg A. Holt, Nicole Stark, Sreekala G. Bajwa, and Mohiuddin Quadir. Silane compatibilzation to improve the dispersion, thermal and mechancial properties of cellulose nanocrystals in poly (ethylene oxide). *Nanocomposites*, 7(1):87–96, 2021. doi: 10.1080/20550324.2021.1942641.

[43] Mokit Chau, Shivanthi Easwari Sriskandha, Héloïse Thérien-Aubin, and Eugenia Kumacheva. *Supramolecular Nanofibrillar Polymer Hydrogels*, pages 167–208. Springer International Publishing, Cham, 2015. ISBN 978-3-319-15404-6. doi: 10.1007/978-3-319-15404-6_5. URL `https://doi.org/10.1007/978-3-319-15404-6_5`.

[44] Fanch Cherhal, Fabrice Cousin, and Isabelle Capron. Influence of charge density and ionic strength on the aggregation process of cellulose nanocrystals in aqueous suspension, as revealed by small-angle neutron scattering. *Langmuir*, 31(20):5596–5602, 2015. ISSN 0743-7463. doi: 10.1021/acs.langmuir.5b00851. URL `https://doi.org/10.1021/acs.langmuir.5b00851`. doi: 10.1021/acs.langmuir.5b00851.

[45] Michel Cloître and Roger T. Bonnecaze. A review on wall slip in high solid dispersions. *Rheologica Acta*, 56:283–305, 2017.

[46] P. Coussot. *Rheological Aspects of the Solid-Liquid Transition in Jammed Systems*, pages 69–90. Springer-Verlag, Berlin, Heidelberg, 2006. ISBN 978-3-540-33204-6. doi: 10.1007/3-540-33204-9_5.

[47] P. Coussot, Q. D. Nguyen, H. T. Huynh, and D. Bonn. Viscosity bifurcation in thixotropic, yielding fluids. *Journal of Rheology*, 46(3):573–589, 2002. ISSN 0148-6055. doi: 10.1122/1.1459447.

[48] P. Coussot, J. S. Raynaud, F. Bertrand, P. Moucheront, J. P. Guilbaud, H. T. Huynh, S. Jarny, and D. Lesueur. Coexistence of liquid and solid phases in flowing soft-glassy materials. *Physical Review Letters*, 88(21):218301, 2002. doi: 10.1103/PhysRevLett.88.218301.

[49] Philippe Coussot. Progress in rheology and hydrodynamics allowed by nmr or mri techniques. *Experiments in Fluids*, 61(9), 2020. doi: 10.1007/s00348-020-03037-y.

[50] Philippe Coussot, F. Bertrand, and Benjamin Herzhaft. Rheological behavior of drilling muds, characterization using mri visualization. *Oil & Gas Science and Technology-revue De L Institut Francais Du Petrole - OIL GAS SCI TECHNOL*, 59:23–29, 2004. doi: 10.2516/ogst:2004003.

[51] Sabya Das, Neelam Dhankhar, Kashif Hussain, Sima Singh, Afzal Hussain, Dr Faruk, and Mike Tebyetekerwa. Laponite-based nanomaterials for biomedical applications: A review. *Current Pharmaceutical Design*, 25:1–20, 2019. doi: 10.2174/1381612825666190402165845.

[52] Colin J. Davies, Andrew J. Sederman, Chris J. Pipe, Gareth H. McKinley, Lynn F. Gladden, and Mike L. Johns. Rapid measurement of transient velocity evolution using gervais. *Journal of Magnetic Resonance*, 202(1):93–101, 2010. doi: 10.1016/j.jmr.2009.10.004.

[53] Irina Delidovich, Peter J. C. Hausoul, Li Deng, Rebecca Pfützenreuter, Marcus Rose, and Regina Palkovits. Alternative monomers based on lignocellulose and their use for polymer production. *Chemical Reviews*, 116(3):1540–1599, 2016. doi: 10.1021/acs.chemrev.5b00354.

[54] Babak Derakhshandeh, George Petekidis, Sadaf Shafiei Sabet, Wadood Y. Hamad, and Savvas G. Hatzikiriakos. Ageing, yielding, and rheology of nanocrystalline cellulose suspensions. *Journal of Rheology*, 57(1):131–148, 2013. ISSN 0148-6055. doi: 10.1122/1.4764080.

[55] M. Doi and S.F. Edwards. *The Theory of Polymer Dynamics*. Clarendon Press, 1988. ISBN 9780198520337.

[56] Masao Doi. *Soft matter physics*. Oxford University Press, USA, 2013. ISBN 0199652953.

[57] Masao Doi, Takayuki Shimada, and Koji Okano. Concentration fluctuation of stiff polymers. ii. dynamical structure factor of rod-like polymers in the isotropic phase. *The Journal of Chemical Physics*, 88(6):4070–4075, 1988. ISSN 0021-9606 1089-7690. doi: 10.1063/1.453861.

[58] Xue Min Dong and Derek G. Gray. Effect of counterions on ordered phase formation in suspensions of charged rodlike cellulose crystallites. *Langmuir*, 13(8):2404–2409, 1997. ISSN 0743-7463. doi: 10.1021/la960724h. doi: 10.1021/la960724h.

[59] Xue Min Dong, Tsunehisa Kimura, Jean-François Revol, and Derek G. Gray. Effects of ionic strength on the isotropic chiral nematic phase transition of suspensions of cellulose crystallites. *Langmuir*, 12(8):2076–2082, 1996. ISSN 0743-7463. doi: 10.1021/la950133b.

[60] Deepak Doraiswamy. The origins of rheology: a short historical excursion. *Rheology Bulletin*, 71(1):1–9, 2002.

[61] P.G. Drazin and W.H. Reid. *Hydrodynamic Stability*. Cambridge Mathematical Library. Cambridge University Press, 2004. ISBN 9780521525411.

[62] Francis AL Dullien. *Porous media: fluid transport and pore structure*. Academic press, 2012. ISBN 0323139337.

[63] Franck P. Duval, Patrice Porion, and Henri Van Damme. Microscale and macroscale diffusion of water in colloidal gels. a pulsed field gradient and nmr imaging investigation. *The Journal of Physical Chemistry B*, 103(27):5730–5735, 1999. ISSN 1520-6106. doi: 10.1021/jp9909210.

[64] Coro Echeverria, Pedro L. Almeida, Gabriel Feio, João L. Figueirinhas, Alejandro D. Rey, and Maria H. Godinho. Rheo-nmr study of water-based cellulose liquid crystal system at high shear rates. *Polymer*, 65:18–25, 2015. doi: 10.1016/j.polymer.2015.03.050.

[65] Wolfgang Ehlers and Joachim Bluhm. *Porous media: theory, experiments and numerical applications*. Springer Science & Business Media, 2013. ISBN 3662049996.

[66] A. Einstein. Über die von der molekularkinetischen theorie der wärme geforderte bewegung von in ruhenden flüssigkeiten suspendierten teilchen. *Annalen der Physik*, 322(8):549–560, 1905. doi: 10.1002/andp.19053220806.

[67] Allen D. Elster. Active shimming, 2024. URL `https://mriquestions.com/active-shimming.html`.

[68] M. Fixman. Dynamics of semidilute polymer rods: An alternative to cages. *Phys Rev Lett*, 55(22):2429–2432, 1985. ISSN 1079-7114 (Electronic) 0031-9007 (Linking). doi: 10.1103/PhysRevLett.55.2429.

[69] E.J. Fordham, L. Venkataramanan, Mitchell, J., and A. Valori. What are, and what are not, inverse laplace transforms. 2017.

[70] J. J. Fripiat, M. Letellier, P. Levitz, John Meurig Thomas, Leslie Fowden, Richard Maling Barrer, and P. B. Tinker. Interaction of water with clay surfaces. *Philosophical Transactions of the Royal Society of London. Series A, Mathematical and Physical Sciences*, 311(1517):287–299, 1997. doi: 10.1098/rsta.1984.0029.

[71] Mohit Garg, Varvara Apostolopoulou-Kalkavoura, Mathieu Linares, Tahani Kaldéus, Eva Malmström, Lennart Bergström, and Igor Zozoulenko. Moisture uptake in nanocellulose: the effects of relative humidity, temperature and degree of crystallinity. *Cellulose*, 28(14):9007–9021, 2021. ISSN 1572-882X. doi: 10.1007/s10570-021-04099-9.

[72] Yong Geng, Pedro L. Almeida, Gabriel M. Feio, João L. Figueirinhas, and Maria H. Godinho. Water-based cellulose liquid crystal system investigated by rheo-nmr. *Macromolecules*, 46(11):4296–4302, 2013. doi: 10.1021/ma400601b.

[73] J. George and S. N. Sabapathi. Cellulose nanocrystals: synthesis, functional properties, and applications. *Nanotechnol Sci Appl*, 8:45–54, 2015. doi: 10.2147/nsa.S64386.

[74] A. Ghilan, R. Nicu, D. E. Ciolacu, and F. Ciolacu. Insight into the latest medical applications of nanocellulose. *Materials (Basel)*, 16(12), 2023. doi: 10.3390/ma16124447.

[75] Derek G. Gray. Order and gelation of cellulose nanocrystal suspensions: an overview of some issues. *Philosophical Transactions of the Royal Society A: Mathematical, Physical and Engineering Sciences*, 376(2112):20170038, 2018. doi: doi:10.1098/rsta.2017.0038.

[76] A. Gupta, T. Stait-Gardner, and W. S. Price. Is it time to forgo the use of the terms "spin-lattice" and "spin-spin" relaxation in nmr and mri? *J Phys Chem Lett*, 12(27): 6305–6312, 2021. doi: 10.1021/acs.jpclett.1c00945.

[77] Youssef Habibi, Lucian A. Lucia, and Orlando J. Rojas. Cellulose nanocrystals: Chemistry, self-assembly, and applications. *Chemical Reviews*, 110(6):3479–3500, 2010. ISSN 0009-2665. doi: 10.1021/cr900339w.

[78] E.L. Hahn. Spin echoes. *Physical Review*, 80(4):580–594, 1950. doi: 10.1103/PhysRev.80.580. PR.

[79] Hikaru Hasegawa, Yoshiki Horikawa, and Toshiyuki Shikata. Cellulose nanocrystals as a model substance for rigid rod particle suspension rheology. *Macromolecules*, 53(7): 2677–2685, 2020. ISSN 0024-9297 1520-5835. doi: 10.1021/acs.macromol.9b02641.

[80] P.C. Hiemenz and R. Rajagopalan. *Principles of Colloid and Surface Chemistry, Third Edition, Revised and Expanded*. Taylor & Francis, 1997. ISBN 9780824793975.

[81] Asako Hirai, Osamu Inui, Fumitaka Horii, and Masaki Tsuji. Phase separation behavior in aqueous suspensions of bacterial cellulose nanocrystals prepared by sulfuric acid treatment. *Langmuir*, 25(1):497–502, 2009. ISSN 0743-7463. doi: 10.1021/la802947m. doi: 10.1021/la802947m.

[82] W. M. Holmes, M. R. Lopez-Gonzalez, and P. T. Callaghan. Fluctuations in shear-banded flow seen by nmr velocimetry. *Europhysics Letters*, 64(2):274–280, 2003. ISSN 0295-5075. doi: 10.1209/epl/i2003-00613-1.

[83] J.P. Hornak. *The Basics of MRI*. Interactive Learning Software, 2012. URL `http://www.cis.rit.edu/htbooks/mri/`.

[84] S. Jacob, R. R, S. Antony, A. Madhavan, R. Sindhu, M. Kumar Awasthi, M. Kuddus, S. Pillai, S. Varjani, A. Pandey, and P. Binod. Nanocellulose in tissue engineering and bioremediation: mechanism of action. *Bioengineered*, 13(5):12823–12833, 2022. ISSN 2165-5979 (Print) 2165-5979. doi: 10.1080/21655979.2022.2074739.

[85] Jayesha S. Jayaratne, Sarah L. Codd, Rehab N. Al-Kaby, Josephine Maley, Timothy I. Brox, Petrik Galvosas, and Joseph D. Seymour. Large amplitude oscillatory shear rheo-nmr velocimetry. *Physics of Fluids*, 35(9):093105, 2023. ISSN 1070-6631. doi: 10.1063/5.0161704.

[86] Yogesh M Joshi, G.Ranjith K Reddy, Ajit L Kulkarni, Nishant Kumar, and Raj P Chhabra. Rheological behaviour of aqueous suspensions of laponite: new insights into the ageing phenomena. *Proceedings of the Royal Society A: Mathematical, Physical and Engineering Sciences*, 464(2090):469–489, 2008. doi: doi:10.1098/rspa.2007.0250.

[87] Yogesh M. Joshi, Shrajesh Patel, and Khushboo Suman. Aqueous laponite® dispersions are attractive gels, not repulsive wigner glasses: A critical commentary). *Journal of Rheology*, 68(1):145–152, 2024. ISSN 0148-6055. doi: 10.1122/8.0000743.

[88] R. Kadar, S. Spirk, and T. Nypelo. Cellulose nanocrystal liquid crystal phases: Progress and challenges in characterization using rheology coupled to optics, scattering, and spectroscopy. *ACS Nano*, 15(5):7931–7945, 2021. ISSN 1936-0851. doi: 10.1021/acsnano.0c09829.

[89] Manjir Sarma Kataki, Bibhuti Bhusan Kakoti, Kangkan Deka, and Ananya Rajkumari. *Nanotechnology Applications in Natural Nanoclays Production and Application for Better Sustainability*, pages 159–171. 2022. doi: https://doi.org/10.1002/9781119650294.ch10.

[90] J. Keeler. *Understanding NMR spectroscopy*. Chichester, England Hoboken, NJ : Wiley, 2005.

[91] G. Kiaee, N. Dimitrakakis, S. Sharifzadeh, H. J. Kim, R. K. Avery, K. M. Moghaddam, R. Haghniaz, E. P. Yalcintas, N. R. Barros, S. Karamikamkar, A. Libanori, A. Khademhosseini, and P. Khoshakhlagh. Laponite-based nanomaterials for drug delivery. *Adv Healthc Mater*, 11(7):e2102054, 2022. ISSN 2192-2640 (Print) 2192-2640. doi: 10.1002/adhm.202102054.

[92] Dieter Klemm, Dieter Schumann, Friederike Kramer, Nadine Heßler, Michael Hornung, Hans-Peter Schmauder, and Silvia Marsch. Nanocelluloses as innovative polymers in research and application. *Polysaccharides ii*, pages 49–96, 2006. ISSN 3540371028.

[93] Quirine Krol, Evan Scherrer, Matthew Skuntz, Sarah Codd, Alex Hansen, and Joseph Seymour. Rapid mri profiling of liquid water content in snow: Melt and stability during first wetting and rain on snow events. *International Snow Science Workshop*, 2024.

[94] R. Kupferman, M. N. Kawaguchi, and M. M. Denn. Emergence of structure in a model of liquid crystalline polymers with elastic coupling. *Journal of Non-Newtonian Fluid Mechanics*, 91(2-3):255–271, 2000. doi: 10.1016/S0377-0257(99)00098-1.

[95] Romano Lapasin, Mario Grassi, Michela Abrami, and Urška Šebenik. Structural evolution of salt-free aqueous laponite dispersions: A study based on low-field nmr relaxometry and rheological investigations. *Colloids and Surfaces A: Physicochemical and Engineering Aspects*, 602:125126, 2020. ISSN 0927-7757. doi: https://doi.org/10.1016/j.colsurfa.2020.125126.

[96] Ronald G. Larson. *The Structure and Rheology of Complex Fluids*. Oxford University Press, 1999.

[97] Ronald G. Larson and Masao Doi. Mesoscopic domain theory for textured liquid crystalline polymers. *Journal of Rheology*, 35(4):539–563, 1991. ISSN 0148-6055. doi: 10.1122/1.550180.

[98] Malcolm H Levitt. *Spin dynamics: basics of nuclear magnetic resonance*. John Wiley & Sons, 2008. ISBN 0470511184.

[99] Jennifer Lewis and Shmuel Rubinstein. Ap 225: Introduction to soft matter. 2018.

[100] Jianshan Liao, Kim Anh Pham, and Victor Breedveld. Rheological characterization and modeling of cellulose nanocrystal and tempo-oxidized cellulose nanofibril suspensions. *Cellulose*, 27(7):3741–3757, 2020. doi: 10.1007/s10570-020-03048-2.

[101] Daniel López-Angulo, Ana Mônica Q. B. Bittante, Carla G. Luciano, German Ayala-Valencia, Christian H. C. Flaker, Madeleine Djabourov, and Paulo José do Amaral Sobral. Effect of laponite® on the structure, thermal stability and barrier properties of nanocomposite gelatin films. *Food Bioscience*, 35:100596, 2020. ISSN 2212-4292. doi: https://doi.org/10.1016/j.fbio.2020.100596.

[102] James Clerk Maxwell. Iv. on the dynamical theory of gases. *Philosophical Transactions of the Royal Society of London*, 157:49–88, 1867. doi: doi:10.1098/rstl.1867.0004.

[103] D.W. Mccall, D.C. Douglass, and W. Anderson, E. Self-diffusion studies by means of nuclear magnetic resonance spin-echo techniques.

[104] J. T. McNamara, J. L. Morgan, and J. Zimmer. A molecular description of cellulose biosynthesis. *Annu Rev Biochem*, 84:895–921, 2015. doi: 10.1146/annurev-biochem-060614-033930.

[105] S. Meiboom and D. Gill. Modified spin-echo method for measuring nuclear relaxation times. *Review of Scientific Instruments*, 29(8):688–691, 1958. ISSN 0034-6748. doi: 10.1063/1.1716296.

[106] Danila Merino, Bárbara Tomadoni, María Florencia Salcedo, Andrea Yamila Mansilla, Claudia Anahí Casalongué, and Vera Alejandra Alvarez. *Nanoclay as Carriers of Bioactive Molecules Applied to Agriculture*, pages 433–453. Springer International Publishing, Cham, 2021. ISBN 978-3-030-36268-3. doi: 10.1007/978-3-030-36268-3_62.

[107] J. Mewis and Paula Moldenaers. Rheometry of complex fluids. *Korea Aust Rheol J*, 11, 1999.

[108] J. Mewis and N.J. Wagner. *Colloidal Suspension Rheology*. Cambridge University Press, 2012. ISBN 9780521515993.

[109] T.G. Mezger. *Applied Rheology: With Joe Flow on Rheology Road*. Anton Paar GmbH, 2018. ISBN 9783950401608.

[110] Thomas G. Mezger. *The Rheology Handbook*. Vincentz Network, Hannover, 2nd edition, 2006.

[111] Joel Mokyr and Robert H Strotz. The second industrial revolution, 1870-1914. *Storia dell'economia Mondiale*, 21945(1):219–245, 1998.

[112] Aref Abbasi Moud, Mohammad Arjmand, Jie Liu, Yongfei Yang, Amir Sanati-Nezhad, and S. Hossein Hejazi. Cellulose nanocrystal structure in the presence of salts. *Cellulose*, 26(18):9387–9401, 2019. ISSN 1572-882X. doi: 10.1007/s10570-019-02734-0.

[113] Claude-Louis-Marie-Henri Navier. Sur les lois du mouvement des fluides, 1827.

[114] Isaac Newton. *Philosophiae Naturalis Principia Mathematica*. London, 1687.

[115] Theo Odijk. Theory of lyotropic polymer liquid crystals. *Macromolecules*, 19(9):2313–2329, 1986. ISSN 0024-9297.

[116] Hale Oguzlu, Christophe Danumah, and Yaman Boluk. Colloidal behavior of aqueous cellulose nanocrystal suspensions. *Current Opinion in Colloid & Interface Science*, 29: 46–56, 2017. ISSN 1359-0294. doi: https://doi.org/10.1016/j.cocis.2017.02.002.

[117] Xuan-Ran Ong, Adrielle Xianwen Chen, Ning Li, Yi Yan Yang, and He-Kuan Luo. Nanocellulose: Recent advances toward biomedical applications. *Small Science*, 3(2): 2200076, 2023. doi: 10.1002/smsc.202200076.

[118] Shigharu Onogi and Tadahiro Asada. *Rheology and Rheo-Optics of Polymer Liquid Crystals*, pages 127–147. Springer US, Boston, MA, 1980. doi: 10.1007/978-1-4684-3740-9_9.

[119] Lars Onsager. The effects of shape on the interaction of colloidal particles. *Annals of the New York Academy of Sciences*, 51(4):627–659, 1949. ISSN 0077-8923.

[120] G. Ovarlez, S. Rodts, X. Chateau, and P. Coussot. Phenomenology and physical origin of shear localization and shear banding in complex fluids. *Rheologica Acta*, 48 (8):831–844, 2009. doi: 10.1007/s00397-008-0344-6.

[121] Blaise Pascal. *Traitez de l'Equilibre des Liqueurs (Treatise on the Equilibrium of Fluids)*. 1663.

[122] J. K. Phalakornkul, A. P. Gast, and R. Pecora. Rotational and translational dynamics of rodlike polymers: A combined transient electric birefringence and dynamic light scattering study. *Macromolecules*, 32(9):3122–3135, 1999. ISSN 0024-9297 1520-5835. doi: 10.1021/ma981640d.

[123] Tuan Phan-Xuan, Axel Thuresson, Marie Skepö, Ana Labrador, Romain Bordes, and Aleksandar Matic. Aggregation behavior of aqueous cellulose nanocrystals: the effect of inorganic salts. *Cellulose*, 23(6):3653–3663, 2016. ISSN 1572-882X. doi: 10.1007/s10570-016-1080-1.

[124] Rodrigo Cesar Pierozan, Abdurrahman Almikati, Gregorio Luis Silva Araujo, and Jorge Gabriel Zornberg. Optical and physical properties of laponite for use as clay surrogate in geotechnical models. *Geotechnical Testing Journal*, 45(1):79–100, 2022. ISSN 0149-6115. doi: 10.1520/gtj20210100.

[125] Frédéric Pignon, Albert Magnin, and Jean-Michel Piau. Thixotropic colloidal suspensions and flow curves with minimum: Identification of flow regimes and rheometric consequences. *Journal of Rheology*, 40(4):573–587, 1996. ISSN 0148-6055. doi: 10.1122/1.550759.

[126] Frédéric Pignon, Jean-Michel Piau, and Albert Magnin. Structure and pertinent length scale of a discotic clay gel. *Physical Review Letters*, 76(25):4857–4860, 1996. doi: 10.1103/PhysRevLett.76.4857.

[127] Frédéric Pignon, Albert Magnin, and Jean-Michel Piau. Thixotropic behavior of clay dispersions: Combinations of scattering and rheometric techniques. *Journal of Rheology*, 42(6):1349–1373, 1998. ISSN 0148-6055. doi: 10.1122/1.550964.

[128] Tirath Raj, K. Chandrasekhar, A. Naresh Kumar, and Sang-Hyoun Kim. Lignocellulosic biomass as renewable feedstock for biodegradable and recyclable plastics production: A sustainable approach. *Renewable and Sustainable Energy Reviews*, 158: 112130, 2022. doi: 10.1016/j.rser.2022.112130.

[129] Hairunnisa Ramli, Nurul Fatahah Asyqin Zainal, Michael Hess, and Chin Han Chan. Basic principle and good practices of rheology for polymers for teachers and beginners. *Chemistry Teacher International*, 4(4):307–326, 2022. doi: doi:10.1515/cti-2022-0010.

[130] J. D. F. Ramsay. Colloidal properties of synthetic hectorite clay dispersions: I. rheology. *Journal of Colloid and Interface Science*, 109(2):441–447, 1986. ISSN 0021-9797. doi: https://doi.org/10.1016/0021-9797(86)90321-8.

[131] J. D. F. Ramsay and P. Lindner. Small-angle neutron scattering investigations of the structure of thixotropic dispersions of smectite clay colloids. *Journal of the Chemical Society, Faraday Transactions*, 89(23):4207–4214, 1993. ISSN 0956-5000. doi: 10.1039/FT9938904207.

[132] C.D.C. Reeve. *Cratylus*. Hackett Publishing Company, 1998. ISBN 9780872204164.

[133] A. D. Rey and M. M. Denn. Dynamical phenomena in liquid-crystalline materials. *Annual Review of Fluid Mechanics*, 34:233–266, 2002. ISSN 0066-4189. doi: 10.1146/annurev.fluid.34.082401.191847.

[134] Maria J. Rodrigo, Maria J. Cardiel, Jose M. Fraile, Jose A. Mayoral, Luis E. Pablo, and Elena Garcia-Martin. Laponite for biomedical applications: An ophthalmological perspective. *Materials Today Bio*, 24:100935, 2024. ISSN 2590-0064. doi: https://doi.org/10.1016/j.mtbio.2023.100935.

[135] S. Rodts, J. C. Baudez, and P. Coussot. From "discrete" to "continuum" flow in foams. *Europhys. Lett.*, 69(4):636–642, 2005.

[136] S. A. Rogers, D. Vlassopoulos, and P. T. Callaghan. Aging, yielding, and shear banding in soft colloidal glasses. *Physical Review Letters*, 100(12):128304, 2008. doi: 10.1103/PhysRevLett.100.128304.

[137] Sintu Rongpipi, Dan Ye, Enrique D. Gomez, and Esther W. Gomez. Progress and opportunities in the characterization of cellulose – an important regulator of cell wall growth and mechanics. *Frontiers in Plant Science*, 9, 2019. doi: 10.3389/fpls.2018.01894.

[138] W.B. Russel, D.A. Saville, and W.R. Schowalter. *Colloidal Dispersions*. Cambridge University Press, 1991. ISBN 9780521426008.

[139] T.R. Saarinen and C.S. Johnson. Imaging of transient magnetization gratings in nmr. analogies with laser-induced gratings and applications to diffusion and flow. *Journal of Magnetic Resonance (1969)*, 78(2):257–270, 1988. ISSN 0022-2364. doi: https://doi.org/10.1016/0022-2364(88)90269-7.

[140] Joseph D. Seymour, Arvind Caprihan, Stephen A. Altobelli, and Eiichi Fukushima. Pulsed gradient spin echo nuclear magnetic resonance imaging of diffusion in granular flow. *Physical Review Letters*, 84(2):266–269, 2000. doi: 10.1103/PhysRevLett.84.266.

[141] S. Shafiei-Sabet, W. Y. Hamad, and S. G. Hatzikiriakos. Rheology of nanocrystalline cellulose aqueous suspensions. *Langmuir*, 28(49):17124–33, 2012. doi: 10.1021/la303380v.

[142] S. Shafiei-Sabet, W. Y. Hamad, and S. G. Hatzikiriakos. Ionic strength effects on the microstructure and shear rheology of cellulose nanocrystal suspensions. *Cellulose*, 21 (5):3347–3359, 2014. ISSN 1572-882X. doi: 10.1007/s10570-014-0407-z.

[143] Chetan Sharma, Pavan Harshit Manepalli, Aditya Thatte, Sabu Thomas, Nandakumar Kalarikkal, and Sajid Alavi. Biodegradable starch/pvoh/laponite rd-based bionanocomposite films coated with graphene oxide: Preparation and performance characterization for food packaging applications. *Colloid and Polymer Science*, 295(9): 1695–1708, 2017. ISSN 1435-1536. doi: 10.1007/s00396-017-4114-9.

[144] Jamileh Shojaeiarani, Dilpreet S. Bajwa, and Saptaparni Chanda. Cellulose nanocrystal based composites: A review. *Composites Part C: Open Access*, 5:100164, 2021. doi: 10.1016/j.jcomc.2021.100164.

[145] Hartmut Siebert, David A. Grabowski, and Claudia Schmidt. Rheo-nmr study of a non-flow-aligning side-chain liquid crystal polymer in nematic solution. *Rheologica Acta*, 36(6):618–627, 1997. doi: 10.1007/bf00367357.

[146] Shiva Singh, Shakshi Bhardwaj, Pragya Tiwari, Keshav Dev, Kaushik Ghosh, and Pradip K. Maji. Recent advances in cellulose nanocrystals-based sensors: a review. *Materials Advances*, 5(7):2622–2654, 2024. doi: 10.1039/D3MA00601H.

[147] Marian Smoluchowski. On the kinetic theory of the brownian molecular motion and of suspensions. *Annalen der Physik*, 21:756–780, 1906.

[148] Yi-Qiao Song, H. Cho, Tim Hopper, Andrew E. Pomerantz, and Phillip Zhe Sun. Magnetic resonance in porous media: Recent progress. *The Journal of Chemical Physics*, 128(5), 2008. ISSN 0021-9606. doi: 10.1063/1.2833581.

[149] Maribelle A. Stanley, Jayesha S. Jayaratne, Sarah L. Codd, Dilpreet S. Bajwa, James N. Wilking, and Joseph D. Seymour. Rheo-nmr velocimetry of nanocrystalline cellulose suspensions. *Applied Rheology*, 34(1), 2024. doi: doi:10.1515/arh-2024-0026.

[150] Maribelle A Stanley, Jayesha S Jayaratne, Sarah L Codd, James N Wilking, and Joseph D Seymour. Rheo-nmr velocimetry of nanocrystalline cellulose suspensions in sodium chloride. *Cellulose*, 2025. In preparation.

[151] S. T. Stealey, A. K. Gaharwar, and S. P. Zustiak. Laponite-based nanocomposite hydrogels for drug delivery applications. *Pharmaceuticals (Basel)*, 16(6), 2023. ISSN 1424-8247 (Print) 1424-8247. doi: 10.3390/ph16060821.

[152] E.O. Stejskal and J.E. Tanner. Spin diffusion measurements: Spin echoes in the presence of a time-dependent field gradient. *The Journal of Chemical Physics*, 42 (1):288–292, 2004. ISSN 0021-9606. doi: 10.1063/1.1695690.

[153] G.G. Stokes. *On the Theories of the Internal Friction of Fluids in Motion, and of the Equilibrium and Motion of Elastic Solids*. 1845.

[154] A. Stroobants, H. N. W. Lekkerkerker, and T. Odijk. Effect of electrostatic interaction on the liquid crystal phase transition in solutions of rodlike polyelectrolytes. *Macromolecules*, 19(8):2232–2238, 1986. doi: 10.1021/ma00162a020.

[155] Hajime Tanaka, Jacques Meunier, and Daniel Bonn. Nonergodic states of charged colloidal suspensions: Repulsive and attractive glasses and gels. *Physical Review E*, 69 (3):031404, 2004. doi: 10.1103/PhysRevE.69.031404. PRE.

[156] R. Tanaka, Y. Kashiwagi, Y. Okada, and T. Inoue. Viscoelastic relaxation of cellulose nanocrystals in fluids: Contributions of microscopic internal motions to flexibility. *Biomacromolecules*, 21(2):408–417, 2020. ISSN 1526-4602 (Electronic) 1525-7797 (Linking). doi: 10.1021/acs.biomac.9b00943.

[157] Dudley W. Thompson and James T. Butterworth. The nature of laponite and its aqueous dispersions. *Journal of Colloid and Interface Science*, 151(1):236–243, 1992. ISSN 0021-9797. doi: https://doi.org/10.1016/0021-9797(92)90254-J.

[158] H.C. Torrey. Bloch equations with diffusion terms. *Physical Review*, 104(3):563–565, 1956. doi: 10.1103/PhysRev.104.563. PR.

[159] D. Trache, A. F. Tarchoun, M. Derradji, T. S. Hamidon, N. Masruchin, N. Brosse, and M. H. Hussin. Nanocellulose: From fundamentals to advanced applications. *Front Chem*, 2020. doi: 10.3389/fchem.2020.00392.

[160] Esteban E. Ureña-Benavides, Geyou Ao, Virginia A. Davis, and Christopher L. Kitchens. Rheology and phase behavior of lyotropic cellulose nanocrystal suspensions. *Macromolecules*, 44(22):8990–8998, 2011. ISSN 0024-9297. doi: 10.1021/ma201649f.

[161] Liubov Vakhitova, Kostyantyn Kalafat, Ramil Vakhitov, Varvara Drizhd, Nadiia Taran, and Volodymyr Bessarabov. Nano-clays as rheology modifiers in intumescent coatings for steel building structures. *Chemical Engineering Journal Advances*, 16: 100544, 2023. ISSN 2666-8211. doi: https://doi.org/10.1016/j.ceja.2023.100544.

[162] Paul Van der Schoot. Molecular theory of nematic (and other) liquid crystals. *Springer International Publishing*, 1007:978–3, 2022.

[163] H. Van Olphen. Rheological phenomena of clay sols in connection with the charge distribution on the micelles. *Discussions of the Faraday Society*, 11(0):82–84, 1951. ISSN 0366-9033. doi: 10.1039/DF9511100082.

[164] J. Van Rie, C. Schütz, A. Gençer, S. Lombardo, U. Gasser, S. Kumar, G. Salazar-Alvarez, K. Kang, and W. Thielemans. Anisotropic diffusion and phase behavior of cellulose nanocrystal suspensions. *Langmuir*, 35(6):2289–2302, 2019. doi: 10.1021/acs.langmuir.8b03792.

[165] L. Venkataramanan, Song Yi-Qiao, and M. D. Hurlimann. Solving fredholm integrals of the first kind with tensor product structure in 2 and 2.5 dimensions. *IEEE Transactions on Signal Processing*, 50(5):1017–1026, 2002. ISSN 1941-0476. doi: 10.1109/78.995059.

[166] César Viseras, Rita Sánchez-Espejo, Rosanna Palumbo, Ninfa Liccardi, Fátima García-Villén, Ana Borrego-Sánchez, Marina Massaro, Serena Riela, and Alberto López-Galindo. Clays in cosmetics and personal-care products. *Clays and Clay Minerals*, 69(5):561–575, 2021. ISSN 0009-8604. doi: 10.1007/s42860-021-00154-5.

[167] Gert Jan Vroege and Henk NW Lekkerkerker. Phase transitions in lyotropic colloidal and polymer liquid crystals. *Reports on Progress in Physics*, 55(8):1241, 1992. ISSN 0034-4885.

[168] Michael Wendt. Second order shimming of high field magnets.

[169] Norbert Willenbacher. Unusual thixotropic properties of aqueous dispersions of laponite rd. *Journal of Colloid and Interface Science*, 182(2):501–510, 1996. ISSN 0021-9797.

[170] X. Xiao and P. Sheng. Generalized onsager theory of liquid crystals. *Phys Rev E Stat Nonlin Soft Matter Phys*, 88(6):062501, 2013. ISSN 1550-2376 (Electronic) 1539-3755 (Linking). doi: 10.1103/PhysRevE.88.062501.

[171] Y. Xu. *Rheology and Structure of Aqueous Nanocrystalline Cellulose Suspensions*. Thesis, University of Queensland, 2019.

[172] Y. Xu, A. D. Atrens, and J. R. Stokes. Rheology and microstructure of aqueous suspensions of nanocrystalline cellulose rods. *J Colloid Interface Sci*, 496:130–140, 2017. doi: 10.1016/j.jcis.2017.02.020.

[173] Yuan Xu, Aleks D. Atrens, and Jason R. Stokes. "liquid, gel and soft glass" phase transitions and rheology of nanocrystalline cellulose suspensions as a function of concentration and salinity. *Soft Matter*, 14:1953–1963, 2018. doi: 10.1039/C7SM02470C.

[174] Yuan Xu, Aleks Atrens, and Jason R. Stokes. A review of nanocrystalline cellulose suspensions: Rheology, liquid crystal ordering and colloidal phase behaviour. *Advances in Colloid and Interface Science*, 275:102076, 2020. ISSN 0001-8686. doi: https://doi.org/10.1016/j.cis.2019.102076.

[175] Matthew C. Young, Madison L. Nelson, Dylan S. Cousins, David B. Hodge, and Joseph D. Seymour. Nmr relaxometry characterization of water adsorption in corn stover anatomical fractions. *Cellulose*, 30(9):5473–5488, 2023. ISSN 1572-882X. doi: 10.1007/s10570-023-05229-1. URL `https://doi.org/10.1007/s10570-023-05229-1`.

[176] B. Zakani and D. Grecov. Effect of ultrasonic treatment on yield stress of highly concentrated cellulose nano-crystalline (cnc) aqueous suspensions. *Carbohydr Polym*, 291:119651, 2022. doi: 10.1016/j.carbpol.2022.119651.

[177] Hans Christian Öttinger. *Stochastic processes in polymeric fluids : tools and examples for developing simulation algorithms*. Springer, 1996. doi: 10.1007/978-3-642-58290-5.

APPENDIX

SUPPORTING INFORMATION FOR RHEO-NMR VELOCIMETRY OF NANOCRYSTALLINE CELLULOSE SUSPENSIONS IN SODIUM CHLORIDE

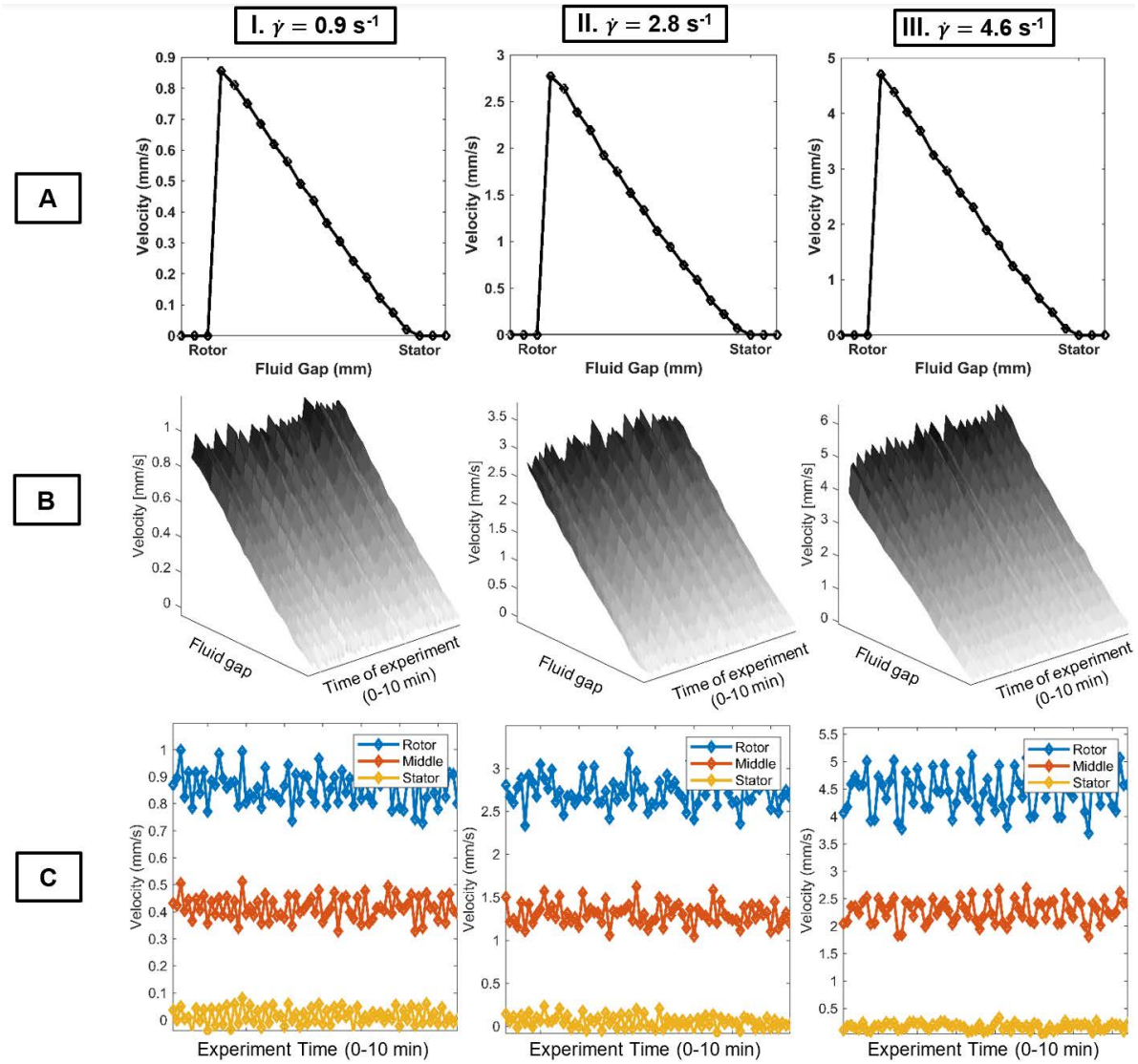


Figure A.1: **Rows A-B, Columns I-III**. 1D NMR velocimetry experiments for a 3% w/v NCC suspension. **Rows A:** Steady state, 1D velocity profiles, with 16 scans and total acquisition time of 1 minute, 12 seconds and a pixel resolution of approximately 65 µm. **B:** Surface plots for 1D velocity profiles from an unsteady-state experiment with 75 experiments averaged over 2 scans and total time acquisition of approximately 10 minutes, 12 seconds. **C:** Velocity profiles from the same unsteady-state experiment as B, but displayed at three discrete points across the 1 mm sample Couette cell fluid gap (rotor, middle and stator) for all time points, which demonstrate velocity changes across the experiment time and fluid gap. **Columns I:** Shear rate of $\dot{\gamma} = 0.9$ s^{-1}; **II:** Shear rate of $\dot{\gamma} = 2.8$ s^{-1}; **III:** Shear rate of $\dot{\gamma} = 4.6$ s^{-1}. The data presents nearly Newtonian behavior for this concentration. Rotor and stator data points are approximately 58.6 µm from the physical walls.

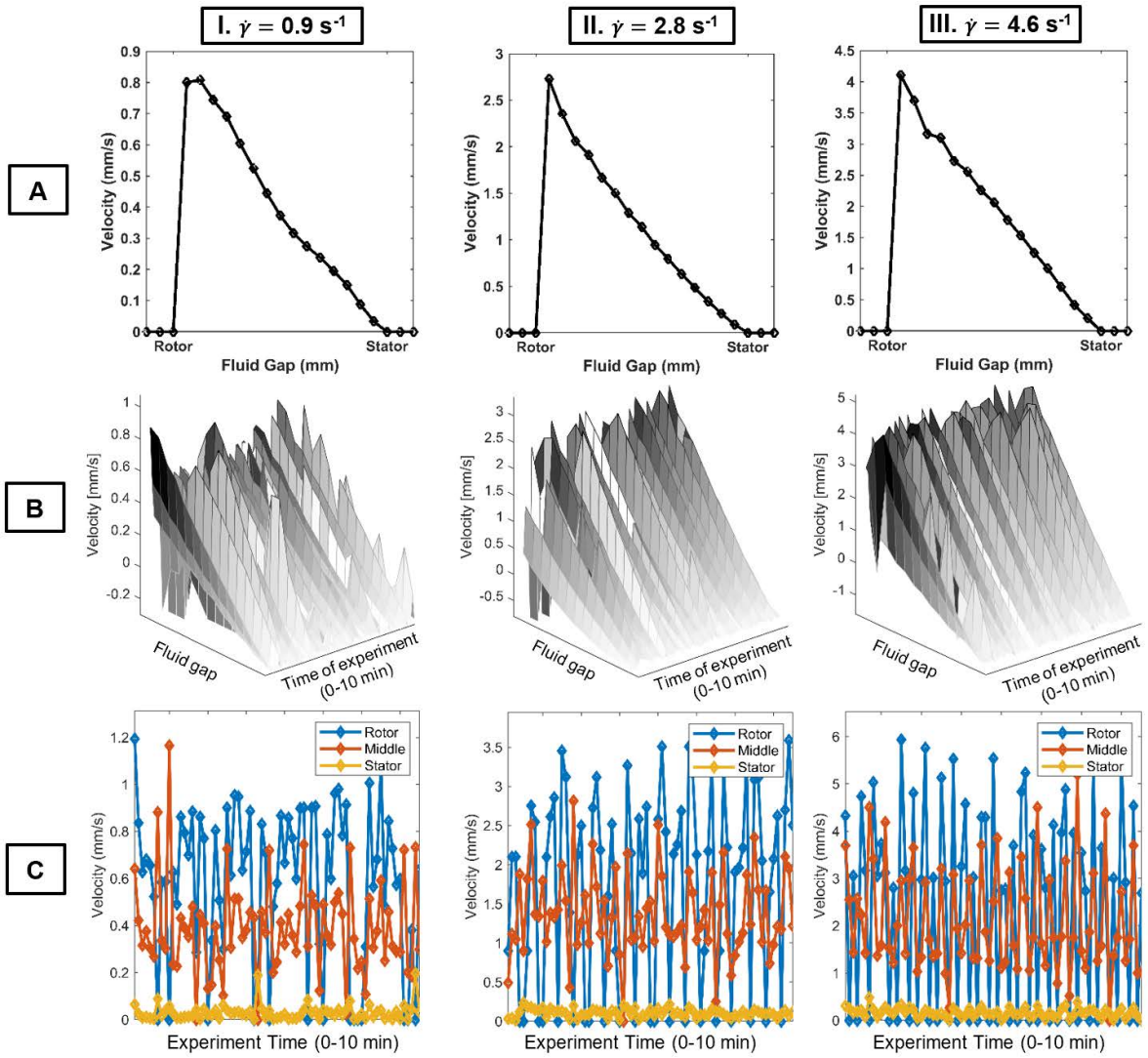


Figure A.2: **Rows A-B, Columns I-III**. 1D NMR velocimetry experiments for a 5% w/v NCC suspension. **Rows A:** Steady state, 1D velocity profiles, with 16 scans and total acquisition time of 1 minute, 12 seconds and a pixel resolution of approximately 65 µm. **B:** Surface plots for 1D velocity profiles from an unsteady-state experiment with 75 experiments averaged over 2 scans and total time acquisition of approximately 10 minutes, 12 seconds. **C:** Velocity profiles from the same unsteady-state experiment as B, but displayed at three discrete points across the 1 mm sample Couette cell fluid gap (rotor, middle and stator) for all time points, which demonstrate velocity changes across the experiment time and fluid gap; significant fluctuations occur at this concentration, with a significant amount of correlation between peaks and troughs. **Columns I:** Shear rate of $\dot{\gamma} = 0.9$ s^{-1}; **II:** Shear rate of $\dot{\gamma} = 2.8$ s^{-1}; **III:** Shear rate of $\dot{\gamma} = 4.6$ s^{-1}. Rotor and stator data points are approximately 58.6 µm from the physical walls.

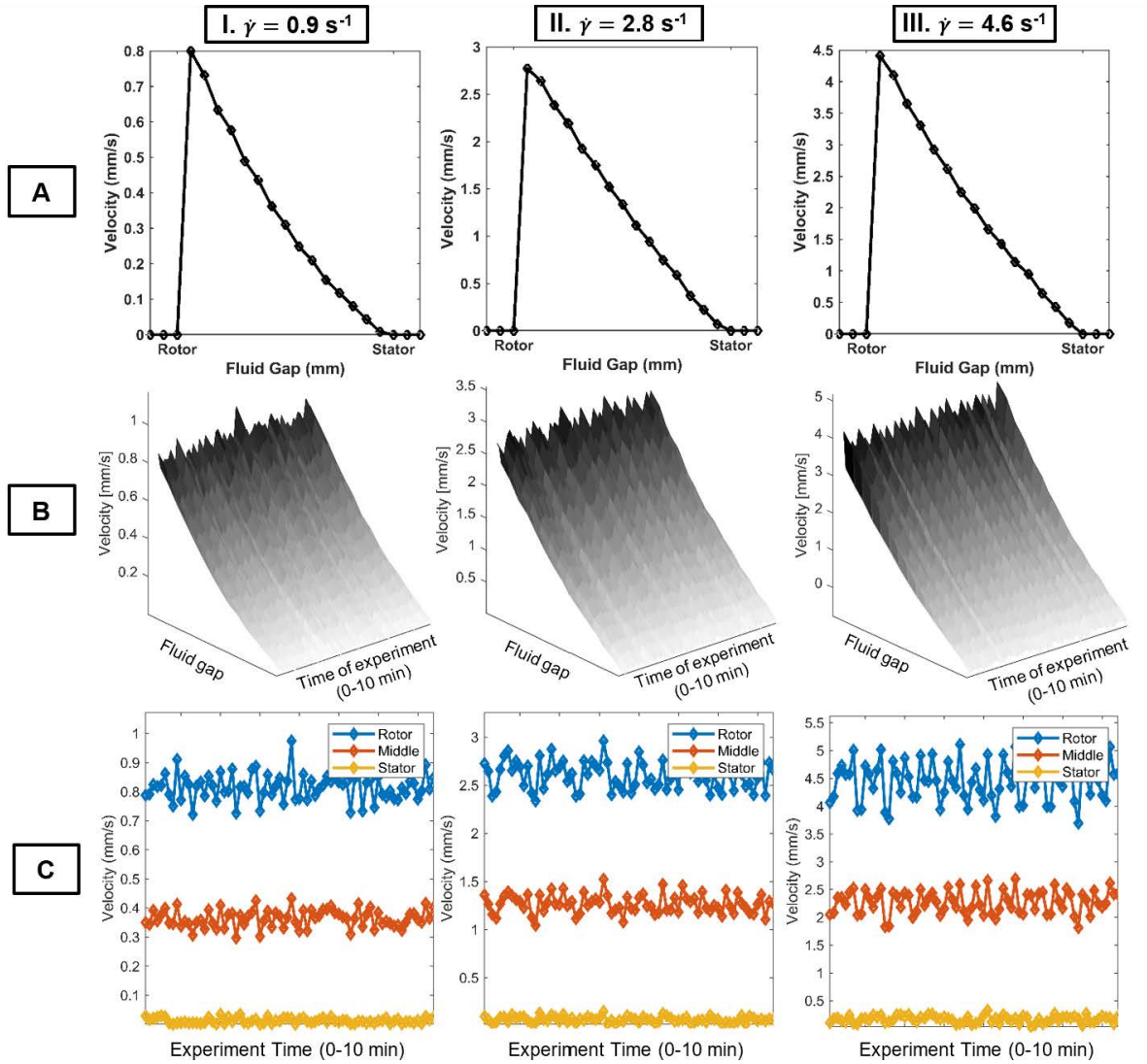


Figure A.3: **Rows A-B, Columns I-III**. 1D NMR velocimetry experiments for a 7% w/v NCC suspension. **Rows A:** Steady state, 1D velocity profiles, with 16 scans and total acquisition time of 1 minute, 12 seconds and a pixel resolution of approximately 65 µm. **B:** Surface plots for 1D velocity profiles from an unsteady-state experiment with 75 experiments averaged over 2 scans and total time acquisition of approximately 10 minutes, 12 seconds. **C:** Velocity profiles from the same unsteady-state experiment as B, but displayed at three discrete points across the 1 mm sample Couette cell fluid gap (rotor, middle and stator) for all time points, which demonstrate velocity changes across the experiment time and fluid gap. **Columns I:** Shear rate of $\dot{\gamma} = 0.9$ s^{-1}; **II:** Shear rate of $\dot{\gamma} = 2.8$ s^{-1}; **III:** Shear rate of $\dot{\gamma} = 4.6$ s^{-1}. The data presents nearly Newtonian behavior for this concentration. Rotor and stator data points are approximately 58.6 µm from the physical walls.

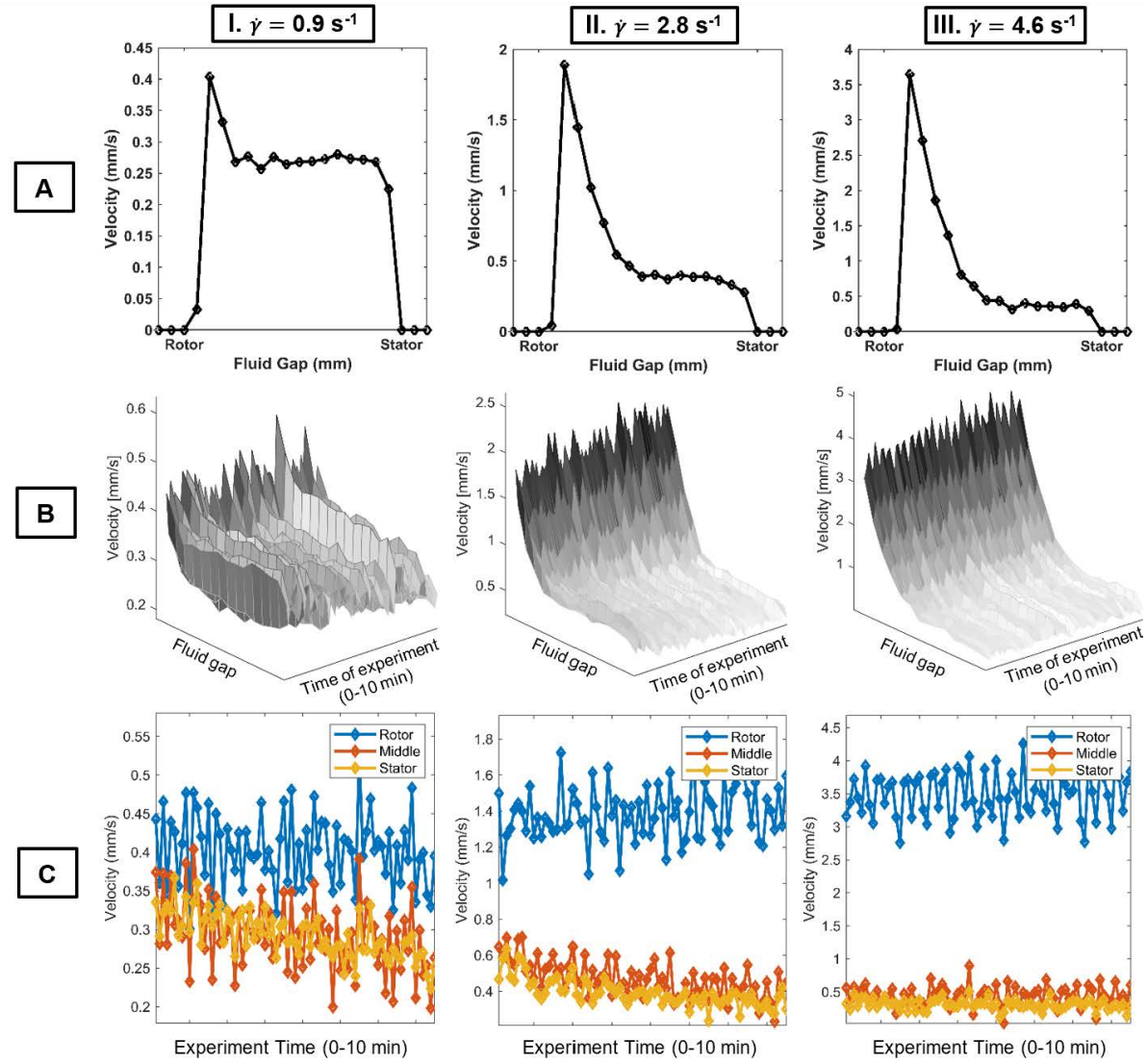


Figure A.4: **Rows A-B, Columns I-III**. 1D NMR velocimetry experiments for a 12% w/v NCC suspension. **Rows A:** Steady state, 1D velocity profiles, with 16 scans and total acquisition time of 1 minute, 12 seconds and a pixel resolution of approximately 65 µm. **B:** Surface plots for 1D velocity profiles from an unsteady-state experiment with 75 experiments averaged over 2 scans and total time acquisition of approximately 10 minutes, 12 seconds. **C:** Velocity profiles from the same unsteady-state experiment as B, but displayed at three discrete points across the 1 mm sample Couette cell fluid gap (rotor, middle and stator) for all time points, which demonstrate velocity changes across the experiment time and fluid gap. **Columns I:** Shear rate of $\dot{\gamma} = 0.9$ s^{-1}; **II:** Shear rate of $\dot{\gamma} = 2.8$ s^{-1}; **III:** Shear rate of $\dot{\gamma} = 4.6$ s^{-1}. The data demonstrates yielding, gel-like behavior for this concentration. Rotor and stator data points are approximately 58.6 µm from the physical walls.

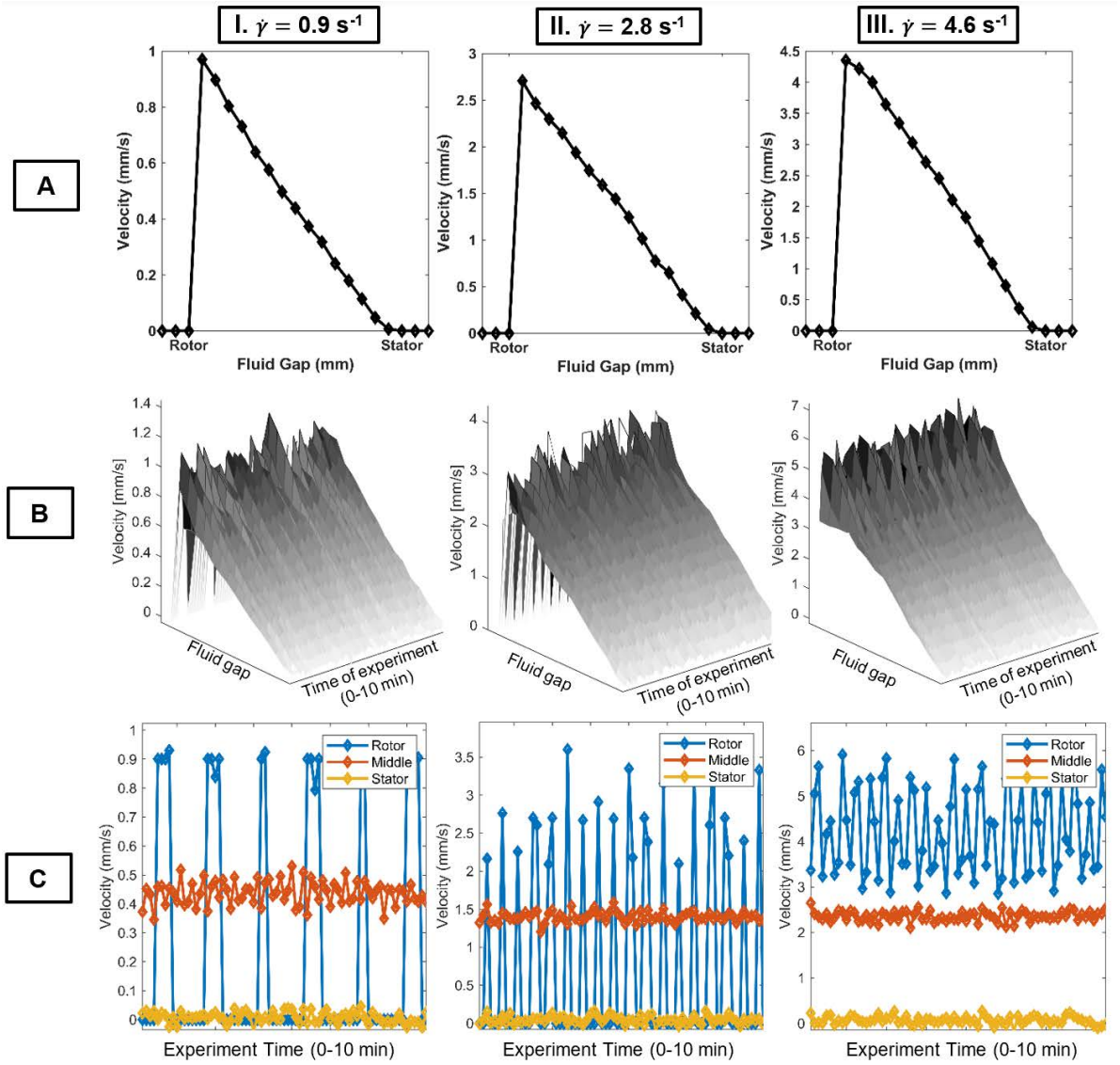


Figure A.5: **Rows A-B, Columns I-III**. 1D NMR velocimetry experiments for a 3% w/v NCC suspension in 0.1 M NaCl. **Rows A:** Steady state, 1D velocity profiles, with 16 scans and total acquisition time of 1 minute, 12 seconds and a pixel resolution of approximately 65 µm. **B:** Surface plots for 1D velocity profiles from an unsteady-state experiment with 75 experiments averaged over 2 scans and total time acquisition of approximately 10 minutes, 12 seconds. **C:** Velocity profiles from the same unsteady-state experiment as B, but displayed at three discrete points across the 1 mm sample Couette cell fluid gap (rotor, middle and stator) for all time points, which demonstrate velocity changes across the experiment time and fluid gap; significant, periodic fluctuations at the rotor occur for this concentration. **Columns I:** Shear rate of $\dot{\gamma} = 0.9$ s^{-1}; **II:** Shear rate of $\dot{\gamma} = 2.8$ s^{-1}; **III:** Shear rate of $\dot{\gamma} = 4.6$ s^{-1}. The data presents a Newtonian-like profile with complex behavior at the rotor. Rotor and stator data points are approximately 58.6 µm from the physical walls.

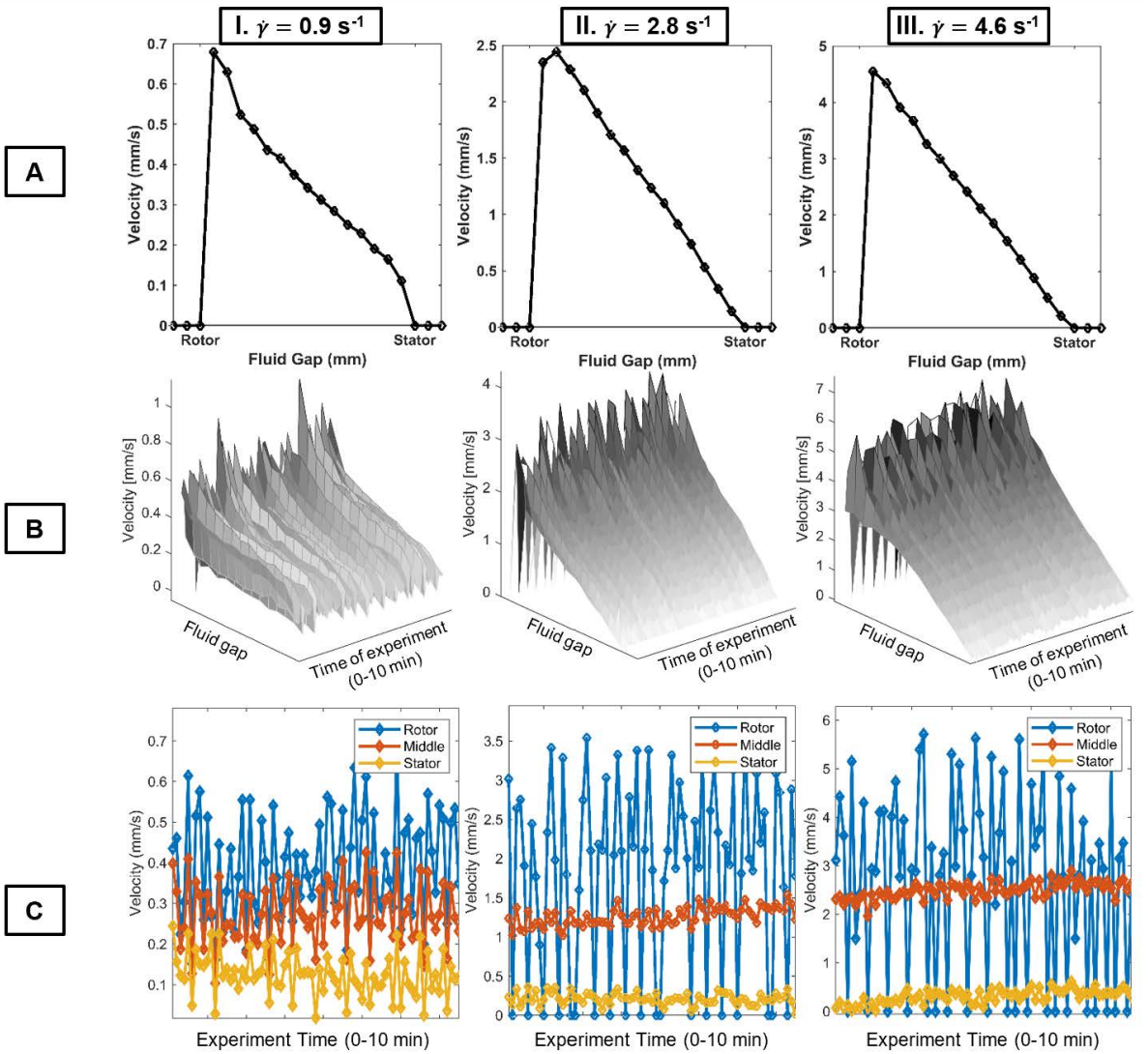


Figure A.6: **Rows A-B, Columns I-III**. 1D NMR velocimetry experiments for a 5% w/v NCC suspension in 0.05 M NaCl. **Rows A:** Steady state, 1D velocity profiles, with 16 scans and total acquisition time of 1 minute, 12 seconds and a pixel resolution of approximately 65 µm. **B:** Surface plots for 1D velocity profiles from an unsteady-state experiment with 75 experiments averaged over 2 scans and total time acquisition of approximately 10 minutes, 12 seconds. **C:** Velocity profiles from the same unsteady-state experiment as B, but displayed at three discrete points across the 1 mm sample Couette cell fluid gap (rotor, middle and stator) for all time points, which demonstrate velocity changes across the experiment time and fluid gap; significant fluctuations occur for this concentration. **Columns I:** Shear rate of $\dot{\gamma} = 0.9$ s^{-1}; **II:** Shear rate of $\dot{\gamma} = 2.8$ s^{-1}; **III:** Shear rate of $\dot{\gamma} = 4.6$ s^{-1}. The data presents shear-banding, chaotic behavior at $\dot{\gamma} = 0.9$ s^{-1} that consigns itself to the rotor at higher applied shear rates. Rotor and stator data points are approximately 58.6 µm from the physical walls.

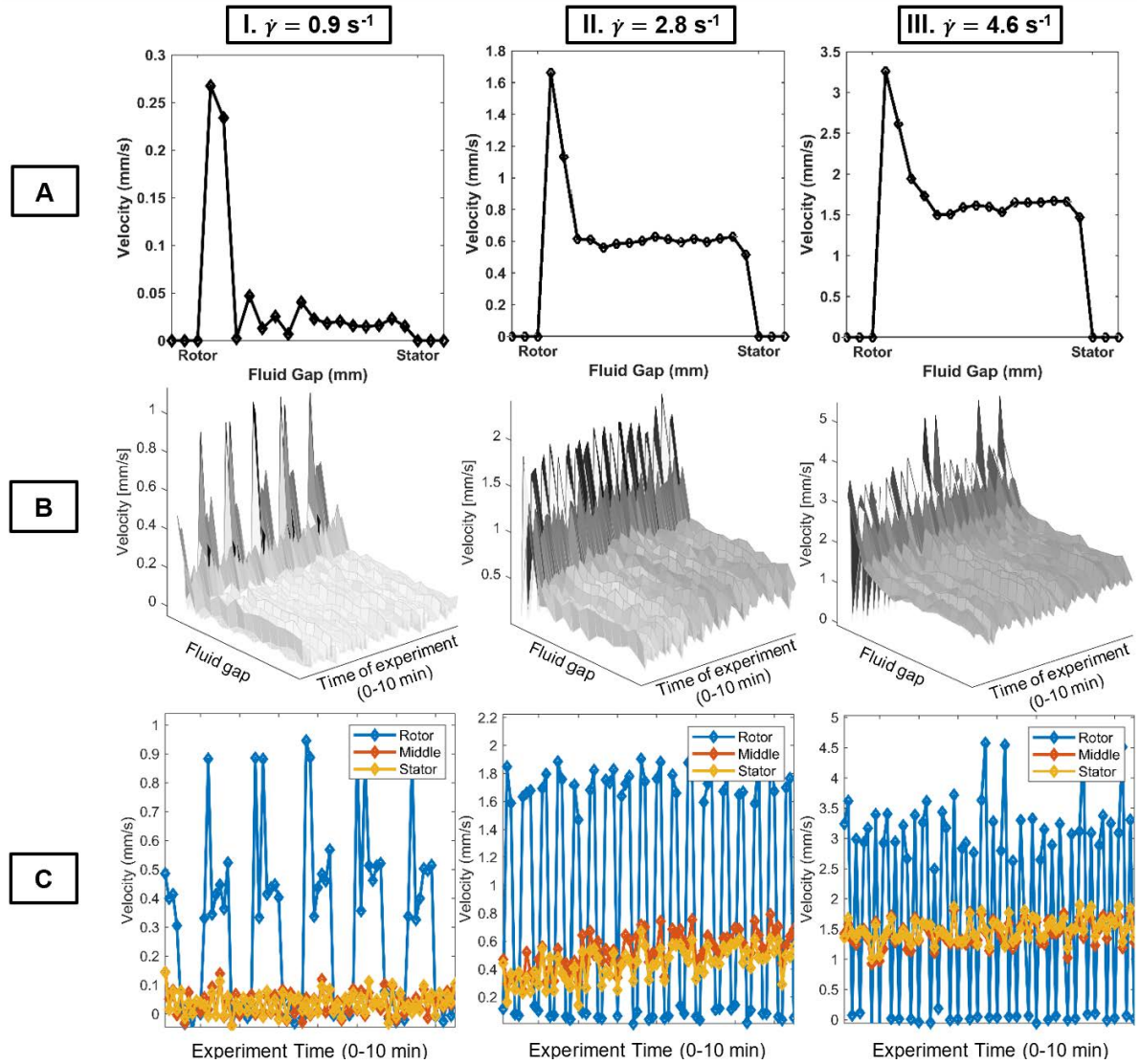


Figure A.7: **Rows A-B, Columns I-III**. 1D NMR velocimetry experiments for a 5% w/v NCC suspension in 0.1 M NaCl. **Rows A:** Steady state, 1D velocity profiles, with 16 scans and total acquisition time of 1 minute, 12 seconds and a pixel resolution of approximately 65 µm. **B:** Surface plots for 1D velocity profiles from an unsteady-state experiment with 75 experiments averaged over 2 scans and total time acquisition of approximately 10 minutes, 12 seconds. **C:** Velocity profiles from the same unsteady-state experiment as B, but displayed at three discrete points across the 1 mm sample Couette cell fluid gap (rotor, middle and stator) for all time points, which demonstrate velocity changes across the experiment time and fluid gap; significant periodic fluctuations occur for this concentration, with patterned behavior at $\dot{\gamma} = 0.9$ s^{-1}. **Columns I:** Shear rate of $\dot{\gamma} = 0.9$ s^{-1}; **II:** Shear rate of $\dot{\gamma} = 2.8$ s^{-1}; **III:** Shear rate of $\dot{\gamma} = 4.6$ s^{-1}. The data presents chaotic, complex behavior accompanied by a potential shear-thickening. Rotor and stator data points are approximately 58.6 µm from the physical walls.

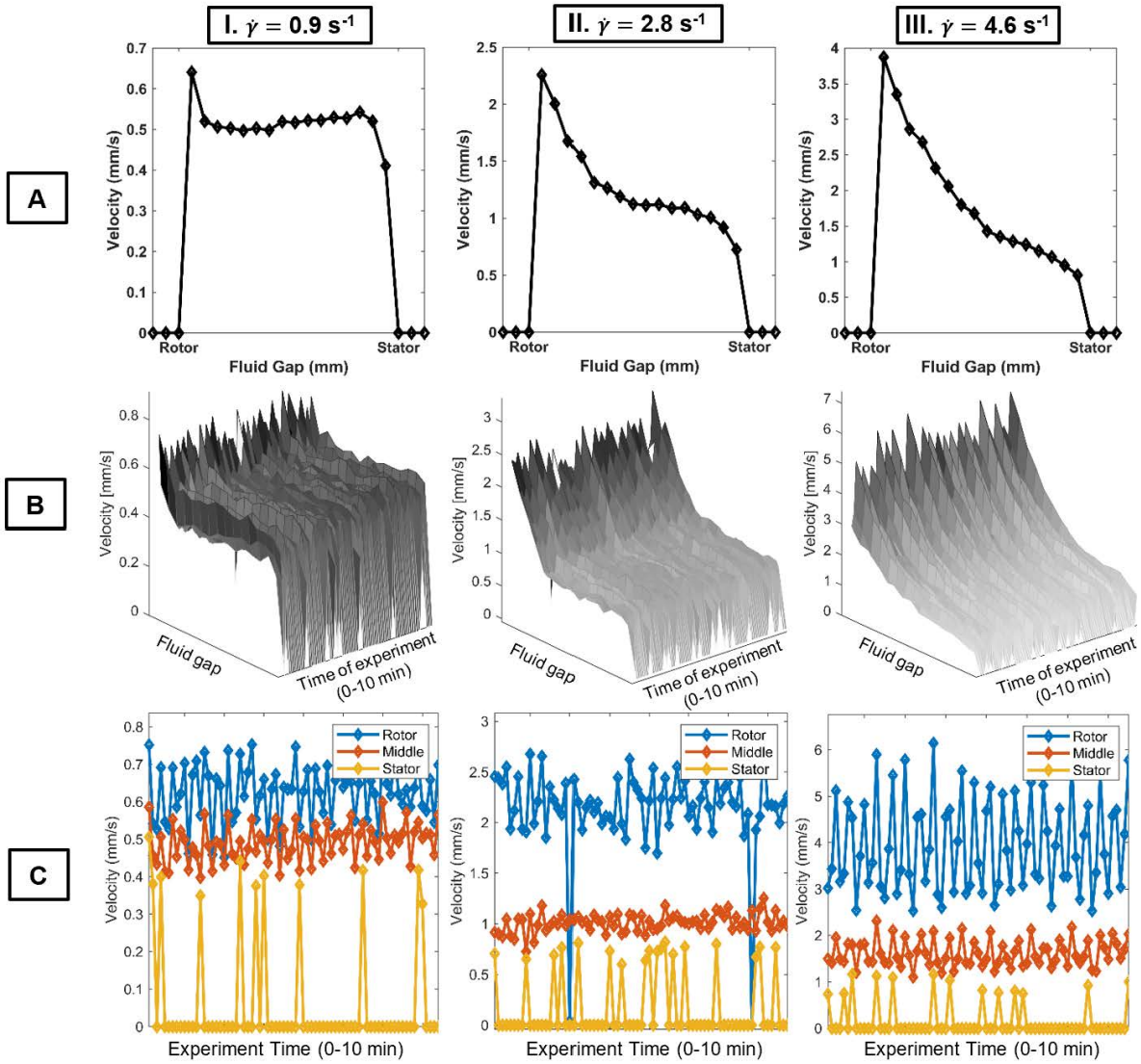


Figure A.8: **Rows A-B, Columns I-III**. 1D NMR velocimetry experiments for a 7% w/v NCC suspension in 0.1 NaCl. **Rows A:** Steady state, 1D velocity profiles, with 16 scans and total acquisition time of 1 minute, 12 seconds and a pixel resolution of approximately 65 µm. **B:** Surface plots for 1D velocity profiles from an unsteady-state experiment with 75 experiments averaged over 2 scans and total time acquisition of approximately 10 minutes, 12 seconds. **C:** Velocity profiles from the same unsteady-state experiment as B, but displayed at three discrete points across the 1 mm sample Couette cell fluid gap (rotor, middle and stator) for all time points, which demonstrate velocity changes across the experiment time and fluid gap; fluctuations occur mainly at the stator for this concentration. **Columns I:** Shear rate of $\dot{\gamma} = 0.9$ s^{-1}; **II:** Shear rate of $\dot{\gamma} = 2.8$ s^{-1}; **III:** Shear rate of $\dot{\gamma} = 4.6$ s^{-1}. The data presents a yielding behavior accompanied by shear banding at $\dot{\gamma} = 2.8$ s^{-1}. Rotor and stator data points are approximately 58.6 µm from the physical walls.

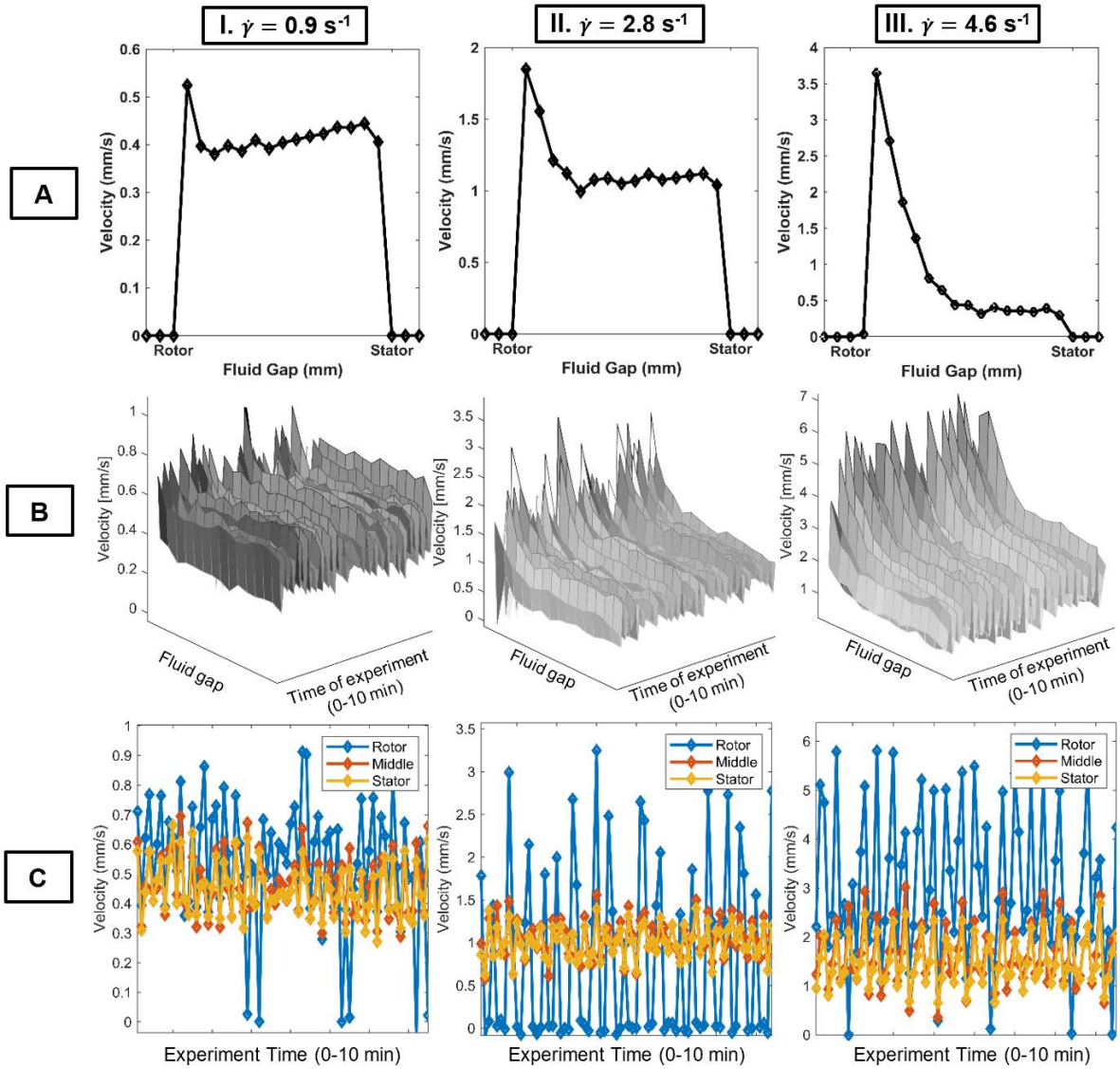


Figure A.9: **Rows A-B, Columns I-III**. 1D NMR velocimetry experiments for a 12% w/v NCC suspension in 0.1 NaCl. **Rows A:** Steady state, 1D velocity profiles, with 16 scans and total acquisition time of 1 minute, 12 seconds and a pixel resolution of approximately 65 µm. **B:** Surface plots for 1D velocity profiles from an unsteady-state experiment with 75 experiments averaged over 2 scans and total time acquisition of approximately 10 minutes, 12 seconds. **C:** Velocity profiles from the same unsteady-state experiment as B, but displayed at three discrete points across the 1 mm sample Couette cell fluid gap (rotor, middle and stator) for all time points, which demonstrate velocity changes across the experiment time and fluid gap; for this concentration, significant, periodic fluctuations occur at the rotor, with a large degree of correlation across the gap. **Columns I:** Shear rate of $\dot{\gamma} = 0.9$ s^{-1}; **II:** Shear rate of $\dot{\gamma} = 2.8$ s^{-1}; **III:** Shear rate of $\dot{\gamma} = 4.6$ s^{-1}. The data presents a yielding behavior accompanied by shear banding at $\dot{\gamma} = 2.8$ s^{-1}. Rotor and stator data points are approximately 58.6 µm from the physical walls.

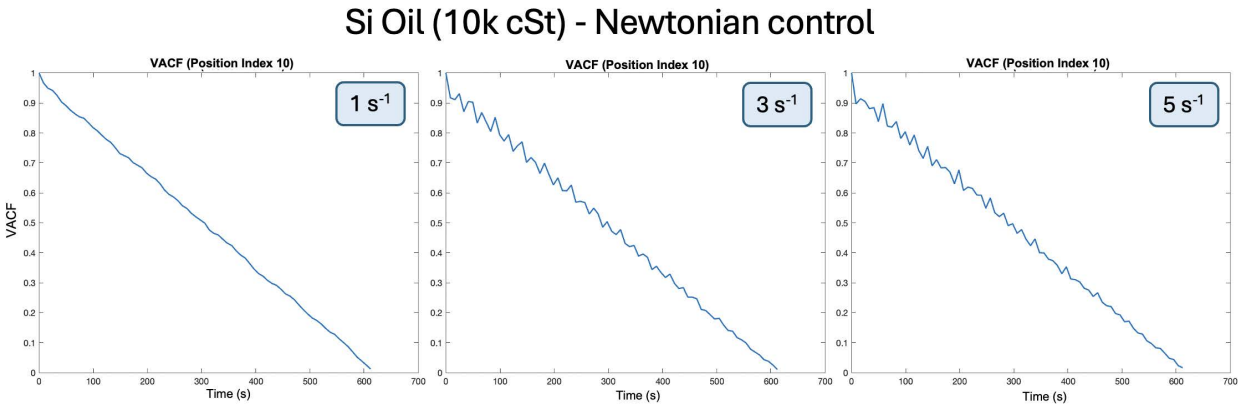


Figure A.10: Velocity autocorrelation functions for 10k cSt silicone oil Newtonian control at shear rate set points of $\dot{\gamma} = 1$, 3, and 5 s^{-1}.

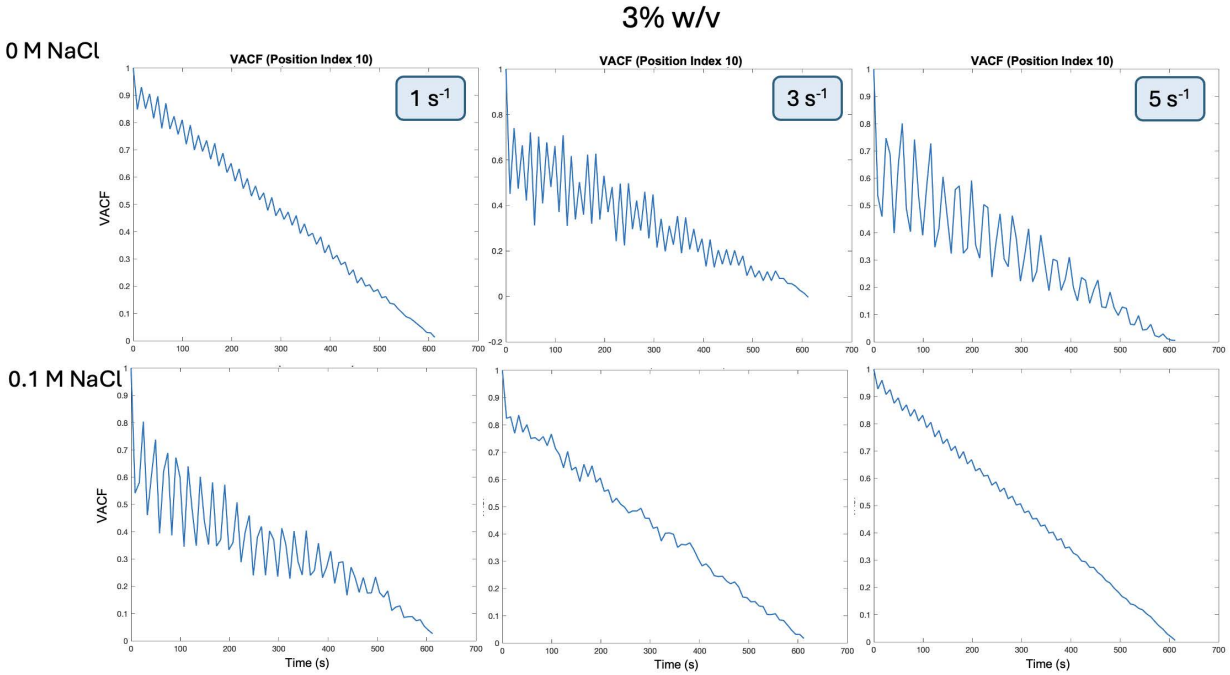


Figure A.11: Velocity autocorrelation functions for 3% w/v NCC with 0 and 0.1 M NaCl at shear rate set points of $\dot{\gamma} = 1$, 3, and 5 s^{-1}.

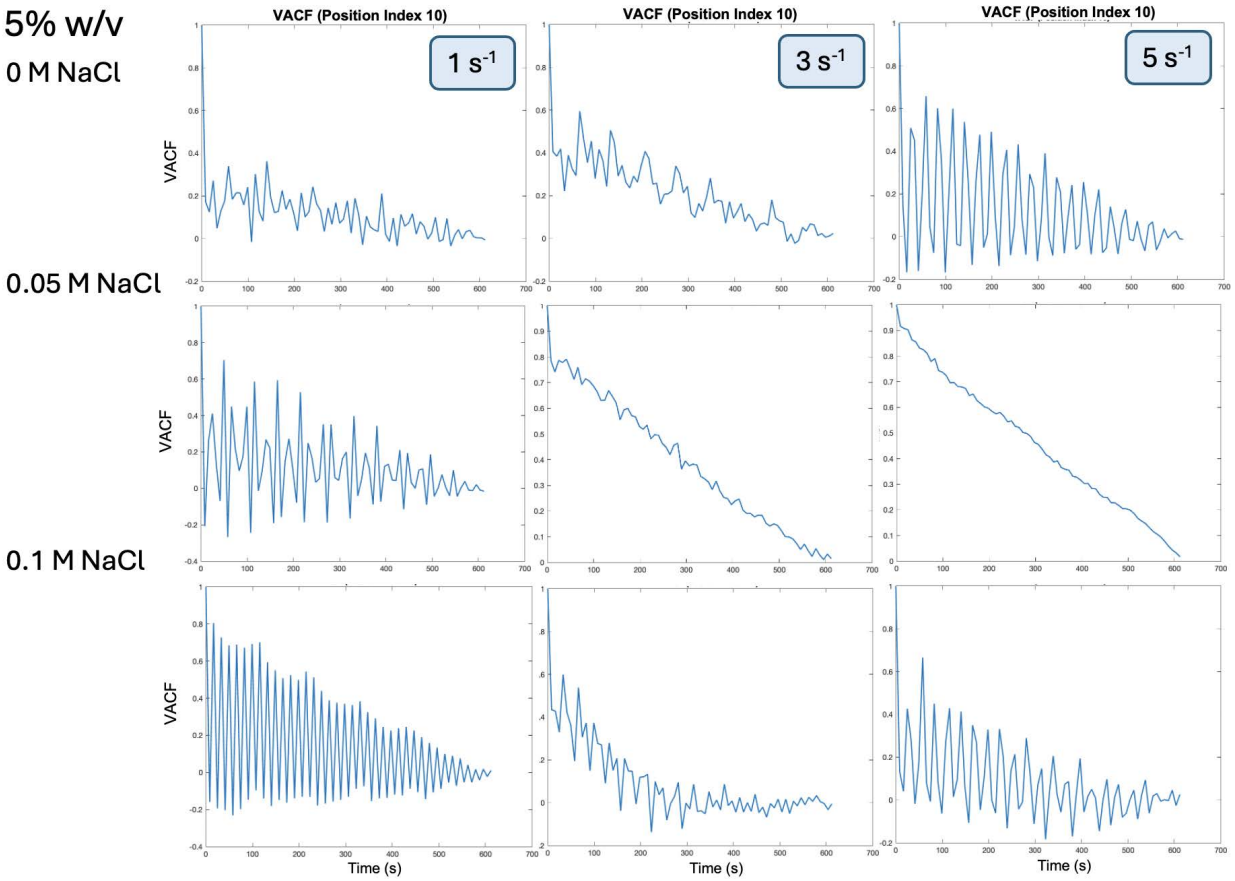


Figure A.12: Velocity autocorrelation functions for 5% w/v NCC with 0, 0.05, and 0.1 M NaCl at shear rate set points of $\dot{\gamma} = 1$, 3, and 5 s^{-1}.

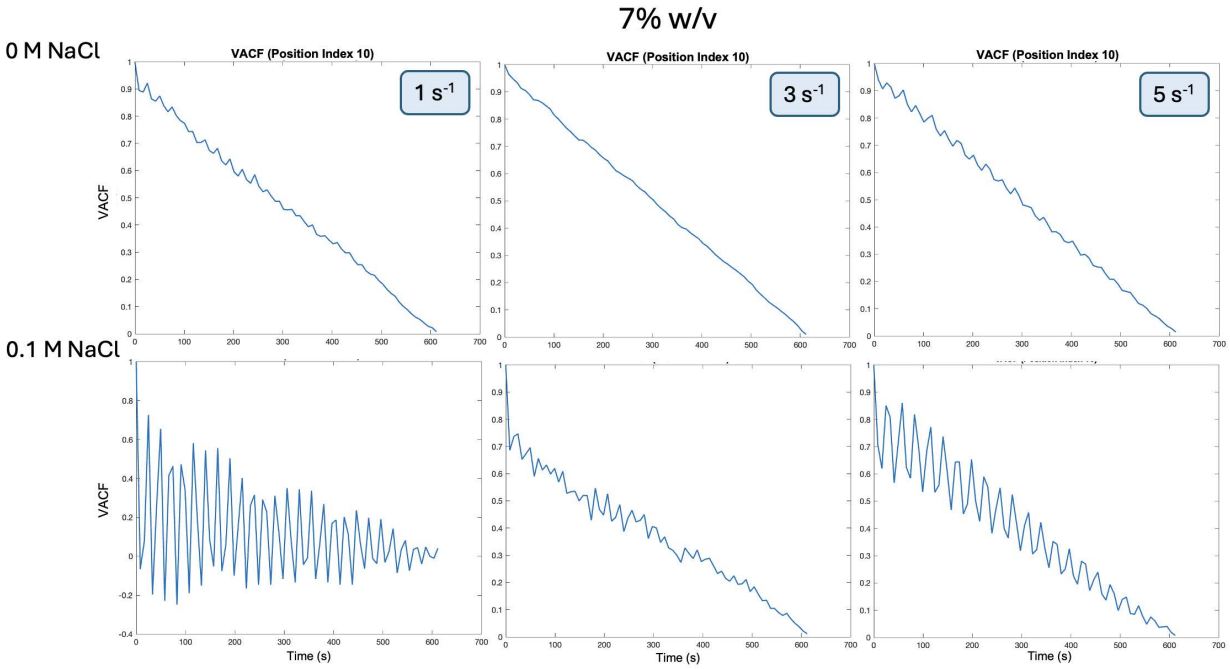


Figure A.13: Velocity autocorrelation functions for 7% w/v NCC with 0 and 0.1 M NaCl at shear rate set points of $\dot{\gamma} = 1$, 3, and 5 s^{-1}.

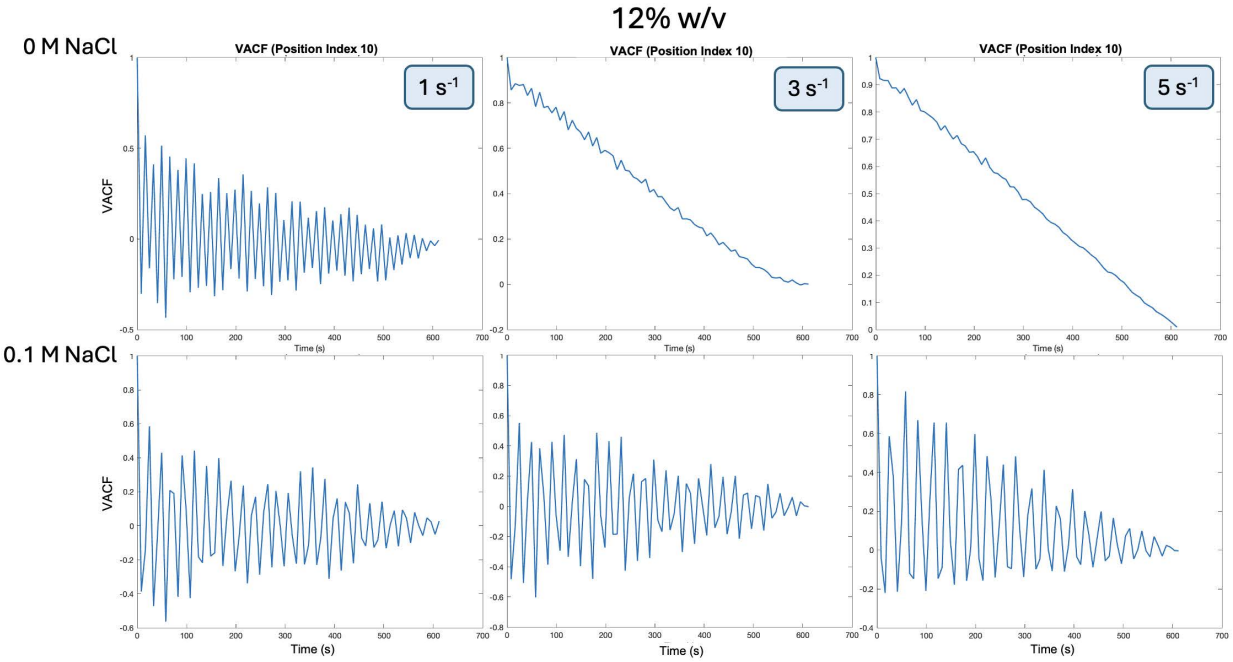


Figure A.14: Velocity autocorrelation functions for 12% w/v NCC with 0 and 0.1 M NaCl at shear rate set points of $\dot{\gamma} = 1$, 3, and 5 s^{-1}.

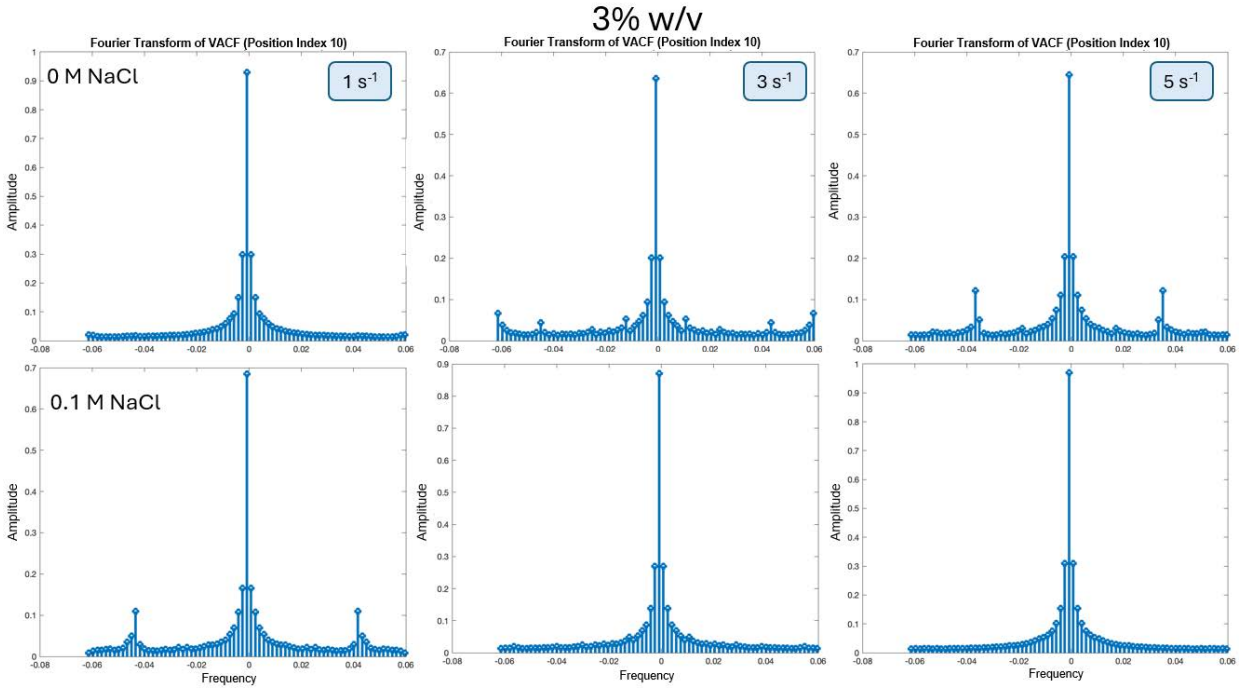


Figure A.15: Fourier transforms of velocity autocorrelation functions for 3% w/v NCC with 0 and 0.1 M NaCl at shear rate set points of $\dot{\gamma} = 1$, 3, and 5 s^{-1}.

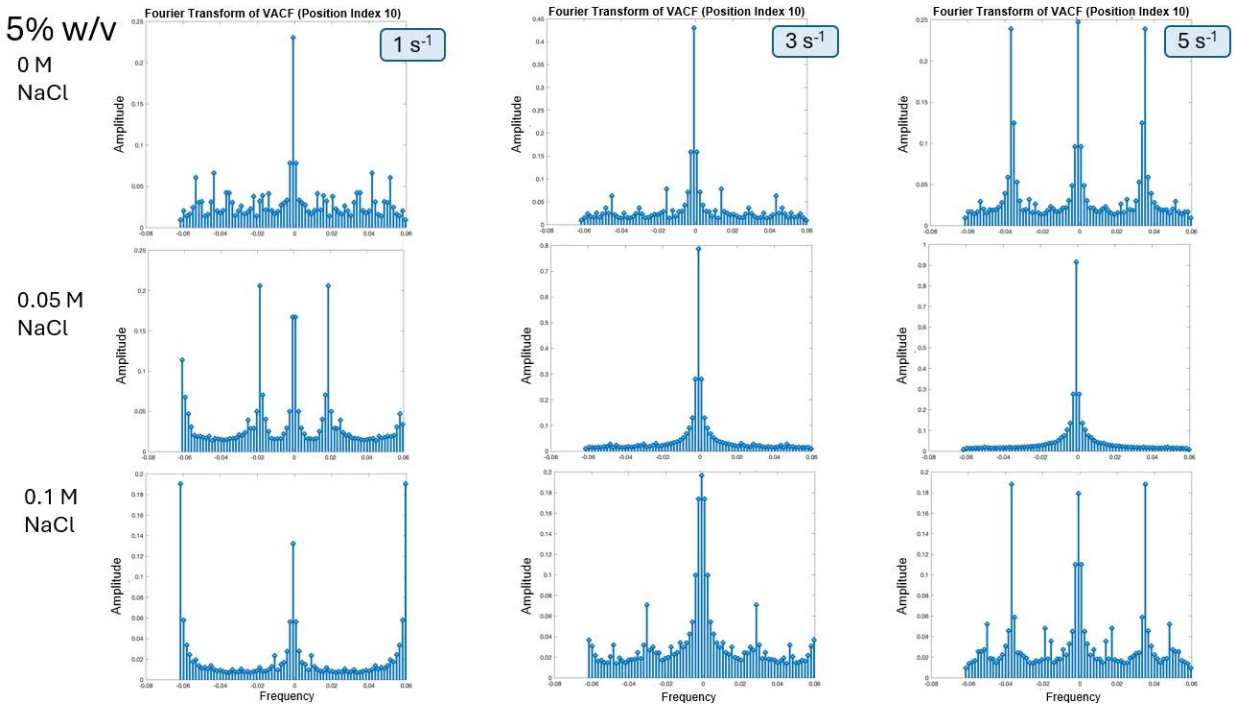


Figure A.16: Fourier transforms of velocity autocorrelation functions for 5% w/v NCC with 0, 0.05, and 0.1 M NaCl at shear rate set points of $\dot{\gamma} = 1$, 3, and 5 s^{-1}.

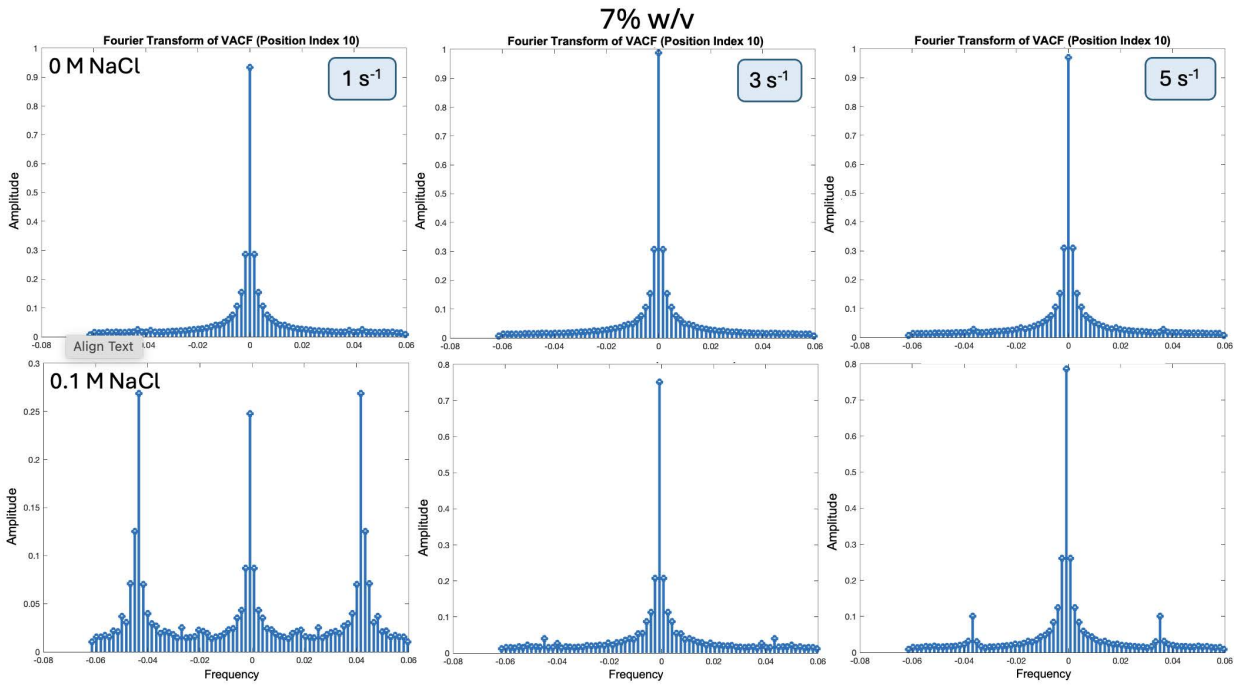


Figure A.17: Fourier transforms of velocity autocorrelation functions for 7% w/v NCC with 0 and 0.1 M NaCl at shear rate set points of $\dot{\gamma} = 1$, 3, and 5 s^{-1}.

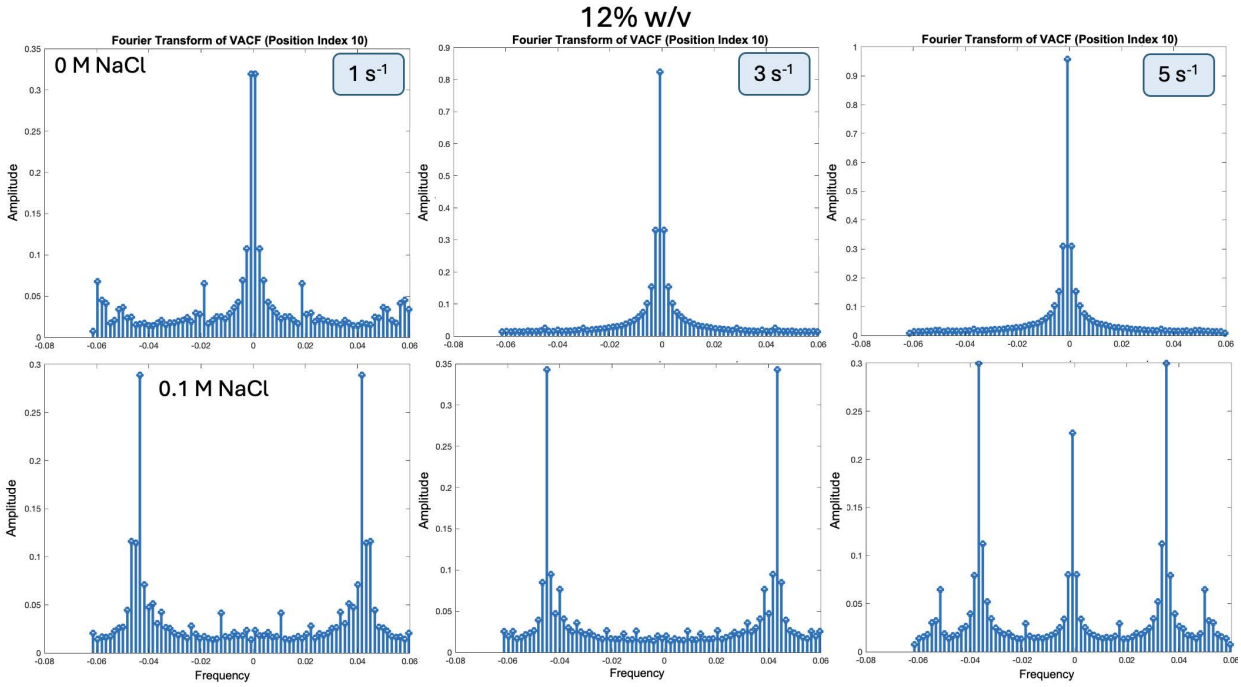


Figure A.18: Fourier transforms of velocity autocorrelation functions for 12% w/v NCC with 0 and 0.1 M NaCl at shear rate set points of $\dot{\gamma} = 1$, 3, and 5 s^{-1}.